

*Novel method to measure deformation  
stress at high pressure and temperature*

DISSERTATION

submitted to obtain the academic degree of Doctor of Natural Sciences

(Dr. rer. nat.)

of the Bayreuth Graduate School of Mathematical and Natural Sciences

(BayNAT)

of the University of Bayreuth

***Jonathan David Dolinschi***

from *Timișoara, Romania*

Bayreuth, 2024



This doctoral thesis was prepared at the department of *Bayerisches Geoinstitut* at the University of Bayreuth from *May 2020* until *May 2024* and was supervised by Prof. Dr. Daniel Frost.

This is a full reprint of the thesis submitted to obtain the academic degree of Doctor of Natural Sciences (Dr. rer. nat.) and approved by the Bayreuth Graduate School of Mathematical and Natural Sciences (BayNAT) of the University of Bayreuth

Form of the dissertation: Monographic thesis

Date of submission: 05.06.2024

Admission by the executive board: 13.06.2024

Date of defence: 16.08.2024

Acting director: Prof. Dr. Jürgen Köhler

Doctoral committee:

Prof. Dr. Daniel Frost (reviewer)

Prof. Dr. Johannes Buchen (reviewer)

PD Dr. Gerd Steinle-Neumann (chairman)

Prof. Dr. David Rubie

## Acknowledgements

First and foremost, I would like to acknowledge the vast amount of work put forth by all technicians at BGI. Their tireless work is not usually represented on the co-author's list in published papers, but everyone at BGI can confirm that without them, very little would get done here. The excellent sample prep technicians, Raphael Njul and Alexander Röther, whose expert hands could not be replicated by anyone else, are crucial for every experiment. Even during beamtime crunch, they always came through. The chemist, Ulrike Trenz, never left the chemistry lab unstocked. If I needed a chemical, she would source it, no questions asked. Scientists may put together the assembly parts for every experiment, but without the world-class machinists Heinz Fischer and Stefan Übelhack, there would be no parts to assemble. Their ability to interpret the chicken-scratch designs and drawings handed over by scientists without an engineering bone in them is near-to-miraculous. My work especially relied heavily on the electronics and software technicians, Gerald Bauer and Linhardt Sven. I began this work as a geologist with rocks on the brain but, because of their endless patience dealing with my questions and fumbling suggestions, ended with a head half-full of circuits and equations. When it comes to trusting excitable researchers with expensive equipment, the equipment technicians at BGI, Dorothea Wiesner and Detlef Krauß, had perhaps too much faith in us not to hit the polepiece or ram some expensive detector against our sample. Thankfully, I avoided both. The secretaries worked tirelessly to reduce the paperwork load on us. Janina Scharnagel and Petra Buchert know well enough that a scientist will gladly read 20 pages of published papers but dread having to fill in a simple form. Without them, I'd still be filling out forms to this day.

When it comes to the research itself, we are lucky to have such a deep pool of expertise at BGI. First and foremost, Dr. Dan J. Frost. I may have gone radio silent sometimes, but after smashing my head against a problem by myself, a short meeting with him would immediately give me new possible solutions to try. Dr. Tiziana Boffa and Dr. Alex Kurnosov did an excellent job at giving me a crash-course in Brillouin spectroscopy when I suddenly announced I needed to use the technique. Also, Dr. Sergio Speziale at Helmholtz-Zentrum Potsdam, who provided me not only with access to his equipment at the Brillouin setup in DESY, but also his time and knowledge. No matter how long we talked, he still had more to teach me. For beamtime help and general advice and guidance, I must thank Dr. Adrien Néri, Lianjie Man, Melanie Pöppelbaum, Dr. Lin Wang, and Dr. Amrita Chakraborti. They provided not only scientific help, but friendship too that will follow me long after my time at BGI. Dr. Robert Farla, the beamline scientist at P61B in PETRA-III, was endlessly gracious with his time and equipment. He sets a high standard for beamline scientists.

To the rest of the people here who made my stay in Bayreuth enjoyable with friendship and time away from work too, Pedro Valdivia Munoz, Dr. Edith Kubik, Lara Munoz, Philipp Scholz, Dr. Kiril Vlasov, and many others too. You helped keep me sane, even through the worst of it. My family too – parents, sisters, uncles, aunts, and cousins – of course, who I wish I could've seen more during my time here, but world events and travel prices kept it just out of reach. Above all, Britany Kulka, because without you I wouldn't try so hard to accomplish something with my life.



<b>ABSTRACT</b> .....	<b>I</b>
<b>ZUSAMMENFASSUNG</b> .....	<b>III</b>
<b>SYMBOLS AND UNITS</b> .....	<b>VI</b>
<b>1. INTRODUCTION</b> .....	<b>1</b>
1.1. HIGH PRESSURE TECHNIQUES .....	1
1.1.1. History of large volume presses.....	1
1.1.2. Deformation at high pressure .....	5
1.1.3. Synchrotron x-ray diffraction .....	12
1.1.4. Stress measurement with XRD.....	14
1.2. STRAIN.....	21
1.3. STRESS .....	22
1.4. ELASTICITY .....	25
1.5. DIELECTRICS .....	29
1.5.1. Dielectric polarization.....	29
1.5.2. Dielectric electrical resistivity.....	32
1.5.3. Piezoelectric Phenomenon.....	34
1.5.4. Piezoelectric tensors.....	38
1.5.5. Piezoelectric crystal orientations .....	41
1.6. BRILLOUIN SPECTROSCOPY .....	42
<b>2. METHODS</b> .....	<b>50</b>
2.1. LARGE VOLUME PRESS FOR DEFORMATION .....	50
2.1.1. 6-ram press .....	50
2.1.2. Displacement encoder calibration.....	54
2.2. PIEZOELECTRIC ASSEMBLY.....	60
2.2.1. 15/10 cubic assembly design .....	60
2.2.2. Electrical conductivity design considerations .....	66
2.2.3. Thermally activated electrical conduction design considerations .....	69
2.2.4. Effects of change in electric resistivity .....	71
2.2.5. Deformation geometry.....	78
2.2.6. Charge measurement process.....	81
2.3. PIEZOELECTRIC CRYSTALS .....	85
2.3.1. Quartz.....	85
2.3.2. CTGS.....	93
2.4. X-RAY DIFFRACTION .....	99
2.4.1 X-ray diffraction to verify piezoelectric assembly .....	99
2.4.2. P61B beamline at DESY.....	101
2.4.3. P61B anvils and pressure/temperature calibration.....	106

2.4.4. Strain measurement at the beamline.....	115
2.5. BRILLOUIN SPECTROSCOPY OF CTGS AT HIGH PRESSURE .....	118
2.6. SAMPLE SYNTHESIS .....	124
2.6.1. MgO.....	125
2.6.2. Mg-Al Spinel.....	125
2.6.3. San Carlos olivine .....	126
2.6.4. Single crystal MgO and Fo.....	128
<b>3. RESULTS .....</b>	<b>128</b>
3.1. SAN CARLOS OLIVINE, MGO, AND SPINEL DEFORMATION AT SYNCHROTRON .....	128
3.2. SAN CARLOS OLIVINE DEFORMATIONS WITH XRD.....	130
3.2.1. Linear compression deformation on San Carlos olivine .....	130
3.2.2. Linear tension deformation on San Carlos Olivine .....	137
3.2.3. Stepped deformation of San Carlos olivine .....	146
3.2.4. Oscillation deformation of San Carlos olivine .....	151
3.3. LINEAR COMPRESSION AND TENSION DEFORMATIONS ON MGAL <sub>2</sub> O <sub>4</sub> SPINEL AT ROOM TEMPERATURE WITH XRD .....	158
3.4. LINEAR COMPRESSION AND TENSION DEFORMATIONS ON MGO AT ROOM TEMPERATURE WITH XRD.....	167
3.5. SINGLE CRYSTAL MGO AND FO DEFORMATION IN THE CREEP REGIME .....	174
3.6. RAMAN SPECTROSCOPY OF CTGS.....	180
3.7. BRILLOUIN SPECTROSCOPY RESULTS.....	185
<b>4. DISCUSSION .....</b>	<b>190</b>
4.1. SAN CARLOS OLIVINE DEFORMATION WITH XRD .....	190
4.2 ANVIL POSITION DISCREPANCY .....	197
4.3. SINGLE CRYSTAL DEFORMATION WITHOUT XRD .....	200
4.4. BRILLOUIN SPECTROSCOPY ON CTGS .....	207
4.4.1 Linear modeling of elastic stiffness coefficients .....	207
4.4.2. Elastic compliance coefficient $S_{14}$ of CTGS.....	209
4.4.3. Third order finite strain modeling of elastic stiffness coefficients .....	213
4.4.4. Born stability criteria of CTGS.....	215
<b>5. CONCLUSION.....</b>	<b>218</b>
<b>BIBLIOGRAPHY .....</b>	<b>222</b>

## Abstract

High pressure and temperature deformation experiments, which require deviatoric stress measurements to be made as a function of sample strain rate, are important for determining the rheological properties of mantle rocks, which control plate motions and mantle convection. Classical deformation devices only operate at pressures up to 2 GPa. Large volume presses (LVP) can be used to deform rocks at higher pressures, but stresses must then be determined from the analysis of the distortion of powder X-ray diffraction (XRD) Debye rings, which not only requires a synchrotron X-ray source but results in large uncertainties and low sensitivity. This thesis describes the development, design, and testing of a novel method of stress determination in the LVP, which uses piezoelectric single crystal disks. A piezoelectric disk is placed in the deformation column of a 10 mm cubic LVP assembly with electrodes attached to the opposing faces. When the assembly is deformed at high pressure in a six ram multianvil press, the force applied to the crystal can be determined from the resulting piezoelectric charge. Using the area of the piezoelectric crystal and measured force, the deviatoric stress can be calculated. Piezoelectric crystals exhibit an Arrhenius-like decrease in electrical resistivity with increasing temperature, due to charge leakage. To mitigate this, the design incorporates several strategies: a large temperature gradient in the assembly to maintain low crystal temperatures during heating with an offset furnace, heating electrodes placed at a 90° angle to deformation direction to reduce ripple noise and keep the hot electrodes distant, a diamond heat sink between the piezoelectric crystal, and anvil and single crystal MgO surrounding the crystal to limit grain-boundary conduction.

The assembly has been tested at pressures between 1–7 GPa and temperatures of 25–1300 K. Initial experiments with  $\alpha$ -quartz revealed excessive voltage drift during heating and anomalous charge reversals during deformation that can be attributed to ferroelastic twinning driven by deviatoric stress. The critical switching stress is 400 MPa at 300 K and below 100 MPa at 473 K. Among quartz-structured materials, the critical switching stress should be inversely proportional to the magnitude of the  $S_{14}$  elastic compliance coefficient. To address these issues,  $\text{Ca}_3\text{TaGa}_3\text{Si}_2\text{O}_{14}$  (CTGS) was used to replace  $\alpha$ -quartz in the assembly. CTGS exhibits significantly higher electrical resistance across all temperatures and does not undergo ferroelastic switching. Literature data at 1 bar confirms that the  $S_{14}$  for  $\alpha$ -quartz is 70 times larger than that for CTGS.

To test the accuracy of piezoelectric stress determinations, deformation experiments were performed on San Carlos olivine at the P61B beamline of the DESY synchrotron at 1–7 GPa

and 600–1300 K. Stress determinations were also made by examining the distortion of sample XRD Debye rings. This results in a substantial spread in stress determination, however, depending on which reflections from lattice planes are examined. For San Carlos olivine, for example, stresses in some cases ranged between -2 to 4 GPa when 23 different lattice places were considered. The average XRD stress was found to be in good agreement with the piezoelectric-derived stress. However, whereas XRD cannot resolve stresses below 0.1 GPa and has uncertainties of  $\pm 0.1$  GPa, the piezoelectric method is sensitive to stresses as low as 0.01 GPa with an 18.5% uncertainty. One experiment revealed a ferrobielastic switch in CTGS. Four compression deformation experiments entered the steady state creep regime, which allowed parameters for a unified exponential flow law to be calculated, that agreed well with the range of previous literature values. Piezoelectric and XRD-calculated stresses were also in good agreement for room temperature deformation measurements made on Mg-Al spinel and MgO samples.

Deformation experiments were also performed on single crystals of MgO and forsterite between 1.5–3.0 GPa and 600–1300 K, with stresses measured only with the piezoelectric method. The experiments that reached creep regime were analyzed using the power law creep equation. The activation energies ( $E^*$ ), 67 kJ/mol for forsterite, 77 kJ/mol for MgO, fit within the range of literature values. However, the activation volumes, 6.5 cm<sup>3</sup>/mol for forsterite, 9.9 cm<sup>3</sup>/mol for MgO, are larger than reported values from XRD measurements.

To determine the effect of pressure on the  $S_{14}$  of CTGS and to determine its mechanical stability according to the Born stability criteria, Brillouin spectroscopy measurements were performed on CTGS in a diamond anvil cell (DAC) up to 10 GPa. The CTGS  $S_{14}$  value is average  $5.5 \times 10^{-5}$  GPa<sup>-1</sup> compared to  $\alpha$ -quartz,  $2.1 \times 10^{-3}$  GPa<sup>-1</sup>, across the experimental pressure range, only surpassing it above 8 GPa. Additionally, the Born stability criteria were violated only at 104 GPa, indicating that CTGS is exceptionally stable, unlike  $\alpha$ -quartz, which undergoes amorphization by 35 GPa. This novel assembly and stress determination method will allow deformation experiments at pressures relevant to the Earth's mantle to be performed with a higher accuracy than XRD measurements and without the need of a synchrotron facility.

## Zusammenfassung

Deformationsversuche bei hohem Druck und hoher Temperatur, bei denen die deviatorischen Spannungsmessungen als Funktion der Probenverformungsgeschwindigkeit durchgeführt werden, sind wichtig, um die rheologischen Eigenschaften von Mantelgesteinen zu bestimmen, die die Plattenbewegungen und die Mantelkonvektion steuern. Klassische Deformationsgeräte arbeiten nur bei Drücken bis zu 2 GPa. Großvolumenpressen (LVP) können verwendet werden, um Gesteine bei höheren Drücken zu verformen, aber die Spannungen müssen dann aus der Analyse der Verzerrung von Pulver-Röntgenbeugungs-Debye-Ringen (XRD) bestimmt werden, was nicht nur eine Synchrotron-Röntgenquelle erfordert, sondern auch große Unsicherheiten und eine geringe Empfindlichkeit mit sich bringt. Diese Dissertation beschreibt die Entwicklung, das Design und die Prüfung einer neuartigen Methode zur Spannungsbestimmung in der LVP, die piezoelektrische Einkristallscheiben verwendet. Eine piezoelektrische Scheibe wird in die Deformationssäule einer 10 mm kubischen LVP-Anordnung mit an den gegenüberliegenden Flächen angebrachten Elektroden eingesetzt. Wenn die Anordnung unter hohem Druck in einer Sechs-Stempel-Pressen verformt wird, kann die auf den Kristall ausgeübte Kraft aus der resultierenden piezoelektrischen Ladung bestimmt werden. Unter Verwendung der Fläche des piezoelektrischen Kristalls und der gemessenen Kraft kann dann die deviatorische Spannung berechnet werden. Piezoelektrische Kristalle zeigen mit zunehmender Temperatur aufgrund von Ladungsverlusten einen Arrhenius-ähnlichen Rückgang des elektrischen Widerstands. Um dies zu mindern, beinhaltet das Design mehrere Strategien: ein großes Temperaturgefälle in der Anordnung, um niedrige Kristalltemperaturen während des Heizens mit einem versetzten Ofen aufrechtzuerhalten, Heizelektroden, die in einem Winkel von 90° zur Deformationsrichtung angeordnet sind, um Rauschstörungen zu reduzieren und die heißen Elektroden fernzuhalten, ein Diamant-Wärmeleiter zwischen dem piezoelektrischen Kristall und dem nächstgelegenen Stempel sowie Einkristall-MgO um den Kristall, um die elektrische Leitung an Korngrenzen zu minimieren.

Die Anordnung wurde bei Drücken zwischen 1–7 GPa und Temperaturen von 25–1300 K getestet. Erste Experimente mit  $\alpha$ -Quarz zeigten während des Heizens eine übermäßige Spannungsdrift und anomale Ladungsumkehrungen während der Verformung, die auf ferroelastische Zwillingsbildung durch deviatorische Spannung zurückgeführt werden können. Die kritische Umkehrspannung beträgt 400 MPa bei 300 K und unter 100 MPa bei 473 K. Unter den Quarz-strukturierten Materialien sollte die kritische Umkehrspannung umgekehrt proportional zur Größe des  $S_{14}$ -Elastizitätsmoduls sein. Um diese Probleme zu lösen, wurde  $\text{Ca}_3\text{TaGa}_3\text{Si}_2\text{O}_{14}$  (CTGS) verwendet, um  $\alpha$ -Quarz in der Anordnung zu ersetzen. CTGS zeigt

über alle Temperaturen hinweg einen deutlich höheren elektrischen Widerstand und unterliegt keinem ferroelastischen Verhalten. Literaturdaten bei 1 bar bestätigen, dass das  $S_{14}$  für  $\alpha$ -Quarz 70-mal größer ist als das für CTGS.

Um die Genauigkeit der piezoelektrischen Spannungsbestimmungen zu testen, wurden Deformationsversuche an San Carlos-Olivin an der P61B-Strahllinie des DESY-Synchrotrons bei 1–7 GPa und 600–1300 K durchgeführt. Spannungsbestimmungen wurden auch mithilfe der elastischen Verzerrung von XRD-Debye-Ringen durchgeführt. Dies führt jedoch zu einer erheblichen Streuung der Spannungsbestimmung, abhängig davon, welche Gitterebenen untersucht werden. Bei San Carlos-Olivin beispielsweise reichten die Spannungen in einigen Fällen zwischen -2 und 4 GPa, wenn 23 verschiedene Gitterebenen betrachtet wurden. Die durchschnittliche XRD-Spannung stimmte gut mit der piezoelektrisch abgeleiteten Spannung überein. Während XRD jedoch keine Spannungen unter 0,1 GPa auflösen kann und Unsicherheiten von  $\pm 0,1$  GPa aufweist, ist die piezoelektrische Methode empfindlich gegenüber Spannungen von bis zu 0,01 GPa mit einer Unsicherheit von 18,5 %. Ein Experiment zeigte einen ferroelastischen Übergang in CTGS. Vier Kompressionsverformungsexperimente erreichten den stationären Kriechbereich, was die Berechnung von Parametern für ein einheitliches exponentielles Fließgesetz ermöglichte, die gut mit dem Bereich vorheriger Literaturwerte übereinstimmten. Piezoelektrische und XRD-berechnete Spannungen stimmten auch bei Raumtemperaturverformungsmessungen an Mg-Al-Spinel- und MgO-Proben gut überein.

Deformationsversuche wurden auch an Einkristallen von MgO und Forsterit zwischen 1,5 – 3,0 GPa und 600–1300 K durchgeführt, wobei die Spannungen nur mit der piezoelektrischen Methode gemessen wurden. Die Experimente, die den Kriechbereich erreichten, wurden unter Verwendung der Kriechgleichung des Potenzgesetzes analysiert. Die Aktivierungsenergien ( $E^*$ ), 67 kJ/mol für Forsterit, 77 kJ/mol für MgO, liegen innerhalb des Bereichs der Literaturwerte. Die Aktivierungsvolumina, 6,5 cm<sup>3</sup>/mol für Forsterit, 9,9 cm<sup>3</sup>/mol für MgO, sind jedoch größer als die berichteten Werte aus XRD-Messungen.

Um den Effekt des Drucks auf das  $S_{14}$  von CTGS zu bestimmen und seine mechanische Stabilität nach den Born-Stabilitätskriterien zu überprüfen, wurden Brillouin-Spektroskopiemessungen an CTGS in einer Diamant-Stempelzelle (DAC) bis zu 10 GPa durchgeführt. Der CTGS  $S_{14}$ -Wert beträgt im Durchschnitt  $5,5 \times 10^{-5}$  GPa<sup>-1</sup> im Vergleich zu  $\alpha$ -Quarz,  $2,1 \times 10^{-3}$  GPa<sup>-1</sup>, über den gesamten experimentellen Druckbereich und übertrifft ihn nur bei über 8 GPa. Zusätzlich wurden die Born-Stabilitätskriterien erst bei 104 GPa verletzt, was

darauf hindeutet, dass CTGS außergewöhnlich stabil ist, im Gegensatz zu  $\alpha$ -Quarz, der bei 35 GPa amorph wird. Diese neuartige Anordnung und Methode zur Spannungsbestimmung ermöglicht Deformationsversuche bei Drücken, die für den Erdmantel relevant sind, mit höherer Genauigkeit als XRD-Messungen und ohne die Notwendigkeit einer Synchrotronanlage.

## Symbols and Units

Symbol	Meaning	Units
$P_o$	hydraulic oil pressure	bar
$\rho$	density	$\text{g/cm}^3$
$R$	electrical resistance	ohm ( $\Omega$ )
$\rho_R$	electrical resistivity	$\Omega \cdot \text{m}$
$T$	temperature	K, $^\circ\text{C}$
$E_a$	activation energy	eV
$\tau$	RC time constant	seconds
$F$	force	N
$\sigma_Y$	yield strength	MPa, GPa
$P_h$	hydrostatic pressure	MPa, GPa
$D_{a,b}, d_{a,b}$	press ram $a$ to ram $b$ distance	mm
$q$	electric charge	C
$P$	electric polarization	$\text{C/m}^2$
$E$	electric field	V/m
$\chi_e$	dielectric susceptibility	dimensionless
$\epsilon_0$	permittivity of free space	$8.854 \cdot 10^{-12} \text{ F/m}$
$k$	Boltzmann constant	$8.617 \cdot 10^{-5} \text{ eV/K}$
$\epsilon_r, \kappa$	relative permittivity, dielectric constant	F/m
$D$	electric induction	$\text{C/m}^2$
$\sigma_{ij}$	stress component	$\text{N/m}^2$
$\epsilon_{ij}$	strain component	dimensionless
$c_{ij}$	generalized elastic coefficient	dimensionless
$S_{ij}$	elastic compliance coefficient	$\text{m}^2/\text{N}$
$C_{ij}$	elastic stiffness coefficient	$\text{N/m}^2$
$d_{ij}$	piezoelectric strain coefficient	C/N
$e_{ij}$	piezoelectric stress coefficient	$\text{C/m}^2$
$X, Y, Z$	axes used to describe the orientation of piezoelectric crystal cuts	dimensionless
$a, b, c$	unit cell lattice parameters	$\text{\AA}$
$\alpha, \beta, \gamma$	angles between the unit cell lattice axes	degrees
$C_F$	capacitance of integrating capacitor	F
$A$	area	$\text{m}^2$
$\lambda$	wavelength	nm, $\text{\AA}$ , m
$d_{(hkl)}$	(hkl) lattice plane d-spacing	$\text{\AA}$
$G_r$	Reuss shear modulus	Pa
$G_v$	Voigt shear modulus	Pa
$G$	Gibb's free energy	J
$V$	Unit cell volume	$\text{\AA}^3$
$K$	bulk modulus	GPa
$E$	Young's modulus	GPa
$n$	stress exponent	dimensionless
$\mu$	shear modulus	GPa



# 1. Introduction

Stress measurements in deformation experiments are crucial for understanding the rheology and viscosity of the Earth's mantle. These measurements help reveal how materials behave under different pressure and temperature conditions, which is essential for modeling mantle convection and tectonic processes. However, with the advent of large volume presses, traditional methods of calculating deviatoric stresses from applied loads have become less reliable. Frictional losses from gaskets and the transition from fluid to solid pressure media at higher pressures contribute to this issue. Earlier methods relied on fluid media like gas and liquid, which provided more accurate stress transmission. The solid media now used at higher pressures introduce additional friction and complexities, further complicating stress calculations. This necessitates the development of new techniques to accurately measure stresses within large volume devices. This thesis aims to address this challenge by first reviewing the evolution of large volume devices capable of high-pressure deformation experiments and then focusing on the detailed use of the 6-ram press. This review is essential as many critical procedures for calibrating and performing deformation experiments with this apparatus have not been previously documented.

## 1.1. High pressure techniques

### 1.1.1. History of large volume presses

Percy William Bridgman heralded the age of high-pressure experiments in 1905. In that year, he pushed the experimental pressure limits available to researchers from 2,000 atmospheres, 0.2 GPa, to over 7,000 atm. He continued his work, breaking through the 10,000 atm barrier (1 GPa) and into the gigapascal age (McMillan, 2005).

## 1. Introduction



*Figure 1. The hydraulic press Percy Bridgman built, as described by Percy Williams in *The Physics of High Pressure* (1931) (Bridgman, 1931)*

By the time he won the Nobel Prize in Physics in 1946, the invention of what he called “Carboloy”, now commonly known as tungsten carbide, allowed for pressures above 100,000 atm, or 10 GPa, to be reached (Bridgman, 1946). These first devices consisted of a single ram forcing a piston into a stationary confining chamber. Such a device would later be developed into what is now referred to as a piston-cylinder. Bridgman initially applied force using a screw compressor turned with an almost 2-meter-long wrench, but later advanced to using a hydraulic press.

Further increases of pressure started to stagnate due to the limit of uniaxial compression inherent in piston-cylinder type of devices. A breakthrough occurred in 1958 when H. Tracy Hall published his design for the first multi-anvil apparatus (Hall, 1958) (MAA). This design

## 1. Introduction

was a tetrahedral anvil apparatus, utilizing four separate hydraulic rams driven into a central tetrahedral-shaped cavity, where a high-pressure assembly consisting of a pyrophyllite tetrahedron was placed. The eventual dominance of MAA in large volume press designs can be traced back to this development. His first design could only reach 10 GPa and 3000°C (Hall, 1958), but it opened the door to further improvements, and soon Akimoto and Fujisawa published their seminal paper on phase relations in the  $Mg_2SiO_4$ - $Fe_2SiO_4$  system (Akimoto & Fujisawa, 1968) at high pressure and temperature, and the study of the mantle beyond the transition zone began.

Further improvements then came quickly, and Hall once again was the first to publish a cubic anvil design in 1967 in which 6 independent rams were employed, advancing into a cubic space (Hall, 1967).

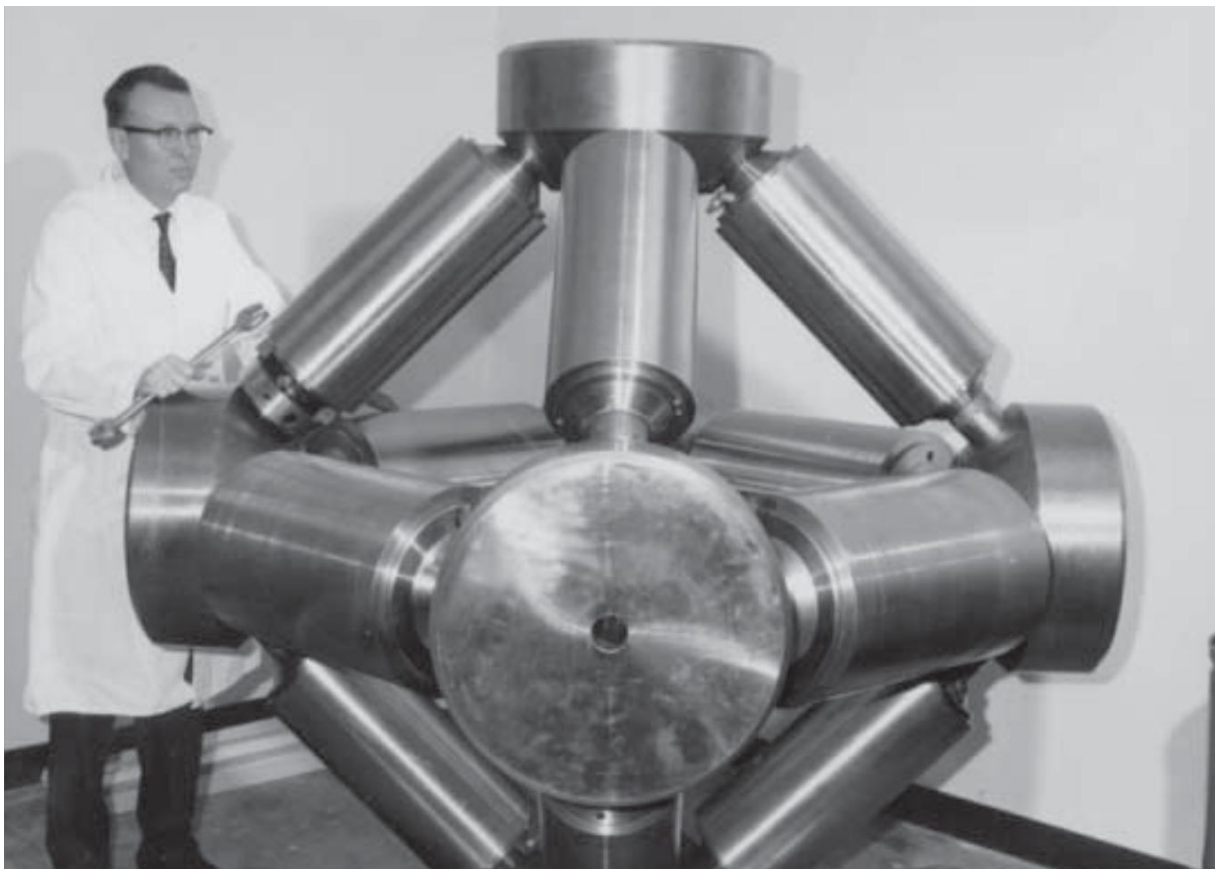


**Figure 2.** Tracy Hall and the cubic anvil apparatus that was developed at Brigham Young University, from Liebermann (2011) (Liebermann, 2011).

Issues remained, however, with synchronization of the independent anvil movements to ensure a cubic space is maintained. To maintain equal ram advancement, the initial designs for 6 ram presses utilized a single hydraulic ram applying force along a single vertical axis. Four trapezoid

## 1. Introduction

end blocks, which could slide along the inner surfaces of the upper and lower pyramid guide blocks, then converted this single vertical force to two horizontal perpendicular components (Osugi et al., 1964). In this way, the advancement of the horizontal rams matched the movement of the top ram. This design, known as the DIA-type (after ‘diamond’) was first described in literature in 1964 (Osugi et al., 1964).

The nominal upper limit of tetrahedral- and cubic-anvil devices remained about 10 GPa due to insurmountable limitations of the design. Naoto Kawai wanted to go beyond this limit, and guided by his belief that maximum pressures that can be generated by MAA’s would be proportional to the  $3/2$  power of the number of anvils (Kawai, 1966; Liebermann, 2011), he decided to design an 8-anvil, or octahedral MAA to achieve higher pressures (Kawai, 1966). He did this by taking a sphere of a hard material, and dividing it by three planes into a number of tapering cones or wedge-shaped anvils, in this case eight, that when assembled back together formed an octahedral cavity where the high-pressure assembly was placed (Kawai, 1966).

Kawai’s belief held, and pressures of up to 50 GPa were achieved by this split-sphere design (Kawai et al., 1970; Kawai & Endo, 1970). The design was, however, quite cumbersome, requiring careful alignment of all the wedges, covering of the entire sphere with a single-use rubber shell, and then all soaked in an oil reservoir. As the sizes of the sphere increased, it magnified all the issues (Kawai et al., 1973). In 1973, Kawai simplified the design immensely (Kawai et al., 1973). By utilizing eight second-stage WC cubes, with one corner truncated on each, a central octahedral cavity was created by the inwards-oriented corner truncations, when the cubes were stacked in a  $2 \times 2 \times 2$  three-dimensional arrangement. This became known as a “Kawai cell” (Price, 2010).

The second stage anvils consist of a sphere split into 6 wedges, with the apex truncated to form a square surface, which when assembled, three on the bottom, and three on the top, form a cubic cavity. Each set of 3 wedges are glued together in a hollow cylinder. The two cylinders are arranged opposing each other in a uniaxial press, with the top being lowered onto the bottom, and the Kawai cell placed in the cubic cavity. This final development of the design created the well-known and widely used Kawai-type apparatus known today.

Generally, today, the most widely used MAA comes in two broad forms. MA 6-8 is the configuration that utilizes six outer anvils that when driven inwards transfer force into a cubic space that consists of eight inner cubic anvils truncated to form an octahedral space for the assembly. MA 6-6 meanwhile utilizes the same six outer anvils, but they drive inwards onto six

## 1. Introduction

more truncated inner anvils, forming a cubic space for the assembly. Generally, MA 6-8 is capable of higher pressures than MA6-6. The MA 6-8 geometry currently holds the record for the highest pressures achieved in a large volume press, reaching up to 120 GPa at room temperature and 105 GPa at 1673 K (Yamazaki, 2020) with sintered diamond cubes. In practice, these pressures are difficult to achieve, requiring expensive cubes and vastly increased blowout rates. Most experimental work is done at lower pressures as ultra-high pressures shrink the sample volume so much that they approach those that can be produced in laser heated diamond anvil cells (DACs).

A DAC is a high-pressure device that primarily uses two opposing diamonds, with parallel polished flat culet surfaces, to exert pressure onto a sample inside a metal gasket squeezed between the culet surfaces. While the DAC technique allows extremely high pressures, up to 1 TPa (Dubrovinskaia et al., 2016) but usually below 400 GPa for beveled diamonds (O'Bannon et al., 2018), to be obtained, the sample volumes are notably small, often limiting the amount of material available for study. Nevertheless, mainly due to their suitability for *in situ* measurements, DACs have played a pivotal role in understanding material properties at conditions relevant to the deep Earth and other planetary interiors.

### 1.1.2. Deformation at high pressure

While high pressure records were being beaten through continuous developments in MAA devices, the goal of most researchers was to equalize stresses within the sample chamber and achieve pressures that were as close to hydrostatic as possible. This is only truly achievable if samples are surrounded by a fluid (Bassett, 2006). All high-pressure devices that use a solid pressure transmitting medium will invoke some amount of deviatoric stress due to the finite shear strength of all solids. Even so, most research aims to minimize deviatoric stress through strategic choices of confining material, annealing by heating, and precision of machining.

Precision of machining is crucial in the design and operation of high-pressure apparatus because it ensures the geometric accuracy of the sample chamber, which is essential for distributing stresses evenly across the sample. However, the Earth is a dynamic system driven by heat flow from the interior to the exterior, most efficiently transported through convection. The internal transportation of solid material is driven by stresses generated through this heat-loss process, that in turn result in material strain. To experimentally simulate the dynamics of Earth and planetary interiors requires an understanding of the stress–strain response of materials under high pressures and temperatures.

## 1. Introduction

In parallel with the development of higher confining pressures in MAA, work was being performed to increase the confining pressure limit at which samples could be exposed to controlled deviatoric stresses. The earliest pioneering work on deforming materials at high pressure was performed by F. D. Adams (Adams et al., 1901). It was self-evident that rocks, under a high differential load, crack and fail in a brittle manner, but geological field work showed that rocks can fold or even ‘flow’ under certain deformation conditions (Adams et al., 1901). An obvious factor that allowed the ductile flow of rocks was pressure.

These early experiments used a thick sleeve of wrought iron that was shrink-fitted by heating around a column of marble to provide confining pressure. Opposing hard pistons were then driven into the sample column to apply deviatoric stress (Adams et al., 1901). Adams succeeded in proving that rocks behave differently under confining pressure, changing in their response to stresses from brittle to more plastic behavior (Griggs, 1936). However, limitations in the process prevented him from measuring the strength of the materials.

David Griggs used Bridgman’s new high-pressure apparatus (Bridgman, 1931) of two opposing pistons that used liquid as the confining pressure within the pressure cavity and a steel jacket to withstand the higher pressures. In addition to the method of measuring hydrostatic pressures, he obtained some of the first measurements of the strength of minerals at high pressure (Griggs, 1936). By using a bottom piston to pressurize liquid kerosene surrounding a sample, a hydrostatic pressure of 10,000 atmospheres, or 1 GPa was achieved. By applying force to a secondary piston from above that was in direct contact with the sample, he could then apply a deviatoric stress, and by measuring the force applied and the sample displacement, it was finally possible to measure the strength of materials at high pressure.

At some point in his career Griggs also developed a cubic-anvil device, where all six-anvils could be actuated independently (Wentorf, 1962) to obtain hydrostatic pressures up to 8 GPa. However, he later returned to his original piston-cylinder based concept and continued the development of what would come to be referred to as the Grigg’s apparatus. This design was similar to his first piston-cylinder-type devices, but instead of using a liquid confining pressure, he instead switched to using a solid pressure medium, which allowed higher pressures to be achieved. Pressures of approximately 4 GPa have been reached in modern Grigg’s apparatus’ (Kaboli et al., 2017; Renner et al., 2001; Weidner et al., 1998).

Still, the use of a gas pressure medium has clear benefits. By using a gas or liquid, friction within the solid pressure transmitting medium is eliminated, and the force imposed through the

## 1. Introduction

rams onto the sample to deform it can be assumed to be the actual stress on the sample (Griggs, 1936; Paterson, 1970). By doing so, more accurate measurements can be made of the strength of materials. One such example of deformation experiments in a Grigg's apparatus with direct stress measurement of single crystal olivine (Fo) is displayed in **Figure 3**, modified from (Demouchy et al., 2013). Notice that even with a direct and in situ measurement, there is still a wide spread in the measured stress-strain curves. However, the downside is that liquids and gases solidify at relatively lower pressures than can be reached by modern MAA (Klotz et al., 2009). Silicone oils and various mixing ratios of ethanol, methanol, and water are ultimately limited to below 10 GPa before the mixtures freeze (Klotz et al., 2009).

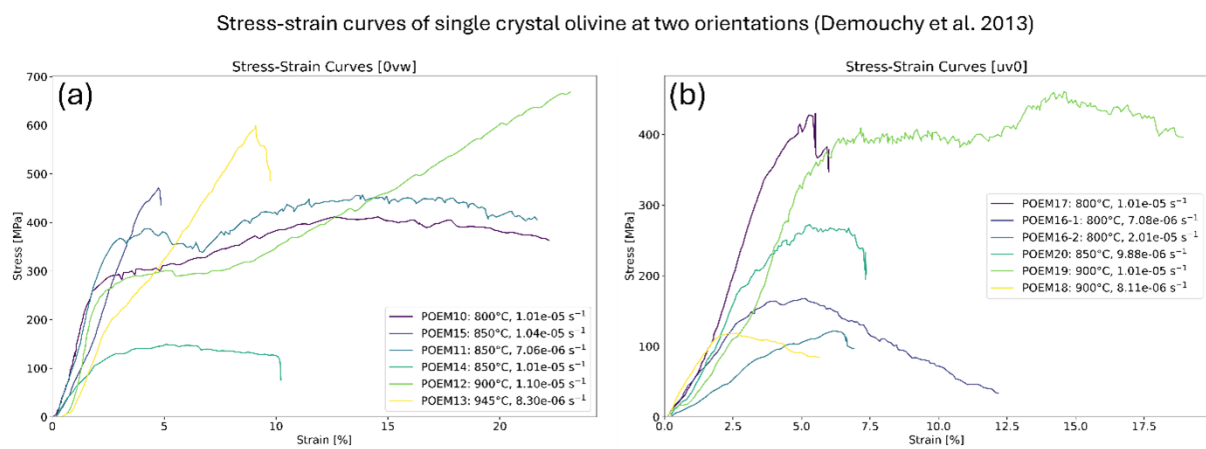


**Figure 3.** Stress versus strain for constant displacement rate experiments on deformed olivine single crystals. (a) For group 2, illustrating the mechanical responses of olivine crystals under tri-axial compression parallel to directions  $[0vw]$ , showing varying degrees of work hardening at different temperatures and strain rates. (b) For group 3, demonstrating the stress-strain behavior of olivine crystals under compressive loading parallel to directions  $[uv0]$ , highlighting the complex mechanical responses and strain softening at different temperatures and strain rates. The experiments were conducted using a high-resolution gas-medium high-pressure Grigg's apparatus with a hydrostatic confining pressure of 300 MPa. Stresses measured in situ with a strain sensor. Modified from (Demouchy et al., 2013).

Higher pressures can be achieved with heating to the melting temperature of the pressure medium, but high pressure and temperature gases and liquids retain large amounts of elastic energy. A gasket failure would then be dangerous and could result in an explosive release of pressure. These safety aspects have limited this technique to small pressure cavities, such as in the DAC. Various gases have been tested, but usually limited to noble gases and nitrogen to

## 1. Introduction

eliminate chemical reactions between the gas and the sample. The best of these, He, still freezes at 11.6 GPa at room temperature (Zha et al., 2004). Even so, for truly hydrostatic conditions and the elimination of frictional-induced deviatoric stresses during deformation, a liquid or gas pressure transmitting medium is required.

Paterson built upon Grigg's design and developed the Paterson apparatus, or Paterson rig (Paterson, 1970), described in 1970, that uses a gaseous pressure transmitting medium. This, however, limits pressures to below 1 GPa generally (Paterson, 1990) with no heating, and for deformation experiments the limit is generally below 500 MPa (Li et al., 2023; Paterson, 1990). With heating, the pressure is also generally limited to below 500 MPa, regardless of the deformation geometry (Paterson, 1970). Another deformation geometry possible in the Paterson rig is that of a rotational, or torsion experiment. In this geometry, the piston, instead of being driven inwards, is connected to a motor, and rotated. The rotation applies torsion deformation on the sample through the frictional coupling between the sample and the piston. High strains can be accomplished by rotating the piston beyond a single rotation.

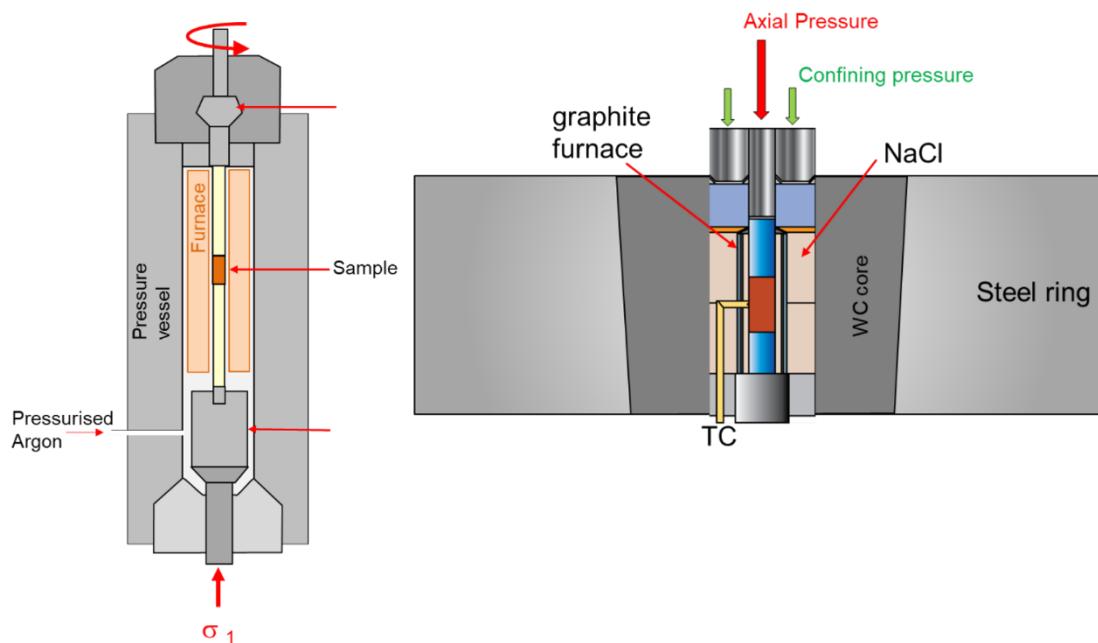


**Figure 4.** Schematic design of a Paterson (left) and Griggs (right) apparatus.

Several further devices have been developed in order to perform deformation experiments at pressures exceeding those that can be reached in the Griggs apparatus. A modified rotational Drickamer-type apparatus (Rotational Drickamer Apparatus, or RDA) has been shown to be capable of achieving very high strains and strain rates (0 to  $10^{-3} \text{ s}^{-1}$ ) in torsion, at pressures up to 15 GPa (Yamazaki & Karato, 2001). The Drickamer-type apparatus is an opposed anvil

## 1. Introduction

design, similar to the Bridgman anvil apparatus or a DAC, but with a containment ring around the anvils. Deformation in an RDA is achieved through rotation of one anvil with a rotational motor or actuator (Yamazaki & Karato, 2001).

However, quantifying the stress-strain relationships of materials is difficult. One of the reasons for this is because of the assumptions that must be made regarding the stress distribution across the sample (Kerber et al., 2019; Pugh, 1979). Apart from this, at higher pressures the hydrostatic stress across the sample is not uniform due to the torsion deformation. This can cause partial extrusion of the sample outwards and cause non-uniform strain around a specific radius around the circular sample. As a result of both of these complexities, the stress-strain relationship is difficult to characterize precisely or accurately (Pugh, 1979).

The need for controlled, uniaxial or triaxial deformation at high-pressures led to further developments of the aforementioned DIA by Yanbin Wang et al., (Wang et al., 2003). Starting with a typical DIA geometry, two additional hydraulic rams were added within the guide blocks, referred to as differential rams, that advance the upper and lower anvils. The differential-DIA, or D-DIA was thus created.

## 1. Introduction

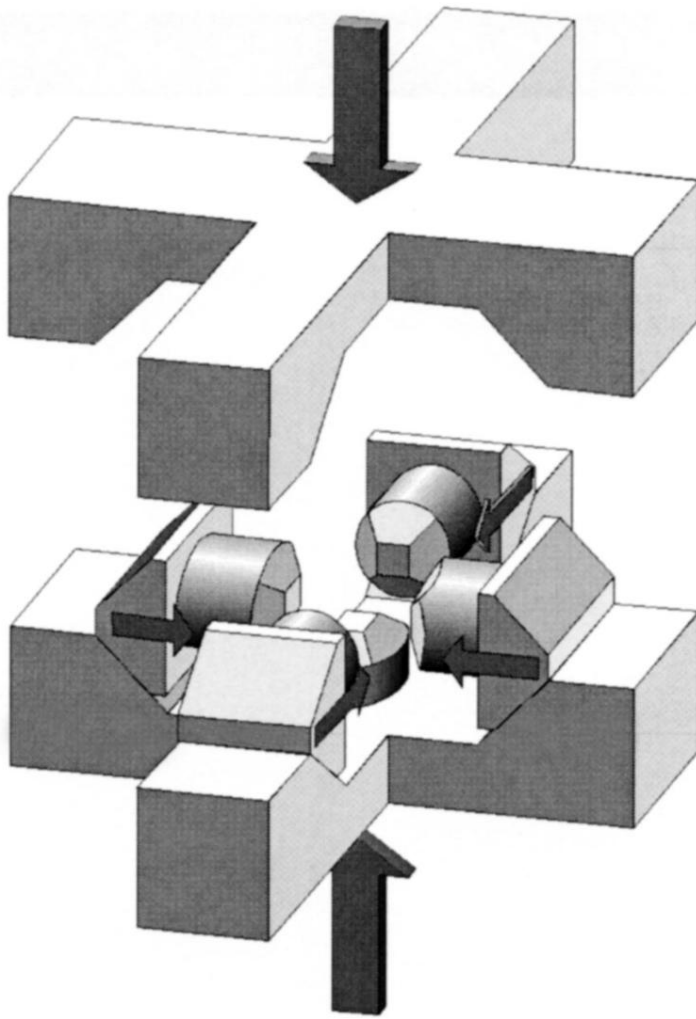


**Figure 5.** Conceptual diagram of the principle of operation of a D-DIA and how deviatoric stresses can be applied once at high-pressure. Figure from Wang et al. (2003) (Wang et al., 2003).

The typical operational temperature and pressure range is the same as the DIA. The upper and lower outer guide block rams are brought to the target hydraulic oil pressure, while the differential rams are kept fully retracted. This results in the compressed assembly remaining cubic. To deform the sample, the hydraulic oil pressure in the differential rams is increased, advancing them into the assembly at a controlled rate. At the same time, the hydraulic oil pressure is reduced in the guide block rams, causing the four side anvils to retract (Wang et al., 2003).

By using linear displacement transducers in the guide blocks, the horizontal side rams, and the differential ram displacement rates can be measured to high precision, with rates of  $10 \mu\text{m/s}$

## 1. Introduction

being possible. The deformation of the cubic assembly allows a cylindrical sample within the central column of the assembly, surrounded by hard materials such as alumina, to be deformed in pure shear, with no increase in confining pressure during deformation. The development of the D-DIA opened the door to solid-state deformation at axial strains beyond 30%, at hydrostatic pressures up to 15 GPa as reported by Wang et al., (2003).

Since then, advancements in anvil material hardness, reduction of truncation sizes, and refinement of the design has enabled the D-DIA to reach hydrostatic pressures of up to 25 GPa (Kawazoe et al., 2010). Since 2003, many D-DIAs have been built and operated at synchrotron beamlines and labs around the world. Because the D-DIA operates with six truncated anvils compressing a cubic assembly, it fundamentally operates on the same principle as the initially developed cubic MAA. However, in a DIA, as well as all D-DIA, the cubic cavity in which the assembly is compressed does not remain uniform at very high loads because of elastic deformation of the guide blocks as well as non-uniform friction between the sliding surfaces (Manthilake et al., 2012). As the load is increased to achieve higher pressures, small differences in the coefficient of friction between the surfaces have a larger and larger effect, and coupled with deformation in a D-DIA, the compressed assembly becomes non-cubic.

As opposed to a D-DIA, in a cubic press each anvil can be individually controlled by adjusting the oil pressure to each independent ram (Kawazoe et al., 2010; Manthilake et al., 2012; Osugi et al., 1964). The displacement rate can be dynamically adjusted to account for differential friction and ensure that the assembly remains cubic. However, the operation and control of ram displacements with sufficient precision to deform samples at controlled, low strain rates has been historically difficult and expensive (Carter et al., 1964; Shimada, 1981; Wang et al., 2003). Initial attempts suffered because anvils tended to advance at stepped, differential rates that were too slow to react to changes in sample strength. There were therefore issues with the precise control of strain rates (Carter et al., 1964; Shimada, 1981).

Advancements in technology have made the implementation of high-pressure deformation experiments in a 6-ram cubic press viable (Manthilake et al., 2012; Sano-Furukawa et al., 2014). The ram positions can be measured accurately using various types of linear encoders. The oil pressure of each ram can be independently and precisely controlled, allowing the Programmable logic controller (PLC) to control absolute anvil movements with sub-micron precision. This is achieved through the use of independently driven oil pressurization pistons, which employ a closed-loop control function that combines information on the ram positions from the encoders.

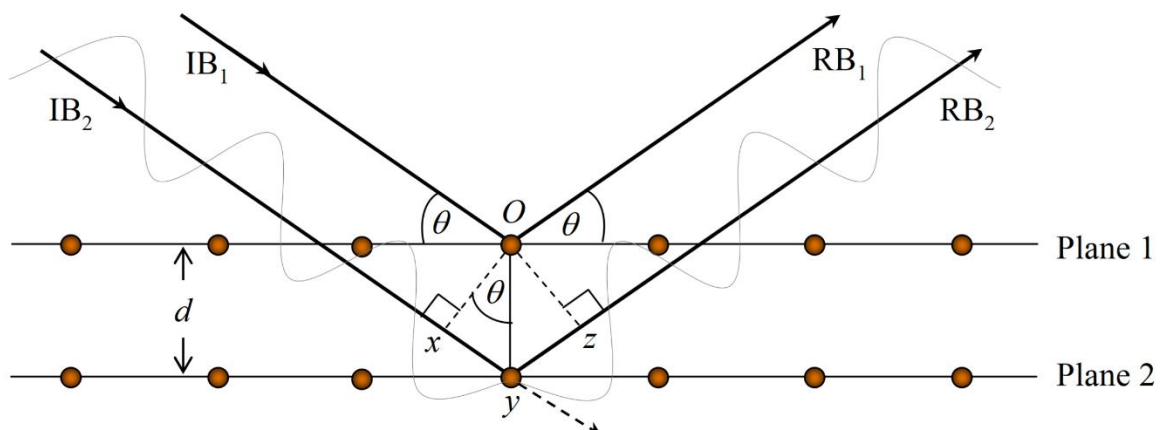
## 1. Introduction

### 1.1.3. Synchrotron x-ray diffraction

X-ray diffraction (XRD) is a powerful method for determining the structure of crystalline materials by exploiting the diffraction phenomenon that occurs along the atomic planes of a crystal. These planes, integral to the crystal's structure, are part of what is known as the crystal's Bravais lattice. Their orientation, relative to the crystal lattice's parameters, is denoted using Miller indices, which are three integers labeled  $h$ ,  $k$ , and  $l$ . Each trio of Miller indices specifies a unique set of parallel lattice planes within the crystal, characterized by an arrangement of atomic positions on a plane. The distance between these parallel planes, orthogonal to their surface, is termed the d-spacing and is typically measured in Angstroms. A single set of these parallel planes is represented by the notation  $(hkl)$ .

When the symmetry elements of the crystal lattice's space group are applied to a plane, the resulting set of planes, generated through the symmetry operations, are denoted as  $\{hkl\}$ . This notation represents a family of lattice planes that are equivalent from a crystallographic perspective (Powell, 2010; Kholkin et al., 2008; Sun et al., 2020). The assortment of  $\{hkl\}$  planes a crystal exhibits is distinctive to its space group, making the identification and characterization of crystalline materials based on their  $\{hkl\}$  planes and respective d-spacings an invaluable tool. This characterization process aids in identifying the crystal structure, provides insights into the material's composition when atomic positions are known, and facilitates phase identification, crystallinity assessment, and the detection of defects or impurities within the lattice.

When an X-ray beam interacts with a crystal lattice, the electrons surrounding the atoms act as diffraction centers. Given that the X-ray wavelength is on the order of atomic spacing, diffraction by lattice planes can lead to either constructive or destructive interference of the X-rays, depending on the angle of diffraction and the lattice d-spacing.



## 1. Introduction

**Figure 6.** A schematic drawing of the principle of XRD diffracting and constructively interference from a set of lattice planes with a given d-spacing,  $d$ . Bragg's Law is derived utilizing the given geometries. Figure modified from (Thomas, 2006).

Illustrated in **Figure 6** are two parallel planes within the crystal, referred to as Plane 1 and Plane 2, each defined by a unique  $(hkl)$  and separated by a distance  $d$ , the d-spacing. These planes act akin to partially reflective surfaces for incoming X-ray beams, labeled  $IB_1$  and  $IB_2$ , which strike the lattice planes at an angle,  $\theta$ , known as the incident angle. This angle is identical for  $IB_1$  and  $IB_2$ , considering the parallel nature of Plane 1 and Plane 2. As a result, both,  $IB_1$  and  $IB_2$  after diffracting from their respective planes, exit in the same direction, maintaining the angle  $\theta$  as their reflection angle. However, the path traversed by  $IB_1$  is shorter than that of  $IB_2$ , as it reflects off the upper plane. This difference in path length leads to a phase shift between the two beams upon reflection. For the phenomenon of constructive interference to occur, the path difference between the two beams must be an integer multiple of the X-rays' wavelength,  $\lambda$ . This condition ensures that the multitude of diffracted rays from the crystal lattice planes will predominantly constructively interfere. In **Figure 6**, this path difference is quantified as twice the distance of  $xy$ . Given that  $Oxy$  forms a right triangle, the path difference can be calculated as described in Eq. 1. As depicted, if the path difference,  $2xy$ , equates to an integer multiple,  $n$ , of the X-ray wavelength,  $\lambda$ , constructive interference occurs. This relationship forms the basis of Eq. 2 known as the Bragg equation, which articulates Bragg's Law of X-ray diffraction (Thomas, 2006).

$$xy = d \sin \theta \quad \text{Eq. 1}$$

$$n\lambda = 2d_{hkl} \sin \theta \quad \text{Eq. 2}$$

The Bragg condition is pivotal for the constructive interference of an X-ray beam, which occurs when the incident beam and the diffracted are at an angle  $\theta$  relative to the lattice plane. The diffraction angle, denoted as  $2\theta$ , is the angle between the incoming and the diffracted beams. This angle is intricately linked to the wavelength ( $\lambda$ ) of the X-ray beam and the interplanar spacing ( $d_{hkl}$ ) of the crystal lattice according to Bragg's law in Eq. 2. As different lattice planes have variable d-spacings, a monochromatic X-ray beam, characterized by a single wavelength, will diffract at different angles  $\theta$ , resulting in a range of  $2\theta$  values observed. This forms the basis of angle dispersive X-ray diffraction (XRD), where the diffraction pattern is analyzed as a function of the  $2\theta$  angle. Conversely, when the incident X-ray beam comprises a continuous

## 1. Introduction

spectrum of wavelengths, known as a white beam, the diffraction can be studied in an energy dispersive manner, rather than angle dispersion.

The intensity of the X-ray source plays a pivotal role in the efficiency of XRD analysis. Brighter sources lead to higher counts in the detected X-ray signals, enabling quicker acquisition of diffraction patterns. Synchrotron facilities stand out as the premier sources of intense X-ray beams, thanks to their ability to accelerate electrons to high speeds along a circular trajectory with the aid of powerful magnets. These magnets provide the centripetal force necessary to keep the electrons in their circular path, causing them to emit radiation, including X-rays, as a byproduct of their acceleration. The high-energy environment of synchrotrons thus generates exceptionally intense X-ray beams.

This intense X-ray illumination from synchrotrons opens advanced possibilities for XRD analysis. By directing this beam onto a sample situated in a press, XRD under specific conditions, such as elevated temperatures and high pressures, can be performed. This capability is crucial for identifying crystal phases, calculating unit cell volumes, and characterizing changes within the sample under study. Furthermore, the application of a wide X-ray beam enables the imaging of the sample via X-ray tomography. This technique leverages the differential absorption of X-rays by materials of varying densities within the sample, providing a detailed visualization of its internal structure without physical sectioning.

### 1.1.4. Stress measurement with XRD

X-ray diffraction (XRD) serves as a powerful method for quantifying lattice strain and estimating deviatoric stress by measuring variations in d-spacing between lattice planes. In a powder sample, crystallites aligned with the (hkl) plane under the Bragg condition have their plane normals at an angle of  $90^\circ - \theta$  relative to the incident X-ray beam. These normals can orient in any direction around the incident beam axis, forming a continuous circular distribution. This distribution yields a diffraction cone that, upon intersecting with a detector, produces a Debye ring.

Ideally, with a sufficient number of randomly oriented crystallites, this ring exhibits uniform diffraction intensity across its 360-degree azimuthal span, measured from the beam's direct path. If the sample lacks a sufficient count of crystallites, the ring appears discontinuous or spotty, as selective diffraction occurs when each crystallite's lattice plane redirects diffraction towards a specific azimuthal angle of the ring, correlating with the plane's orientation perpendicular to

## 1. Introduction

the direct beam. A non-random orientation of diffractions from lattice planes in the sample concentrates intensity towards certain azimuthal angles, indicative of a preferred orientation.

The sensitivity of the diffraction's azimuthal angle to the orientation of lattice planes directly reflects variations in d-spacing across these planes, accommodating orientations ranging from vertical to horizontal and any intermediate angle. This attribute of angle-dispersive XRD is crucial for identifying differences in d-spacings among lattice planes, thereby enabling the assessment of internal or microstress within the sample. In the context of stress analysis, angle-dispersive XRD can reveal distortions in the Debye rings, transforming them from perfect circles into ellipses. This alteration signifies the presence of deviatoric stress, with the ellipse's minor axis indicating the direction of maximal stress and its major axis, the minimal stress direction.

The Bragg equation, as shown in Eq. 3, elucidates the relationship between d-spacing,  $d$ , and  $\theta$ .

$$\theta = \sin^{-1}\left(\frac{n\lambda}{2d}\right) \quad \text{Eq. 3}$$

It underscores the inverse relationship between d-spacing within the lattice and the diffraction angle  $\theta$ , with an increase in d-spacing leading to a decrease in  $\theta$ , and vice versa. Consequently, the azimuthal angle's linkage to d-spacing is inherently contingent on the orientation of the

## 1. Introduction

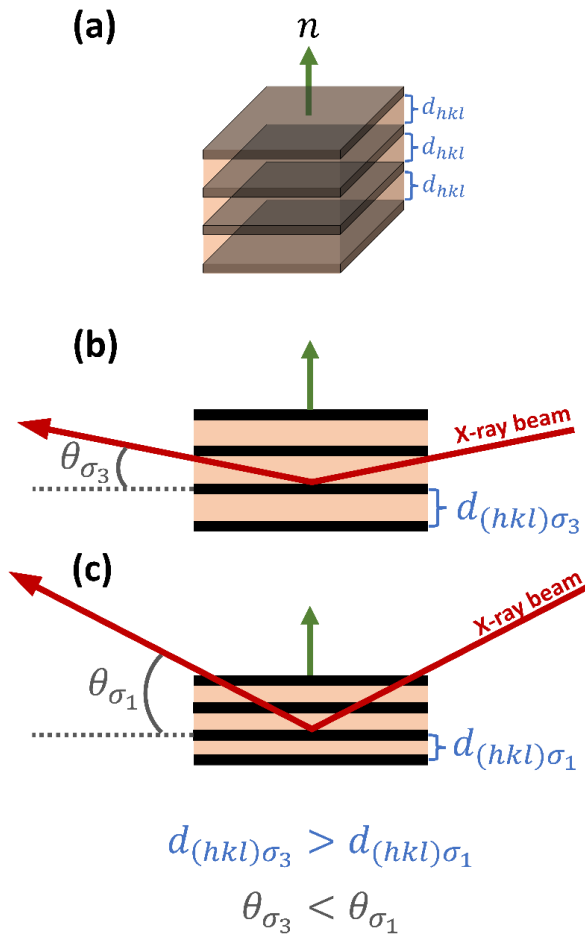


**Figure 7.** Schematic diagram, side view or perpendicular to the X-ray beam, illustrating how the d-spacing affects the diffraction angle  $\theta$ .  $\sigma_1$  is the higher deviatoric stress state (vertical in the diagram) and  $\sigma_3$  is the lower deviatoric stress state. The red beam is the incoming X-ray beam that then diffracts from the lattice planes, shown as black bands. The 3D view of the crystallite is shown at the top with the normal to the planes marked with the green arrow and  $n$ .

diffracting crystal lattice relative to the external stress. Specifically, the crystal lattice normal, when projected forward onto the detector screen, defines that crystal lattice's azimuthal diffraction angle.

A conceptual model illustrating this phenomenon is presented in **Figure 7** (a) provides a 3-dimensional explanation of the diffraction from lattice planes within the crystal. They are shown as black bands and the normal to the lattice planes, in green, is labeled  $n$ . Below that, (b) and (c) are viewed from the side, perpendicular to the X-ray beam in a 2-dimensional view. As the d-spacing,  $d_{(hkl)\sigma_3}$ , of the crystallite is smaller in (b) as compared to the d-spacing,  $d_{(hkl)\sigma_1}$ , in (c) of the crystallite, the diffraction angle  $\theta$  is inversely related and smaller in (c) than (b).

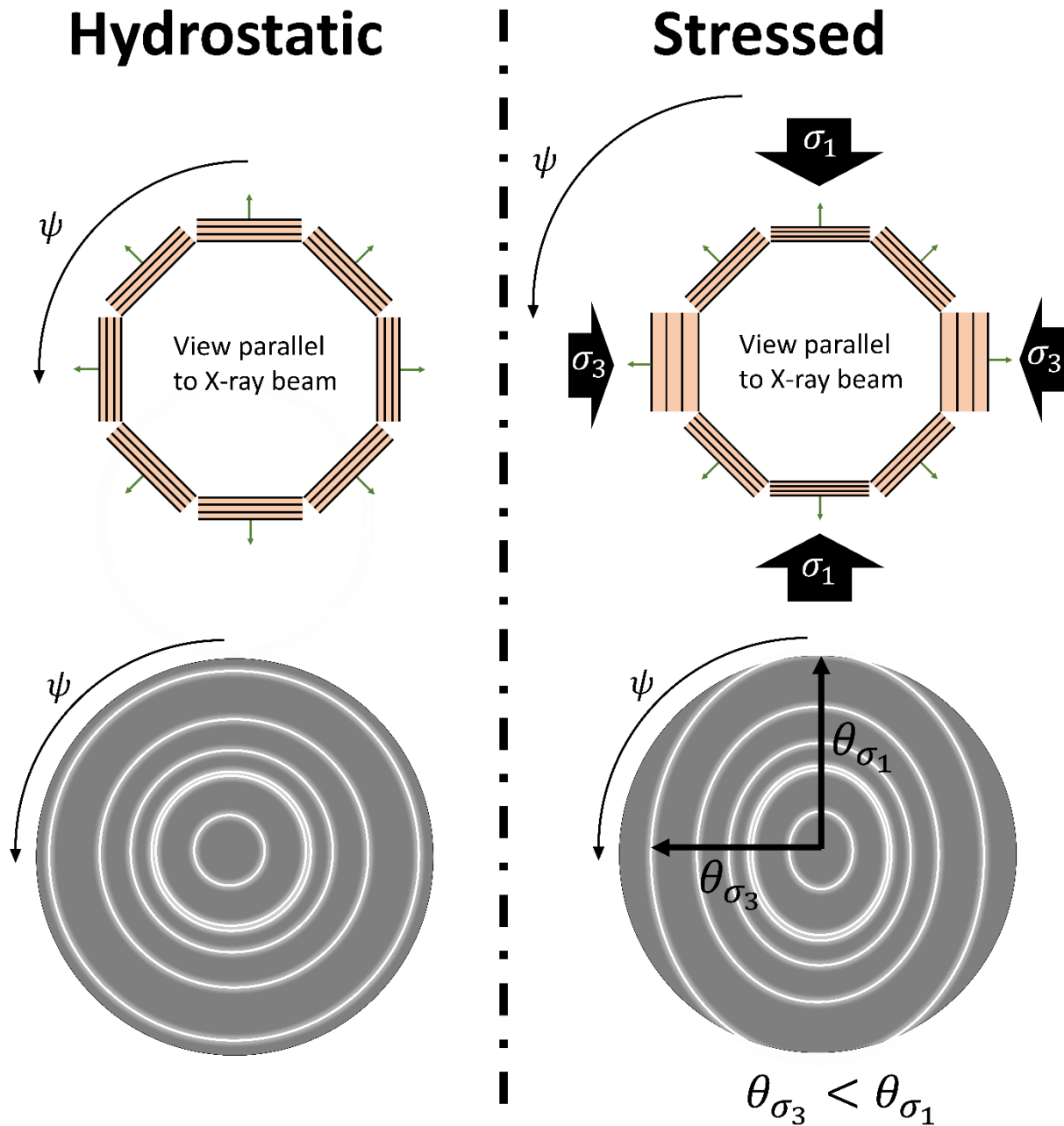


**Figure 8.** The same color and explanation for crystallites with lattice planes, as in **Figure 7**. Now, the view is parallel or along the X-ray beam. A subset of crystallites, with normals to the lattice planes marked with green arrows, is shown at different azimuthal angles of the normals.  $\sigma_1$  is the higher deviatoric stress direction, vertical in this case. The d-spacings of the lattice planes are smaller in the direction of their normals parallel to the higher deviatoric stress. The d-spacing shrinking is greatly exaggerated. The left side is in a hydrostatic condition, the right in a stressed state. The bottom half shows the resultant diffraction rings, in white, on the detector screen, in gray.

## 1. Introduction

When multiple crystallites within the sample are considered, the idea is expanded in **Figure 8**. Now, a small subpopulation of the total crystallites is considered. The view is now parallel to, or down the X-ray beam.  $\sigma_1$  is now vertical and  $\sigma_3$  is horizontal. The smaller d-spacings of the crystallites with normals parallel to  $\sigma_1$  cause a larger diffraction angle  $\theta$ . When the detector screen records the diffraction rings, they are now elliptical in the stressed state as compared to the hydrostatic state. The degree of this ellipticity is defined by the  $\psi$  to  $\theta$  relation which is, through the elasticity of the crystal, related to the stress state of the crystals.

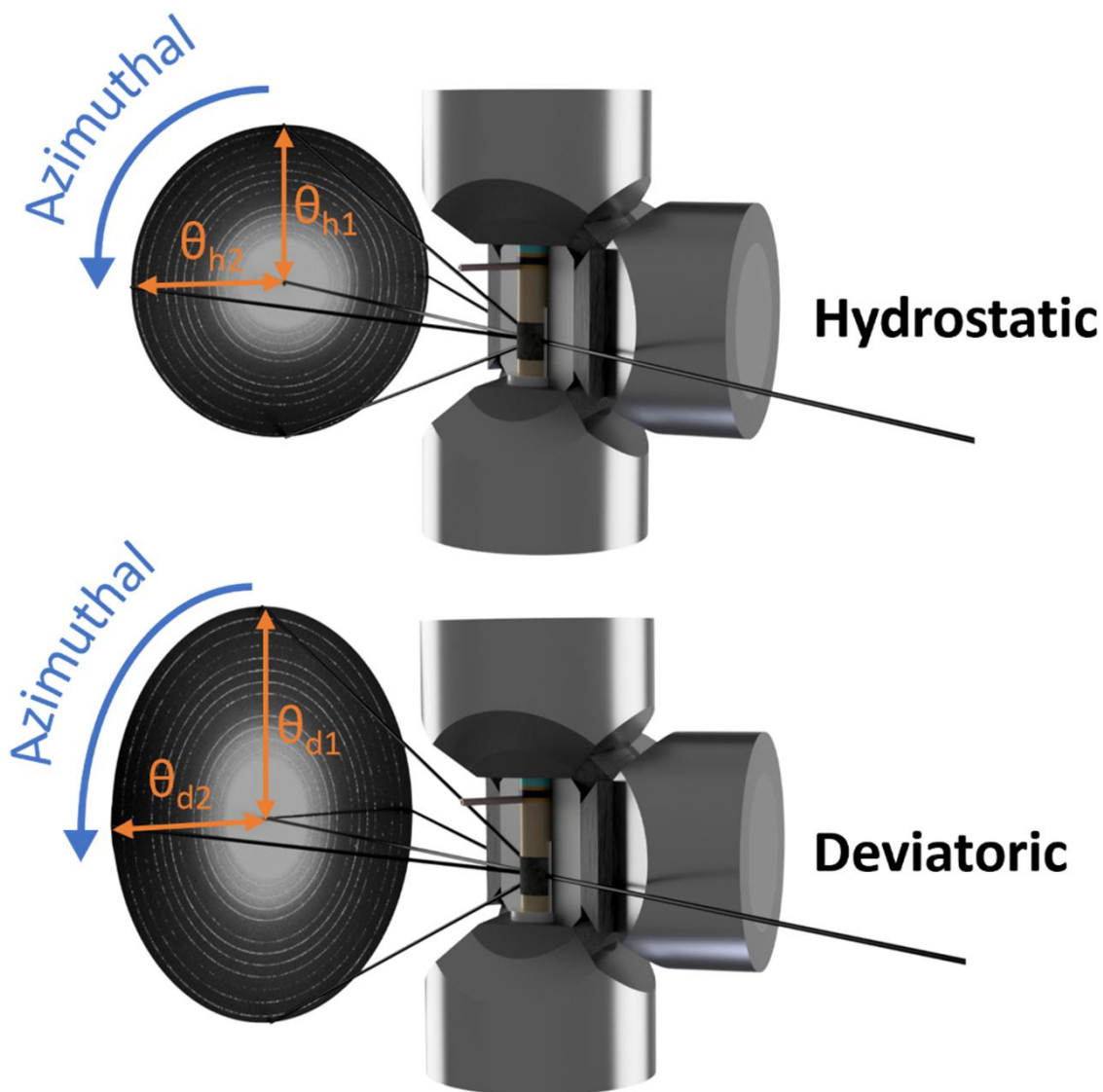


**Figure 9.** Schematic model of a diffraction experiment. Some anvils are removed and the assembly is cross-sectioned for clarity. The top section shows a hydrostatic condition. The bottom shows a deviatoric condition.

## 1. Introduction

**Figure 9** illustrates the effect of deformation on the resulting powder XRD pattern. Typically, the pattern's top is designated as an azimuthal angle of  $0^\circ$ , increasing counterclockwise. The X-ray beam enters from the right, and as it diffracts through the sample, it forms Debye cones, which appear as bright circles on a 2D detector. Under hydrostatic conditions,  $\theta_{h1} = \theta_{h2}$ . However, under deviatoric stress, these cones become elliptical, altering the 2D pattern such that  $\theta_{d1} > \theta_{d2}$  indicating maximum diffraction angle at an azimuthal angle of  $0^\circ$  and minimum at  $90^\circ$ . From the variation as a function of azimuthal angle, the crystal's stress can be determined through lattice microstrain calculations, leveraging the material's known elastic compliance or stiffness coefficients.

This methodology, initially described by (Singh et al., 1998) and further refined in subsequent studies (Burnley, 2015; Burnley & Kaboli, 2019; Duffy, Shen, Heinz, et al., 1999; Duffy, Shen, Shu, et al., 1999; Merkel et al., 2002), utilizes the following equations:

$$\varepsilon(hkl) = \frac{d(hkl) - d_0(hkl)}{d_0(hkl)} \quad \text{Eq. 4}$$

$$d(hkl) = d_0(hkl)[1 + (1 - 3 \cos^2(\psi))Q(hkl)] \quad \text{Eq. 5}$$

$$Q(hkl) = \left(\frac{\sigma}{3}\right) \{\alpha[2G_r(hkl)]^{-1} + (1 - \alpha)[2G_v(hkl)]^{-1}\} \quad \text{Eq. 6}$$

In the context of X-ray diffraction analysis, the microstrain,  $\varepsilon(hkl)$ , is quantified through Eq. 4. This equation delineates the relationship between the d-spacing under deviatoric stress,  $d(hkl)$ , and the d-spacing in a state of hydrostatic equilibrium,  $d_0(hkl)$ . The resultant value of  $\varepsilon(hkl)$  falls within a range from 0 to 1, offering a measure of the microstrain induced in the d-spacing that is independent of the material's properties, being analogous to macrostrain that is simply a measure of the change in length compared to the initial length. Eq. 5 further elaborates on the interplay between the azimuthal angle,  $\psi$ , and the measured d-spacing at this angle.  $Q(hkl)$  is the lattice strain parameter and describes the stress experienced by a specific lattice plane by Eq. 6. This encapsulates the stress distribution within the crystal lattice, quantifying the deviation from the ideal, unstressed state. It's a composite parameter that integrates the material's microscopic stress,  $\sigma$  (Bassett, 2006; Lin et al., 2022; Merkel, 2006), with its microscopic elastic response, represented by the reciprocal of the Reuss and Voigt shear moduli  $G_r(hkl)$  and  $G_v(hkl)$ , respectively.

## 1. Introduction

The weighting factor,  $\alpha$ , allows for the interpolation between these two moduli, reflecting the degree to which the material behaves according to Reuss's assumption of uniform stress (Reuss, 1929) or Voigt's assumption of uniform strain (Woldemar, 1928) continuities across the boundaries separating the crystallites, which have been shown to define the upper and lower bounds of the moduli (Singh et al., 1998). In the Reuss case, the stress is uniform throughout the polycrystalline aggregate. This implies that all crystallites experience the same stress, regardless of their orientation. Under this assumption, the strain in each crystallite may vary, depending on its orientation and elastic properties. The Reuss average represents the lower bound of the elastic moduli, as it assumes the most compliant response in the crystal. On the other hand, the Voigt assumption proposes that the strain is uniform across all crystallites in the polycrystalline material. That suggests that each crystallite undergoes the same amount of deformation, irrespective of its orientation. Consequently, the stress in each crystallite may differ, depending on its orientation and elastic properties. The Voigt average provides the upper bound of the elastic moduli, as it assumes the stiffest possible response of the material. The shear moduli  $G_r(hkl)$  and  $G_v(hkl)$  are defined distinctively for each crystallographic system, owing to the adaptability of this model to various material structures. For the cubic crystal system, the expressions for these moduli are specified in Eq. 7, Eq. 8, and Eq. 9 (Hearmon, 1956; Singh et al., 1998)

$$\Gamma(hkl) = \frac{h^2k^2 + k^2l^2 + l^2h^2}{(h^2 + k^2 + l^2)^2} \quad \text{Eq. 7}$$

$$[2G_r(hkl)]^{-1} = [S_{11} - S_{12} - 3(S_{11} - S_{12} - \frac{1}{2}S_{44})\Gamma(hkl)] \quad \text{Eq. 8}$$

$$G_v = \frac{3S_{11} - 3S_{12} + S_{44}}{S_{44}(S_{11} - S_{12})} \quad \text{Eq. 9}$$

$\Gamma(hkl)$  is a geometric factor that relates the orientations of the crystal planes to their elastic response. For the other crystal systems, Eq. 7, Eq. 8, and Eq. 9 are different, generally increasing in complexity with decreasing crystal system symmetry. Fortunately, even when the crystal lattice is subjected to strain, it's feasible to ascertain the d-spacing as if the crystal were under hydrostatic conditions. This is accomplished by setting  $d(hkl) = d_0(hkl)$ , which necessitates that the expression  $(1 - 3 \cos^2(\psi)) = 0$ . Solving for  $\psi$  yields the azimuthal angle where the observed d-spacing aligns with what would be expected in a hydrostatic scenario. This angle, often referred to as the 'magic angle' (Guignard & Crichton, 2015) in literature, is  $\psi = 54.74^\circ$ . At this specific azimuthal angle, the d-spacing measured corresponds to the d-spacing

## 1. Introduction

anticipated under hydrostatic conditions, facilitating the computation of hydrostatic pressure from the diffraction data.

### 1.2. Strain

Strain is a measure of the response of a material to stress. As a stress is applied to a crystal, the crystal will deform in some way, either elastically or inelastically. Elastic deformation is recoverable because it does not break bonds in the crystal lattice. Inelastic deformation does break bonds and because of this is not recoverable, at least not without the input of energy to return to the initial state.

Within the elastic limit, strain is defined by considering an infinitesimal and uniform change in the position of points as compared to the unstrained body. The following formulation follows the method described by Patterson & Bailey (Patterson & Bailey, 2018). If we consider an initial set of orthogonal axes  $\mathbf{i}, \mathbf{j}, \mathbf{k}$  in the unstrained crystal, under a strain we would expect a change to a not necessarily orthogonal set  $\mathbf{i}', \mathbf{j}', \mathbf{k}'$ . With this, we can now define  $\varepsilon_{ij}$  as the symbol for strain, with dimensionless units, in Eq. 10 to Eq. 12.

$$\mathbf{i}' = (1 + \varepsilon_{xx})\mathbf{i} + \varepsilon_{xy}\mathbf{j} + \varepsilon_{xz}\mathbf{k} \quad \text{Eq. 10}$$

$$\mathbf{j}' = \varepsilon_{yx}\mathbf{i} + (1 + \varepsilon_{yy})\mathbf{j} + \varepsilon_{yz}\mathbf{k} \quad \text{Eq. 11}$$

$$\mathbf{k}' = \varepsilon_{zx}\mathbf{i} + \varepsilon_{zy}\mathbf{j} + (1 + \varepsilon_{zz})\mathbf{k} \quad \text{Eq. 12}$$

If we define a point  $r$  on an unstrained crystal that becomes  $r'$  under a uniform infinitesimal strain, we can define Eq. 13 and Eq. 14.

$$\mathbf{r} = x\mathbf{i} + y\mathbf{j} + z\mathbf{k} \quad \text{Eq. 13}$$

$$\mathbf{r}' = x\mathbf{i}' + y\mathbf{j}' + z\mathbf{k}' \quad \text{Eq. 14}$$

By defining the displacement of the point as  $\mathbf{u} = \mathbf{r}' - \mathbf{r}$ , we can define the effects of the transformation on each individual dimension with Eq. 15 to Eq. 17.

$$u_x = x\varepsilon_{xx} + y\varepsilon_{yx} + z\varepsilon_{zx} \quad \text{Eq. 15}$$

$$u_y = x\varepsilon_{xy} + y\varepsilon_{yy} + z\varepsilon_{zy} \quad \text{Eq. 16}$$

$$u_z = x\varepsilon_{xz} + y\varepsilon_{yz} + z\varepsilon_{zz} \quad \text{Eq. 17}$$

Finally, we can define the strain tensor in matrix notation by taking the partial derivative of each function above with respect to the dimensional axes they define, forming the strain tensor according to Eq. 18 to Eq. 23.

$$\varepsilon_1 = e_{xx} = \frac{\partial u_x}{\partial x} \quad \text{Eq. 18}$$

## 1. Introduction

$$\varepsilon_2 = e_{yy} = \frac{\partial u_y}{\partial y} \quad \text{Eq. 19}$$

$$\varepsilon_3 = e_{zz} = \frac{\partial u_z}{\partial z} \quad \text{Eq. 20}$$

$$\varepsilon_4 = 2e_{yz} = 2e_{zy} = \frac{\partial u_y}{\partial z} + \frac{\partial u_z}{\partial y} \quad \text{Eq. 21}$$

$$\varepsilon_5 = 2e_{xz} = 2e_{zx} = \frac{\partial u_z}{\partial x} + \frac{\partial u_x}{\partial z} \quad \text{Eq. 22}$$

$$\varepsilon_6 = 2e_{xy} = 2e_{yx} = \frac{\partial u_x}{\partial y} + \frac{\partial u_y}{\partial x} \quad \text{Eq. 23}$$

Thus, like stress, strain forms a second rank tensor with 6 independent strain components, as shown in Eq. 24. In this way, it is possible to categorize different types of deformation in materials.

$$\boldsymbol{\varepsilon}_i = \begin{bmatrix} \varepsilon_1 & \varepsilon_6 & \varepsilon_5 \\ \varepsilon_6 & \varepsilon_2 & \varepsilon_4 \\ \varepsilon_5 & \varepsilon_4 & \varepsilon_3 \end{bmatrix} \quad \text{Eq. 24}$$

### 1.3. Stress

Stress is fundamentally defined as the force,  $F$ , per unit area,  $A$ , acting on an infinitesimally small material element, and it is described by a second-order tensor. When a material is subjected to hydrostatic loading, the forces are applied uniformly in all directions, resulting in an isotropic stress tensor whose normal components are identical. This common value is defined as pressure. In contrast, a general stress state may include both normal components, which resemble pressure, and shear components that lead to distortions in shape. The stress tensor can therefore be decomposed into an isotropic part, corresponding to the hydrostatic pressure, and a deviatoric part, which represents the shear stresses. Stress is usually denoted by the symbol  $\sigma_{yx}$  with units  $\text{N/m}^2$ . Stress will be described following the formulation of Patterson & Bailey (Patterson & Bailey, 2018). The subscript indicates that the force in the  $y$ -direction acts on the face perpendicular to the  $x$ -axis. **Figure 10** illustrates how the stress components on the face normal to the  $x$ -axis, as expressed in Eq. 25, Eq. 26, and Eq. 27, combine to describe any possible state of stress on that face.

$$\sigma_{yx} = \frac{\Delta F_y}{\Delta y \Delta z} \quad \text{Eq. 25}$$

1. Introduction

$$\sigma_{xx} = \frac{\Delta F_x}{\Delta y \Delta z} \quad \text{Eq. 26}$$

$$\sigma_{zx} = \frac{\Delta F_z}{\Delta y \Delta z} \quad \text{Eq. 27}$$

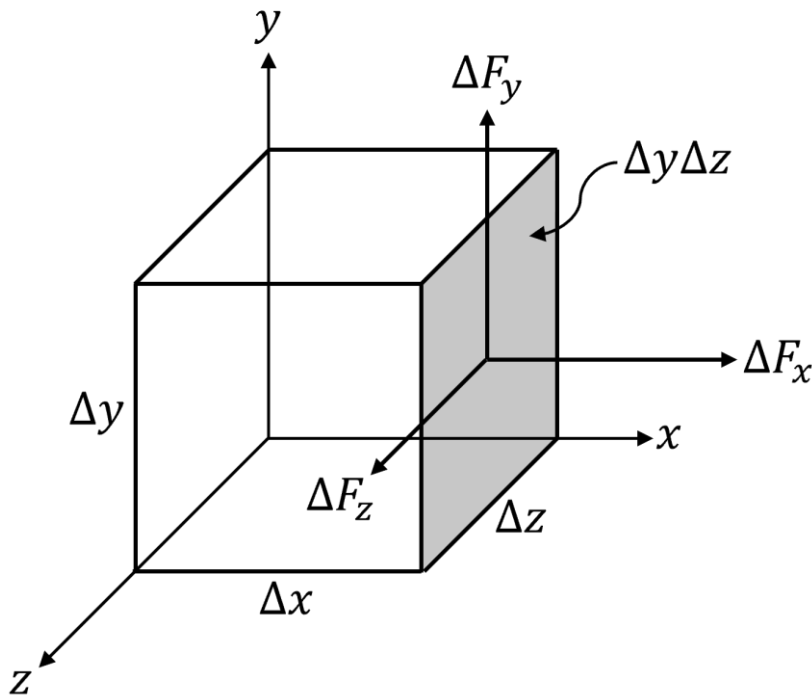


**Figure 10.** Schematic definition of stress tensor  $\sigma_{ij}$ , with only the forces on the  $\Delta y \Delta z$  face shown for simplicity. Each unique face of the cube thus defines three stress vectors.

By systematically listing all the stresses possible on each face of the cube, a total of 18 stress components can be defined. However, if the cube is taken to be infinitesimally small, opposing faces vanish and the actual number of defined stress components collapses to just 9 components, forming a second-rank tensor shown in Eq. 28.

$$\sigma_{ij} = \begin{bmatrix} \sigma_{xx} & \sigma_{xy} & \sigma_{xz} \\ \sigma_{yx} & \sigma_{yy} & \sigma_{yz} \\ \sigma_{zx} & \sigma_{zy} & \sigma_{zz} \end{bmatrix} \quad \text{Eq. 28}$$

For convenience, the subscripts will be switched from tensor notation to matrix notation. The substitutions are shown in Table 1.

## 1. Introduction

*Table 1. Notation conversion table between tensor and matrix notation for subscripts.*

Tensor notation	11	22	33	23, 32	31, 13	12, 21
Matrix notation	1	2	3	4	5	6

The stress tensor is symmetric, meaning  $\sigma_{ij} = \sigma_{ji}$ , and this will collapse the stress tensor to only 6 independent stress components, shown in Eq. 29 to Eq. 34, and the final second-rank tensor that is formed with matrix notation in Eq. 35.

$$\sigma_1 = \sigma_{xx} \quad \text{Eq. 29}$$

$$\sigma_2 = \sigma_{yy} \quad \text{Eq. 30}$$

$$\sigma_3 = \sigma_{zz} \quad \text{Eq. 31}$$

$$\sigma_4 = \sigma_{yz} = \sigma_{zy} \quad \text{Eq. 32}$$

$$\sigma_5 = \sigma_{xz} = \sigma_{zx} \quad \text{Eq. 33}$$

$$\sigma_6 = \sigma_{xy} = \sigma_{yx} \quad \text{Eq. 34}$$

$$\sigma_i = \begin{bmatrix} \sigma_1 & \sigma_6 & \sigma_5 \\ \sigma_6 & \sigma_2 & \sigma_4 \\ \sigma_5 & \sigma_4 & \sigma_3 \end{bmatrix} \quad \text{Eq. 35}$$

With this definition, the stress components  $\sigma_1$ ,  $\sigma_2$ , and  $\sigma_3$  are the stresses normal to the face and are called the principal stresses.  $\sigma_4$ ,  $\sigma_5$ , and  $\sigma_6$  on the other hand are the shear stresses. It becomes clear that if a crystal is held under hydrostatic pressure and no shear stresses are applied, the shear components go to zero (Eq. 36) and the principal stresses can be used to define the hydrostatic pressure,  $P_h$  (Eq. 37).

$$\sigma_4 = \sigma_5 = \sigma_6 = 0 \quad \text{Eq. 36}$$

$$P_h = \frac{\sigma_1 + \sigma_2 + \sigma_3}{3} \quad \text{Eq. 37}$$

While stress might be defined through the force on a crystal face, implying a mechanical force, the stress may come from many sources. Non-uniform heating, electric fields, and chemical diffusion can all impart stress on a material. In the case of electric fields, the coefficient that defines how much stress is generated by a unit of electric field, or vice-versa, in other words the slope of the correlation of a linear equation, is defined by the piezoelectric coefficients, as will be seen later. It is useful to define here special cases of stress that are named for ease of use. The name of the stress geometry along with the tensor form is shown in Eq. 38 to Eq. 41.

## 1. Introduction

$$\boldsymbol{\sigma}_{uniaxial} = \begin{bmatrix} \sigma & 0 & 0 \\ 0 & 0 & 0 \\ 0 & 0 & 0 \end{bmatrix} \quad Eq. 38$$

$$\boldsymbol{\sigma}_{hydrostatic} = \begin{bmatrix} \sigma & 0 & 0 \\ 0 & \sigma & 0 \\ 0 & 0 & \sigma \end{bmatrix} \quad Eq. 39$$

$$\boldsymbol{\sigma}_{pure\ shear} = \begin{bmatrix} \sigma & 0 & 0 \\ 0 & -\sigma & 0 \\ 0 & 0 & 0 \end{bmatrix} \quad Eq. 40$$

$$\boldsymbol{\sigma}_{simple\ shear} = \begin{bmatrix} 0 & \sigma & 0 \\ \sigma & 0 & 0 \\ 0 & 0 & 0 \end{bmatrix} \quad Eq. 41$$

Deviatoric stress is the component of the stress tensor that represents shear stress and causes distortion or deformation in a material without changing its volume. It is defined by subtracting the isotropic pressure component from the total stress tensor, effectively isolating the shear component responsible for the shape changes. From this point forward, the symbol  $\sigma$  will be used exclusively to represent deviatoric stress to simplify the notation when discussing generalized deviatoric stress. Mathematically, if the total stress tensor is given by  $\sigma_{total}$ , then the deviatoric stress tensor is expressed as

$$\sigma_{dev} = \sigma_{total} - \frac{1}{3} \text{tr}(\sigma_{total})I \quad Eq. 42$$

where  $\text{tr}(\sigma_{trace})$  is the trace of the stress tensor and  $I$  is the identity tensor. This quantity represents the stresses that cause shape changes (shear deformations) without altering the volume. In the subsequent sections,  $\sigma_1$ ,  $\sigma_2$ , and  $\sigma_3$  will denote the principal stresses, ordered such that  $\sigma_1$  is the maximum,  $\sigma_2$  is the intermediate, and  $\sigma_3$  is the minimum deviatoric stress. These values represent the magnitudes of the deviatoric stress along their principal directions and should not be confused with the diagonal elements of the full stress tensor (i.e., the hydrostatic stress). The only exception is in equations where the tensor notation is used precisely to refer to the complete stress state, including both deviatoric and hydrostatic components, in which case the full subscripted representation is maintained. Additionally, the term ‘stress’ will be used to describe deviatoric stress only, and not hydrostatic stress, or pressure, unless specifically referred as hydrostatic stress.

### 1.4. Elasticity

As previously mentioned, a material is said to undergo elastic strain if it is energetically reversible. In other words, if a material is deformed below the elastic limit, the stress placed on the material will cause strain but if the stress is removed, the material will revert to the initial shape before the application of stress with no additional energy input required. Since the bonds of the crystal are not broken within the elastic limit, only stretched or bent, Hooke’s law can be used to describe the deformation (C. Powell, 2010).

## 1. Introduction

$$\sigma_{ij} = \sum_{kl} C_{ijkl} \varepsilon_{kl} \quad \text{Eq. 43}$$

$$\varepsilon_{ij} = \sum_{kl} S_{ijkl} \sigma_{kl} \quad \text{Eq. 44}$$

Eq. 43 and Eq. 44 introduces  $C_{ijkl}$  and  $S_{ijkl}$ , which are generalized elastic coefficients of materials. Depending on whether stress or strain is to be calculated, the tensor required to describe either is given a specific name and symbol. As seen in Eq. 43, if the strain is known and the stress is to be calculated, the elastic stiffness  $C_{ijkl}$  must be used. As a corollary, if the stress is known and the strain is to be calculated, the elastic compliance  $S_{ijkl}$  is used.  $C_{ijkl}$  and  $S_{ijkl}$  are both elasticity coefficients, related by a tensor inversion. The elastic constants define the proportionality factor of strain to stress in the crystal, with the caveat that the strain is within the elastic limits of the crystal (Pabst & Gregorová, 2013).

To relate two second rank tensors mathematically, a fourth rank tensor is necessary, which in matrix notation would be shown with two subscripts, as in Table 1. The compliance elastic tensor has an additional set of rules when simplifying the subscripts from tensor to matrix notation, as shown in Eq. 45.

$$\begin{aligned} S_{mn} &= S_{ijkl} & \text{when } m \text{ and } n \text{ are } 1, 2, 3 \\ S_{mn} &= 2S_{ijkl} & \text{when } m \text{ or } n \text{ is } 4, 5, 6 \\ S_{mn} &= 4S_{ijkl} & \text{when } m \text{ and } n \text{ are both } 4, 5, 6 \end{aligned} \quad \text{Eq. 45}$$

$$\varepsilon_1 = S_{11}\sigma_1 + S_{12}\sigma_2 + S_{13}\sigma_3 + S_{14}\sigma_4 + S_{15}\sigma_5 + S_{16}\sigma_6 \quad \text{Eq. 46}$$

In Eq. 46, an example calculation is shown for calculating the strain in the 1 direction in matrix notation, or 11 in tensor notation using the stress and elastic stiffness components. Physically, this means that to calculate the strain in the  $x$ -axis direction on the face of the material normal to the same axis, the stress from every other direction must be considered. Intuitively, this makes sense because at its core, this behavior stems from the interplay between atomic and molecular bonds in the crystal lattice. When stress is applied in one direction, it does not just cause strain in that single axis. Due to the interconnected nature of the lattice, stress in one direction can influence strain in others. This interdependence across different directions is why there is a need for the fourth-rank tensor: it provides a precise way to account for these multi-directional interactions.

## 1. Introduction

Essentially, the tensor rank gives us the tools to describe how atoms and molecules in a material respond collectively to external forces (Powell, 2010). If the same process as Eq. 46 is repeated for all six strain components, six equations are necessary and, in each equation, there are six elastic constants. Even though they are fourth rank tensors, they do not contain 81 terms as expected ( $3 \times 3 \times 3 \times 3 = 81$ ). They reduce due to symmetry to 36 independent components,  $6 \cdot 6 = 36$ . A further reduction in the number of actual independent elastic constants arises from the property that strain and stress are symmetric tensors, shown using the full tensor notation in Eq. 47.

$$c_{ijkl} = c_{ijlk} = c_{jikl} = c_{klij} \quad \text{Eq. 47}$$

This will then reduce the number of independent elastic constants to the final count of 21, with the full fourth rank tensor of elastic constants shown in Eq. 48 with tensor notation.

$$c_{ij} = \begin{bmatrix} c_{11} & c_{12} & c_{13} & c_{14} & c_{15} & c_{16} \\ c_{12} & c_{22} & c_{23} & c_{24} & c_{25} & c_{26} \\ c_{13} & c_{23} & c_{33} & c_{34} & c_{35} & c_{36} \\ c_{14} & c_{24} & c_{34} & c_{44} & c_{45} & c_{46} \\ c_{15} & c_{25} & c_{35} & c_{45} & c_{55} & c_{56} \\ c_{16} & c_{26} & c_{36} & c_{46} & c_{56} & c_{66} \end{bmatrix} \quad \text{Eq. 48}$$

The Neumann-Curie principle also applies to the elastic constants. The higher the symmetry of the crystal, the fewer the independent terms required (Patterson & Bailey, 2018). For example, in cubic crystals the three lattice parameters are equal. This symmetry results in Eq. 49 and Eq. 50 reducing the diagonal to only two independent constants. Inversion symmetry of the unit cell simplifies many of the off-diagonal elastic constants to zero (Eq. 51), and finally the mirror elements result in Eq. 52. Thus, in a cubic crystal, there are only three independent elastic constants.

$$c_{11} = c_{22} = c_{33} \quad \text{Eq. 49}$$

$$c_{44} = c_{55} = c_{66} \quad \text{Eq. 50}$$

$$0 = c_{14} = c_{15} = c_{16} = c_{24} = c_{25} = c_{26} = c_{34} = c_{35} = c_{36} = c_{45} = c_{46} = c_{56} \quad \text{Eq. 51}$$

$$c_{12} = c_{13} = c_{23} \quad \text{Eq. 52}$$

$$c_{ij} = \begin{bmatrix} c_{11} & c_{12} & c_{12} & 0 & 0 & 0 \\ c_{12} & c_{11} & c_{12} & 0 & 0 & 0 \\ c_{12} & c_{12} & c_{11} & 0 & 0 & 0 \\ 0 & 0 & 0 & c_{44} & 0 & 0 \\ 0 & 0 & 0 & 0 & c_{44} & 0 \\ 0 & 0 & 0 & 0 & 0 & c_{44} \end{bmatrix} \quad \text{Eq. 53}$$

## 1. Introduction

The full elastic coefficient tensor of cubic crystals is, therefore, simplified to Eq. 53. The same process can be repeated for all 7 crystal systems. The symmetries of the resultant elastic constant tensors are shown in **Figure 11**. The symmetries present in each crystallographic point group simplify the elastic tensors as shown in the figure. Each tensor is symmetric, therefore, only the top half is shown. The cubic system has the most symmetry elements and thus the simplest tensor. The lack of symmetry elements in the triclinic crystal system means that each elastic component in the tensor is unique and is required to fully describe the elastic structure of the crystal. The rest of the systems are in between these two extremes. In the figure, matching colors signifies that the components are equal in value, and a black border is equal in value but opposite in sign.

# 1. Introduction

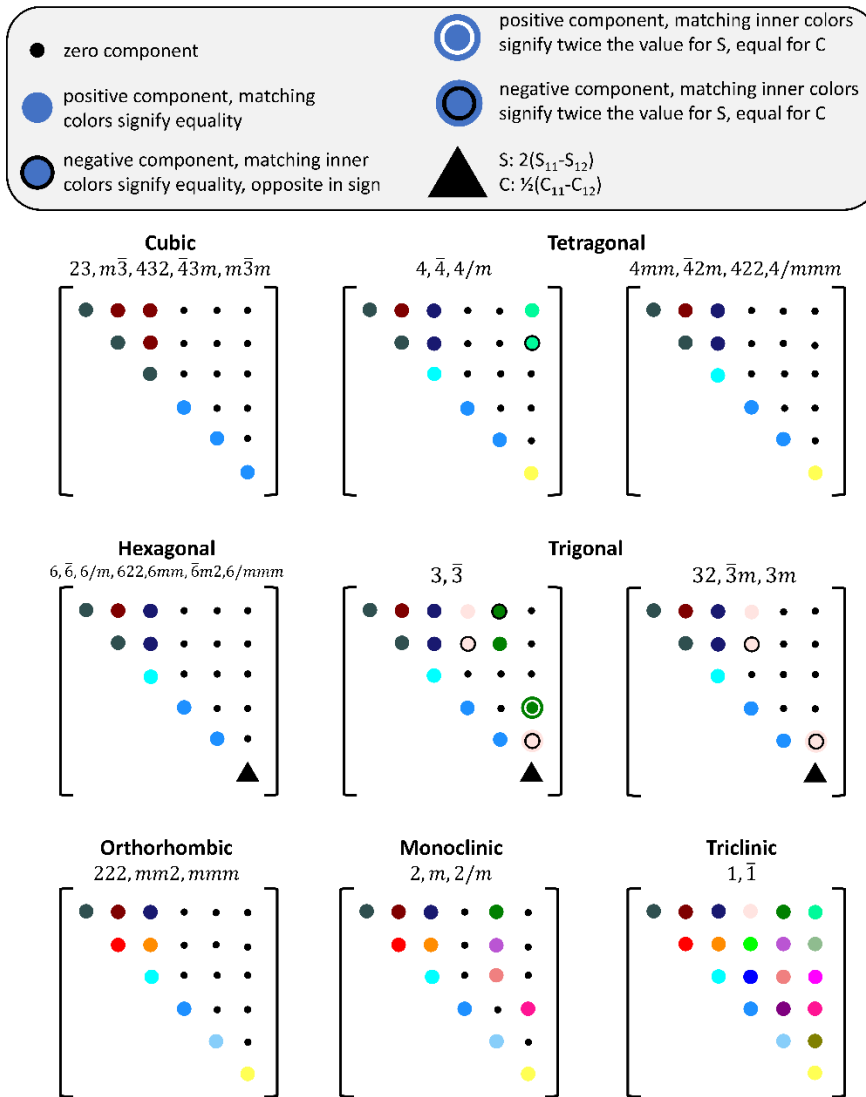


**Figure 11.** Elastic tensors for all seven crystallographic systems. Each is shown under the crystallographic point groups they represent. Colors signify if the components are equal, including sign changes.

## 1.5. Dielectrics

### 1.5.1. Dielectric polarization

When any dielectric is placed within an electric field,  $\mathbf{E}$  (with unit V/m), pre-existing dipole moments within the constituent molecules redistribute microscopically to align with the surrounding field or new dipole moments are created through charge separation, inducing a macroscopically polarized state. Dipole moments,  $\mathbf{p}$ , form through the separation of positive and negative charges, of strength  $q$ , to a distance  $x$ . By convention it is a vector that points from the positive to the negative charge, described by Eq. 54.

## 1. Introduction

$$\mathbf{p} = qx \quad \text{Eq. 54}$$

$$\mathbf{P} = Nqx \quad \text{Eq. 55}$$

The polarization,  $\mathbf{P}$ , of the bulk crystal is expressed by the summation of the  $N$  number of dipole moments within the volume, as seen in Eq. 55. The unit for  $P$  is  $C/m^2$ . This corresponds to another definition of  $\mathbf{P}$  as the surface density of bound charges near electrodes of a polarized dielectric capacitor. If the external electric field is sufficiently weak, the polarization of the dielectric, which opposes the external electric field, varies linearly with the strength of the external electric field (Patterson & Bailey, 2018), i.e.,

$$\mathbf{P} = \varepsilon_0 \chi_e \mathbf{E} \quad \text{Eq. 56}$$

where  $\chi_e$  is the dielectric susceptibility, a dimensionless parameter, and  $\varepsilon_0$  is the permittivity of free space, often referred to as the electrical constant, with the value  $\varepsilon_0 = 8.854 \cdot 10^{-12}$  F/m (American & Standard, 1984).  $\chi_e$  is zero in a vacuum. Thus,  $\mathbf{P}$  describes the polarization as a product of the material properties of the dielectric in question. However, as can be seen by the non-zero value of  $\varepsilon_0$ , space itself holds energy in an electric field. The result is that in a dielectric, one must account for both the polarization arising from the material itself and from the space it occupies. This results in an equation for the total electrically induced polarized state,  $\mathbf{D}$ , or in other words the electrical induction:

$$\mathbf{D} = \varepsilon_0 \mathbf{E} + \mathbf{P} \quad \text{Eq. 57}$$

Combining Eq. 56 and Eq. 57, we can define the relative permittivity as  $\varepsilon_r = 1 + \chi_e$  and therefore,

$$\mathbf{D} = \varepsilon_r \varepsilon_0 \mathbf{E} \quad \text{Eq. 58}$$

Finally, we reach a definition of the dielectric constant  $\kappa$ , which is equivalent to the relative permittivity  $\varepsilon_r$ . The relative permittivity depends on a multitude of factors relating to the material in question. While the relative permittivity is typically called the dielectric constant, this is not entirely accurate as it is not truly a constant. It is only a constant if the material and the external conditions it is subjected to are the same as when it was measured. The relative permittivity depends on factors such as, but not limited to, temperature, frequency of the external electric field, total strength of the external electric field, pressure, and the history of the material (Kholkin et al., 2008; Tichý et al, 2010; Yang, 2004).

If the external electric field varies with time, in other words has a non-zero frequency, the relative permittivity varies with this frequency. Additionally, if the externally applied electric

## 1. Introduction

field exceeds a material's dielectric strength, dielectric breakdown occurs and the dielectric becomes a conductor, losing most of its electrically insulating properties. The exact mechanism of dielectric breakdown varies with specific materials. In solids the general mechanism is the stripping of outer valence electrons from the structure's atoms, which then act as the charge carriers in the material and transport the electric charge. However, below the dielectric breakdown, polarization  $P$  is induced according to Eq. 55. through microscopic charge redistribution, characterized by either the formation of new dipole moments or the alignment of pre-existing dipole moment (Yang, 2004).

On a macroscopic level, if the electric field is not oscillated at a sufficiently high frequency (Guo, 2010; Kholkin et al., 2008; Tichý et al, 2010), but is kept static, the exact mechanism of microscopic redistribution has little effect. However, for transient or changing electric fields, the distinctions matter. The four atomic origins of dielectric polarization are electronic, ionic, orientational, and quasifree electron gas (Yang, 2004).

Electronic polarization occurs on an atom-by-atom basis, as the electronic charge clouds around individual atoms are distorted in response to the external electric field (Patterson & Bailey, 2018). The electronic charge cloud is created by the electron orbitals around the atom, which distort to oppose the electric field, forming dipole moments. Electronic polarization occurs in all dielectrics, whether ionic or covalent.

Ionic polarization occurs through the physical displacement of ions in the structure. In an ionic crystal, the external electric field distorts the structure because of its interaction with the ions, causing displacements in ionic positions through bond angle bending and stretching. Negative and positive ions move in opposite directions relative to each other to oppose the electric field by inducing dipole moments. If the polarization can 'freeze in' below a critical temperature, the crystal is ferroelectric. Otherwise, if the polarization cannot be frozen in, the displacement recovers once the external electric field is removed, defining the material as non-ferroelectric.

Orientational polarization occurs in molecules with permanent dipole moments. When an external electric field is applied, the molecules re-orient through rotational displacements to oppose the electric field. This is mostly relevant for liquids or gases and not solids where bonds within the structure restrict rotational movement.

Quasifree electron gas polarization, is limited to metals (Patterson & Bailey, 2018) and is less relevant to this work, but originates when free electrons in the metal structure interact via the

## 1. Introduction

Coulomb force and act as a quasifree electron gas. The source of polarization relevant to this work is ionic polarization, which gives rise to the piezoelectric effect in crystals.

### 1.5.2. Dielectric electrical resistivity

Apart from dielectric materials' ability to develop a polarization in electric fields, they are also characterized by much lower resistivity compared to metals. Specifically, the DC charge transference is very low compared to metals (Poplavko, 2019). Since dielectrics typically have conduction band electron abundances that are many orders of magnitude below those of metals, electrical charge conduction is greatly hindered. Even so, no material has infinite resistance. Apart from the very few conduction band electrons, dielectrics can also conduct some charge through the movement of charged particles in the crystal lattice (Poplavko, 2019; Tichý et al, 2010).

Beyond the limited number of conduction band electrons, dielectrics can also permit some degree of charge movement through the migration of charged particles within their crystal lattice (Poplavko, 2019; Tichý et al, 2010). In an undisturbed state, without external influences, free charge carriers within dielectrics engage in random motion, driven by thermal energy (Gregori et al., 2017; Patterson & Bailey, 2018). The application of an external electric field, or in certain cases like pyroelectric crystals, the introduction of a temperature gradient, can instigate the movement of these charge carriers, enabling them to traverse the crystal structure, thereby facilitating charge transport and conduction (Gregori et al., 2017; Sherrit et al., 1992).

Dielectric materials exhibit various modes of DC electrical conductivity, each influenced by their intrinsic properties, such as crystal structure, defect levels, and purity. One significant conduction method in dielectrics is ionic conductivity, which emerges primarily due to the movement of ions within the material. This mode is especially pronounced in ionic crystals or materials with a substantial ionic character. As the temperature rises, the kinetic energy of ions increases, overcoming potential barriers and leading to a heightened ionic mobility (Gregori et al., 2017; Lazzari et al., 1988). This relationship results in an exponential surge in conductivity with temperature, often described by the Arrhenius equation. For electrical resistivity, the equation is expressed as shown in Eq. 59.

$$\rho_R(T) = \rho_0 e^{\left(\frac{E_a}{kT}\right)} \quad \text{Eq. 59}$$

$\rho_R(T)$  is the electrical resistivity at temperature  $T$ ,  $\rho_0$  is a constant representing resistivity at an infinitely high temperature and is dependent on material properties, also commonly called the pre-exponential factor,  $E_a$  is the activation energy necessary for ion migration,  $k$  is the

## 1. Introduction

Boltzmann constant, and  $T$  is the absolute temperature in Kelvin. The term  $e^{\left(\frac{E_a}{kT}\right)}$  illustrates the temperature's impact on resistivity. As temperature increases, the exponential term decreases, thus reducing the resistivity. The activation energy  $E_a$  indicates the energy barrier ions must surmount to migrate. A lower  $E_a$  facilitates ion movement, leading to decreased resistivity.

As an example of the effects of this exponential temperature correlation, the resistivity of CTGS, a dielectric crystal with composition  $\text{Ca}_3\text{TaGa}_3\text{Si}_2\text{O}_{14}$ , is plotted in **Figure 12**. versus temperature in degrees Celsius (Zhang & Yu, 2011). As can be seen, the resistivity of dielectrics as defined by the Arrhenius equation results in a rapidly decreasing resistance with temperature.

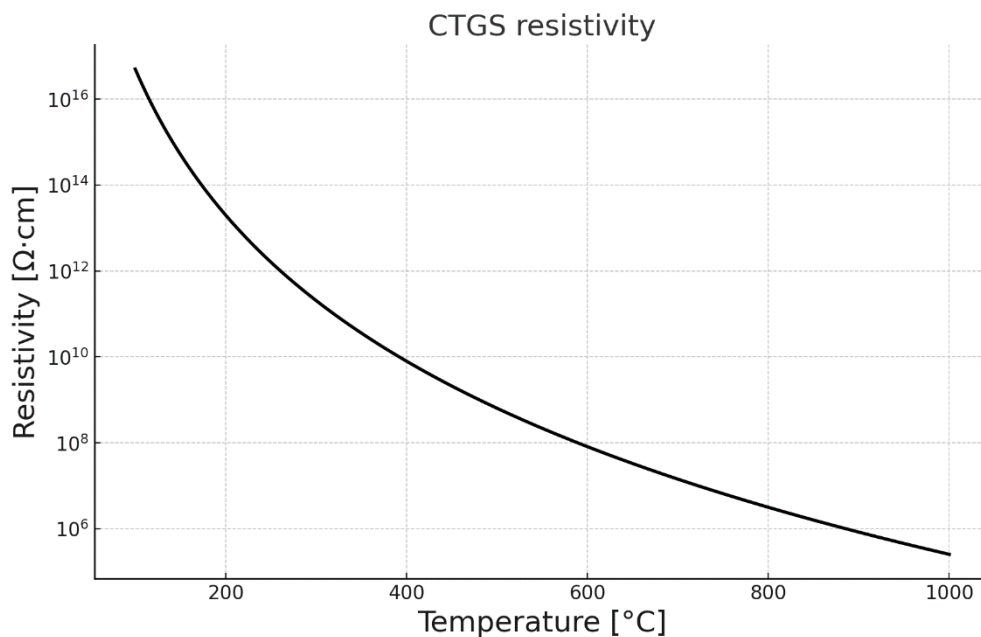


**Figure 12.** CTGS resistivity as measured experimentally versus temperature. Modified from (Zhang & Yu, 2011).

Oxygen vacancies in the crystal structure of certain dielectrics play a significant role by providing channels for ion migration, particularly for cations. These vacancies lower the activation energy ( $E_a$ ), facilitating ion movement even at lower temperatures (Gregori et al., 2017; Nuernberg, 2020). The presence of oxygen vacancies thus significantly impacts the material's resistivity by enabling easier ion migration through the crystal lattice (Gregori et al., 2017; Xiuwei, 2016).

Another important aspect of dielectric conductivity is electronic conductivity. While typically low in dielectrics, it can become more pronounced in specific materials or under certain conditions. This form of conductivity involves the transport of electrons and holes and can be

## 1. Introduction

influenced by impurities and defects. As temperature increases, more electrons gain sufficient energy to cross the band gap, enhancing electronic conductivity (Poplavko, 2019). Hopping conduction is relevant in amorphous materials or those with high disorder levels, where charge carriers (electrons or holes) move through localized states. Its temperature dependence is complex but generally increases with temperature as thermal activation aids the hopping process. Protonic conductivity is also notable, especially in materials containing hydrogen ions (protons), such as hydrates or those with hydrogen bonding. Like ionic conductivity, protonic conductivity increases with temperature as proton mobility improves (Poplavko, 2019; Tichý et al, 2010).

Space charge conduction arises from the accumulation of charge carriers at interfaces or inhomogeneities within the dielectric (Gregori et al., 2017; Lazzari et al., 1988). Its temperature dependence varies, depending on the nature of the interfaces and the mobility of charge carriers involved. Although polarization and relaxation processes are not direct conduction mechanisms, they can contribute to apparent DC conductivity, especially at lower frequencies. These processes are highly temperature-sensitive, with different relaxation mechanisms becoming more significant at various temperatures.

The contribution of each conduction mechanism depends heavily on the material's characteristics and environmental conditions. For these experiments, the primary contributors to conduction are space charge conduction and the mobility of charge carriers influenced by temperature. Within the piezoelectric crystal, increased charge carrier mobility is likely the dominant source of conduction. At the crystal's surface, particularly along grain boundaries, interfacial conduction is probably the main source of charge movement, especially in high hydrostatic pressure environments like those inside an LVP, where grain boundaries play a crucial role in charge conduction.

### 1.5.3. Piezoelectric phenomenon

Piezoelectricity was first noted by Jacques Curie and Pierre Curie in 1880 (Curie & Curie, 1880). The Curie brothers only initially discovered the direct piezoelectric effect, i.e., a build-up of voltage across the crystal faces under mechanical pressure of certain crystals. The first reported piezoelectric crystals were tourmaline, quartz, topaz, cane sugar, and Rochelle salt (potassium sodium tartrate). Further investigation in 1881 deduced that the converse piezoelectric effect must also exist according to fundamental thermodynamic principles (Lippmann, 1881). That same year, the Curie brothers confirmed and reported the existence of the converse effect (Jacques & Curie, 1881).

## 1. Introduction

The name chosen for this phenomenon was piezoelectricity, coming from the Greek *piezein*, meaning “pressure” coupled with “electricity” (Kholkin et al., 2008). The Curie brothers observed that when certain crystals had mechanical force applied across them, any electrodes placed on opposite crystal faces along the applied force, or stress, developed a voltage across them. By thermodynamic principles, the crystals must, as was discovered, also develop stress across them when placed inside an electric field, as shown in **Figure 13**. Although both the converse and direct effects are thermodynamically equivalent, since piezoelectricity was first discovered through the application of a force and the measurement of a voltage, the naming convention has remained.

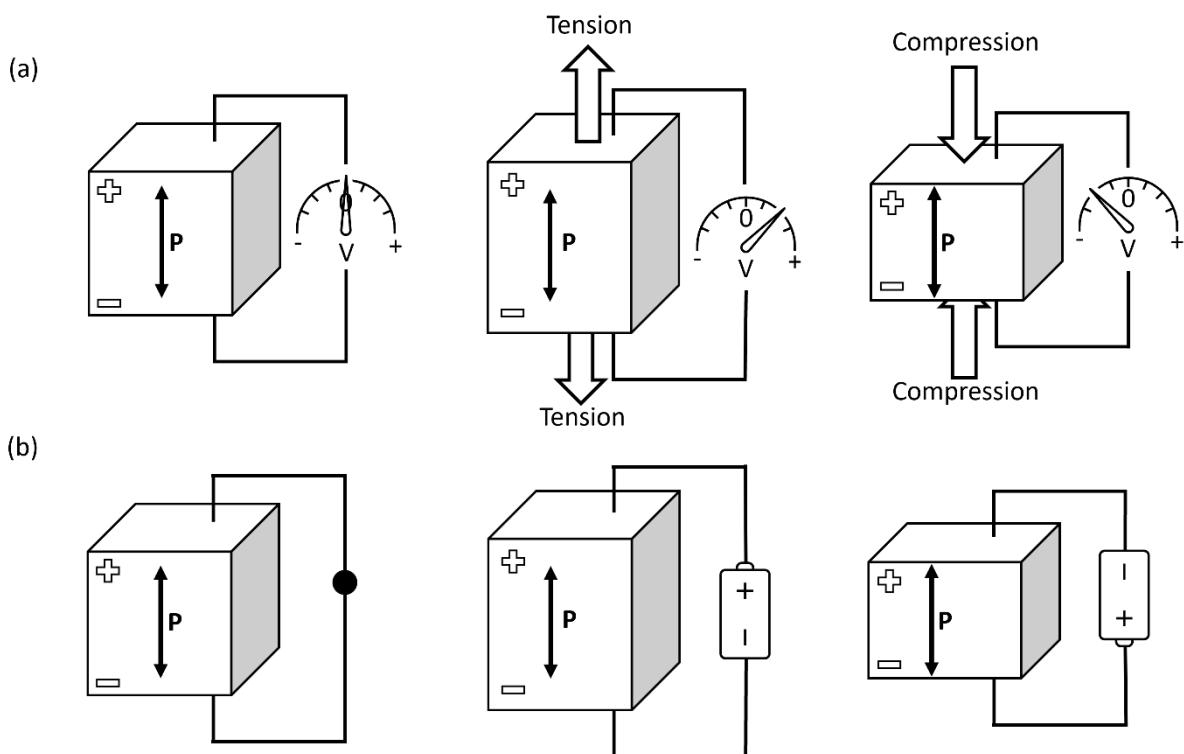


**Figure 13.** Conceptual diagram of the (a) direct and (b) converse piezoelectric effect in static, compression, and tension. The double-ended arrow with a ‘P’ on the crystal indicates the direction of the dipole moments in the crystal under consideration, and the positive and negative signs indicate the polarized direction of the dipole moments in the crystal.

Early on, it was noted that not all crystals are piezoelectric, with the reason for this becoming clear with the development of the theory of piezoelectricity and continual development in the understanding of the underlying crystallography that gives rise to piezoelectricity. Piezoelectricity relies on a separation of charges through the displacement of ions. If the crystal structure is symmetric, a displacement of, for example, a positive ion in one direction would be

## 1. Introduction

accompanied by the displacement of a negative ion in the opposite direction by an equal amount (Kholkin et al., 2008), resulting in a net neutral charge. Because of this, only polar structures can give rise to unsymmetric charge separations. This immediately eliminates all nonpolar crystals from displaying any sort of piezoelectric effect, in accordance with the Neumann-Curie principle: (Poplavko, 2019)

*The symmetry of a physical property of a crystal is not lower than the symmetry of the structure.*

In other words, if the crystal structure is symmetric (i.e., has a center of inversion), then any physical properties will also be symmetric. Any positive charge displacement is counteracted by an equal negative charge displacement, resulting in a neutral charge.

Of the 32 crystallographic classes, 21 have no inversion point. In other words, they are non-centrosymmetric. Although cubic class 432 has no inversion point, piezoelectric charges developed along the  $\langle 111 \rangle$  polar axes cancel each other out, eliminating the possibility of a piezoelectric effect in this class. Thus, only 20 crystallographic classes can potentially exhibit piezoelectric effects. In this group, 10 crystallographic classes are pyroelectric. Pyroelectric crystals develop a voltage potential across the crystal faces with a change in uniform heating, similar to how piezoelectric crystals only generate a voltage potential across the crystal faces with a change in uniform stress (Poplavko, 2019).

The 10 pyroelectric crystallographic classes are further subdivided into the ferroelectric and the non-ferroelectric crystals. Ferroelectric crystals, as described previously, become electrically polarized in an externally applied electric field, as do all dielectrics. However, the distinguishing feature of ferroelectric crystals is that they can retain a spontaneous nonzero polarization even when the applied electric field is removed. Additionally, the direction of the dipole moment can be flipped with sufficiently high application of a reverse electric field. The spontaneous nonzero polarization is limited to temperatures below the Curie temperature of the specific material. Above this, the thermal energy and subsequent lattice vibrations are high enough to disrupt the induced polarization by overcoming the energy barrier needed to revert the ionic positions to their original position and reduce the dipole moment to zero. Non-ferroelectric crystals as a corollary cannot retain a spontaneous non-zero polarization upon removal of the electric field. The other 10 piezoelectric classes are not pyroelectric and exhibit only mechanical stress induced polarization. **Table 2** breaks down the 32 crystallographic classes into their respective electric properties.

## 1. Introduction

**Table 2.** Breakdown of the 32 crystallographic classes into the properties of ferroelectricity, pyroelectricity, piezoelectricity, and the leftover classes with no asymmetric electrical properties.

32 crystallographic classes			
21 non-centrosymmetric			11 centrosymmetric $\bar{1}, 2/m, mmm, 4/m, 4/mmm, \bar{3}, \bar{3}m, 6/m, 6/mmm, m3, m3m$
20 piezoelectric		1 non-piezoelectric 432	
10 pyroelectric 1, 2, m, mm2, 3, 3m, 4, 4mm, 6, 6mm	10 non-pyroelectric 222, $\bar{4}$ , 422, $\bar{4}2m$ , 32, 6, 622, $\bar{6}2m$ , 23, $\bar{4}3m$		
ferroelectric	non-ferroelectric		

Piezoelectric crystals, being non-centrosymmetric, consist of an ordered arrangement of positive and negative ions with no center of inversion. The dipole moment of each individual unit cell within the crystal lattice structure can be described by the location of the average center of positive charge from the cations and the average center of negative charge from the anions that make-up the unit cell respectively. In the non-ferroelectric and non-pyroelectric crystals in a hydrostatic stress state and at a steady-state uniform temperature, the crystals always have overlapping centers of the positive and negative charge in space. So,  $x = 0$  for each unit cell according to Eq. 54 and with no dipole moments, there is no polarization  $\mathbf{P}$  of the crystal from ionic sources.

Thermal energy is always present in any real-world material and the effect is a constant vibrational motion of the ions in the unit cell. By chance, these vibrations can induce a temporary dipole moment if the negative and positive charge centers from the ions happen to separate. However, these dipole moments are generally disregarded on any meaningful timescale. Entropically, it is unlikely given a large ensemble of states that the unit cells, when taken over a macroscopic volume, would acquire a non-zero polarization state. Furthermore, these states are brief in time and averaged over a meaningful time scale the centers of negative and positive charge overlap.

When a deviatoric stress is applied to a crystal, such as through a mechanical load, the crystal initially deforms elastically. This elastic strain is recoverable after the removal of stress because the atomic bonds are only stretched or rotated, not broken. In piezoelectric crystals, elastic microstrain gives rise to polarization. In non-centrosymmetric crystals, elastic strain causes asymmetric distortion of anions and cations within the unit cell, creating charge separation, as illustrated in **Figure 14**. This charge separation generates a dipole moment, which collectively defines the polarization of the crystal. Even in polycrystalline materials with randomly oriented grains (i.e., no fabric or lattice preferred orientation), the material can remain macroscopically neutral.

## 1. Introduction

When a mechanical force is applied to a piezoelectric crystal, the elastic strain distorts the unit cell both macroscopically and microscopically. Due to the lack of inversion symmetry, this distortion shifts the positions of anions and cations non-symmetrically. If the dielectric had low electrical resistance, charges could flow and neutralize the polarization quickly. However, because dielectrics typically have high resistance, the polarization leads to a relatively stable and static induced charge across opposing faces of the crystal.

By attaching electrodes to the crystal faces, the polarization induces a charge in the electrodes themselves through Eq. 57, proportional to the polarization. This induction of charges on the electrodes is what is measured in piezoelectric stress sensors, usually by measuring the flux of electric charges from opposing electrodes, in other words the electric current.

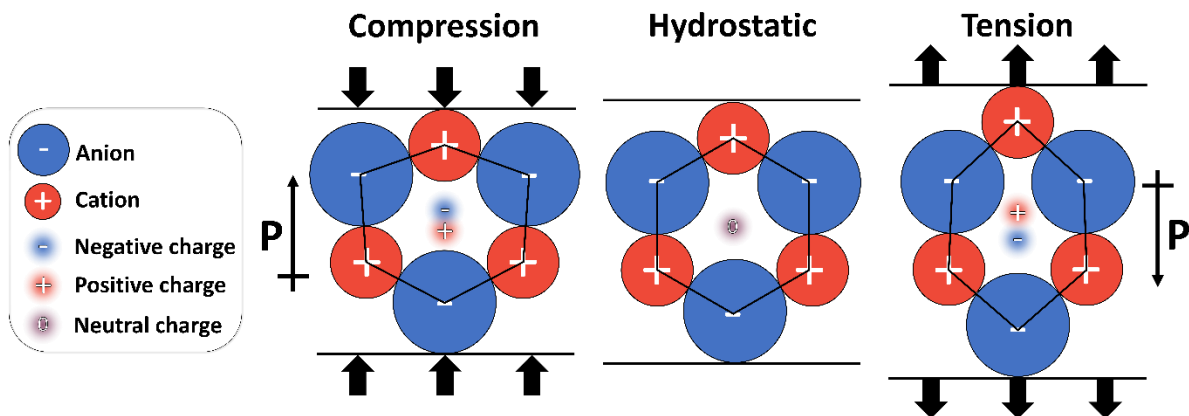


**Figure 14.** Conceptual diagram of a simplified explanation of the atomistic origin of the piezoelectric effect. Shown is a generalized cross-section of a hexagonal crystal lattice. The averaged positive and negative charges are shown for each, as well as the dipole moment orientation, or polarization. The crystal under elastic compression, hydrostatic conditions, and under elastic tension is shown.

The unique properties of dielectrics, mainly the fact that they consist of ionically bonded anions and cations and the high electrical resistance owing to no electrons in the conduction bands, is what allows a measurable piezoelectric effect. Piezoelectric materials are widely used in both engineering and scientific applications, such as electric actuators, high-frequency transducers, stress sensors, and many more applications too numerous to list.

### 1.5.4. Piezoelectric tensors

As discussed previously, the piezoelectric property of a crystal describes the proportionality of the mechanical stress of the crystal lattice to the induced charge polarization in the bulk crystal. The polarization, since it is the sum of all dipole moments in the crystal (Eq. 55) in other words

## 1. Introduction

a summation of vectors, is also a vector (C. Powell, 2010). A vector is a first-rank tensor. To be able to relate a first-rank tensor to a second-rank tensor, a third-rank tensor is required (Patterson & Bailey, 2018). In this case, polarization is the first-rank tensor, stress is the second-rank tensor, and piezoelectricity is thus the third-rank tensor.

$$\mathbf{P} = \mathbf{d}\boldsymbol{\sigma} \quad \text{Eq. 60}$$

$$P_k = \sum_{ij} d_{kij} \sigma_{ij} \quad \text{Eq. 61}$$

$$P_k = \sum_{ij} e_{kij} \varepsilon_{ij} \quad \text{Eq. 62}$$

This is described by Eq. 60, using the full tensor notation for the subscripts.  $P$  is the polarization vector,  $d$  is the piezoelectric strain coefficient, and  $\sigma$  is the stress. The piezoelectric charge coefficient has units of C/N (Tichý et al, 2010). To relate the strain,  $\varepsilon$ , to the polarization  $P$ , a second piezoelectric coefficient, called the stress coefficient, is defined in symbol  $e$ . The unit for this is C/m<sup>2</sup>(Tichý et al, 2010). These two ways to describe the piezoelectric properties of a material can be related to each other through the elasticity, described in Eq. 63.

$$e_{ijk} = d_{iqp} C_{qpjk} \quad \text{Eq. 63}$$

Once again, the fact that stress is a symmetric tensor means that the notation can be simplified to the matrix notation for both piezoelectric coefficients. For  $e$ , the notation is straightforward, but  $d$  requires the conversion rules in Eq. 64.

$$\begin{aligned} d_{iq} &= d_{ikl} \text{ when } k = l \text{ and } q \text{ is } 1, 2, 3 \\ d_{iq} &= 2d_{ikl} \text{ when } k \neq l \text{ and } q \text{ is } 4, 5, 6 \end{aligned} \quad \text{Eq. 64}$$

Expanding Eq. 61 to the full tensor form but simplifying the subscripts to the matrix notation, the calculation of the induced polarization from a stress state on the crystal can be calculated if the full piezoelectric charge tensor is known for the crystal as in the middle matrix in Eq. 65 (C. Powell, 2010).

$$\begin{bmatrix} P_1 \\ P_2 \\ P_3 \end{bmatrix} = \begin{bmatrix} d_{11} & d_{12} & d_{13} & d_{14} & d_{15} & d_{16} \\ d_{21} & d_{22} & d_{23} & d_{24} & d_{25} & d_{26} \\ d_{31} & d_{32} & d_{33} & d_{34} & d_{35} & d_{36} \end{bmatrix} \begin{bmatrix} \sigma_1 \\ \sigma_2 \\ \sigma_3 \\ \sigma_4 \\ \sigma_5 \\ \sigma_6 \end{bmatrix} \quad \text{Eq. 65}$$

Once again, crystal symmetries work in our favor. The complexity reduces greatly for most crystal systems as the symmetry elements drive many of the components in the piezoelectric

## 1. Introduction

charge coefficient tensor to zero. Quartz, for example, at ambient pressure and temperature is stable in the  $\alpha$ -quartz phase which has the  $P3_121$  or  $P3_221$  space group, which are enantiomorphic, with hexagonal point group 32 (Cook & Weissler, 1950; Mansfel'd et al., 1997). In this space group, only two independent piezoelectric charge coefficients are required to fully describe this crystal's piezoelectric properties.

$$d_{ij} = \begin{bmatrix} d_{11} & -d_{11} & 0 & d_{14} & 0 & 0 \\ 0 & 0 & 0 & 0 & -d_{14} & 2d_{11} \\ 0 & 0 & 0 & 0 & 0 & 0 \end{bmatrix} \quad \text{Eq. 66}$$

The piezoelectric charge coefficient tensor is shown in Eq. 66 using matrix notation. If the values of  $d_{11}$  and  $d_{14}$  are known the expected polarization vector induced by the crystal during any known stress state can be calculated. First, the hydrostatic stress state is calculated below to show that under hydrostatic stress, the piezoelectric state does not generate any polarization. Using Eq. 35, Eq. 39 and Eq. 66 and the relationship between them described by Eq. 65, the polarization of  $\alpha$ -quartz in the hydrostatic state can be calculated with Eq. 67.

$$\begin{bmatrix} P_1 \\ P_2 \\ P_3 \end{bmatrix} = \begin{bmatrix} d_{11} & -d_{11} & 0 & d_{14} & 0 & 0 \\ 0 & 0 & 0 & 0 & -d_{14} & 2d_{11} \\ 0 & 0 & 0 & 0 & 0 & 0 \end{bmatrix} \begin{bmatrix} \sigma_1 \\ \sigma_2 \\ \sigma_3 \\ 0 \\ 0 \\ 0 \end{bmatrix} \quad \text{Eq. 67}$$

Decomposing the matrix multiplication to explicit algebraic equations, Eq. 68 to Eq. 70 is defined.

$$P_1 = d_{11}\sigma_1 - d_{11}\sigma_2 \quad \text{Eq. 68}$$

$$P_2 = 0 \quad \text{Eq. 69}$$

$$P_3 = 0 \quad \text{Eq. 70}$$

Since a hydrostatic condition is assumed,  $\sigma_1 = \sigma_2$ , and thus  $P_1 = 0$ , and no piezoelectric polarization is induced in the crystal as all polarization vector components are equal to zero. This holds true for all non-pyroelectric piezoelectric crystals (C. Powell, 2010). Because of this, even if the crystal is under high pressure, for example pressures expected in the Earth's lower crust or upper mantle, if the pressure is hydrostatic, no piezoelectric charges are generated on the crystal faces. This property of piezoelectric crystals is what allows the deviatoric stress, regardless of the magnitude of the hydrostatic stress, to be measured.

## 1. Introduction

### 1.5.5. Piezoelectric crystal orientations

In the industrial manufacturing and preparation of piezoelectric crystals, the system to describe the orientation of prepared crystals has been largely standardized (American & Standard, 1984). To simplify the description of crystal orientations required for a specific use-case, the X, Y, Z axes are defined. These are defined to always be at right angles to each other in space and form a right-handed system.

Since the  $a, b, c$  lattice parameters that define the edges of the unit cells of crystals are not necessarily at right angles, except for the cubic, tetragonal, and orthorhombic, the XYZ axis system does not necessarily correspond to the lattice parameters of the crystal. The choice of how to align the XYZ axes to the crystal lattice parameters is defined to coincide with specific sign conventions.

Not all the sign conventions are necessary to be described, but since the two piezoelectric crystals under consideration are in the 32 point group, P321 space group, discussion of these is necessary. Since they are in the trigonal crystal system, the symmetry consists of a three-fold rotation, the axis of which is called the  $c$  axis. Trigonal systems have three equivalent secondary axes,  $a_1, a_2,$  and  $a_3$ . These lie 120 degrees apart on the plane normal to the  $c$  axis (American & Standard, 1984; C. Powell, 2010).

When defining the orientation of the XYZ axis to the trigonal crystal system, the first step is to define the Z axis parallel to the  $c$  axis. The direction of the X axis is then assigned to coincide with any of the  $a$  axes, and finally the Y axis is defined as perpendicular to both the Z and X axes, the direction of which is assigned to form a right-handed system.

The question remains as to which of the  $a$  axes are assigned to the X axis. By conventional standard, +X is assigned to the  $a$  axis that results in a positive piezoelectric coefficient along it (American & Standard, 1984). The geometrical relationship between these can be visualized, as in **Figure 15**, shown in relation to the trigonal unit cell such as that of  $\alpha$ -quartz and CTGS crystals.

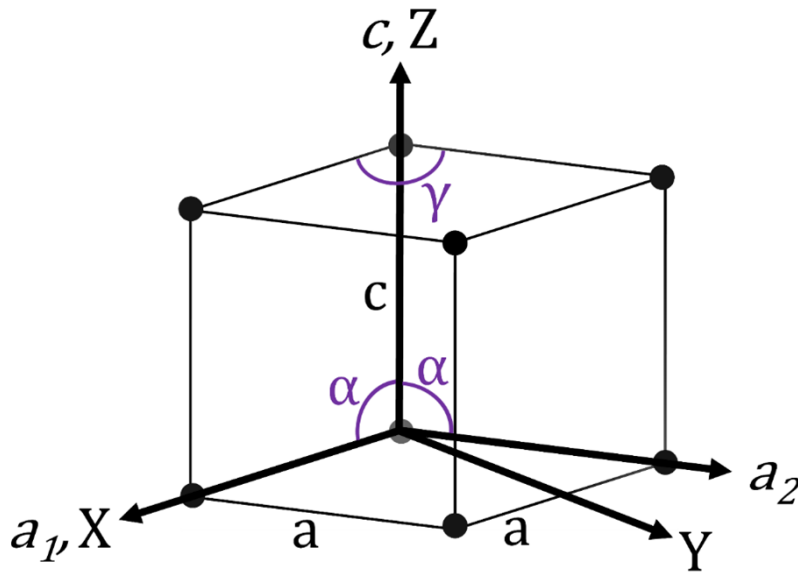


**Figure 15.** Trigonal unit cell shown with the unit cell axes  $a_1$ ,  $a_2$ , and  $c$  shown as well as the  $X$ ,  $Y$ , and  $Z$  axes used to define the piezoelectric crystal cuts. Also shown are the  $a$  and  $c$  unit cell parameters and the right-handed  $\alpha$  and  $120^\circ$   $\gamma$  angles.

When specifying piezoelectric crystals, manufacturers will label them with terms such as “X-cut”, “Y-cut”, etc. This describes a crystal oriented such that the normally parallel cut surface of interest is the plane that has the named axis normal to it. Therefore, an X-cut  $\alpha$ -quartz crystal, for example, would be a crystal where the surface of interest is oriented such that it has the  $X$  axes and crystallographic  $a_1$  axis normal to it, with the  $Y$  and  $Z$  axes, as well as the  $c$  axis, in the plane (American & Standard, 1984). In this orientation, when a deviatoric stress is applied to the crystal faces parallel to the X-cut plane, the piezoelectric coefficients used to calculate either the stress or strain experienced by the crystal, for both  $\alpha$ -quartz and CTGS, are  $d_{11}$  and  $e_{11}$  respectively.

## 1.6. Brillouin Spectroscopy

Brillouin spectroscopy is a technique that probes the velocities of phonons within a crystal structure using their interaction with photons. This offers insights into the mechanical properties and acoustic phonon dispersion. This interaction leads to a shift in the energy and momentum of the scattered photons, providing a direct probe into the material’s mechanical and elastic properties (Wolff et al., 2021).

When light passes through a transparent crystal, most photons are elastically scattered through so-called Rayleigh scattering. These photons retain their energy and thus the incoming light has the same wavelength as the outgoing light. However, a small fraction undergoes inelastic

## 1. Introduction

scattering with the phonons, exchanging energy with the material's vibrational modes. This energy exchange results in a frequency and wavelength shift of the scattered light. If the photon gains energy it is defined as an anti-Stokes shift and if it loses energy, it is a Stokes shift (Wolff et al., 2021).

The frequency shift of the small fraction of photons that interact inelastically is directly related to the acoustic phonon velocities in the material, which in turn are governed by its mechanical properties such as elasticity (Ugarak et al., 2023). By analyzing the distribution of this Brillouin phase shift, one can infer the material's elastic moduli and other mechanical characteristics.

This is a similar process to Raman scattering (RS) spectroscopy; however, RS is the photon's interaction with the optical modes of the crystal lattice which cause a shift in the photon's energy that is multiple orders of magnitude higher, typically larger than 1 THz (Scarponi et al., 2017). Because of this, Brillouin spectroscopy requires spectrometers that are exceptionally sensitive to small frequency shifts, much more-so than Raman spectrometers. The shifts are on the order of double-digit GHz in Brillouin spectroscopy for most materials, corresponding to phonon wavelengths on the order of the optical wavelength used in the experiment (Ugarak et al., 2023).

The principle of Brillouin spectroscopy relies on the conservation of energy and momentum during the light-phonon interaction, described by Eq. 71 and Eq. 72 respectively (Wolff et al., 2021).

$$E_{incident} - E_{scattered} = \pm E_{phonon} \quad Eq. 71$$

$$\vec{k}_{incident} - \vec{k}_{scattered} = \pm \vec{q}_{phonon} \quad Eq. 72$$

$E$  and  $\vec{k}$  represent the energy and momentum of the photons, and  $\vec{q}_{phonon}$  represents the momentum of the phonons. The plus sign represents the anti-Stokes scattering and the minus sign the Stokes scattering.

In a typical Brillouin spectroscopy measurement, the basic components are a laser source with a precise monochromatic wavelength, a goniometer to allow access to the sample's anisotropy, and a high-resolution spectrometer. Typically, the interferometer used in Brillouin spectroscopy, and the one used in this study, is a Fabry-Pérot (Blachowicz et al., 1996; Ike et al., 2007). It exploits the interference of multiple beams reflected between two parallel, highly reflective surfaces to selectively transmit light of specific wavelengths. Its implementation in Brillouin spectroscopy is required because of the minute frequency shifts, offering the required resolution to separate the shift from the Rayleigh scattered portion.

## 1. Introduction

When light enters the interferometer, it is repeatedly reflected between the two mirrors, accumulating a phase difference with each reflection (Dil et al., 1981; Mock et al., 1987). For certain wavelengths, the phase difference results in constructive interference, similar to XRD but in the visible portion of the light spectrum. In this case, the constructive and destructive interference is described by Eq. 73.

$$2d \cos(\theta) = m\lambda \quad \text{Eq. 73}$$

In this equation,  $d$  is the separation between the mirrors,  $\theta$  is the angle of the incidence of the light within the interferometer,  $m$  is an integer that describes the order of the interference, and  $\lambda$  is the wavelength of the light. By precisely moving one of the mirrors using a highly precise piezoelectric actuator, the distance between the mirrors can be scanned through the wavelength range under consideration. Using a Fabry-Pérot interferometer, enough precision is gained in selectively allowing specific wavelengths of light to pass through so that it becomes possible to separate the small shift from the Rayleigh scattering.

In addition to determining photon speeds, Brillouin spectroscopy is a robust method for assessing the directional dependence of these speeds in single crystals. This approach can even be applied under extreme conditions, such as within diamond anvil cells, to probe material behavior at high pressures. In a typical experiment, the incident light is inelastically scattered by thermally excited acoustic photons, leading to subtle shifts in its frequency. These shifts, which usually fall in the range of 0.01 to 10 GHz (Kojima, 2022; Speziale et al., 2014), are directly related to the collective motion of particles in the medium. Because the dispersion of these frequency shifts reflects the viscoelastic properties of the material, this method provides critical insights into its elastic moduli, internal stresses, and anisotropic characteristics.

As described previously, the frequencies of the incident light,  $k_s$ , and scattered light,  $k_i$  are approximately equal,  $k_s \approx k_i$ . The scattering geometry between the incident and scattered wave normal defines the wavevector,  $q$ , of induced vibrational energy within the medium, the geometry of which is shown schematically in **Figure 16** (Dil et al., 1981; Kojima, 2022; Mock et al., 1987).

## 1. Introduction

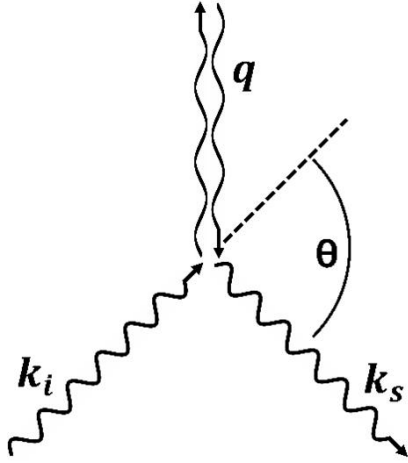


**Figure 16.** Schematic diagram of the incident and scattered light and the wavevector of the induced vibrational energy within the medium. The scattering angle is also shown. Figure modified from (Speziale et al., 2014).

The relationship between the incident light and wavevector is described below, Eq. 74.

$$q = 2k_i \sin\left(\frac{\theta}{2}\right) \quad \text{Eq. 74}$$

$$\omega_s = \omega_i \pm 2vk_i \sin\left(\frac{\theta}{2}\right) \quad \text{Eq. 75}$$

In these equations,  $q$  is the magnitude of the scattering wave vector,  $k_i$  is the wave vector of the incident light,  $\theta$  the scattering angle,  $\omega_s$  the frequency of the scattered light,  $\omega_i$  frequency of the incident light, and  $v$  the velocity of the acoustic phonons in the medium. Eq. 74 describes the magnitude of the scattering wave vector and Eq. 75 the frequency of the scattered light relative to the incident frequency.

The similarity to the Bragg equation is because fundamentally, both involve a scattering of electromagnetic radiation through interaction with a medium (Powell, 2010; Patterson & Bailey, 2018). The spectrum of the scattered light creates doublets at frequencies described by Eq. 75 due to the  $\pm$ . The two-way interaction with  $k_s$  and  $k_i$  by the wavevector  $q$  increases or decreases the energy of the scattered light. An increase in energy of the scattered light increases the frequency, called an Anti-Stokes scattering, as opposed to a Stokes scattering event in which the energy and thus frequency is reduced (Speziale et al., 2014; Wolff et al., 2021).

## 1. Introduction

In the Brillouin spectroscopy method this minute frequency shift is measured. Crystalline solids contain three acoustic modes.  $V_{s1}$  is the fast quasi-shear acoustic mode,  $V_{s2}$  is the slow quasi-shear acoustic mode, and  $V_p$  is the quasi-longitudinal mode. Each of these, in an idealized Brillouin spectrum, creates a doublet of Stokes and Anti-Stokes scattering peaks when plotted as intensity versus frequency shift. An idealized spectrum is illustrated in **Figure 17** (Speziale et al., 2014).

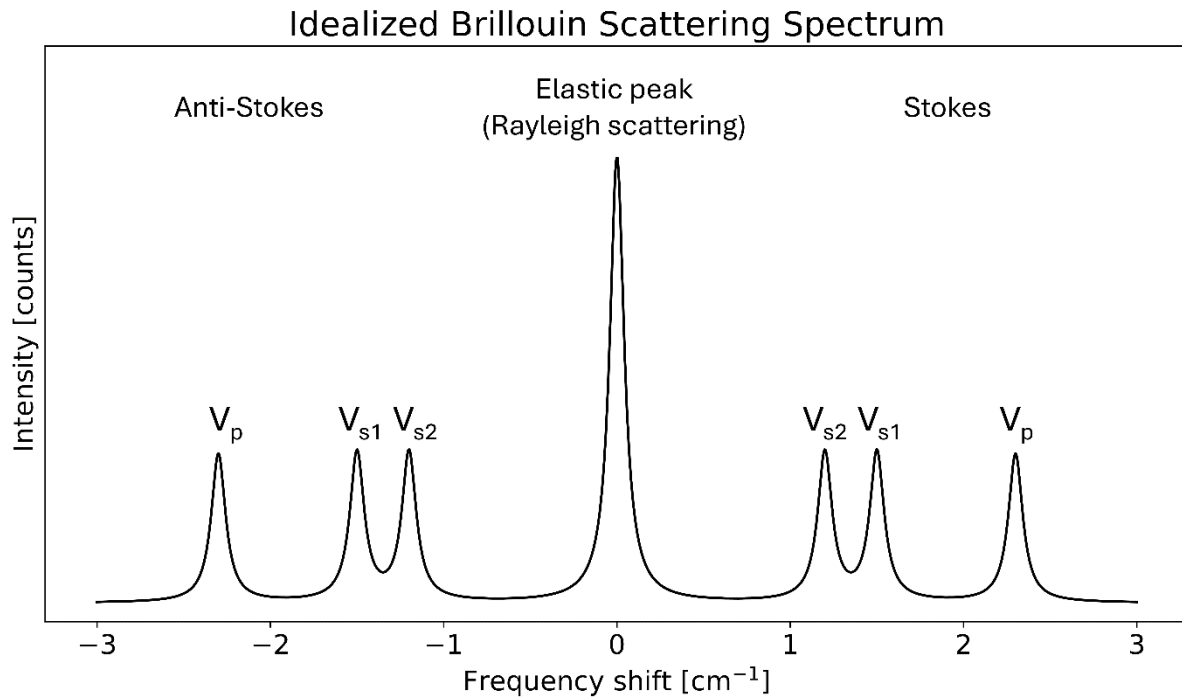


**Figure 17.** Idealized Brillouin spectrum showing the elastic peak and the Anti-Stokes and Stokes velocity peaks from the material. There are two shear and one longitudinal peak.

Fundamentally, Brillouin and Raman spectroscopy both measure phonons within the crystal lattice. However, Brillouin spectroscopy measures low energy, long-range phonons on the acoustic branch of the frequency and wavevector dispersion relation. Raman measures higher frequency and thus higher energy phonons on a unit cell scale, probing the optical branch instead (Polian, 2003). The wavenumber of typical Raman measurements ranges from a minimum of roughly 100 cm<sup>-1</sup> to over 2000 cm<sup>-1</sup>, while Brillouin spectroscopy is lower energy and within the single-digit wavenumbers.

Since the Brillouin peaks are much closer to the elastic peak, or the Rayleigh scattered peak, a much more precise interferometer is required to separate the small frequency shift from the much brighter elastic peak. A Faby-Perot interferometer is capable of the precision necessary

## 1. Introduction

to separate the peaks from the elastic peak. For this work, the TFP-1 tandem 3+3 pass Fabry-Perot interferometer was used from Table Stable Ltd (Lindsay et al., 1981; Mock et al., 1987). The internal operating principle is described by the schematic in **Figure 18**.

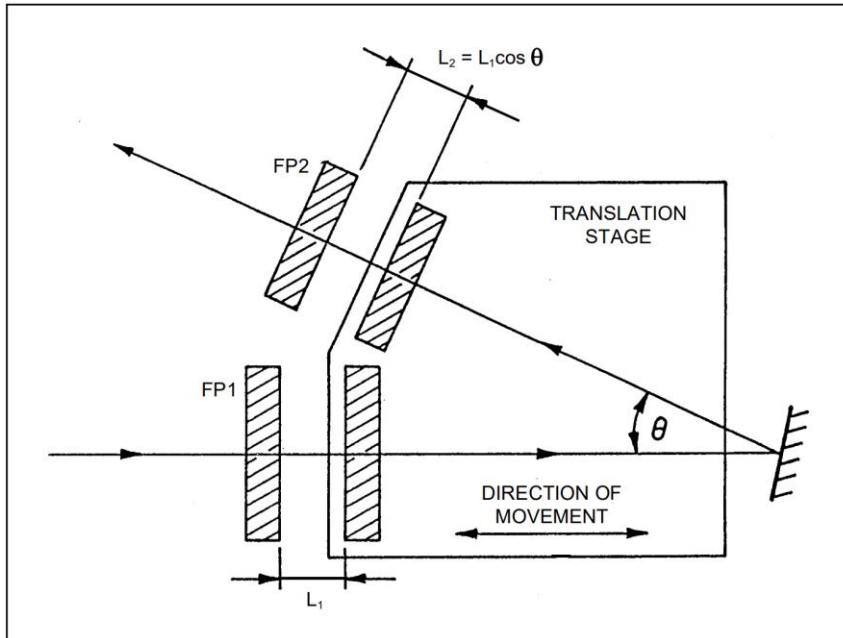


**Figure 18.** Schematic diagram of the operating principle of the TFP-1 tandem 3+3 pass Fabry-Perot interferometer from the operating manual of the Table Stable Ltd TFP-1 interferometer. FP1 is the first Fabry-Perot etalon that the light encounters and FP2 is the second etalon in the sequence.  $L_1$  is the distance between the mirrors of FP1 while  $L_2$  represents the effective optical path length of the second Fabry-Perot etalon FP2, given by the equation provided.  $\theta$  is the angle of the translation stage. This adjusts the alignment of FP2 to control the optical path difference. The direction of movement arrows move the whole stage to scan  $L_1$  and  $L_2$  distances.

Light is passed between two parallel mirrors. On each reflection, the light interferes with itself either constructively or destructively depending on the distance between the mirrors,  $L$ , and whether this distance is an integer multiple of the wavelength of light,  $\lambda$ .

$$m\lambda = 2nL \cos(\alpha) \quad \text{Eq. 76}$$

This is described by Eq. 76.  $n$  is the refractive index of the medium between the mirrors,  $m$  is an integer, and  $\alpha$  is the incidence angle which is normally  $0^\circ$ . By setting the mirrors at a specific and precise distance apart, they act as a narrow band-pass filter for that specified wavelength of light (Dil et al., 1981; Speziale et al., 2014).

## 1. Introduction

In a Fabry-Perot interferometer, the translation stage is scanned back and forth to vary the mirror gap, labeled in Eq. 93. This makes it possible to scan through the wavelengths that are transmitted, resulting in a variable narrow band-pass filter. The tandem portion of the description describes the use of two mirror gaps that are scanned and the 3+3 pass means that light is reflected by the mirrors to pass through the mirror gap three times (Lindsay et al., 1981; Mock et al., 1987). By synchronizing the timing of the variable mirror gap with the photon counter, the photons can be accurately assigned to the correct wavelengths, ensuring the frequency resolution necessary for Brillouin spectroscopy.

Brillouin spectroscopy can be used on both opaque bulk material and transparent materials through transmission. In this work, measurements were taken on thin, transparent platelets in a forward symmetric geometry. The advantage is that knowledge of the refractive index of the material is not necessary (Speziale et al., 2014). The geometry is shown schematically in **Figure 19**. In this geometry, the incident laser light, 532 nm from a Nd:YVO<sub>4</sub> source, enters the thin sample and refracts at a scattering angle of  $\theta$  along  $k_s$ .

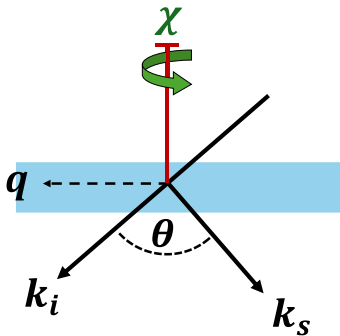


**Figure 19.** Forward symmetric geometry on a thin, transparent platelet sample for Brillouin spectroscopy.

The plane wave of the acoustic lattice vibrations within the sample travel along  $q$ . This vector defines the direction along which the velocity measurements are taken. By rotating the thin platelet around the normal vector to the surface, at angles of  $\chi$ , sound velocity measurements are taken along the plane of the platelet. The wave equation for a linear elastic anisotropic solid, in a Cartesian reference system, is described by Eq. 78. Plane wave solutions of the equation come in the form of Eq. 77 and substituting this into Eq. 78, Eq. 79 is created. By defining

## 1. Introduction

direction cosines  $n = q/|q|$  and phase velocity  $v = \omega/q$ , Eq. 80 below can be created (Speziale et al., 2014).

$$u_i = u_i^0 e^{i(qx - \omega t)} \quad \text{Eq. 77}$$

$$\rho \frac{\partial^2 u_i}{\partial t^2} = C_{ijkl} \frac{\partial^2 u_k}{\partial x_j \partial x_l} \quad \text{Eq. 78}$$

$$(C_{ijkl} q_j q_l - \rho \omega^2 \delta_{ik}) u_k^0 = 0 \quad \text{Eq. 79}$$

$$|C_{ijkl} n_j n_l - \rho v^2 \delta_{ik}| = 0 \quad \text{Eq. 80}$$

In the equations,  $u_i^0$  is the polarization,  $\delta_{ik}$  is Kronecker delta and  $\rho$  the density of the crystal.  $v$  is the sound velocity as measured from the Brillouin spectra peaks. The equation is a cubic equation in  $v^2$  with three real solutions that can be expressed in closed form with Cardan's method. This is solved numerically using a least-square method to determine the independent  $C_{ijkl}$  elastic stiffness coefficients.

Since point group 32 has 6 independent elastic stiffness coefficients (Powell, 2010; Kholkin et al., 2008), two platelets at different lattice orientations are required to solve for all 6 coefficients. Since ferroelastic twinning in both  $\alpha$ -quartz and CTGS depends on the magnitude of the  $S_{14}$  elastic stiffness coefficient, determining this value at multiple pressures is required for determining the relative ferroelastic twinning potential of CTGS, as compared to  $\alpha$ -quartz. Ideally,  $S_{14}$  should be as small as possible to avoid ferroelastic twinning.

As described previously, the elastic stiffness matrix  $C_{ij}$  is inverted to derive the elastic compliance matrix  $S_{ij}$ . For point group 32, the Voigt elastic stiffness and compliance tensors are listed in Eq. 81 and Eq. 82 (Powell, 2010).

$$C_{ij} = \begin{pmatrix} C_{11} & C_{12} & C_{13} & 0 & 0 & 0 \\ C_{12} & C_{11} & C_{13} & 0 & 0 & 0 \\ C_{13} & C_{13} & C_{33} & 0 & 0 & 0 \\ 0 & 0 & 0 & C_{44} & 0 & 0 \\ 0 & 0 & 0 & 0 & C_{44} & C_{14} \\ 0 & 0 & 0 & 0 & C_{14} & \frac{1}{2}(C_{11} - C_{12}) \end{pmatrix} \quad \text{Eq. 81}$$

## 2. Methods

$$S_{ij} = \begin{pmatrix} S_{11} & S_{12} & S_{13} & S_{14} & 0 & 0 \\ S_{12} & S_{11} & S_{13} & -S_{14} & 0 & 0 \\ S_{13} & S_{13} & S_{33} & 0 & 0 & 0 \\ S_{14} & -S_{14} & 0 & S_{44} & 0 & 0 \\ 0 & 0 & 0 & 0 & S_{44} & -2S_{14} \\ 0 & 0 & 0 & 0 & -2S_{14} & 2(S_{11} - S_{12}) \end{pmatrix} \quad \text{Eq. 82}$$

Eq. 80 solves for the elastic stiffness coefficients. Conversion between  $C_{ij}$  and  $S_{ij}$  is described by Eq. 83.

$$S_{ij} = C_{ij}^{-1} \quad \text{Eq. 83}$$

The piezoelectric crystal measures the deformation stresses at high hydrostatic pressure above 1 GPa. The elastic stiffness tensor of CTGS has been previously measured at room pressure (Dudka, 2016; Shi et al., 2007; Suhak et al., 2018; Zu et al., 2016) but no high-pressure measurements have been made. To acquire Brillouin spectra on CTGS at higher pressures a diamond anvil cell (DAC) was utilized.

## 2. Methods

### 2.1. Large volume press for deformation

#### 2.1.1. 6-ram press

The MAVO LPQ7-2400-100 is a large loading capacity press (24 MN), manufactured by Max Voggenreiter GmbH in Mainleus, Germany. It employs six individual rams actuating into a central cubic cavity. The rams are maintained in position by a radially symmetrical support frame made up of 4×4 hardened steel plates arranged contrarily to counterbalance the outward thrust exerted by the rams. The press is designed to handle 8 MN of force from each ram at a maximum oil pressure of 630 bar (Manthilake et al., 2012). Each ram has a stroke of 100 mm, permitting a wide range of assembly sizes. The manufacturer specifies that the oil pressure to load relation is linear and is described by Eq. 84, where  $F_r$  is the force per ram in MN and  $P_o$  is the hydraulic oil pressure in bar.

$$F_r = \frac{4P_o}{315} \quad \text{Eq. 84}$$

Each of the six rams is fitted with a Heidenhain linear displacement encoder—positioned behind each ram between the hardened steel plates that comprise the press frame. They are connected to the rear surface of each anvil post through a steel rod which passes through the

## 2. Methods

center of the hydraulic ram. The anvil positions are tracked through the relative distance between the rear of the anvil and the ideally rigid steel outer frame. These sensors have a precision of 0.1  $\mu\text{m}$ . Based on the data gathered from these sensors, the press can be programmed to extend or retract any opposing pair of rams at a user-defined speed, specified in microns per minute, thereby achieving uniaxial deformation under high pressure conditions.

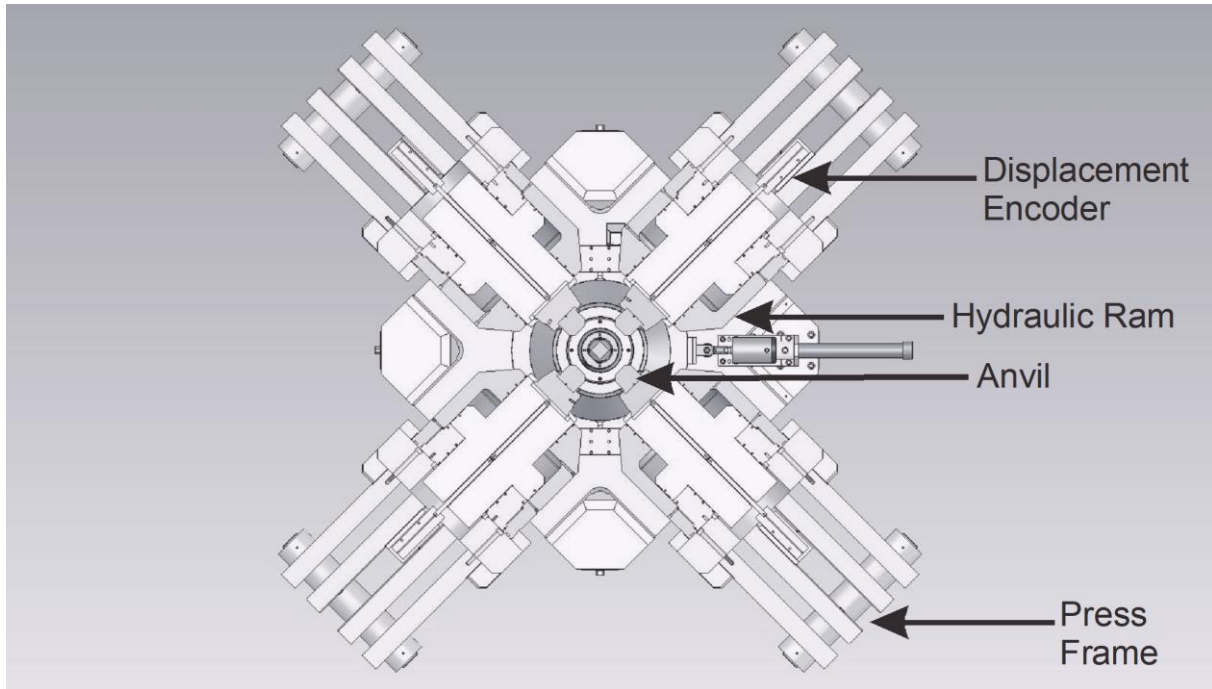


**Figure 20.** The MAVO 6-ram press as described in the text. A horizontal section is shown through the central region of the press. Four of the hydraulic rams and the rods which connect the displacement encoders with the rear surface of the rams are shown, with the top ram removed in the image for clarity (Manthilake et al., 2012).

The six exterior rams, or first stage anvils, incorporate 27 mm truncated edge length (TEL) tungsten core anvils, which drive second stage anvils. These second stage anvils consist of a tungsten-carbide (WC) core and an outer steel casing for support. The steel casing has a diameter of 50 mm, pressure-fitted around a 35 mm diameter WC core. These secondary anvils, measuring 37.5 mm in height, press onto a cubic assembly along a square 10 mm TEL. Multiplying the area of each anvil surface by the number of rams, 6, provides a combined pressing area of 600 mm<sup>2</sup>. By utilizing the simple relation of force per area, high-pressures,  $P$ , can, in theory, be achieved according to Eq. 85.

$$P = \frac{F}{A} \quad \text{Eq. 85}$$

## 2. Methods

Where  $F$  is force, and  $A$  is area. If we solve this simple relation for a force of 8 MN (the maximum force per ram) and an area of  $100 \text{ mm}^2$ , we arrive at a naïve pressure of 80 GPa as the maximum theoretical pressure utilizing the 10 mm TEL anvils. In reality, the maximum achievable pressure is much lower due to effects of gasket friction, material flow, and ultimate strength limits of anvil materials.

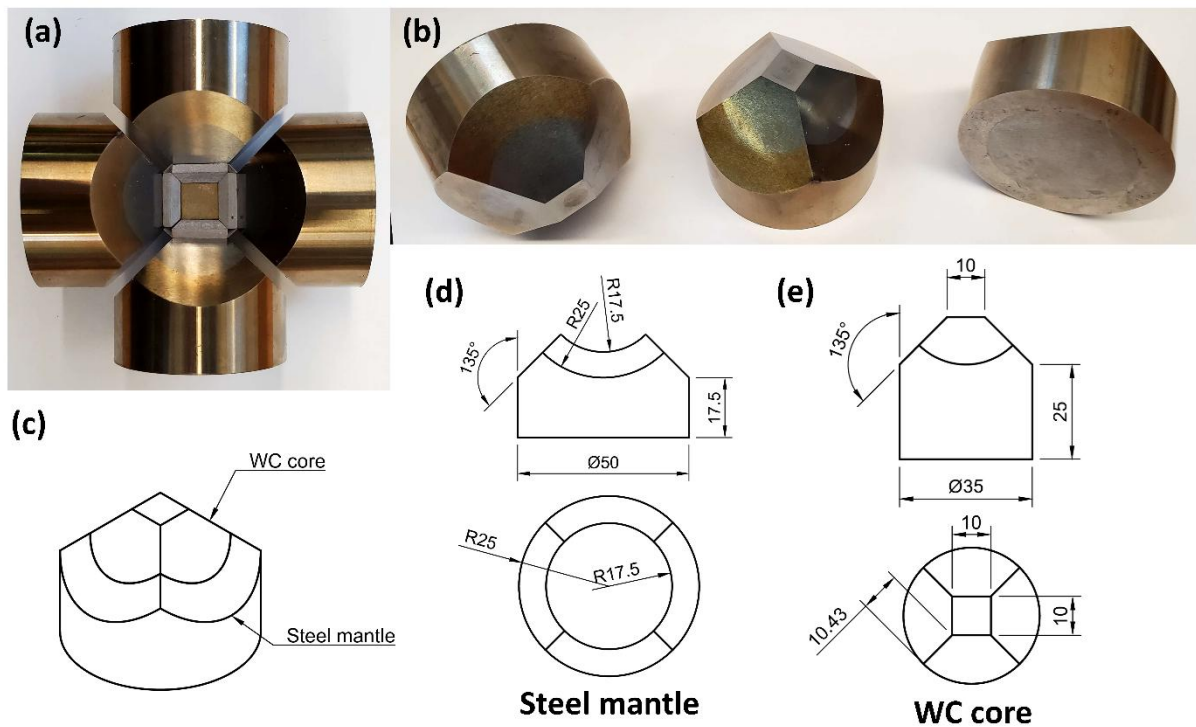


**Figure 21.** The second stage anvils images and drawings. (a) a section of the assembly, with only four anvils shown and the placement of gaskets and the central cubic assembly. (b) three different views of an anvil. (c) A drawing of the anvil with the WC core and steel mantle labeled. (d) Drawing of the steel mantle with measurements in units of mm. (e) Drawing of the WC core that is fit into the steel mantle, once again with units of mm.

The second stage anvils used are manufactured by Hawedia (type ha-co6%). The tungsten carbide contains 6% cobalt as a binder and has a grain size  $<0.6 \mu\text{m}$ . Hawedia's catalogue claims that their WC ha-co6% material has a Vickers hardness (HV) of 1800HV30, however, in the literature it is reported to be up to 2040HV30 (Ishii et al., 2016). Vickers hardness is measured by indenting a square-based pyramid at a fixed load, in this case HV30 referring to 30 kilogram-force (kgf). By measuring the diagonal length left by the indenter in the material

## 2. Methods

and thus the surface area of imprint, once can calculate the Vickers hardness number, or HV, according to Eq. 86.

$$HV = \frac{\text{indenter force [kg]}}{\text{surface area of the imprint [mm}^2\text{]}} \quad \text{Eq. 86 (Tekkaya \& Lange, 2000)}$$

An empirical relationship between Vickers hardness and yield strength ( $\sigma_Y$ ) in MPa for an isotropically hardening material is described by

$$HV = \frac{2.475 \sigma_Y}{9.807 [m/s^2]} \quad \text{Eq. 87 (Tekkaya \& Lange, 2000)}$$

When calculated using Eq. 87 for 1800HV30,  $\sigma_Y$  is found to be 7130 MPa, or 7.13 GPa. For 2040HV30,  $\sigma_Y$  is found to be 8080 MPa, or 8.18 GPa. This correlates well with the manufacturer's claim of a 'compressional strength' >7 GPa (Ishii et al., 2016). This simple calculation agrees remarkably well with quasi-static compression experiments on commercially available tungsten carbide. Hydro Carbide Tool Company brand HCUS06 tungsten carbide material with 6% Co and 0.8  $\mu\text{m}$  grain size failed in compression at  $7.4 \pm 0.1$  GPa (Swab & Pittari III, 2023) under quasi-static compression. This calculation is without considering the effect of the gaskets or frictional losses. The empirical relationship in Eq. 87 applies solely to the physical properties of the tungsten carbide itself, without accounting for the specific application geometry.

If the desire is to stay below a pressure of 7 GPa on the second stage anvil's truncation, i.e. the surface that acts directly upon the cubic assembly, to avoid anvil breakage and a blowout, we can calculate, using Eq. 85, the force that can be safely imparted by the first stage anvils. Assuming the area of the second stage anvil truncation to be  $100 \text{ mm}^2$ , the force beyond which  $\sigma_Y$  is overcome, per anvil, is calculated as 700 kN, or 0.7 MN. In practice, however, gasket extrusion increases this limit by a substantial amount.

Because of gasket extrusion into the space between the anvils, the effective surface area on which the ram force acts is increased due to gasket-anvil friction (Zhang et al., 2018). The result is that the actual pressure experienced by the second stage anvils decreases. Commonly, gaskets are manufactured from pyrophyllite, a mineral with the chemical formula  $\text{Al}_2\text{Si}_4\text{O}_{10}(\text{OH})_2$ . Pyrophyllite has been traditionally used owing to its ease of machining, relatively small compressibility, low strength, and good thermal and electrical insulation (Fang et al., 2007). As the press load increases, the low strength pyrophyllite begins to flow outwards through the gap,

## 2. Methods

increasing its surface area. This supports the anvils and allows higher ram loads to be applied before breakage.

Initially, the internal pressure of the gasket ( $P_g$ ) lags behind the pressure inside the cubic assembly ( $P_c$ ). The amount of flow depends on multiple factors, but the result is that the surface area of gasket-to-anvil contact increases (Zhang et al., 2018). At sufficiently high loads, the ratio of the surface area on the truncation of the relatively incompressible second stage anvils, versus the area on the sides of the anvils supported via gasket extrusion, decreases enough that the gaskets support the majority of the additionally added press load. As a result,  $P_g > P_c$ , and increasing ram load serves to increase  $P_g$  more than  $P_c$  (Li et al., 2007; Zhang et al., 2018). The pressure inside the cubic assembly will then start to plateau, limiting the maximum attainable pressures. The pressure gradient across the gasket can also limit the maximum attainable pressure.

$$\Delta P = P_c - P_g \quad \text{Eq. 88 (Zhang et al., 2018)}$$

If  $\Delta P$ , defined in Eq. 88 is not too large, it can be overcome by the static friction between the gasket and anvil and by the internal friction of the gaskets, confining the pressure. This pressure gradient across the gasket is what limits the attainable pressure in the assembly. However, when  $\Delta P$  passes a certain threshold, one study has proposed this to be 0.9 GPa (Zhang et al., 2018), either the static friction or internal friction or both, can be exceeded, causing a sudden and uncontrolled outward extrusion of material. This is referred to as a ‘blowout’. Usually, this limit is reached before the  $\sigma_Y$  of the anvils themselves.

Gasket extrusion thus has multiple effects. First, it allows for higher press loads to be applied by distributing the load over a larger surface area of the secondary anvils, limiting the pressure on the anvils but also on the central cubic assembly. Secondly, through friction it serves to contain the pressure of the assembly within the cubic space defined by the second stage anvils, that would otherwise cause material to flow out through the anvil gaps. Finally, it ultimately limits the highest achievable hydrostatic pressure in the cubic assembly through static and internal friction failure.

### 2.1.2. Displacement encoder calibration

The encoders that measure the displacement of each ram are attached to their respective steel frame plates. Therefore, all anvil displacements are measured relative to the outer steel frame of the press. As mentioned, each ram acts upon four steel frames that form complete rings around the whole press vertically, so that each opposing ram acts outwardly upon the same set of steel plates. Each steel plate is 90 mm thick and all four create a strong frame that can

## 2. Methods

withstand, at the highest achievable press load, up to 8 MN of force acting outwards. This is because each anvil, at the maximum oil pressure, can apply 8 MN of force. However, the frame does still bow outwards elastically.

Ideally, if the frame was entirely symmetric, the elastic deformation would be isotropic and the compressed internal cavity would remain uniformly cubic. However, while the horizontal rams deform the press frame in a mainly isotropic manner due to the symmetry of the press frame in this plane, the vertical axis does not have the same symmetry and is anisotropic compared to the horizontal plane. Because of this anisotropy, as the frame elastically deforms during press loading the encoders either underestimate or overestimate the anvil positions differentially along the 3 axes.

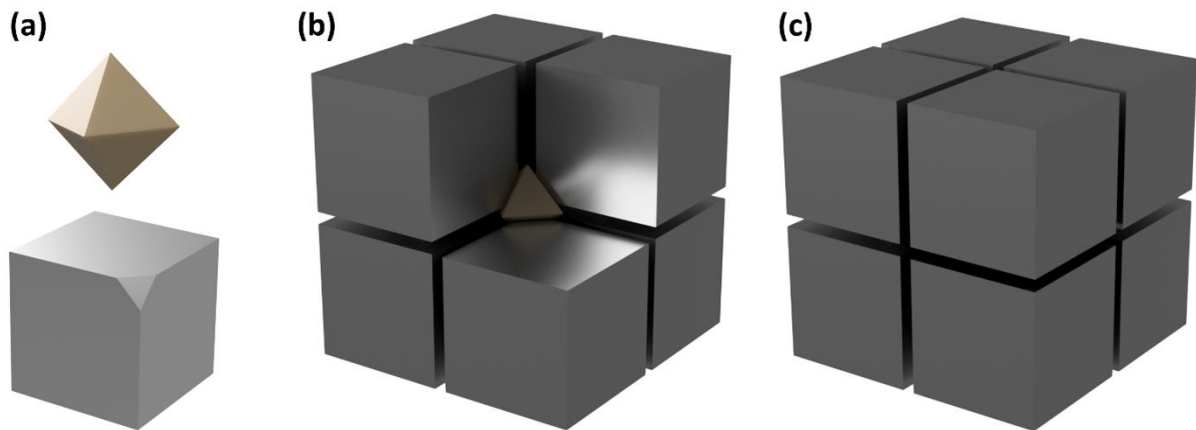


**Figure 22.** Render of MA 6-8 geometry. (a) The central octahedron shown above with the truncated cube below. The octahedron is shown larger for clarity. (b) The assembly geometry before the insertion of the last anvil. The truncated corners are inserted against the central octahedron. (c) Finally, the complete assembly ready to be inserted into the MAA. The assembly shown is a 14/8, defined as an edge length of 14 mm for the octahedron and a truncated edge length of 8 mm on the cubic anvils. Gaskets are not shown.

This positioning mismatch results in a lowering in symmetry of the otherwise cubic space at high press loads. In the MA 6-8 geometry, shown in **Figure 22**, the non-uniform chamber compressed by the first stage anvils results in high differential stresses on the second stage anvils, which drastically lowers the maximum achievable pressure. This is because some of the anvils will advance further than others and the gasket materials along the anvil edges experience a higher  $P_g$ .

## 2. Methods

As the  $P_c$  could still be similar because it is defined by the average load from all anvils, according to Eq. 88 (Zhang et al., 2018), the  $\Delta P$  for the gaskets and anvils that have advanced further is higher than for those that have not. If this reaches a critical threshold, the internal or static friction of the gasket material can be exceeded, resulting in a sudden outflow of gasket or assembly material and a rapid forward movement of the cubic anvil. This often leads to a full blowout and a failure of the experiment, in addition to anvil destruction. The MA 6-6 geometry can experience similar problems, but it is less sensitive to mismatch in the position of the first stage rams. In the MA 6-8 geometry, each inner cubic anvil is in contact with three outer rams. Any differential outer ram movement will cause massive internal shear stresses on the inner second-stage anvils. The MA 6-6 inner anvils are in contact with only one outer ram, such that differential outer ram movement will not induce large shear stresses on the inner anvils. In this geometry, mismatch errors in ram position result in non-hydrostatic stress in the assembly instead of catastrophic failure.

Regardless, as hydrostatic stress is at least the initial goal, the elastic deformation of the outer frame needs to be compensated by proportionately increasing the stroke of rams experiencing the most frame deformation. This calibration will be referred to as the frame bending calibration. If the amount of frame bending is known at specific hydraulic oil pressures along the MAA's full pressure range, an equation can be fitted to compensate the mismatch on the ram position. Using this mismatch error equation, the software corrects for the anvil displacement as the pressure increases to maintain cubic compression of the inner anvils.

There are multiple ways to measure the amount of press frame bending. Since the bending is relative to the press itself, one can measure the frame displacement relative to the laboratory frame of reference, as has been successfully performed in the past (Sano-Furukawa et al., 2014). Another method is to measure the anvil gap within the inner cubic space at different press loads. By placing a material within the inner cubic space that can flow and plastically deform and retain the deformation after load is removed, one can measure the opposing face-to-face distances on the resulting cube. Any differences in the resulting form are the result of the frame bending.

In this study, the press was calibrated using this method by employing a copper polyhedron. Copper is soft and plastically deforms under stresses typically applied by the first stage anvils, making it ideal for this type of anvil geometry calibration. If the copper flows outwards sufficiently far enough to form gaskets between the anvils, friction will begin to support the

## 2. Methods

ram load and frictional isotropy cannot be assumed. For this reason, the load is limited to avoid gasket formation.

The first stage tungsten cored anvils have 27 mm edge length faces. This would form a 19.68 cm<sup>3</sup> cubic volume if the anvils were to be driven forward until the edges were in contact. A copper edge-truncated cube is employed with a 35 mm edge length and with edges truncated inwards to create square faces 10 mm in length. This forms a polyhedron with 12 hexagonal faces and 8 cubic faces. The volume is 21.78 cm<sup>3</sup>, ensuring that even if the copper was to be entirely deformed into a cube, it would not allow the brittle first stage anvils to make contact. The copper polyhedron is placed in the press and a specified ram load is applied, dwelling for about 10 minutes, and then decompressed. The copper is pressed into a cube with rounded edges that have not formed gaskets as the material flows outwards. By measuring the face-to-face length of each axis, keeping track of the face alignment, the divergence in the ram encoder position can be measured. This is then repeated for multiple pressures as the frame bends nonlinearly with pressure.

The rams below and above, ram 1 and 2 respectively, are taken as the baseline and the position encoding of the other ram pairs, rams 3 and 4, and rams 5 and 6, is adjusted to match them. Once multiple hydraulic oil pressures have been measured in this way, a polynomial function is fitted to the residuals and added to the anvil positions to correct for the frame bending. The process for the frame bending correction for rams 3 and 4 is shown below, along with an illustration of the geometry and measurement variables in Figure 24. The same process is repeated for rams 5 and 6. The calibration procedure was first developed and described in Manthilake et al. (2012).

After compression, the deformed copper cube face-to-face distances are measured with a micrometer with 1 μm precision, defining  $d_{3,4}$  and  $d_{1,2}$ .

$$d_{3,4} = \text{distance ram 3,4}$$

$$d_{1,2} = \text{distance ram 1,2}$$

$$\frac{d_{1,2} - d_{3,4}}{2} = \text{ram 3,4 correction factor} = C_{3,4} \quad \text{Eq. 89}$$

$$D_{3,4(c)} = D_{3,4} + C_{3,4}$$

The ram 3,4 correction factor,  $C_{3,4}$ , calculated per Eq. 89, is added to the position of rams 3 and 4, correcting for the frame bending along that axis. The same procedure is applied to rams 5 and 6. Each correction is for a specific hydraulic oil pressure. The process is repeated at multiple

## 2. Methods

oil pressures and a polynomial equation is fitted to the correction factors for each opposing ram pair as a function of oil pressure.

During normal operation, the required frame bending correction is determined from each polynomial at each oil pressure and the result is added to the linear encoder distance measurements, which allows the PLC to automatically correct for frame bending at any pressure. The correction polynomials used at the time of the experiments in this study is plotted in **Figure 23**. Subsequent runs have shown that this method results in a cubic compression precision of  $\pm 10 \mu\text{m}$  along each axis.

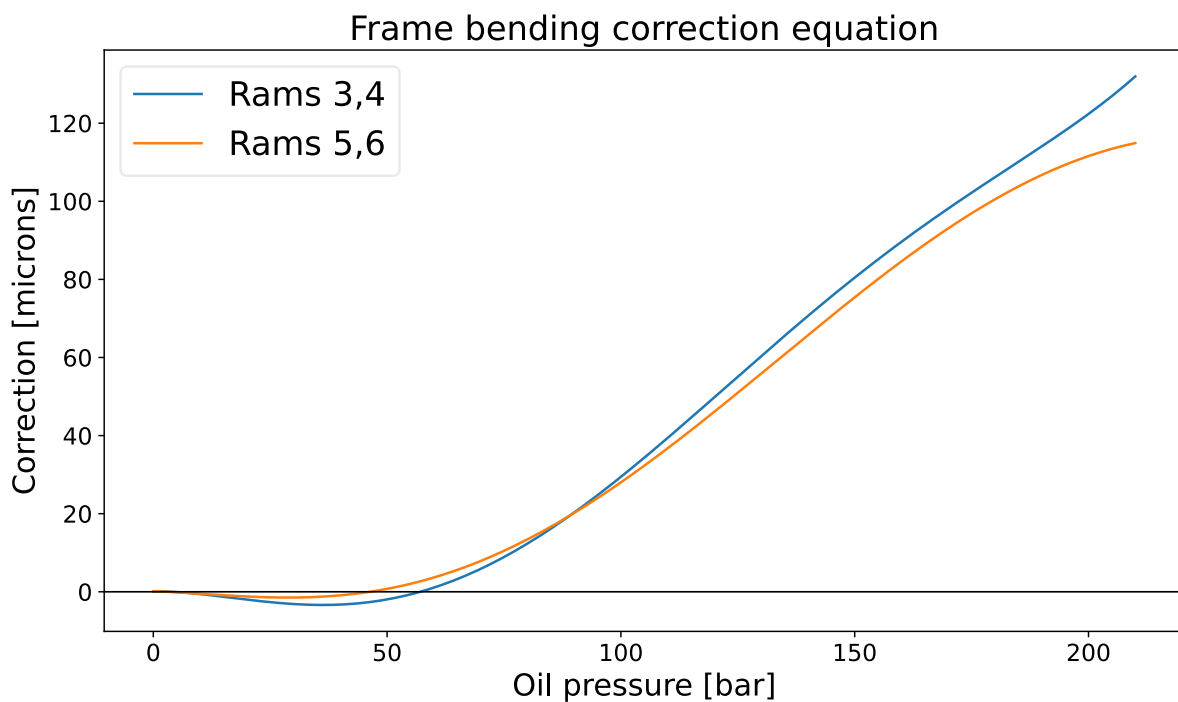


**Figure 23.** Frame bending correction polynomials of rams 3 and 4 (3,4) and 5 and 6 (5,6). The correction is added to the ram position to ensure a cubic space between the anvils.

## 2. Methods

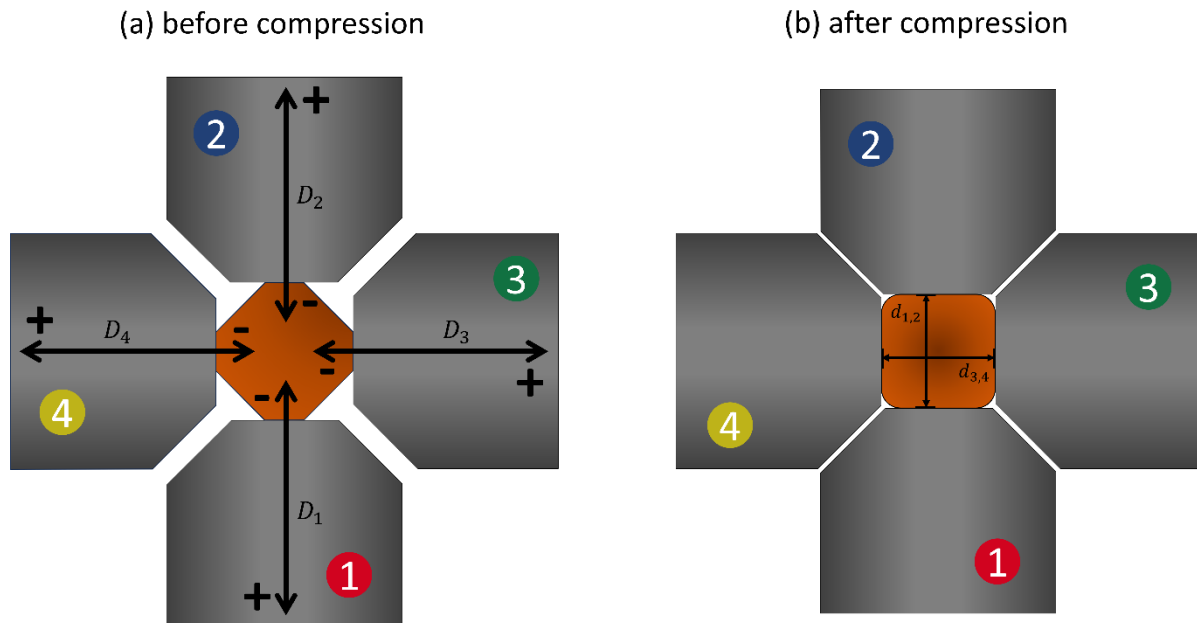


**Figure 24.** Geometry and measurement variables of a frame bending calibration run, showing a cross section through rams 1, 2, 3, and 4. (a) Ram and copper arrangement before deformation.  $D_x$  shows the ram advancement and retraction directions, and the signs the positive and negative directions of the ram movement directions. (b) Rams and copper arrangement after deformation.  $d_{x,y}$  marks the face-to-face distance measurements made, as per Eq. 89.



**Figure 25.** Image of a copper edge-truncated cube before deformation (left) and the resultant shape after deformation (right). The deformed copper on the right was deformed to 4 MN. For scale, the edge length of the square face of the copper polyhedra on the left is 10 mm in length.

## 2. Methods

### 2.2. Piezoelectric assembly

#### 2.2.1. 15/10 cubic assembly design

For the following description of the cubic assembly, the part label will be provided in parenthesis. The part labels will refer to **Figure 26**, **Table 3**, and **Figure 27**. In **Figure 26**, images were taken of all the parts laid out to provide a sense of scale between them and the full parts list required, with the top providing the part labels and the bottom a more oblique view. **Table 3** provides the bill of materials (BOM) of the assembly, with the part label, part name, quantity required for one full assembly, and the material of each part.

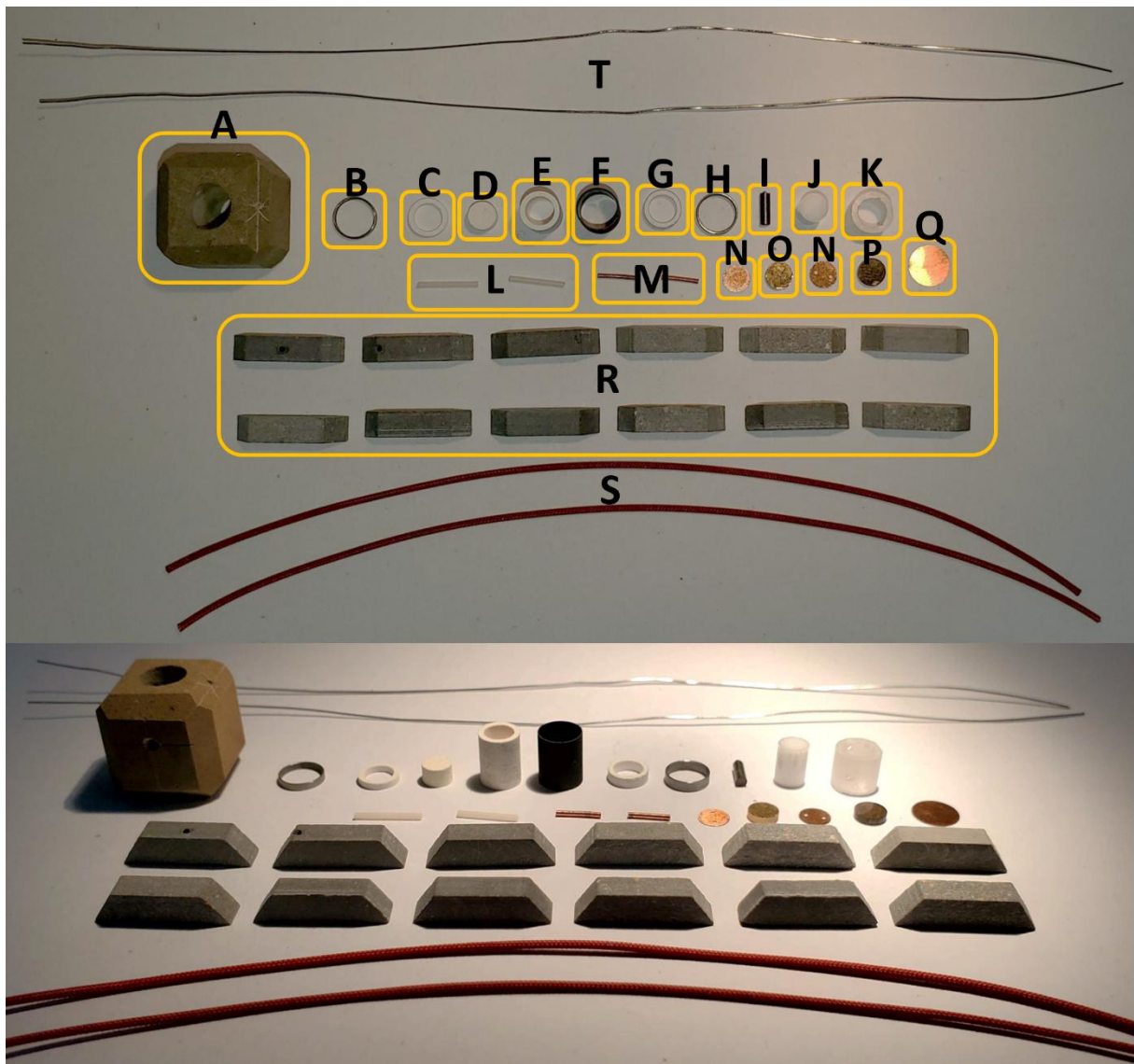


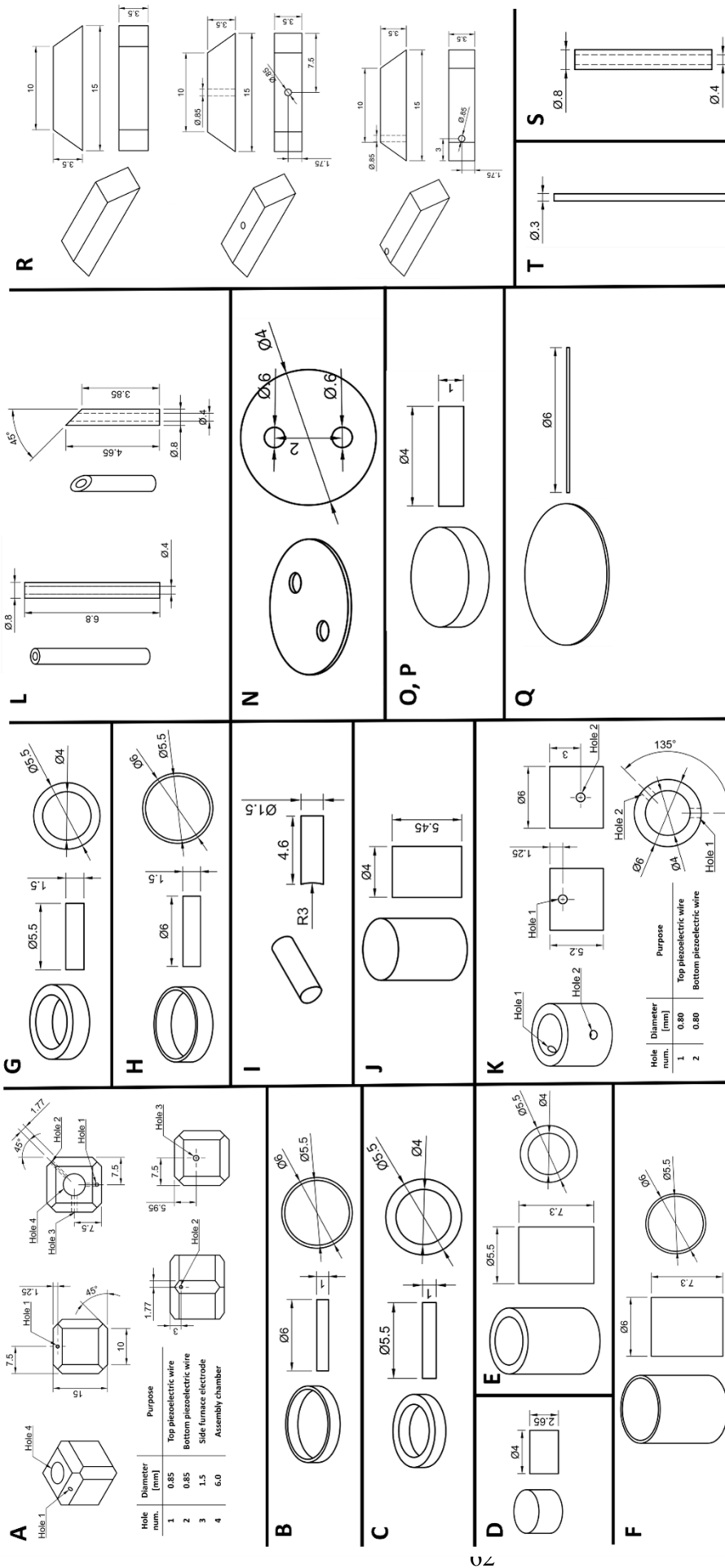
**Figure 26.** Images taken of the assembly parts laid out. The top picture shows a top view with the parts labeled. The bottom picture shows a side view. The anvils and alignment cage are omitted from the image and described elsewhere.

## 2. Methods

**Table 3.** *The bill of materials (BOM) for the 15/10 assembly. The anvils and alignment cage are omitted.*

Part label	Part name	Quantity	Material
A	Truncated cube	1	Cr-doped magnesia
B	Bottom electrode	1	Molybdenum
C	Bottom insulating ring	1	Magnesia
D	Bottom plug	1	Porous zirconia
E	Furnace sleeve	1	Magnesia
F	Furnace	1	Graphite
G	Top insulating ring	1	Magnesia
H	Top electrode	1	Molybdenum
I	Side electrode	1	Molybdenum
J	Top plug	1	Non-porous zirconia
K	Piezoelectric stack sleeve	1	Single-crystal magnesia
L	Insulating rods	2	Alumina ceramic
M	Protective coils	2	Copper
N	Piezoelectric electrodes	2	Copper
O	Piezoelectric crystal	1	Quartz/CTGS
P	Heat sink disk	1	Diamond
Q	Protective foil	1	Copper
R	Gaskets	12	Pyrophyllite
S	Wire insulation	2	PTFE
T	Piezoelectric wires	2	Platinum

## 2. Methods



## 2. Methods

**Figure 27.** *Assembly part dimensions and blueprints, organized by part label. See text and Table 3 for full description.*

The cubic assembly consists of a 15 mm cube, with edges cut to create 10 mm edge length faces suitable for the anvils (A). The assembly utilizes Chromium-doped magnesium oxide (MgO), or magnesia. Within the cube, a 6 mm hole is drilled directly through the center of the cube between opposing faces, wherein the assembly column is positioned. At the top, it contains a sintered diamond disk, 4 mm diameter and 1 mm in height (P). To safeguard the tungsten carbide anvil from the diamond disk potentially indenting it, a copper foil of 80  $\mu\text{m}$  thickness and 6 mm in diameter (Q) is placed on top of the diamond disk, between it and the anvil.

Below this, the top piezoelectric electrode is placed, a copper foil, 80  $\mu\text{m}$  thickness and 4 mm in diameter (N). Into this copper foil two holes, 0.6 mm in diameter, are laser cut, 2 mm apart. Through these holes a 0.3 mm platinum wire is weaved through and pressed flat (T), as seen in **Figure 28** (c). This wire conducts the piezoelectric charge from the top of the crystal out of the assembly to be measured. Below this, the piezoelectric crystal is placed, 4 mm in diameter and 1 mm thick (O). The piezoelectric crystal is X-cut. To ensure full surface conduction from the crystal into the copper foil and platinum wire, the crystal is sputter gold-coated using a Cressington Sputter Coater 108-Auto.

Before sputtering, cyanoacrylate glue is applied to the outside edges of the piezoelectric crystal as shown in **Figure 28** (a). To properly measure the charges across the disk surfaces, they must be kept electrically isolated, and the glue ensures that no gold is sputtered onto the edges, thus keeping the two opposing faces electrically isolated. Once the glue is applied, the gold is sputtered to each side of the crystal, three times per side for 120 seconds per application. A total of 360 seconds of gold sputtering is applied per side to ensure that the gold layer is thick enough for high electrical conductivity. According to the manufacturer's specifications, this results in a total gold sputtering thickness of 120 nm. After sputtering, the cyanoacrylate glue is carefully removed with a razor blade. It's critical that no glue residue is left on the edges as it acts as an electrical conductor at high pressures, so the crystal edges are briefly sanded using 600 grit SiC sandpaper to remove all glue residue, with the final gold coated crystal shown in **Figure 28** (b).

Below the piezoelectric crystal, another identical copper foil (N) is placed, with the same two holes laser cut and the platinum wire (T) weaved through them and pressed flat. This acts as the second, bottom face piezoelectric electrode.

## 2. Methods

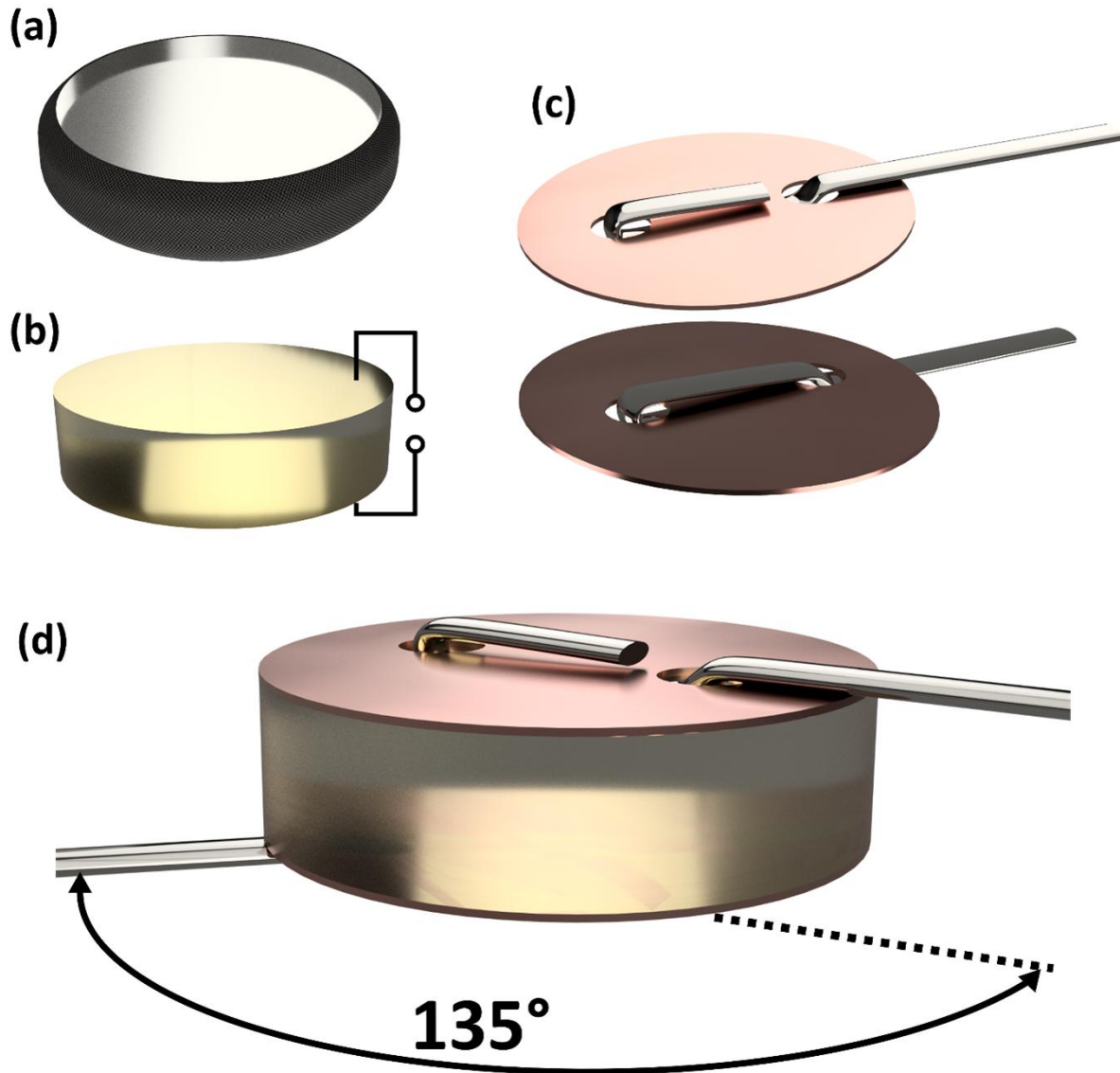


**Figure 28.** The piezoelectric stack construction is shown. (a) shows the crystal before gold coating, with just the glue applied on the outer edges. (b) is after gold coating and removal of the glue. The circuit diagram shows that the opposing faces are not electrically connected. (c) is how the platinum wire is weaved through the copper disks, the top and bottom respectively. Finally, (d) is the full piezoelectric stack, with the top and bottom copper foils with the platinum wire weaved through. To line up with the holes in the magnesia sleeve (K), the wires are aligned  $135^\circ$  apart.

Finally, the whole piezoelectric stack, the final construction shown in **Figure 28** (d), with the diamond disk is placed in a single-crystal MgO, or magnesia sleeve (K), with appropriate holes, 0.85 mm diameter, drilled through with a diamond drill bit for the platinum wires (N). The

## 2. Methods

piezoelectric stack is supported by a nonporous yttria-stabilized zirconia plug (J). This zirconia is nonporous so it acts as a strong deformation piston on the sample. The stronger the other parts within the deformation column, the more the strain applied to the assembly will be accommodated by the sample. Zirconia was chosen over alumina due to the lower thermal conductivity of zirconia as opposed to alumina. Zirconia's thermal conductivity varies with the porosity and temperature, but literature suggests a range of 2—3  $\text{Wm}^{-1}\text{K}^{-1}$  (Klemens, 1996; Schlichting et al., 2001). Compared to this, alumina's thermal conductivity varies from 10—30  $\text{Wm}^{-1}\text{K}^{-1}$  (Bansal & Zhu, 2005; Sciamanna et al., 2015).

Below this zirconia plug is the sample chamber, 4 mm in diameter and 4 mm in height, that holds the sample to be deformed. Below the sample is another zirconia plug (D), but this one is porous. This is to ensure that there is some porosity in the deformation column to accommodate the initial required shrinkage during compression up to the target pressure. For sample heating, a graphite furnace (F) is placed on the outside of a magnesia sleeve (E) that contains the sample chamber. The graphite furnace is electrically connected to the side anvil at 90 degrees to the deformation column with a molybdenum ring (H) that is placed around another magnesia electrical insulation ring (G). Through the 1.5 mm hole drilled through the side of the magnesia cube (A), a molybdenum rod (I) is inserted that contacts this top molybdenum ring (H). The Mo rod acts as the top furnace electrode, allowing the side anvil to provide the electrical charge to heat up the sample. Thus, the assembly uses an unconventional heating geometry where the bottom anvil and the side anvil, forming a 90° angle, are used as the charge conductors for heating.

Two holes are drilled into the magnesia cube (A) for the platinum wires (T) that connect to the piezoelectric crystal (O). The hole placements and geometry are shown in **Figure 27**. To accommodate these two wires, the gaskets that attach to those edges have matching holes drilled into them (R). These are shown in the figure as the two gaskets with holes. The rest of the gaskets (R), which with the two drilled gaskets form a total of 12 pyrophyllite gaskets, are whole and undrilled. Finally, the two alumina rods (L) are inserted around the platinum wires (T) and into the magnesia cube (A), from the cube surface to the single-crystal magnesia sleeve (K) around the piezoelectric stack. These are placed to provide some tougher protection for the wires. Without these, the failure rate due to the platinum wires (T) pinching and breaking was unacceptably high.

As protection for the platinum wires (T) in the pyrophyllite gaskets as the gaskets extrude (R), copper coils (M) are inserted around the wires through the pyrophyllite gaskets. As the gaskets

## 2. Methods

extrude, these copper coils slide and extend along the platinum wire, in a sense ‘lubricating’ the wire at high pressure so they don’t get pulled and cut by the flowing pyrophyllite at high pressure.

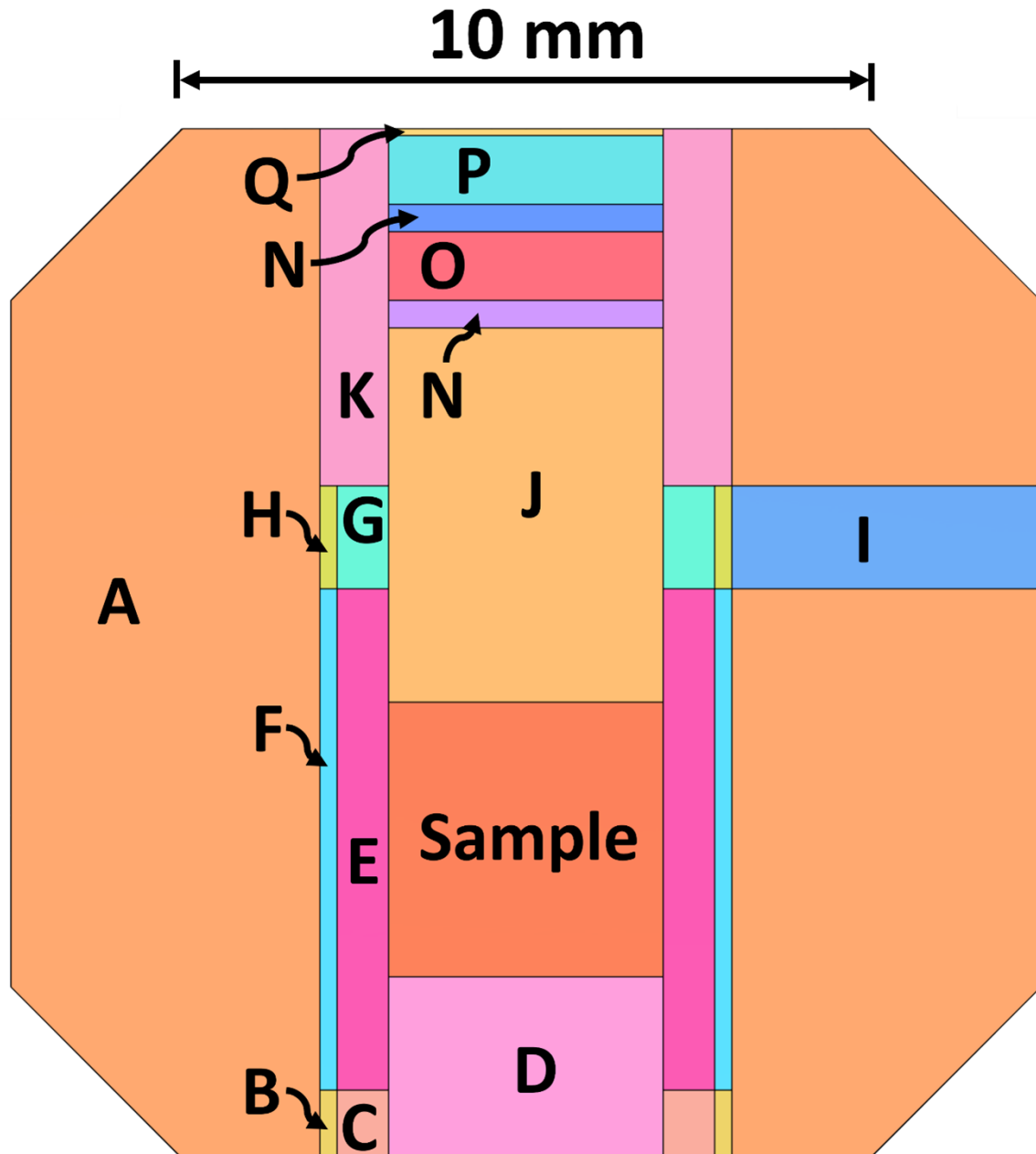


**Figure 29.** A cross-section of a completed assembly, showing the orientation of the parts and general geometry.

### 2.2.2. Electrical conductivity design considerations

Due to the high sensitivity of these techniques to electrical resistance, the assembly was designed to:

## 2. Methods

- (1) minimize electrical conductivity around the crystal through the surrounding material, and
- (2) keep the piezoelectric crystal below 200 °C during deformation experiments, even if the sample is heated to high temperatures.

These two requirements constrained and largely guided the design of the assembly.

For consideration (1), both the materials surrounding the piezoelectric crystal and the assembly process itself were iterated and refined over time. To ensure near-anhydrous run conditions, parts A, C, D, E, G, J, and K were fired at 1000 °C for at least 1 hour before final assembly, a common practice in large volume press experiments (Keshav et al., 2005; Leinenweber et al., 2012). If the assembly could not be completed and run within a few hours after firing, the parts were stored in a 120 °C drying oven to prevent moisture absorption. Firing effectively removed both water and oils potentially transferred from handling. In this study, experiments with unfired parts encountered issues with low resistivity, particularly under high pressures, resulting in significant voltage drift.

To minimize contamination, all fired parts were handled with latex or nitrile gloves, as oils from hands can introduce organic materials that act as charge carriers. These materials shift resistivity from bulk conduction through the ceramic to surface conduction along grain boundaries, with organic ions acting as charge carriers (Freund et al., 1993; Korobeynikov et al., 2005; Malki et al., 2014). Magnesia (MgO), in particular, is prone to surface conduction along grain boundaries. As temperature rises, bulk charge carriers form within the magnesia crystals, typically as electron holes or cation vacancies, and gradually diffuse to the surface. Once at the surface, these carriers move more rapidly along grain boundaries than through the bulk (Freund et al., 1991, 1993; Kang, 1994).

Two methods are essential to limit this electrical conduction mechanism: preventing the introduction of charge carriers like water or organic material and reducing the number of grain boundaries. This was the primary reason for using a single-crystal magnesia sleeve (K) around the piezoelectric crystal. Although the sleeve inevitably cracked under compression, breaking into smaller pieces, it still significantly reduced the number of grains and grain boundaries. The switch from polycrystalline to single-crystal magnesia dramatically improved experimental success rates and minimized voltage drift, especially at higher temperatures.

Additionally, because the platinum wires carrying the piezoelectric charge must pass through pyrophyllite gaskets, which form a contact point between the anvils, electrical conduction through the pyrophyllite becomes a concern. Pyrophyllite, a hydrated aluminous phyllosilicate

## 2. Methods

mineral with the chemical formula  $\text{Al}_2\text{Si}_4\text{O}_{10}(\text{OH})_2$ , has a high electrical resistivity of approximately  $10^{11} \Omega\cdot\text{m}$  at room temperature and 1 bar (Hicks & Secco, 1997). However, at elevated temperatures, pyrophyllite undergoes a dehydroxylation reaction that releases  $\text{H}_2\text{O}$ , which not only alters the  $\text{H}_2\text{O}$  fugacity but also introduces charge carriers, significantly reducing its resistivity (Hicks & Secco, 1997; H. Wang et al., 2011). This reduction forms a conductive path that lowers the resistance across the piezoelectric crystal, allowing current to pass from one platinum wire to the anvil, through the extruded pyrophyllite gasket, and along the second platinum wire.

Early experiments in this project revealed unexpectedly high conductivity as the sample was heated, a phenomenon consistent with previous findings. At pressures of 4–7 GPa, the resistance in the temperature range of 285–450 K remains similar to that at room temperature and 1 bar, but above approximately 500 K, the resistance drops sharply (Hicks & Secco, 1997). Given the high power required to heat such a large assembly, the pyrophyllite gaskets can exceed 500 K during experiments, which likely triggers a shift in conduction mechanism—from electronic to ionic—driven by dehydration and the release of charge carriers within the pyrophyllite (Fang et al., 2007; Hicks & Secco, 1997; Ter Heege & Renner, 2007).

To mitigate this, the pyrophyllite gaskets are pre-fired at temperatures above 950 K to induce partial dehydration and remove excess  $\text{H}_2\text{O}$ , ensuring that less water is released under high-pressure, high-temperature conditions (Leinenweber et al., 2012; Sano-Furukawa et al., 2014; Wang et al., 2003). Firing above 1300 K causes further decomposition of pyrophyllite into mullite and silica phases, which is undesirable (Hulse & Graf, 1965). Therefore, to reduce electrical conductivity during experiments, the gaskets are fired at 1073 K for 3 hours before use, and if assembly is delayed, they are stored in a 120 °C drying oven. After implementing these procedures, the sudden drop in electrical resistance at higher temperatures was no longer observed.

Additionally, to further reduce the risk of electrical conduction, particularly in the presence of high humidity or surface contamination, polyimide tape (commonly known by the trademark Kapton® from DuPont) is applied to the exposed surfaces of the anvils. As the pyrophyllite gaskets extrude outward, this tape provides a high-resistivity barrier that limits conduction, especially if moisture in the air ‘wets’ the extruded gaskets. The tape is applied to the anvils 3.5 mm below the un-extruded gasket location, as shown in **Figure 30**.

## 2. Methods



**Figure 30.** Anvil wrapped in polyimide film tape, illustrating two different views. The square truncated edge length, clearly visible on the left anvil, is 10 mm in length.

### 2.2.3. Thermally activated electrical conduction design considerations

Since both the piezoelectric crystal (O) and the surrounding material (K) are dielectrics, the electrical resistivity drops exponentially with increasing temperature. Additionally, as the temperature increases, changes in temperature have a larger effect on the voltage drift of the measurements. The requirement that temperature be kept to a minimum at the piezoelectric crystal is what led to the current design of the assembly, shown in **Figure 29**.

The assembly was specifically designed to keep the piezoelectric crystal at the lowest possible temperature while heating the sample during an experimental deformation. This was achieved through a furnace (F) that is offset in the assembly, to the lower part away from the piezoelectric crystal, resulting in an asymmetric assembly in the vertical direction. This is also why zirconia was chosen as the plug (J) placed below the piezoelectric crystal rather than other high strength ceramics such as alumina. As mentioned previously, zirconia has a lower thermal conductivity and thus less heat is conducted into the piezoelectric crystal.

Additionally, the top electrode (N) placed on the piezoelectric crystal (O) must be kept electrically isolated from the top anvil, but it also must conduct heat well into the anvil. The ideal material for this is diamond, which is why a sintered diamond disk (P) is placed above the electrode and, along with a thin copper foil, is in contact with the much lower temperature tungsten carbide anvil. In this way, less heat is conducted into the piezoelectric crystal because of the zirconia plug and the heat that is conducted is quickly pulled away through the diamond

## 2. Methods

disk and into the anvil. To categorize the effectiveness of this geometry, a power/temperature calibration run was performed with two thermocouples placed in different positions within the assembly.

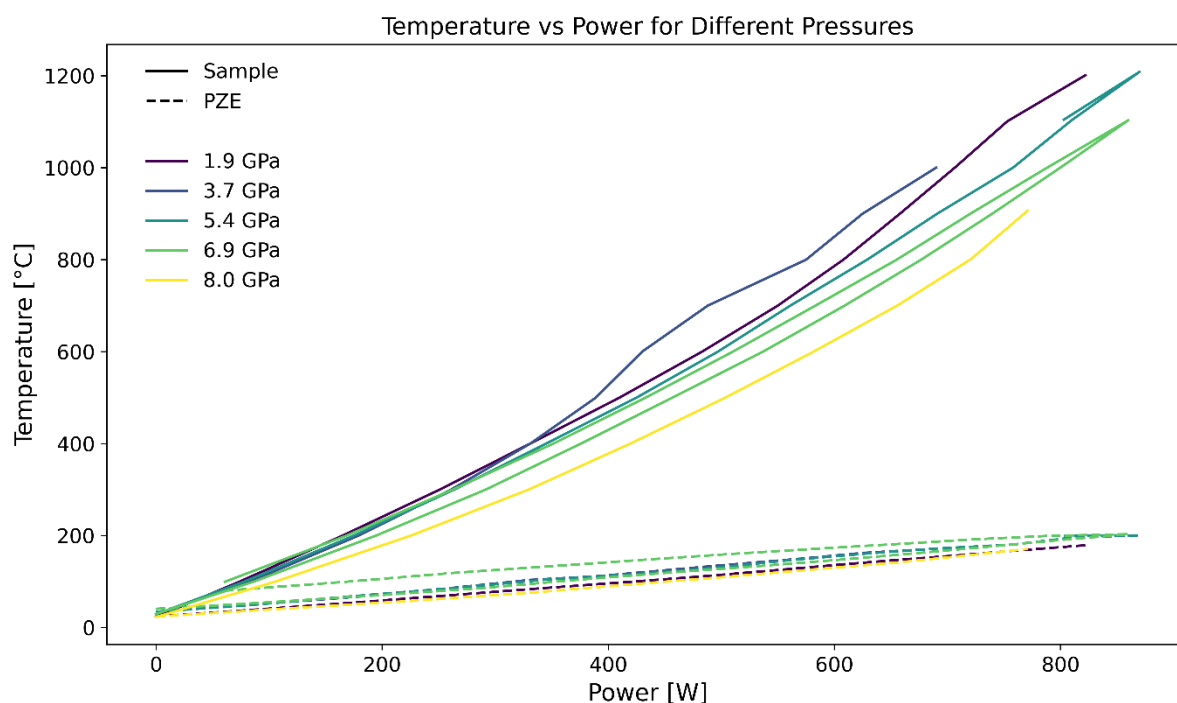


**Figure 31.** The temperature of the sample area and the piezoelectric crystal area (PZE) is plotted versus the power in watts through the furnace. The sample is shown with solid lines and the PZE crystal with dashed lines. Multiple pressures are shown.

The first thermocouple was placed in the piezoelectric crystal area. For this run, the assembly was made with precisely the same geometry, but the piezoelectric crystal was removed and instead a type S thermocouple was placed, welded together right in the middle of where the central point of the piezoelectric crystal would be. A magnesia disk was placed instead of the piezoelectric crystal with a hole drilled through it for the thermocouple wires. In the same assembly, the sample was replaced with another plug of magnesia, and a central well was drilled, and a second type S thermocouple inserted, entering from the bottom of the assembly, and welded together in the central area of the sample region. A four-hole alumina rod was used to guide the wires into the assembly.

Then, the sample was heated to 25—1200 °C at five different pressures, starting from 1 GPa to 5 GPa, in increments of 1 GPa. The temperature at the piezoelectric crystal (PZE) and the sample region was measured for each heating cycle. As can be seen in **Figure 31**, the

## 2. Methods

temperature at the piezoelectric crystal region is between 4 to 6 times lower than the sample region and never goes above 200 °C. The offset furnace as well as the zirconia plug and diamond disk thus ensures the piezoelectric crystal does not get hot enough for thermally activated electrical conduction to be unmanageable. Changes in temperature are still certainly an issue and a source of error since the charge integrating device is highly sensitive to resistance changes. However, since the piezoelectric crystal does not, under normal experimental conditions, go above 200 °C, the voltage drift resulting from temperature changes is low.

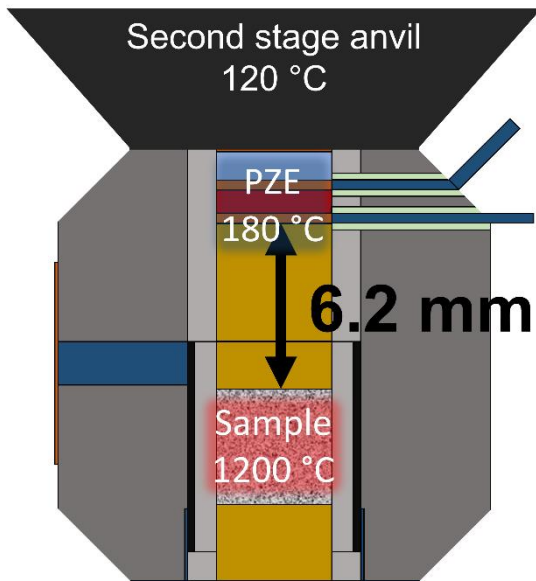


**Figure 32.** Schematic diagram of the assembly showing the temperature distribution and temperature gradient within the assembly. PZE is the piezoelectric crystal (red in this diagram), and sample is the heating temperature at the sample area.

### 2.2.4. Effects of change in electric resistivity

The design of the integrating capacitor in our voltage measurement device comes with a critical limitation: any pre-existing charge on the capacitor can dissipate if the resistance across it decreases. Indeed, due to the operational characteristics of the IVC102 switched integrator transimpedance amplifier, any resistance lower than infinite will gradually discharge the capacitor, even when the integrated charge is ostensibly zero.

To quantify this effect, a Hochpräzisions-Widerstands-Dekade Typ 1424, which is utilized for precision resistance calibrations, was employed to measure the voltage drift across the capacitor at various resistance levels, ranging from 0.1  $\Omega$  to 100 k $\Omega$ . This device boasts a minimal error margin of 0.1% as claimed by the manufacturer. Furthermore, additional ceramic capacitors

## 2. Methods

were integrated to broaden the resistance scope up to  $170 \text{ M}\Omega$ , albeit with a slightly higher claimed error rate of 1%.

The resulting voltage drift on the integrator device is plotted in **Figure 33**. For each specified resistance value, the voltage was recorded for approximately one minute. The plot reveals that the maximum drift peaks at  $-35 \text{ volts/second}$  near zero ohms, subsequently diminishing as resistance rises. For instance, at the highest resistance the device can muster, i.e.  $111,111 \Omega$ , the drift measures  $-0.77 \text{ volts/second}$ .

Under experimental conditions akin to those described in Eq. 97 and Eq. 98 this level of drift would impose an error of  $-152 \text{ MPa per second}$  on the calculated stress. Such a significant drift would render the device incapable of accurately measuring stress during deformation experiments. To mitigate this, the device features a front-mounted dial, denoted as 'C' in **Figure 37**. This dial allows for the introduction of an artificial voltage drift, in either direction, to counterbalance the observed drift. By carefully adjusting the dial while monitoring the measurement software, one can effectively neutralize the drift resulting from resistance. The dial's range extends to a maximum of  $1.836 \text{ V/s}$  in the positive direction and  $-2.186 \text{ V/s}$  in the negative.

Any residual drift, due to imprecisions in the dial's setting, can be accounted for by subtracting the baseline voltage drift recorded before deformation begins. By fitting a linear line to this baseline drift and deducting it from the voltage readings, one could, in theory, nullify any measurement errors attributable to electrical resistance.

## 2. Methods

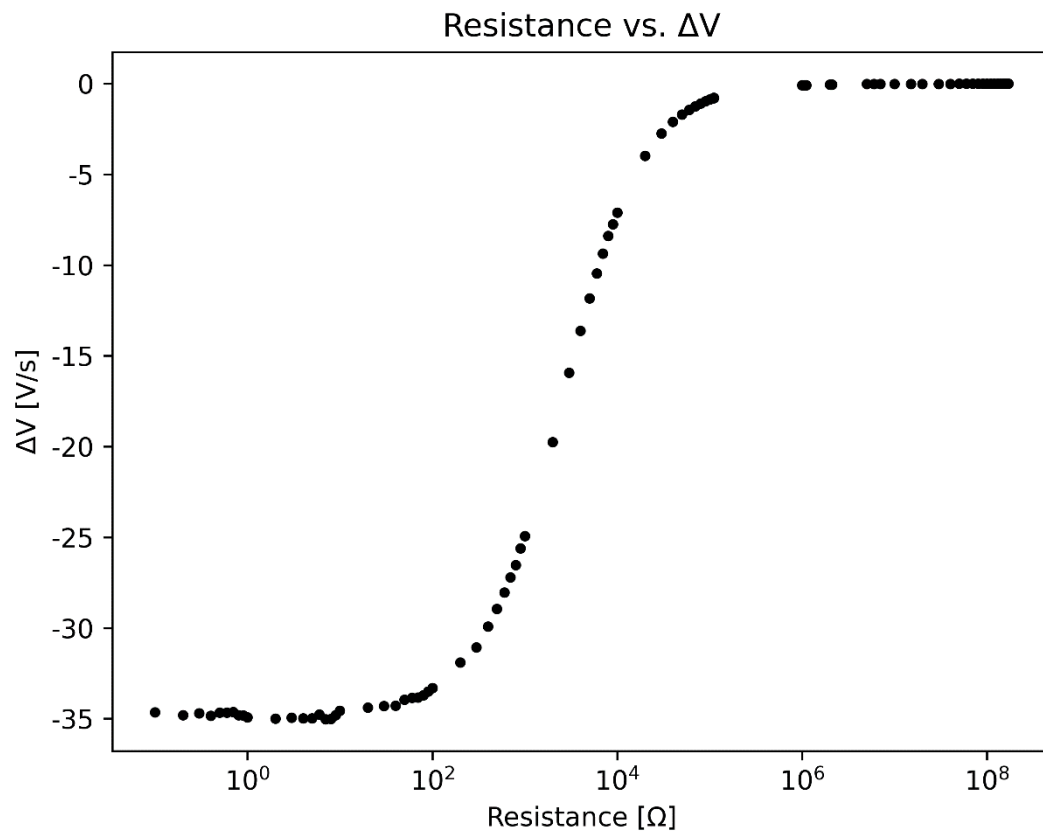


**Figure 33.** Voltage drift across the capacitor at multiple resistance values. The vertical axis units are volts/second of drift. The horizontal axis is plotted in logarithmic scale and is the resistance in ohms.

In the initial stages of experimentation, it was observed that, despite utilizing the front-mounted dial to counteract initial voltage drift, the voltage readings during deformation exhibited excessively rapid changes. These variations were so swift that they suggested two possibilities: either the stress measured was reaching implausibly high levels in the order of hundreds of gigapascals, or the voltage drift was fluctuating within the duration of the experiment. The latter was considered the more probable scenario, given the inherent sensitivity of voltage drift to resistance changes. Even minor fluctuations in resistance can result in a significant alteration of the voltage drift.

The relationship between voltage drift and resistance was analyzed. Data from these observations, as seen in **Figure 33**, were employed to derive Eq. 90, an empirical formula capturing the essence of this relationship:

## 2. Methods

$$\Delta V = -a \cdot e^{-b/R} + d \cdot \tan^{-1}(e - R) + c \quad \text{Eq. 90}$$

fitting parameters =  $a, b, c, d, e$

Here,  $\Delta V$  represents the voltage drift in volts per second,  $R$  the resistance in ohms, and  $a, b, c, d, e$  are fitting parameters. Through fitting of these constants, the equation achieved an exceptional goodness of fit, with  $R^2 = 0.999967$ . For the fitting process, the inherently negative voltage drift was multiplied by -1 to facilitate a more straightforward fitting procedure.

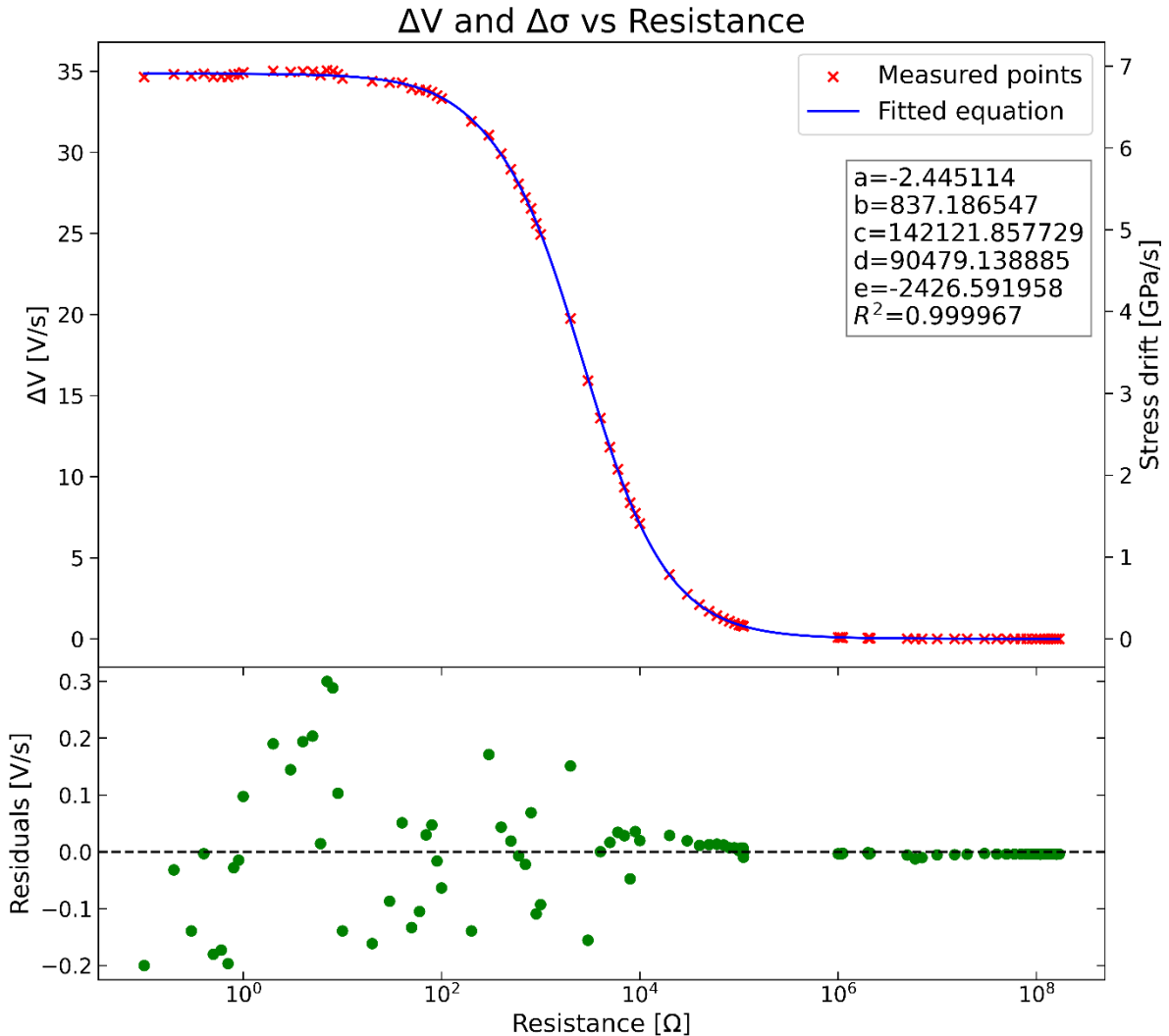


**Figure 34.** The voltage drift vs. resistance across the charge integrating device is plotted, similar to **Figure 33**, but the data is now fitted with Eq. 90. The value of the fitting parameters is shown below the legend. The residuals of the fitting are shown in the bottom plot.

This precise fit allows the equation to serve as a predictive tool for estimating voltage drift as a function of resistance. For example, if the resistance encountered by the piezoelectric crystal during an experiment is 50 M $\Omega$ , application of Eq. 90 yields a voltage drift of  $1.167 \times 10^{-2}$  volts/second. Unaccounted for, this drift introduces an error in the measured stress of 2.313

## 2. Methods

MPa per second according to Eq. 95 and Eq. 96. If resistance drops by  $0.2 \text{ M}\Omega$  to  $49.8 \text{ M}\Omega$  during the experiment, this results in a new drift error of  $2.314 \text{ MPa per second}$ . This seemingly negligible change, if not detected, manifests as an apparent stress change on the crystal, undetectable through voltage measurements alone. The induced error accumulates at a rate of  $1.406 \times 10^{-3} \text{ MPa per second}$ , calculated by the difference in the drift rates. Over an hour, the cumulative error in stress would amount to  $5.063 \text{ MPa}$ , the product of the drift error rate and the number of seconds in an hour, i.e.,  $1.406 \times 10^{-3} \text{ MPa/second} \times 3,600 \text{ seconds}$ .

Given that both  $\alpha$ -quartz and CTGS crystals are dielectric in nature and their resistance is inversely proportional to temperature as explained by the Arrhenius equation, maintaining a constant temperature during experiments is paramount. This is due to the charge integrator's high resistance sensitivity, which can significantly impact the voltage drift. Although temperature can be largely controlled, some experiments have demonstrated a discernible shift in voltage drift during the deformation phase, evidenced by a change in the drift slope compared to the pre- and post-deformation periods. Without the ability to precisely determine the resistance change over time, a simplified model is applied to experiments that exhibit notable voltage drift shifts. Resistance across the crystal can be measured during the deformation, but not simultaneously with charge integration.

If the charge accumulation in the integrating capacitor is stopped for resistance measurements to be made, any stress accumulated during that time would essentially be lost information. The time spent measuring the resistance would be time in which the stress state is not recorded and since the piezoelectric method only records changes in stress and not the absolute stress, interpolating the stress in this gap of time would be problematic. For all experimental runs, a specialized fitting routine has been developed to adjust for any shift in voltage drift that occurs due to resistance changes during deformation.

In the absence of exact information regarding the timing of the voltage shift, a simplified quadratic equation is utilized, defining a smooth curve to bridge the slope change. This approach is demonstrated in **Figure 35** with data from a deformation experiment. Plot (a) in **Figure 35** presents the raw voltage measurements from the charge integrator. The onset and completion of deformation are indicated by dashed green and red vertical lines, respectively. After adjusting the dial to minimize voltage drift, a span of background drift is recorded for at least one minute before and after deformation. These segments of drift are then linearly fitted, as depicted in plot (b) of **Figure 35** with the red and green lines, showcasing drift rates of  $1.887 \times 10^{-3} \text{ volts per minute}$  before deformation and  $-1.882 \times 10^{-2} \text{ volts per minute}$  post-

## 2. Methods

deformation. The negative shift in slope post-deformation suggests a slight decrease in resistance across the crystal.

To correct this drift, a piecewise quadratic function is formulated, enabling a seamless transition of the slope between the commencement and conclusion of deformation. The time and voltage at the deformation's initiation are denoted as  $x_1$  and  $y_1$  while  $m_1$  is the slope determined from the pre-deformation voltage drift. Conversely, the end time of deformation is represented by  $x_2$  and  $m_2$  is the slope from the linear fit to the post-deformation voltage drift.

$$y = ax^2 + bx + c \quad \text{Eq. 91}$$

$$a = \frac{m_2 - m_1}{2(x_2 - x_1)} \quad \text{Eq. 92}$$

$$b = m_1 - 2ax_1 \quad \text{Eq. 93}$$

$$c = y_1 - ax_1^2 - bx_1 \quad \text{Eq. 94}$$

## 2. Methods

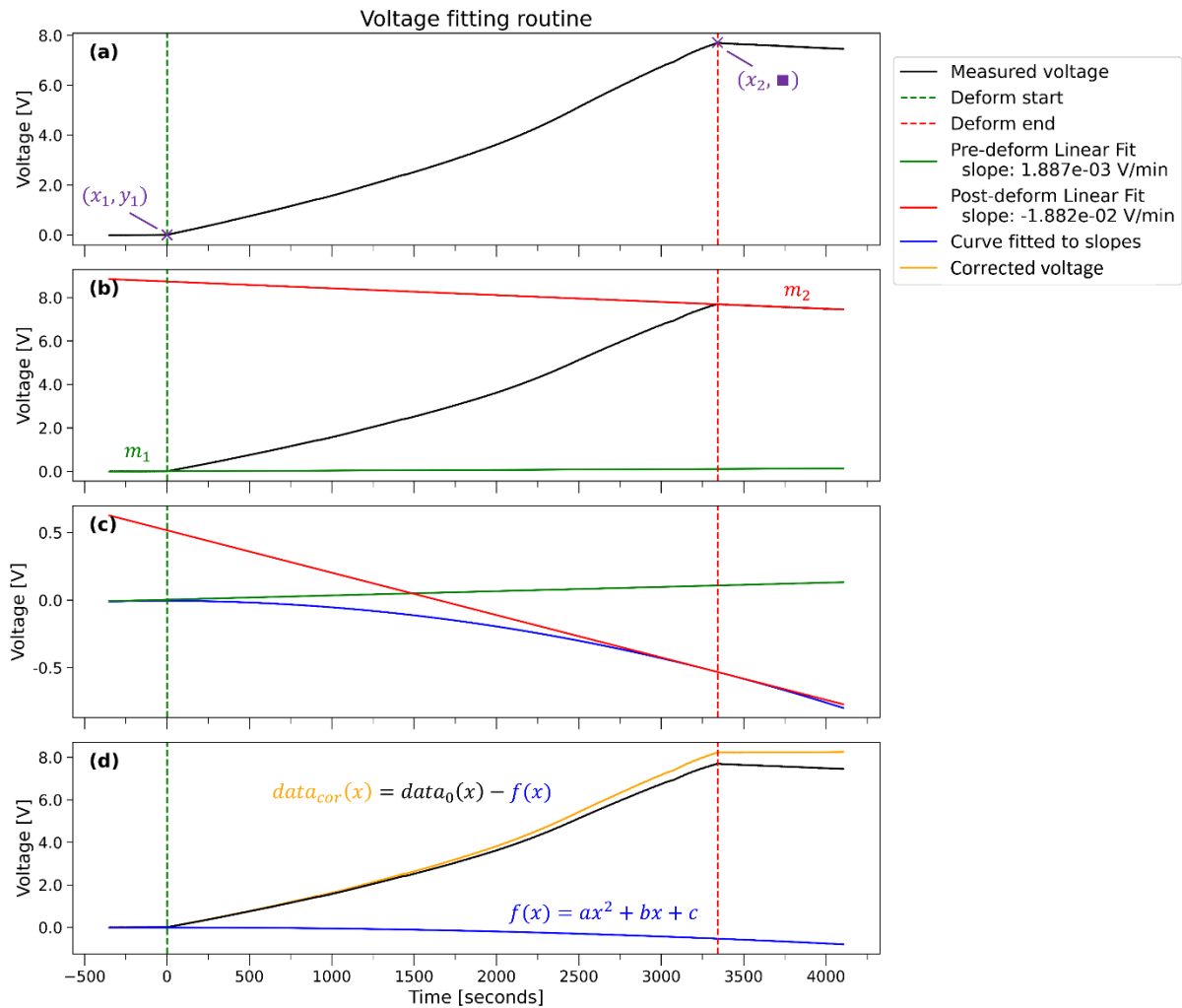


**Figure 35.** An example of data acquired from an experiment, showing the voltage on the vertical axis and time on the horizontal. The progression of fitting from (a) to (d) is described in the text.

Eq. 91 represents the quadratic function employed to adjust for changes in voltage drift during the deformation process. To determine the coefficients of this quadratic function, the points and slopes delineated by the onset and conclusion of the deformation are utilized, following the formulas of Eq. 92, Eq. 93, Eq. 94. The coefficients computed as per the equations listed configure the quadratic curve, which is visualized as a blue curve in plot (c) in **Figure 35**. This curve is designed to align with the solid green and red lines that represent the pre-deformation and post-deformation voltage drift slopes, respectively. The interpolation achieved by the quadratic function is smooth, bridging the gap between the two linear segments effectively.

Once this quadratic correction is applied to each voltage data point, subtracting it yields an adjusted dataset. The resulting corrected voltage data exhibit zero drift in both the pre-

## 2. Methods

deformation and post-deformation phases, depicted as the orange line in plot (d) in **Figure 35**. Given that direct measurement of resistance across the crystal during deformation is not feasible as mentioned previously, the approach of smooth interpolation via the quadratic function acts as a pragmatic approximation.

The correction routine is systematically applied to all experimental readings prior to calculating the deviatoric stress, particularly when a significant variance is observed between the pre- and post-deformation voltage drift slopes. Considering the inability to directly measure the resistance across the crystal concurrently with charge integration, the method of employing a quadratic function for drift correction is acknowledged as a provisional yet pragmatic approach. This technique provides a means to approximate and mitigate the impact of voltage drift on stress calculations, but it is not without its limitations. The quadratic interpolation acts as a best-fit correction for the observed drifts; however, it operates under the assumption that the change in drift is the primary function of resistance alterations, which may not encapsulate all the variables affecting the system. Moreover, the inability to measure resistance in real-time alongside charge integration introduces an element of uncertainty.

Although the fitting process is carefully designed to adjust for drift between known points, the actual resistance path during deformation may involve complexities that the quadratic function cannot fully capture. To enhance the accuracy of this method, future refinements would necessitate a technique that allows for the simultaneous measurement of resistance and charge integration. This concurrent measurement would provide a direct correlation between resistance changes and voltage drift, thereby reducing reliance on post-experimental corrections. Such advancements would significantly improve the precision of stress measurements, ultimately leading to a more accurate interpretation of the crystal's response to deformation. Until such a method is developed, the current approach remains a necessary compromise, enabling the continuation of experiments and providing a foundation for future methodological improvements. Most deformation experiments do not display a significant drift and this technique provides an adequate compromise. If the drift becomes too large, detectable with unreasonably high voltage changes, the deformation is abandoned. Because, with CTGS as the piezoelectric crystal with a diameter of 4 mm, 1 V represents 198 MPa, a reasonable estimate for the stress can be made during the experiment and anomalies in the measurement detected.

### 2.2.5. Deformation geometry

The 6-axis MAVO press has the distinctive capability of allowing individual manipulation of each anvil. Under high-pressure conditions, the anvils can be programmed to move inwards or

## 2. Methods

outwards at a predetermined rate. However, due to the specific role of anvil 1 (the bottom anvil) in managing the sample's hydrostatic pressure, it is not allocated for motion-induced deformation, as its primary function is to maintain the user-determined oil pressure. This static positioning of anvil 1 subsequently requires anvil 2 to remain in a motionless relative position, as it serves as its counterforce.

As a practical workaround to impart deformation at high pressure, anvils 3 and 4 are instructed to move inward at a specified rate, while anvils 5 and 6 are tasked to retreat outwards at an equally defined rate. Theoretically, stress is postulated to be uniaxial and radially symmetric, maintaining a constant volume space, but in practical applications, this is not the case. While volume conservation is observed, the resulting stress deviates from radial symmetry. Within the six-dimensional press structure, anvils 3 and 4 are responsible for applying the  $\sigma_1$  stress, anvils 5 and 6 operate in the  $\sigma_3$  direction through their outward retreat, and anvils 1 and 2 align with the  $\sigma_2$  direction. Consequently, the stress imparted on the sample during deformation exhibits a triaxial nature.

## 2. Methods

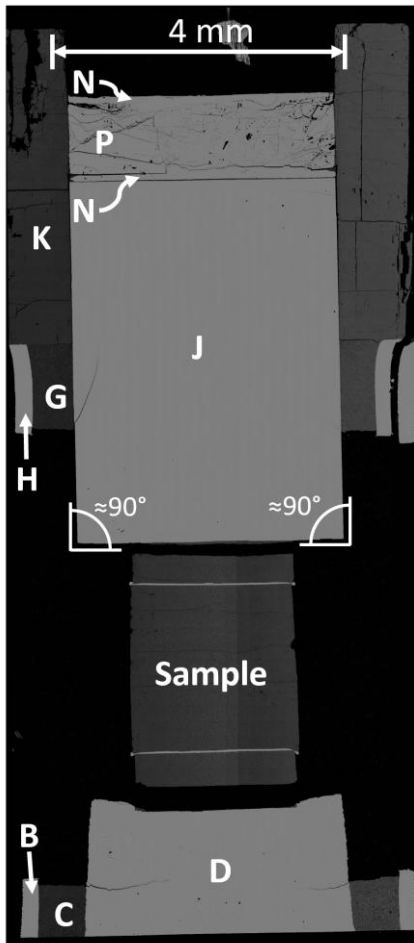


**Figure 36.** Scanning electron microscope image in secondary electron mode of an assembly that was deformed at high pressure and temperature, with parts labeled according to **Table 3**. *J* is the dense zirconia and the edges have been labeled to show that the zirconia rod retains close to 90° angles at the corners. Contrast that with part *D* that is made of crushable, or high porosity, zirconia that shows an indentation into it from the sample, MgO in this case, due to deformation.

To promote a homogenous strain distribution on the sample as the anvils advance, rods made of zirconia, positioned above the sample, are chosen for their high shear strength. Notably, the low-porosity zirconia rod situated atop the sample ensures that the load on the sample is spread uniformly across its surface. This observation was confirmed through Scanning Electron Microscopy (SEM) imaging, which showed that a flat and uniform interface surface is maintained between the sample and zirconia. Notably, the low-porosity zirconia maintained a square corner of 90° angle, deviating by less than one degree, as evidenced by SEM imaging in Secondary Electron (SE) mode.

## 2. Methods

As long as the sample has a lower yield strength than the zirconia rods, the assumption is made that the strain imposed by the anvils during deformation is accommodated by the sample and not other parts within the assembly. This assumption is not necessary in synchrotron experiments, as the strain can be directly measured *in situ* using X-ray radiography during the experiment. This is of course not possible off the beamline.

### 2.2.6. Charge measurement process

In this experimental setup, known as the piezoelectric assembly, a piezoelectric crystal is positioned with electrodes on opposite sides. Platinum wires, insulated with polytetrafluoroethylene (PTFE) sleeves, connect the electrodes, preventing any electrical contact with the second-stage anvils and the outer alignment cube. These wires are threaded through drilled holes in the cube and gaskets, allowing for a clean exit from the assembly. Outside the alignment cube, the wires are soldered to an ultra-low capacitance shielded cable, selected for its optimal electrical properties. The Lapp Kabel UNITRONIC® BUS PB cable, with a maximum mutual capacitance of 30 nF/km and a conductor resistance of 186  $\Omega$ /km is used for this purpose. Its impedance rating of  $150 \pm 50 \Omega$ , makes it particularly well-suited for

## 2. Methods

the experiment. Choosing a cable with low capacitance and resistance is essential due to the small current generated by the crystal during deformation.

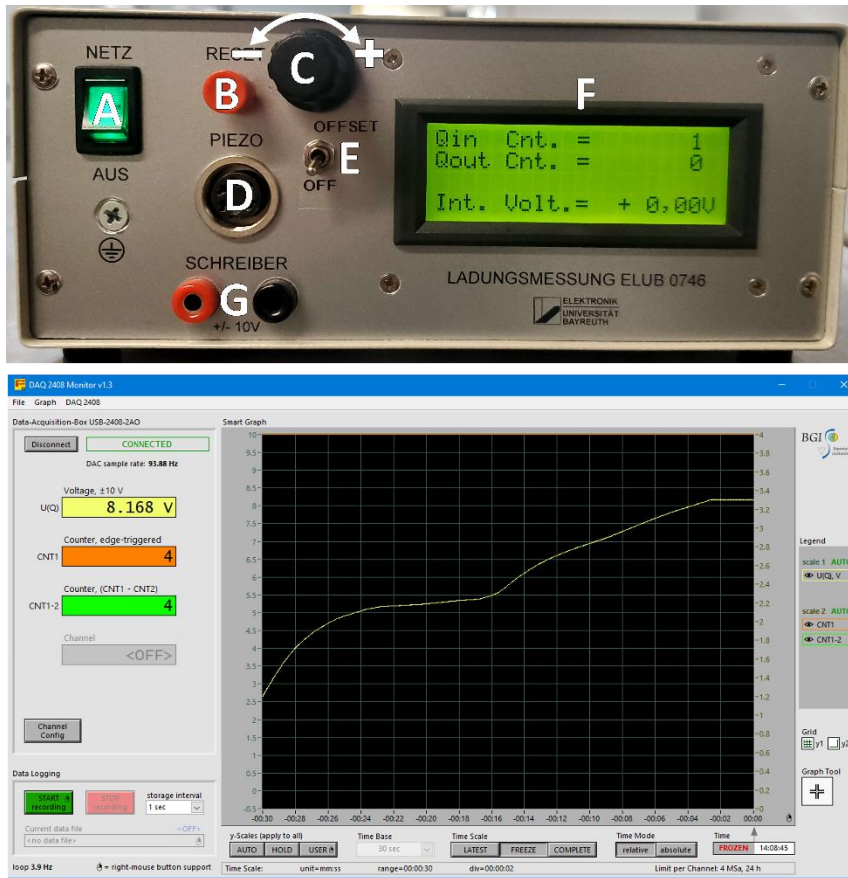


**Figure 37.** The charge integrating device and the software custom built for it. The top image is of the front of the device, with the key front components labeled. The bottom image is a screenshot of the custom software built for measuring the voltage during a deformation experiment. See the text for details on each component. The software was developed by Gerald Bauer (Bayerisches Geoinstitut, University of Bayreuth).

The cable is connected to a charge integrating device built specifically for these experiments. An image of the front of the charge integrating device, as well as a screenshot of the software custom-built for these measurements, is shown in **Figure 37**. In the top part of the figure, components on the front of the device are labeled with letters.

‘A’ is the on/off switch for the device, which powers the entire system. ‘B’ is a button that resets the current voltage as well as the overflow counts, both positive and negative, back to zero. This is essential for initializing the measurement process to avoid overflow above 10 V or below -10 V as the voltage is briefly non-linear during the switch. ‘C’ is the black dial that adds or subtracts a constant voltage drift to the measurement voltage in the integrating capacitor; this is crucial for calibration purposes, and the directions for inducing a positive or

## 2. Methods

negative voltage drift are indicated. ‘D’ is the 5-pin DIN connector port, which connects the cable to the piezoelectric crystal. This DIN connector includes an outer screw for grounding, reducing electrical interference and ensuring accurate measurements. ‘E’ is a switch that enables or disables the voltage drift set by the knob associated with ‘C’. This allows the user to apply or remove the voltage drift during different stages of the experiment. ‘F’ displays the current voltage, labeled as “Int. Volt.”, and keeps a count of the number of positive and negative overflow resets to the voltage, labeled “Qin Cnt.” and “Qout Cnt.”, respectively. This feature allows for monitoring and documenting the experiment's progress in the absence of a connection to a computer. Lastly, ‘G’ comprises two banana plugs that permit the direct measurement of the voltage. These are typically left unplugged during experimental runs to minimize noise and thus maintain the integrity of the data collected. Below the device is a screenshot of the custom software that records voltage measurements during an experiment. The voltage is represented by the yellow line on the plot. On the left side of the interface, the current voltage measurement, denoted as “U(Q)”, and the overflow counts are prominently displayed.

A simplified block diagram of the charge integrator circuit is depicted in **Figure 38**. This device integrates the charge generated by the crystal throughout the experiment by utilizing a capacitor,  $C_x$ . The charge accumulating on the crystal surface causes the capacitor to charge, and this capacitor possesses a capacitance of  $9.964 \times 10^{-9}$  F, with a precision of  $\pm 1\%$ . As the capacitor collects charge, the resulting voltage is measured in real-time. The variation in voltage is then transformed into a digital signal by a digital-to-analog converter (DAC), operating at a sampling rate of 93.88 Hz. This digital signal is transmitted to a computer via USB and logged for analysis. The integrator capacitor has a finite charge capacity; hence, when the voltage reaches the thresholds of +10 V or -10 V, the system activates switch  $S_2$  to discharge the capacitor in less than a microsecond. Concurrently, switch  $S_1$  is opened, temporarily halting charge accumulation. Once the capacitor is discharged to 0 V, switch  $S_2$  opens, and switch  $S_1$  closes, allowing the process of charge accumulation and integration to resume. Consequently, the voltage oscillates between -10 and +10 V.

## 2. Methods

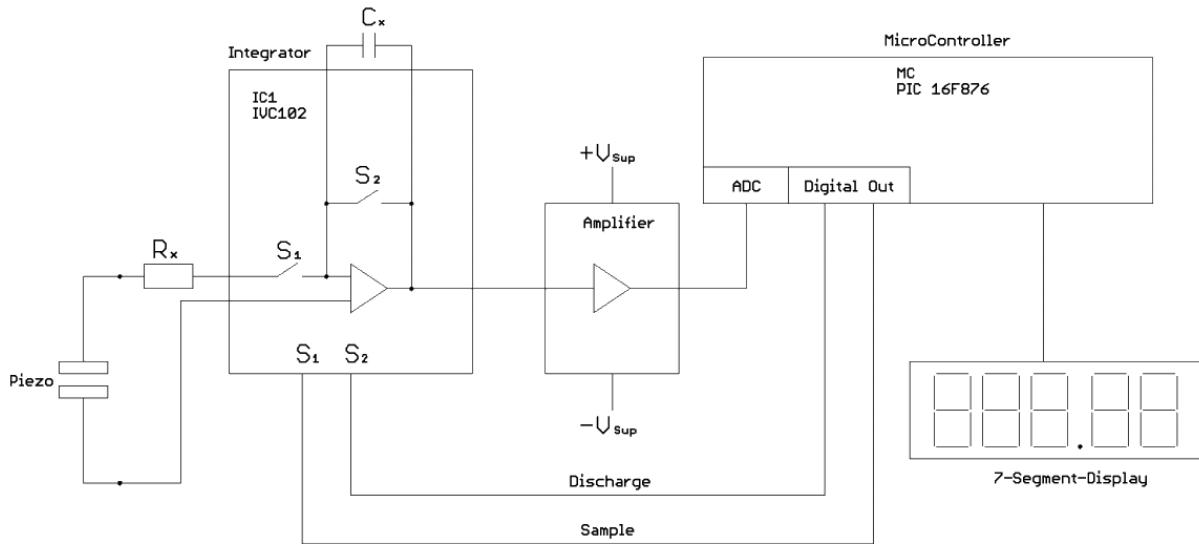


**Figure 38.** Block diagram schematic of the charge integrator. Piezo is the piezoelectric crystal,  $S_x$  are switches,  $C_x$  is the integrating capacitor. Block diagram provided by the electrical engineering team at University of Bayreuth.

This voltage is used to calculate the force exerted on the crystal, as described by Eq. 95:

$$F_N = \frac{\Delta V \cdot C_F}{d_{11}} \quad \text{Eq. 95}$$

In this equation,  $F_N$  is the force in Newtons,  $\Delta V$  the change in voltage,  $C_F$  the capacitance of the integrating capacitor ( $C_x$ ) in Farads, and  $d_{11}$  the piezoelectric strain coefficient specific to an X-cut crystal deformed along the X axis. Given that the diameter and area of the crystal are known, the force measured can be used to determine the deviatoric stress the crystal experiences during deformation, as per Eq. 96:

$$\sigma_{11} = \frac{F_N}{A} \quad \text{Eq. 96}$$

Here,  $\sigma_{11}$  signifies the stress along the  $d_{11}$  axis of the crystal, and  $A$  is the crystal's area along this axis. A pivotal aspect of these measurements is that the absolute voltage measured across the capacitor does not hold significance for our calculations; instead, it is the change in voltage, represented by  $\Delta V$ , that is instrumental. This change in voltage, occurring as a result of the crystal's deformation, is utilized to calculate the stress applied to the crystal. The rationale behind this is that the system is designed to integrate the charge over time. To discern the actual charge from the integrated value, we take the derivative of the voltage measurement. In practical terms, this derivative corresponds to  $\Delta V$ , the change in voltage across the capacitor.

## 2. Methods

"To ensure measurement accuracy and account for potential voltage drift over time, a baseline voltage is established before each experimental run. This baseline is recorded for at least one minute prior to the start of deformation to set a reference point. After deformation, recording continues for a minimum of one minute to capture the final voltage, thus determining the net change. The knob labeled 'C' on the front of the integration device (see **Figure 37**), is used to manually adjust for any baseline voltage drift during the measurements. Although this knob compensates for some drift, any remaining drift constitutes a constant error in the measurement, which should be minimized.

For example, if deformation results in a total  $\Delta V$  of 1 V, Eq. 95 can be used along with the known capacitance of the integrator's capacitor and the piezoelectric strain coefficient for CTGS ( $4.00 \times 10^{-12}$  C/N as per **Table 4**) to calculate the force on the crystal. This force is computed as 2,490 N using Eq. 97. Given a crystal diameter of 4.00 mm (area =  $1.26 \times 10^{-5}$  m<sup>2</sup>), Eq. 98 is then applied to find the stress:

$$F_N = \frac{(1 \text{ V}) \cdot (9.964 \times 10^{-9} \text{ F})}{4.00 \times 10^{-12} \text{ C/N}} = 2,490 \text{ N} \quad \text{Eq. 97}$$

$$\sigma_{11} = \frac{2,490 \text{ N}}{1.26 \times 10^{-5} \text{ m}^2} = 1.98 \times 10^8 \frac{\text{N}}{\text{m}^2} = 198 \text{ MPa} \quad \text{Eq. 98}$$

As shown in Eq. 98, the crystal experiences a deviatoric stress of 198 MPa. It is important to note that any voltage drift not corrected manually introduces a consistent error margin in the stress measurement, quantifiable as a specific number of MPa per second, based on the equations and the observed rate of voltage drift described previously.

## 2.3. Piezoelectric crystals

### 2.3.1. Quartz

Quartz has been widely studied in geological sciences partly as a result of its abundance, forming about 15% of the Earth's crust by mass (Pabst & Gregorová, 2013). but also because of its commercial manufacture and use in a multitude of applications. Quartz has many polymorphs, the most geologically relevant being  $\alpha$ -quartz,  $\beta$ -quartz, coesite, and stishovite. On the other hand, tridymite and cristobalite are rarely found in nature (Pabst & Gregorová, 2013).

However, quartz is also piezoelectric, being non-centrosymmetric. Due to quartz being one of the most common piezoelectric crystals used extensively in manufacturing, sensor applications and computing, the elastic and piezoelectric properties have been very precisely constrained. The piezoelectric properties of  $\alpha$ -quartz have been measured precisely at many temperatures (Cook & Weissler, 1950).

## 2. Methods

$\alpha$ -quartz has a displacive polymorphic, non-quenchable transition, referred to as an inversion, from trigonal ( $P3_121$ ) to hexagonal ( $P6_222$ )  $\beta$ -quartz, at 573 °C at 1 bar (Nesse, 2018). However, since quartz is not commonly used at high temperatures in most applications, there is less precise information on the properties of  $\beta$ -quartz.  $\beta$ -quartz is still piezoelectric, but  $d_{11}$  vanishes at the inversion temperature, and  $d_{14}$  changes from having a strong positive correlation with temperature to having a slight negative one (Cook & Weissler, 1950).

Since  $d_{11}$  varies less than  $d_{14}$  with temperature, for this work, the piezoelectric crystals were X-cut to minimize temperature effects. With an X-cut crystal,  $d_{11}$  is the piezoelectric coefficient that converts stress to charge polarization. Any changes in the piezoelectric coefficient, if left uncorrected, result in a systematic error in the calculation of stress. If the coefficient increases, for example, the slope of the charge generated would also increase. To reduce this source of systematic error,  $d_{11}$  was chosen over  $d_{14}$ . Because  $d_{11}$  vanishes across the  $\alpha$ -quartz to  $\beta$ -quartz transition, it was necessary to keep the temperature of the piezoelectric crystal below the transition temperature of 573 °C at 1 bar of hydrostatic pressure.

Even though the assembly was designed to keep the piezoelectric crystal's temperature below the  $\beta$ -quartz transition, even when the central region of the assembly might reach higher temperatures, other complications emerge when using quartz for stress measurements. A significant issue is that  $\alpha$ -quartz naturally undergoes ferroelastic twinning. In quartz, as in many ferroic materials, the crystal can form mimetic twin domains that are susceptible to reorientation under an appropriate coercive stress (Shiau et al., 1984). In practice, this phenomenon appears in  $\alpha$ -quartz as Dauphiné twinning, or as Brazil law twins when both twin variants coexist within a single crystal.

In both  $\alpha$ -quartz and  $\beta$ -quartz, the structure consists of silica tetrahedra that link together to form spirals, extending parallel to the  $c$ -axis. When viewed down the  $c$ -axis, these spirals produce a hexagonal symmetry in  $\beta$ -quartz (Nesse, 2018). Being a displacive polymorph, in  $\alpha$ -quartz the silica tetrahedra distort, rotating by 23.3° (Thompson et al., 2011), and reducing the symmetry to trigonal. This symmetry is enantiomorphic with space groups of  $P3_221$  and  $P3_121$  respectively, related by a 180° structural rotation about the optic axis (Pabst & Gregorová, 2013).

While the enantiomorphic forms are equivalent from a thermo-mechanical viewpoint, they are sometimes called electric twins because they are not equivalent from a piezoelectric, or dielectric dipole viewpoint. In fact, twins have equal but opposite dipole moments. For the

## 2. Methods

purposes of this work, what this means is that effectively the piezoelectric constant  $d_{11}$  of  $\alpha$ -quartz has the opposite sign between the two Dauphiné twins (Yamni, 2001). Additionally, the signs of the elastic compliance coefficient  $S_{14}$  reverse (Mansfeld et al., 1997). The elastic compliance reversal is not particularly relevant to this work, unlike the reversal of the piezoelectric coefficient.

From a thermodynamic perspective, ferroelastic switching occurs when a twin state attains a lower Gibbs free energy than its counterpart. Importantly, the reorientation involves only minor atomic displacements, so the process does not require the breaking of Si-O bonds. Under constant temperature, the Gibbs free energy difference between the two Dauphiné twin states is expressed by Eq. 99 (Shiau et al., 1984)

$$\Delta G = 2d_{11}(E_1\sigma_1 - E_1\sigma_2 - 2E_2\sigma_6) + 2S_{14}(\sigma_1\sigma_4 - \sigma_2\sigma_4 + 2\sigma_6\sigma_6) \quad \text{Eq. 99}$$

*(Shiau et al., 1984)*

In Eq. 99, the first term emphasizes the contribution of the piezoelectric coefficient  $d_{11}$  along with its driving forces. These are the product of the electric field  $E$  and the stress  $\sigma$ . This ferroelastoelectric term represents the energy difference between the twin states as established by previous experimental studies. (Laughner et al., 1979). Achieving switching via this mechanism requires applying both a high mechanical stress and a strong electric field simultaneously.

In our experimental setup, while there are large mechanical stresses, there is no electric field imposed across the crystal besides the small field imposed by the piezoelectric charge, which is discharged through the electrodes quickly. Thus, this term's contribution to switching and twin-formation is minor. In fact, experiments have shown that with application only of mechanical stress coupling the  $S_{11}$  direction and no electric field, no twinning is observed (Laughner et al., 1979). Therefore, for our experimental setup, only the second term of Eq. 99 is relevant and is responsible for twinning problems present in  $\alpha$ -quartz as a piezoelectric sensor.

The second term of Eq. 99 involves the compliance coefficient  $S_{14}$ . The compliance coefficient,  $S_{ijkl}$ , is given by

$$\varepsilon_{ij} = S_{ijkl}\sigma_{kl} \quad \text{Eq. 100 (Knowles & Howie, 2015)}$$

## 2. Methods

Where  $\varepsilon_{ij}$  is strain and  $\sigma_{kl}$  is stress. By applying various mechanical stress combinations, switching can be achieved, and twins formed. The stress required to initiate twinning is called the coercive stress,  $\sigma_c$ . It has been shown by experimental work that initiation of crystal twinning requires a lower  $\sigma_c$  for higher temperatures, i.e. it has an inverse correlation (Shiau et al., 1984).

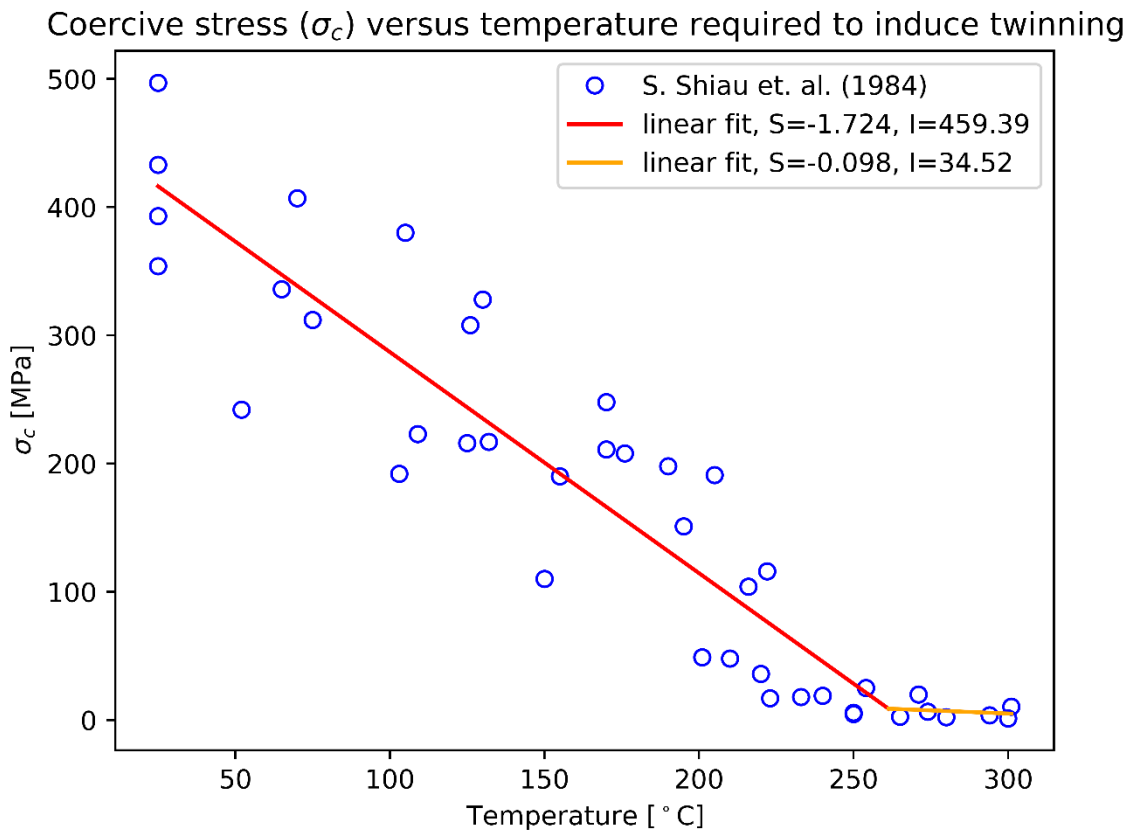


**Figure 39.** Relationship between coercive stress ( $\sigma_c$ ) and temperature. The data points represent experimental results from S. Shiau et al. (Shiau et al., 1984). The two linear fits demarcate the temperature threshold to initiate twinning with a given deviatoric stress, with distinct slopes ( $S$ ) and intercepts ( $I$ ) before and after a sudden change in slope. The point at which the slope changes was optimized for minimal error. This point was determined by systematically sampling values over the temperature range and selecting the value that minimized the difference between the two linear fits.

This type of ferroelastic twinning occurs when stresses are applied transversely to  $d_{11}$ , or X, for example along Y or Z, as shown in **Figure 15**, and not normal to X. However, solid-state deformation, especially at a high confining pressure, is not a simple uniaxial system. Static

## 2. Methods

friction can cause transient stresses in unexpected directional axes to build and release. This is usually only expected during either compression to the necessary hydrostatic pressure or pumping down at the end of the experiment.

As mentioned previously, however, the press does not perform truly uniaxial deformation. While two opposing rams advance along the crystals X direction, increasing  $\sigma_{11}$ , to sustain equal volume in the sample space, some rams must be retracted. Due to inherent design limitations, one set of two opposing rams must be kept at constant pressure and thus cannot advance, leaving the only possibility to retract just two opposing rams. In practice, this results in a pure shear stress on the sample.

In this stress geometry, the second term of Eq. 99 (Shiau et al., 1984) becomes relevant. When the coercive stress is reached, the  $\alpha$ -quartz begins to twin (Shiau et al., 1984; Yamni, 2001). Because the Dauphiné twins have opposite signs of  $S_{14}$  and  $d_{11}$ , a high enough stress can cause the second term to flip the sign of the whole equation and make the opposite Dauphiné twin more stable.

Previous work has shown that if the crystal is small enough and the temperature low enough, the twinning can occur over the whole crystal suddenly. In this case, the polarization vector would switch directions near instantaneously, the result of an enantiomorphic switch from either  $P3_221$  to  $P3_121$ , or vice-versa. If the charge is measured from the crystal during this sudden twinning, the charge would reverse in flow, i.e., the voltage generated reverses in sign suddenly.

However, at higher temperatures (Roughly above  $150^\circ\text{C}$  as reported in literature (Mansfeld et al., 1997; L. A. Thomas et al., 1951; Yamni, 2001), but with a wide range) or higher hydrostatic pressure (Bertagnolli et al., 1979; Laughner et al., 1979), the whole crystal does not twin at once. Dauphiné twinning begins at nucleation sites formed by either point defects or dislocations in the crystal structure (Bertagnolli et al., 1979). These domains then grow over time, slowly twinning the whole crystal.

During this growth, the crystal consists of two distinct domain groups, one with space group  $P3_221$  and another with  $P3_121$ . The polarization vector, as described before, is reversed between these two domains, the result of a sign flip of each component in the  $d_{ij}$  and  $e_{ij}$  tensors. When measuring the voltage or charge on the crystal faces as it deforms, the twinning results in a smooth reversal of the trend. Depending on the number of twin domains formed and the physical size of the crystal, this voltage sign reversal could either occur in larger discrete steps,

## 2. Methods

that could be seen on a time plot of voltage or charge, or form a smooth reversal curve (Shiau et al., 1984).

In this study, any smooth reversal in the charge or voltage caused by Dauphiné twinning would be indistinguishable from a change in stress on the crystal during deformation. The large sensitivity of this switching to coercive stress, temperature, and defect density makes the exact point of twinning unpredictable during deformation experiments. Coercive stress, which is the minimum stress required to initiate twinning, varies significantly with both temperature and the crystal's internal structure. As temperature increases, the crystal's resistance to deformation decreases, lowering the coercive stress needed for twinning (Bertagnolli et al., 1979; Shiau et al., 1984; Yamni, 2001). This temperature-dependent behavior adds complexity, particularly when experiments are conducted over a wide temperature range.

Defects in the crystal structure, such as dislocations or point defects, also play a crucial role in the initiation of twinning. These defects serve as nucleation sites, making twinning highly sensitive to the crystal's defect density (Guzzo & Boy, 2000; Mansfeld et al., 1997). Variations in defect density, whether between different crystals or within a single crystal, further contribute to the unpredictability of the twinning process.

In the context of triaxial deformation using a multi-anvil cubic press, additional complexity arises from the presence of a shear stress component associated with the  $S_{14}$  term. This shear component interacts with the crystal's internal defect structure and plays a significant role in determining the conditions under which the coercive stress is reached, and twinning occurs.

There is also hysteresis in the coercive stress ( $\sigma_c$ ). Each time a crystal twins under stress, the  $\sigma_c$  decreases (Herzbach & Müser, 2006; Yamni, 2001), making subsequent twinning easier. Because of the inherent error introduced by ferroelastic switching in  $\alpha$ -quartz, its use in this study has been limited to low-temperature and low-stress deformation experiments.

## 2. Methods

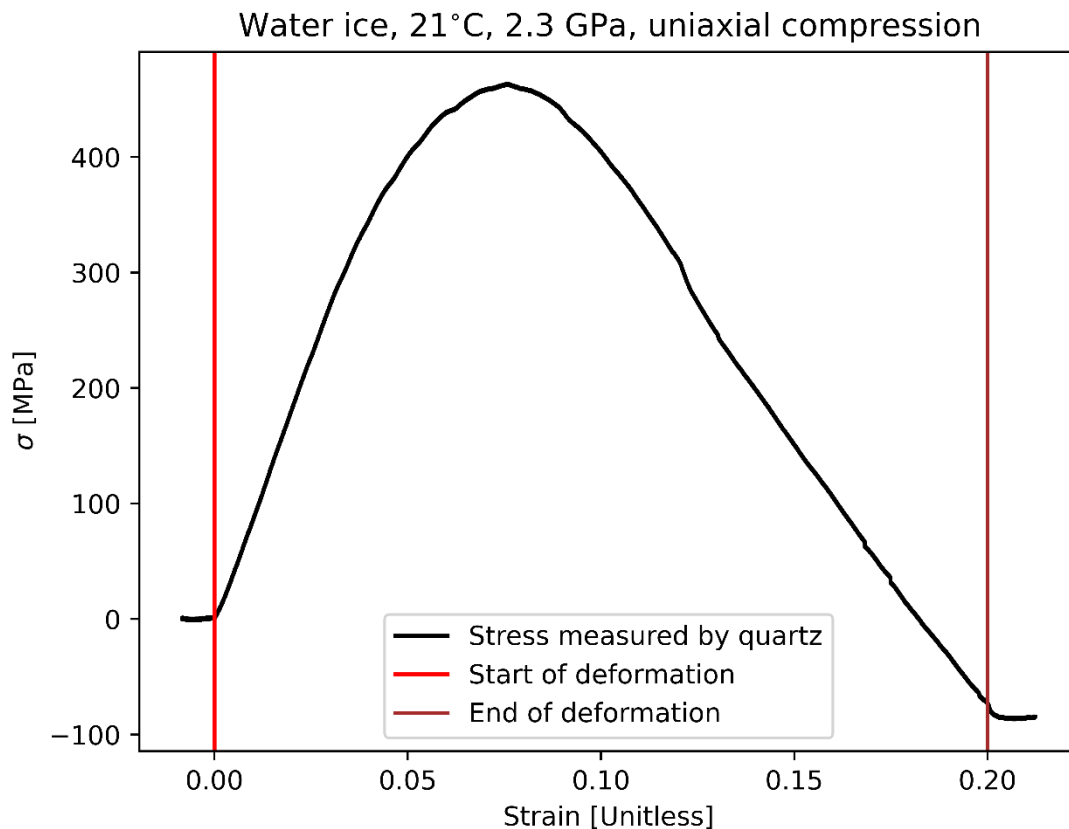


**Figure 40.** An example of the effect of ferrobielastic switching in an experiment conducted with this assembly utilizing  $\alpha$ -quartz as the piezoelectric crystal. The switch is seen happening at around 450 MPa. This experiment was deformation of water ice at 2.3 GPa in compression.

As a clear example of the issue of ferrobielastic switching in  $\alpha$ -quartz for this assembly, **Figure 40** plots the stress, as measured through the charge induced by the polarization of  $\alpha$ -quartz, on the vertical axis and the strain on the horizontal axis, for a deformation experiment performed on water ice at room temperature and 2.3 GPa. At this pressure and temperature, water is solid (French et al., 2009; Salzmann, 2019).

As can be seen by the vertical red line at the start, the initial stress as deformation is started is positive. The stress increases close to linearly until a strain of 0.05. At this point, the slope begins to decrease, which could be interpreted as the end of the elastic regime and the commencement of the creep regime. However, it continues to decrease and at 0.07 strain it actually reverses direction. Even though this is a compressive experiment, and stress should not realistically decrease at such a point, it continues to do so. At the end of the uniaxial compressive experiment, the stress, as measured by the  $\alpha$ -quartz piezoelectric crystal, is

## 2. Methods

apparently negative. This is unlikely and no clear mechanism can explain why a compressive experiment would result in an initial increase in stress, then a plateau followed by a smooth transition to a decrease in stress and finally a negative stress, as compared to the beginning of the deformation, of -80 MPa.

Indeed, according to **Figure 39**, a ferroelastic switch in  $\alpha$ -quartz, at room temperature, would be expected at roughly 400 MPa, and would therefore provide a better explanation of the behavior.

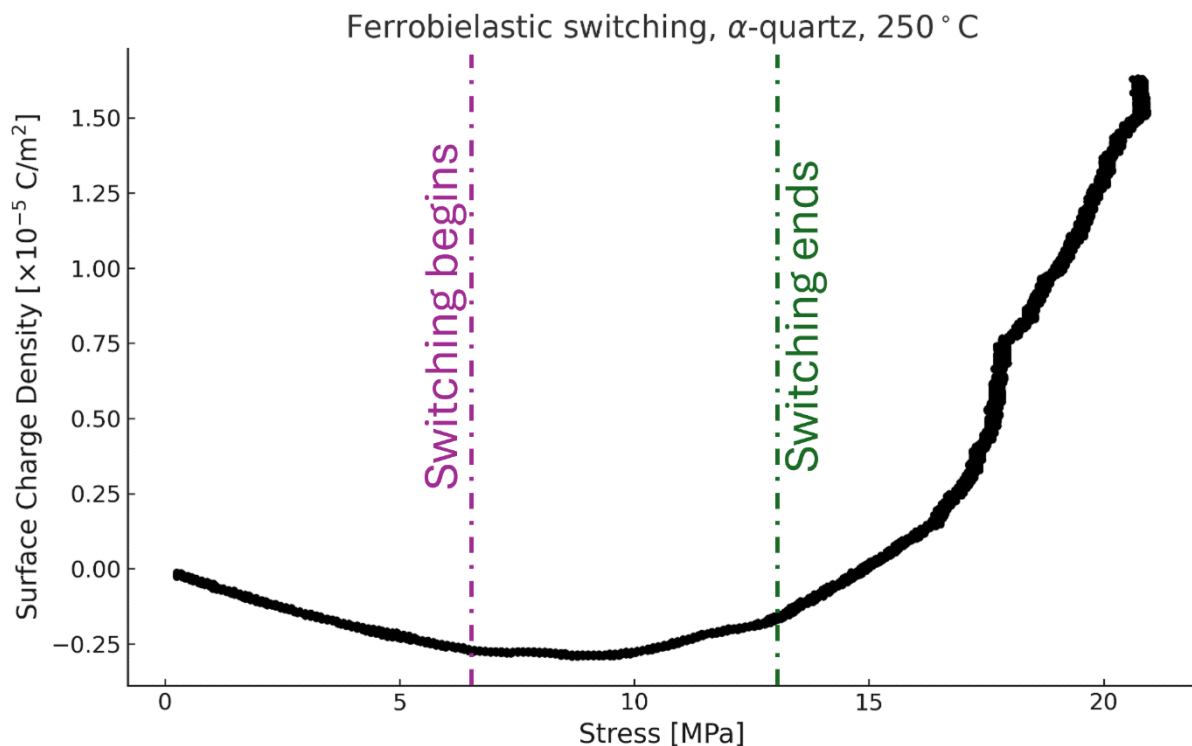


**Figure 41.** Figure 3 modified from Shiau et al. (Shiau et al., 1984) showing force applied on an  $\alpha$ -quartz crystal (horizontal axis) while the charge developed along the surface is measured (vertical axis). Shown is only the compressive section of the curve, with the load reducing section removed for conciseness. The compressive force was applied at 250 °C and 1 bar of pressure.

This case becomes stronger when compared to literature data on surface charge measurements made during compressive force experiments on  $\alpha$ -quartz, as shown in **Figure 41**, which is modified from figure 3 in Shiau et al. (Shiau et al., 1984). In this case, the stress applied, which is plotted on the horizontal axis, is measured externally with a force sensor, and the vertical axis shows the charge developed across the crystal surface.

## 2. Methods

As an analogue to the experimental plot from this study, shown in **Figure 40**, the stress measured in this study is calculated from the surface charge density of the crystal during deformation, so the axes are directly comparable. As can be seen in **Figure 41**, as force, or stress, is applied to the crystal, the charge generated is initially negative. As a result of ferrobielastic switching, there is a change in the gradient of surface charge with stress and the charge then becomes positive. This change in the curvature of the charge density looks remarkably similar to the measurements from this study in **Figure 40**. The similarity in the charge response observed in **Figure 40** and the similar stress state at which it occurs compared to literature data (Mansfeld et al., 1997; Shiao et al., 1984) are strong indicators that ferrobielastic switching is occurring.

The recognition of this effect leads to the search for a different piezoelectric crystal to be used in these experiments.

### 2.3.2. CTGS

The relatively low temperature of transition from  $\alpha$ -quartz to  $\beta$ -quartz (570 °C), coupled with the problem of ferrobielastic twinning, means that for higher temperature and higher stress applications, new piezoelectric crystals are required. While  $\alpha$ -GaPO<sub>4</sub>, which has the same crystal class as quartz, has a higher phase transition temperature to the  $\beta$ -GaPO<sub>4</sub> phase, at 930 °C (Beaurain et al., 2006; Kosinski et al., 2001), it still undergoes ferrobielastic twinning. Another issue with GaPO<sub>4</sub> is that it cannot be grown with the relatively affordable and mass producible Czochralski (CZ) method (Beaurain et al., 2006). It must be grown hydrothermally instead, a slow process that results in much smaller crystal sizes. This makes it commercially unviable for mass production in sensors.

CTGS (Ca<sub>3</sub>TaGa<sub>3</sub>Si<sub>2</sub>O<sub>14</sub>) is a crystal also of the same crystal class as quartz but is part of the langasite group of crystals. The langasite group of crystals was first reported in 1993 (Shannon, 1993), with the name coming from the first described phase being La<sub>3</sub>Ga<sub>5</sub>SiO<sub>14</sub> (commonly reported as LGS), or langasite. The langasite group has the generalized chemical formula A<sub>3</sub>BC<sub>3</sub>D<sub>2</sub>O<sub>14</sub> (Zhang et al., 2009). The A and B sites are a decahedron coordinated by eight oxygen atoms and an octahedron coordinated by six oxygen atoms, respectively. The C and D sites are tetrahedra, with the C being larger than the D site, thus the larger cations tend to go into the C site. The C and D sites form layers, alternating along the *c* axis with the A and B layers.

## 2. Methods

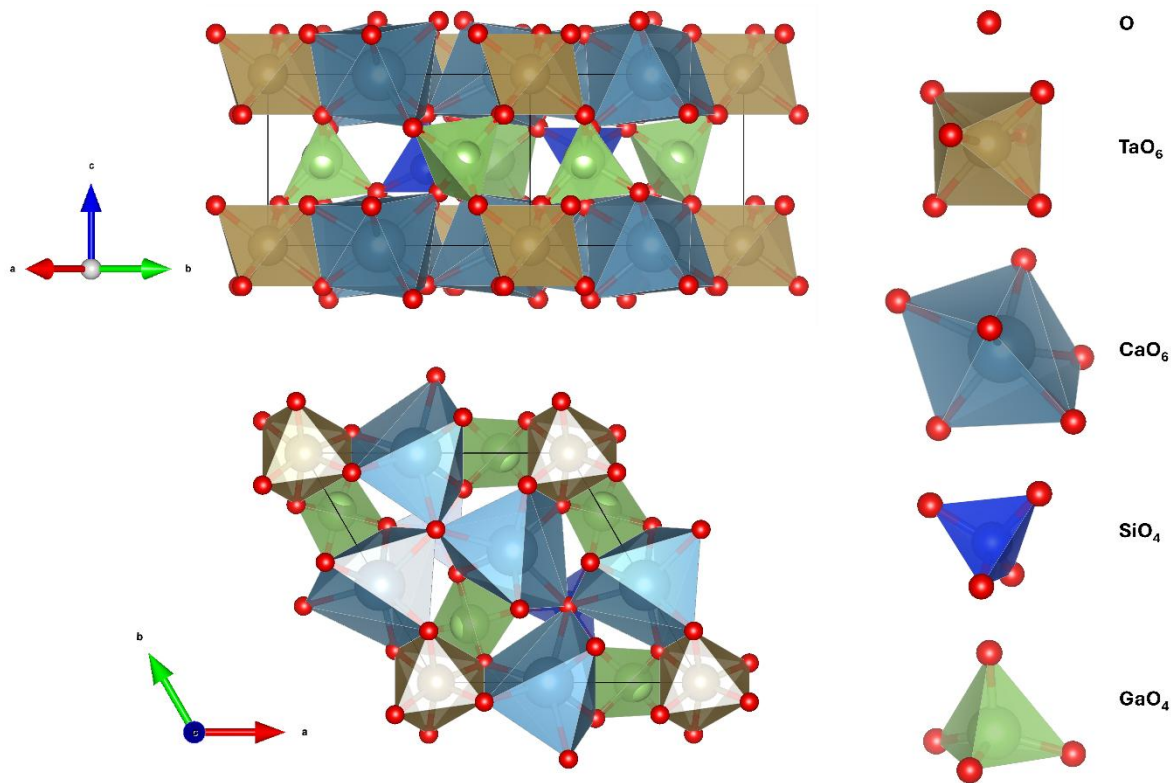


**Figure 42.** Crystal structure of CTGS, generated with the software VESTA (Momma & Izumi, 2011, p. 3). Two views are presented and the lattice orientation described to the left of each. The black lines are unit cell boundaries. The legend of the polyhedra are provided on the right. Crystal structure file from Ai et al., (2024).

The langasite group can be broken down into two subgroups, an ordered and disordered group. In the disordered group,  $\text{Ga}^{3+}$  cations occupy three positions, the B, C, and half of the D sites.  $\text{Si}^{4+}$  occupies the other half of the D site. The ordered group meanwhile has only one cation type occupying each site (S. Zhang et al., 2009). The langasite group is still being studied extensively for use in higher temperature applications where the piezoelectric effect is used to measure environmental properties (Fritze et al., 2003). In general, langasite group crystals have higher piezoelectric strain coefficients than quartz, ranging from factors of 2 to 3. This is desired in almost every application as a higher piezoelectric coefficient means a higher precision in, for example, force measurements.

As can be seen in **Table 4** (Zhang et al., 2009), the disordered langasite structures tend to have lower resistivity. The explanation typically given is that oxygen vacancies are the main charge carriers in langasite group crystals at temperatures below roughly  $300^\circ\text{C}$ , and the activation

## 2. Methods

energy for oxygen vacancy migration is, therefore, the main factor controlling the electrical conductivity (Zhang et al., 2009).

**Table 4.** Properties of disordered and ordered langasite-structure piezoelectric single crystals. All measurements except resistivity ( $\rho_R$ ) taken at room temperature.  $\rho$  is density in  $\text{g/cm}^3$ ,  $\epsilon_{11}$  is the dielectric coefficient,  $S_{11}$  is the compliance coefficient,  $d_{11}$  the piezoelectric coefficient, and  $\rho_R$  is the resistivity. The values in the 11 direction are provided since this is the direction of  $\sigma_1$  in the experiment. Table modified from Zhang et al., (2009).

Name	Composition	Structure	$\rho$ [g/cm <sup>3</sup> ]	$\epsilon_{11}$	$S_{11}$ [m <sup>2</sup> /N] $\times 10^{-24}$	$d_{11}$ [C/N] $\times 10^{-12}$	$\rho_R$ [ $\Omega \cdot \text{m}$ ] At 500° C
LGS	La <sub>3</sub> Ga <sub>5</sub> SiO <sub>14</sub>	Disordered	5.85	18.0	8.86	6.20	$9.0 \times 10^4$
LTG	La <sub>3</sub> Ta <sub>0.5</sub> Ga <sub>5.5</sub> O <sub>14</sub>	Disordered	6.12	19.6	9.07	7.10	$1.5 \times 10^5$
LNG	La <sub>3</sub> Nb <sub>0.5</sub> Ga <sub>5.5</sub> O <sub>14</sub>	Disordered	5.95	20.7	9.27	7.40	$5.0 \times 10^5$
LTGA	La <sub>3</sub> Ta <sub>0.5</sub> Ga <sub>5.3</sub> Al <sub>0.2</sub> O <sub>14</sub>	Disordered	6.07	21.0	9.15	6.60	$2.2 \times 10^5$
LNGA	La <sub>3</sub> Nb <sub>0.5</sub> Ga <sub>5.3</sub> Al <sub>0.2</sub> O <sub>14</sub>	Disordered	5.90	19.5	9.90	6.90	$1.1 \times 10^6$
SNGS	Sr <sub>3</sub> NbGa <sub>3</sub> Si <sub>2</sub> O <sub>14</sub>	Ordered	4.65	12.4	8.80	5.40	$6.3 \times 10^5$
STGS	Sr <sub>3</sub> TaGa <sub>3</sub> Si <sub>2</sub> O <sub>14</sub>	Ordered	5.12	11.8	8.69	4.90	$3.7 \times 10^6$
CNGS	Ca <sub>3</sub> NbGa <sub>3</sub> Si <sub>2</sub> O <sub>14</sub>	Ordered	4.15	17.5	8.75	4.00	$6.9 \times 10^5$
CTGS	Ca <sub>3</sub> TaGa <sub>3</sub> Si <sub>2</sub> O <sub>14</sub>	Ordered	4.63	16.5	8.95	4.00	$1.7 \times 10^7$
CTAS	Ca <sub>3</sub> TaAl <sub>3</sub> Si <sub>2</sub> O <sub>14</sub>	Ordered	4.04	13.0	8.51	4.30	$2.7 \times 10^7$

In the ordered langasite group crystals, the oxygen vacancies are trapped in deeper potential wells due to the longer-range ordering (Pisarevsky et al., 2004). To hopefully optimize the electrical properties of the piezoelectric crystal used in this study, an ordered crystal was chosen. Purchase enquiries for both CTAS and CTGS were made, but CTGS was more readily available and was thus chosen. The crystal structure of CTGS is shown from two views in **Figure 42**. Since low electrical resistance is critical for the stress measurements in this study, CTGS was chosen due to its markedly higher resistance values compared to  $\alpha$ -quartz or even GaPO<sub>4</sub>.

## 2. Methods

Previous literature data has shown that CTGS has an electrical resistance that is several orders of magnitude higher than  $\alpha$ -quartz (S. Zhang et al., 2009).

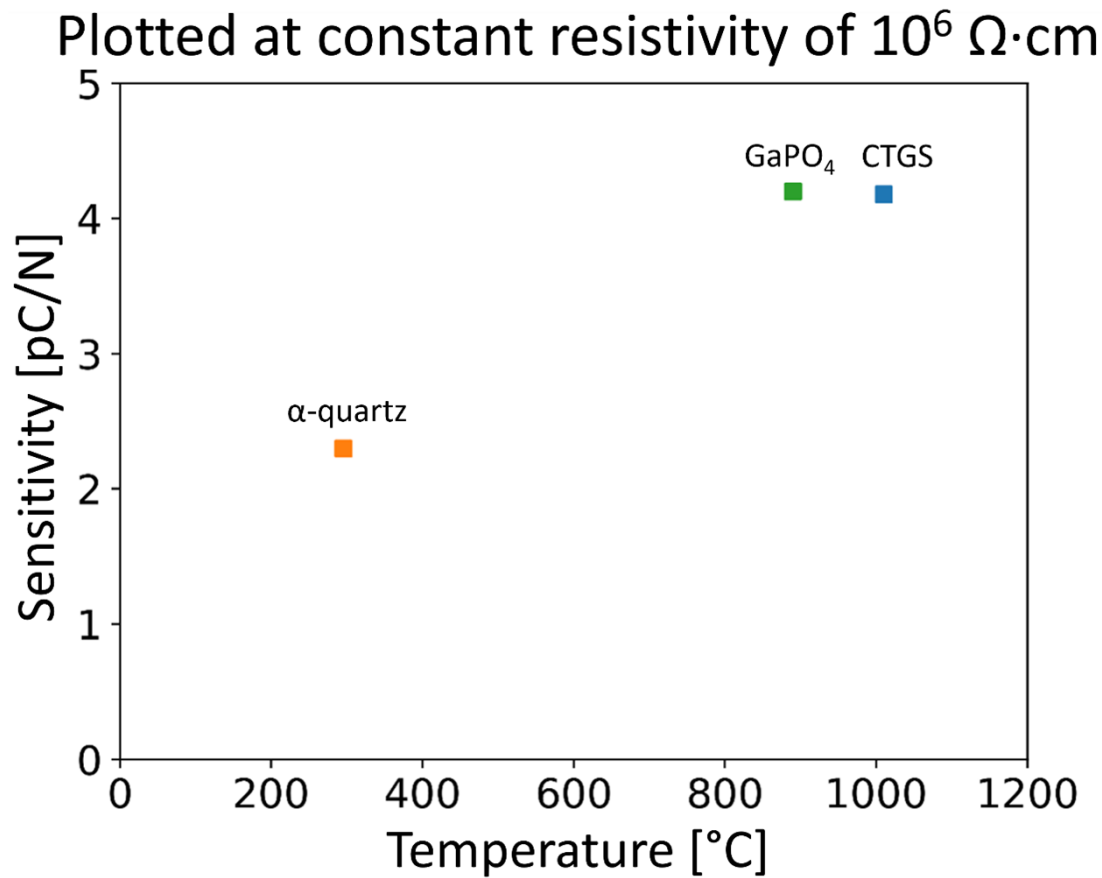


**Figure 43.** Literature data of measured electrical resistivity of  $\alpha$ -quartz, GaPO<sub>4</sub>, and CTGS. Sensitivity, i.e., the piezoelectric strain coefficient  $d_{11}$  in pC/N is on the vertical axis and temperature on the horizontal axis. All crystals plotted at a constant resistivity of  $10^6 \Omega\cdot\text{cm}$ . Modified from Shujun & Yu (Zhang & Yu, 2011)

This is evident in **Figure 43**, where  $\alpha$ -quartz, GaPO<sub>4</sub>, and CTGS are plotted at a constant electrical resistivity of  $10^6 \Omega\cdot\text{cm}$ . As these materials are dielectrics, their electrical resistance decreases with temperature following Arrhenius-like behavior. Consequently  $\alpha$ -quartz at 300 °C has the same resistivity as CTGS at 1000 °C. This trend holds true at all temperatures unless a phase transition is crossed, melting occurs, or new electrical conduction mechanisms are engaged (Zhang et al., 2009; S. Zhang & Yu, 2011). In addition, the piezoelectric strain coefficient  $d_{11}$ , on the vertical axis, shows that CTGS has roughly double the sensitivity as  $\alpha$ -quartz.

## 2. Methods

In addition to these two reasons, and perhaps most critically, CTGS was chosen because, after an extensive literature review, no evidence was found for the occurrence of ferroelastic switching in this material, as found for  $\alpha$ -quartz. Additionally, experimental data from this study measured no ferroelastic switching in any experimental run with CTGS as was seen in  $\alpha$ -quartz commonly, except for perhaps a single one at the beamline. Theoretically, all minerals in the P321 space group have enantiomorphic forms, or electric twins (Konstantinova et al., 2022; Poplavko, 2019). CTGS does grow in one of two twinned forms, P3<sub>2</sub>21 and P3<sub>1</sub>21 (Kong et al., 2018; Konstantinova et al., 2022; Suhak et al., 2018), but it seems to not undergo ferroelastic switching as readily as  $\alpha$ -quartz.

There are multiple possible reasons as to why this is the case. One possibility is that while CTGS does have a small amount of disordering, one study finding that 2.9% of Ca atoms are displaced into the general site that O atoms are normally in (Dudka, 2016), this is still the lowest among the langasite-group crystals (Dudka, 2016; Konstantinova et al., 2022) and CTGS is actually the most ordered in the group. Ferroelastic twinning still requires dislocations or defects to serve as nucleation sites for the twinning process (Guzzo & Boy, 2000; Mansfeld et al., 1997) that allow the twinned domains to grow and ultimately convert the whole crystal. The high-level of ordering in CTGS may result in fewer nucleation sites.

However, the most likely reason for the lack of an observable ferroelastic effect in CTGS is due to the exceptionally low value of the  $S_{14}$  and  $C_{14}$  elastic coefficients. Studies disagree on the precise  $C_{14}$  elastic coefficient of  $\alpha$ -quartz, but most report that at 1 bar and room temperature,  $\alpha$ -quartz'  $C_{14}$  elastic coefficient ranges between -18.20 and -15.7 GPa (Calderon et al., 2007;

## 2. Methods

Heyliger et al., 2003) for both natural and synthetic crystals. However, most work reports that CTGS'  $C_{14}$  elastic coefficient is well below 1 GPa, never exceeding 0.77 GPa (Ma et al., 2017) and some report it as low as 0.44 GPa (Zu et al., 2016).

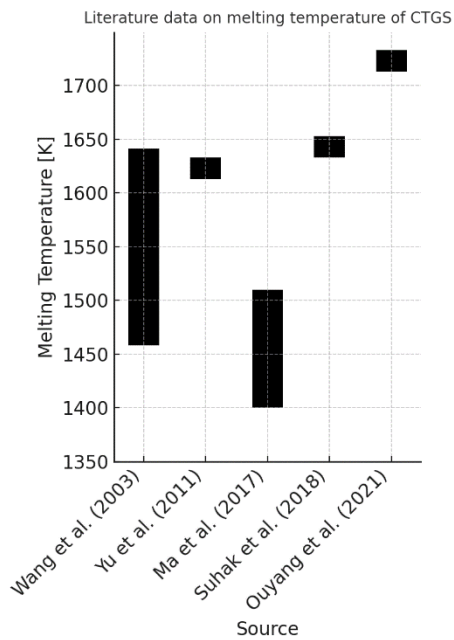


**Figure 44.** Various reported melting temperatures from studies on CTGS. The height of the black bars encompasses each respective studies' reported melting temperature range for CTGS, in K. The sources used are Wang et al. (2003), Yu et al. (2011), Ma et al. (2017), Suhak et al. (2018), and Ouyang et al. (2021).

Recalling Eq. 99 (Shiau et al., 1984), specifically the second term, the whole term is multiplied by  $S_{14}$  twinning under a mechanical load only with no applied electric field (the first term of Eq. 99 (Shiau et al., 1984)), a small value of  $S_{14}$  is preferred. CTGS, among all the langasite-group minerals, fits this criterion best. Since CTGS has no quartz-like  $\alpha$  to  $\beta$  transition, up to its melting temperature, irregularity or a lowering of the piezoelectric sensitivity is avoided. Studies disagree on the 1 bar melting temperature of CTGS, but even the lowest temperature of 1400 K (Ma et al., 2017) is far above any temperatures expected to be imposed onto the crystal during an experimental deformation run. **Figure 44** plots some of the reported melting temperatures of CTGS.

## 2. Methods

By choosing CTGS for the experiments in this study compared to  $\alpha$ -quartz, clear benefits are gained in terms of a higher piezoelectric coefficient, higher resistivity at all temperatures, lack of an  $\alpha$  to  $\beta$  structural transition, and the apparent absence of ferroelastic switching.

### 2.4. X-ray diffraction

#### 2.4.1 X-ray diffraction to verify piezoelectric assembly

High pressure piezoelectric stress determination is a novel method, and an extensive literature review did not reveal any other applications of piezoelectric crystals to measure high-pressure and -temperature deformation stresses in large volume presses. For any new measurement method to be verified for accuracy and precision, a comparison to established or trusted methods must be undertaken.

For example, a naïve assumption could be that measuring the additional oil pressure required to advance the pistons, as compared to the hydrostatic oil pressure, it would be possible to measure the stress required to deform. However, in any apparatus that deforms a solid media, the force applied onto the anvil is not representative of the stress the actual sample within the assembly experiences. Frictional losses with the pyrophyllite gaskets, stress transmitting around the sample through the assembly, and frictional losses within the assembly itself decouple the force to advance the ram from the actual stress the sample is exposed to (Passelègue et al., 2020; Walker et al., 1990).

This method can only be used if the hydrostatic pressure media is a liquid or gas, and the advancing ram is in contact with the sample only. In this case, as it advances within the pressure media, the force required to move it can be considered as directly representative of the force applied to the anvil from the exterior, assuming that the friction along the seal can be quantified beforehand. This technique has been used with Paterson apparatus (Fischer & Paterson, 1992; Paterson, 1970; Violay et al., 2015, 2017) before. Since this high-pressure device uses an inert gas to apply confinement, the assumption of hydrostatic conditions within the sample chamber is safe to make.

In this case, to avoid the issue of seal friction when using an external load cell on the ram, internal load cells can be used. An example of one such internal load cell is a Wheatstone bridge which precisely records resistance variations along a conductor. Since, when a conductor strains the resistance changes due to the change in conduction length through it, a material with known strain-stress relations can be used as a stress sensor (Meyer et al., 2023). This sensor type is relatively robust and can withstand high-pressures and -temperatures, within limits. The pressures are limited by the solidus of the pressure media and the mechanical robustness of the

## 2. Methods

Wheatstone bridge. In practice, this limit is about 500 MPa and up to 800 °C (Cornelio & Violay, 2020; Eccles et al., 2005; Meyer et al., 2023; Noël et al., 2019; Walker et al., 1990).

While useful, this is clearly far below the pressure and temperature capabilities of large volume presses such as D-DIA and cubic presses. The only *in situ* method previously available for measuring the stress of a sample directly has been XRD at a synchrotron facility. By measuring the microstrain of lattice planes within a crystal at pressure, one can derive the stress. Since this technique has been widely used for decades (Burnley & Kaboli, 2019; Duffy, Shen, Heinz, et al., 1999; Singh et al., 1998), this was chosen as the method to verify the viability of the piezoelectric method.

To this end, deformation experiments were undertaken at a synchrotron facility where the stress of a deforming sample was measured using the Singh et al. (1998) method, previously described with Eq. 4 to Eq. 6, and the piezoelectric crystal method simultaneously. The XRD stress measurement method was used as the standard to compare to the piezoelectric crystal method. All experiments were performed at the Deutsches Elektronen-Synchrotron DESY, PETRA-III synchrotron located in Hamburg, Germany. The P61B beamline end station at DESY is ideal for these experiments as it contains a cubic six-ram large volume press, identical in geometry to the press at BGI. The LVP there is an Aster-15 Voggenreiter GmbH 6 ram press with a maximum load on each axis of 5 MN, for a total load of 15 MN (Farla et al., 2022).

Besides the lower achievable maximum force compared to the MAVO press at BGI, the identical geometry of the press at P61B allowed for the maximum possible relation of experiments at the beamline with experiments done in-house at BGI. As such, the cubic assembly itself was kept identical to the experiments at BGI, apart from an initial experimental run at P61B in which the assembly cube was made of boron-epoxy instead of the Cr-doped MgO typically used at BGI. This was chosen at the time due to uncertainty if the x-ray beam was bright enough to pass through the MgO cube. X-ray absorption of materials is positively correlated with increasing atomic number and density (Heismann et al., 2003). By using a boron-epoxy cube, the density is reduced and since boron has a lower atomic number as compared to Mg, the x-rays are attenuated to a lesser degree. The requirement is that the boron is amorphous to avoid diffraction peaks from it (Besson et al., 1992). These can interfere with the peaks from the sample.

## 2. Methods

After that initial beamtime, it was made obvious that the x-ray beam at P61B is sufficiently bright to not cause issues of attenuation from Cr-doped MgO cubes and so subsequent experiments utilized an identical assembly to the one described previously.

### 2.4.2. P61B beamline at DESY

The P61B beamline at PETRA-III is a white beam. The previous discussion on XRD techniques and the measurement of stress assumed a monochromatic x-ray beam. A monochromatic beam consists of x-rays of a singular energy. According to the Bragg equation (Eq. 2), the d-spacing variation in a crystal, measured with a monochromatic beam, alters the diffraction angle as a function of the d-spacing. However, with a white beam, which contains a wide range of x-ray energies, the d-spacing affects the energy distribution at a specific diffraction angle instead.

$$\lambda = 2d_{hkl} \sin \theta \quad \text{Eq. 101}$$

The Bragg equation is shown again above, Eq. 101. In the case of white beam diffraction, the diffraction angle  $\theta$  is kept constant and the d-spacing,  $d_{hkl}$ , will change the energy distribution of the diffracted x-rays. Specifically, if the d-spacing decreases, for example due to stress from the vertical direction, the wavelength  $\lambda$  would decrease. To relate the energy with wavelength, the Planck-Einstein relation in Eq. 102 is used.

$$E = hf \quad \text{Eq. 102}$$

$$E = \frac{hc}{\lambda} \quad \text{Eq. 103}$$

$E$  is the energy of a photon,  $h$  is Planck's constant, and  $f$  is the frequency of the electromagnetic wave. Since the speed of light,  $c$  is related to the wavelength  $\lambda$  and the frequency  $f$  by  $c = \lambda f$ , it can be substituted into Eq. 102 to derive Eq. 103. In this way, the energy of peaks from the XRD pattern can be converted to wavelengths and then using the Bragg equation, the d-spacing  $d_{hkl}$  can be calculated. Thus, the d-spacing of lattice planes can be calculated.

The DESY PETRA-III synchrotron is 6 GeV with a beam current of 100 mA. The circumference is 2304 m. At the P61B beamline, the energy range available for diffraction is 30 – 160 keV with a  $2.2 \times 1.7$  mm beam size. The beam can be blocked with slits to smaller apertures to a minimum of  $10 \times 10 \mu\text{m}$  (Farla et al., 2022). The detection system consists of two high-purity germanium solid-state detectors, Ge-SSD, manufactured by Mirion (Canberra) for ED-XRD. Radiography is used to image the sample and the system at P61B uses a white-beam X-ray microscope manufactured by Optique Peter.

## 2. Methods

The two detectors, D1 and D2, are mounted on translation stages and goniometers, and can be placed at multiple  $2\theta$  and azimuthal angles. D1 can be rotated vertically from  $3^\circ$  to  $23^\circ$   $2\theta$  and horizontally from  $3^\circ$  to  $10^\circ$  to cover a limited azimuthal range. D2 can rotate horizontally between  $3^\circ$  and  $10^\circ$   $2\theta$ . An image of the press inside the experimental hutch with the detectors shown, mounted to the extruded aluminum rails, is shown in **Figure 45**. In hydrostatic experiments, only a single detector is required. However, in deformation experiments the energy distribution around the azimuthal angle is not identical due to stresses. To measure the stress, a minimum of two detectors is required, placed at different azimuthal angles.

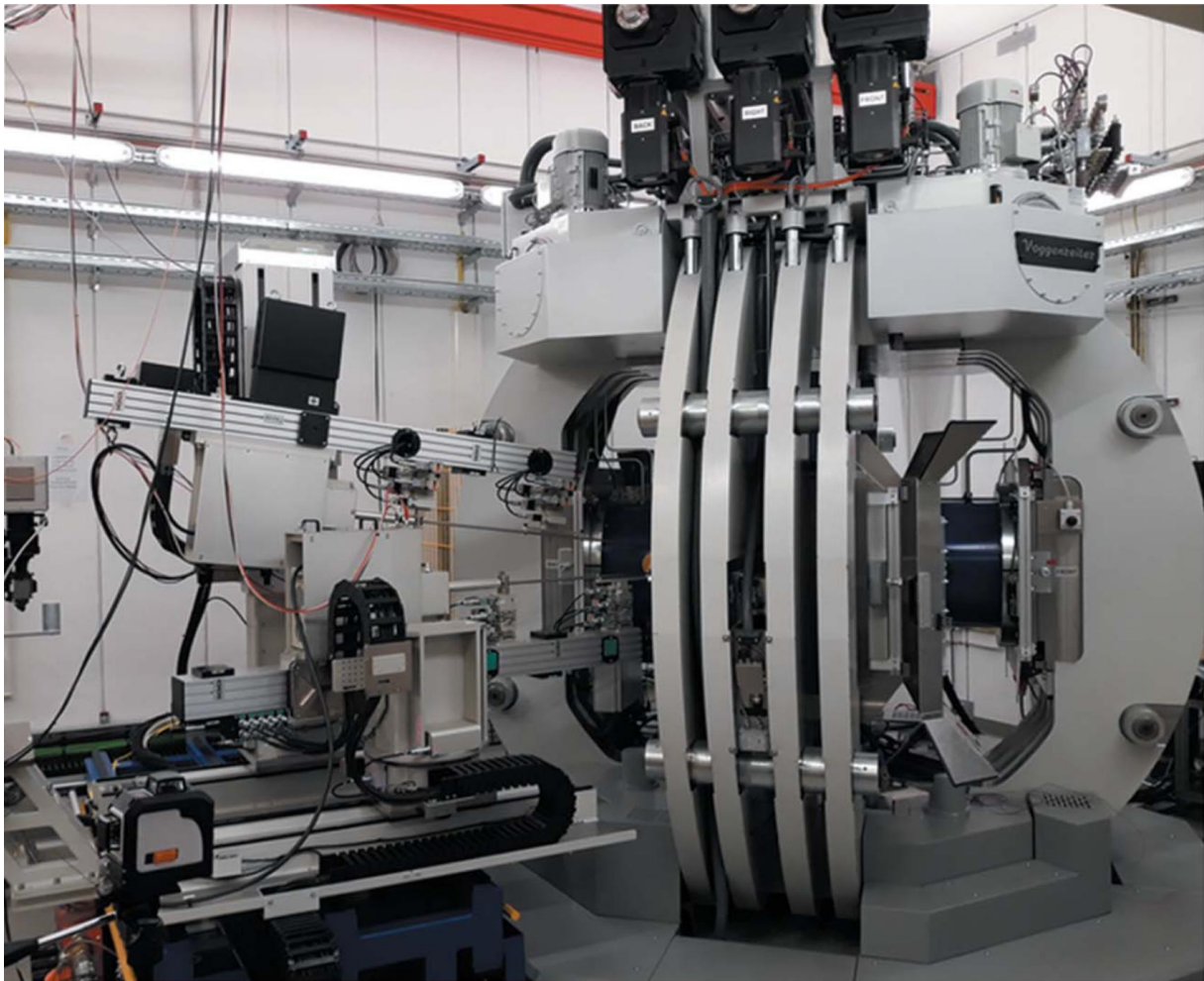


*Figure 45. An image of the P61B beamline hutch. The Aster-15 press is shown to the right and the two detectors on the aluminum rails are on the left side (Farla et al., 2022).*

In the case of the deformation experiments at P61B to verify the piezoelectric stress measurement technique, the detectors were placed at the same angle  $2\theta$ . This simplifies the calculation of stress since if the  $2\theta$  angles are identical any difference in peak positions between the two detectors is due to stress only. To measure stress, the detectors were placed at different

## 2. Methods

positions around the azimuthal angle. D1 was placed at  $0^\circ$  and D2 at  $90^\circ$ . The geometry is shown in **Figure 46**. As stated,  $\theta_1 = \theta_2$ . In the hydrostatic condition, the energy distribution at each point along the diffraction Debye cones is equal along the same  $2\theta$  angle everywhere around the azimuthal angle.

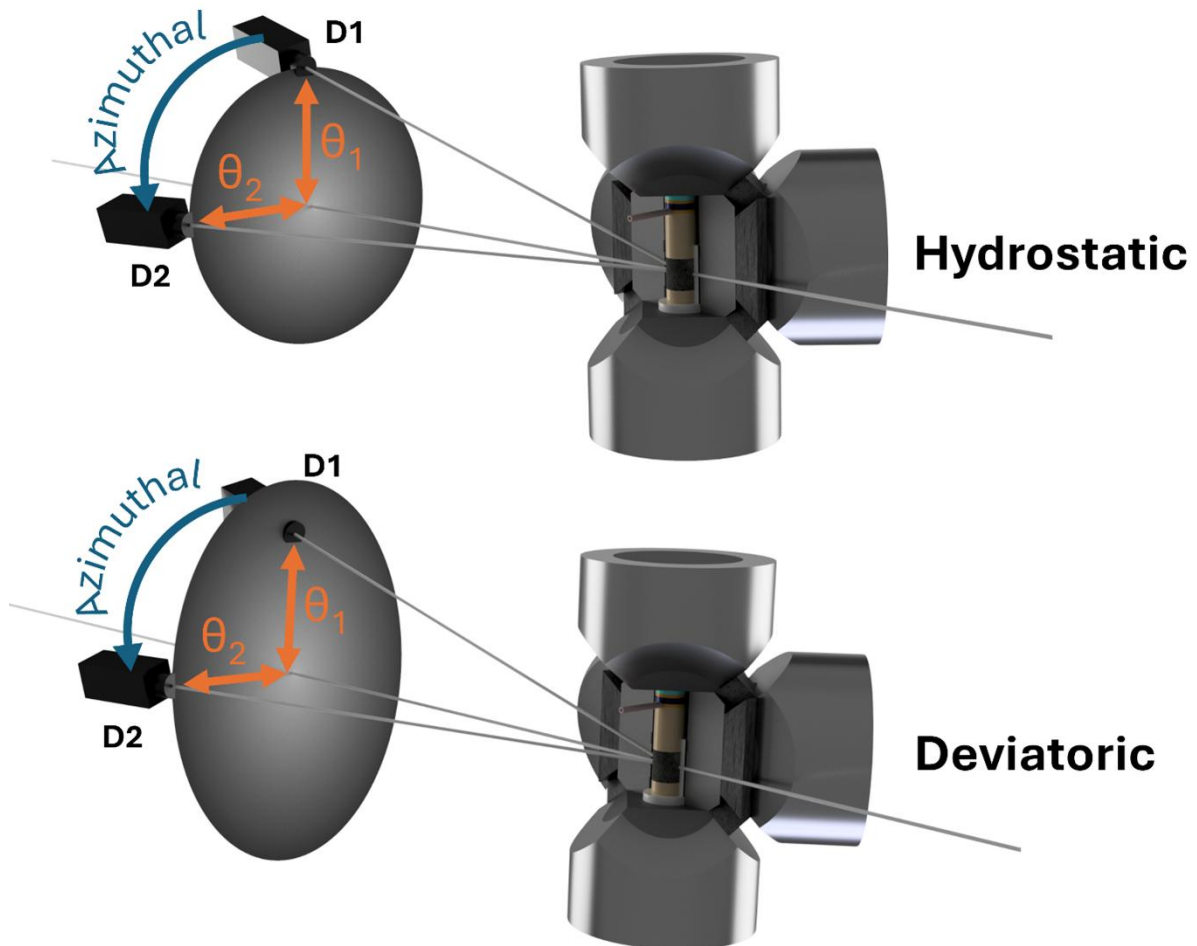


**Figure 46.** A render of the geometry and conceptual explanation of the experimental setup at P61B for the deformation experiments. The hydrostatic condition is shown in the top half and the deviatoric in the bottom half. The x-ray beam enters from the right side into the sample and diffracts to the left side in the diagram.

In the deviatoric stress condition, shown in the bottom half of **Figure 46**, the energy distribution is distorted into an elliptical shape. Because of the placement of D1 and D2, they both capture the maximum and minimum elliptical energy distribution along the azimuthal conditions respectively. D1 is along the deformation axis and D2 perpendicular to this axis. The elliptical distribution with azimuthal angle describes a sinusoidal function, with D1 defining the minimum amplitude and D2 the maximum amplitude. The general convention is to define the

## 2. Methods

vertical axis as  $0^\circ$  azimuth (Burnley, 2015; Burnley & Kaboli, 2019; Duffy, Shen, Heinz, et al., 1999; Singh et al., 1998), increasing counterclockwise so detector D2 is at  $90^\circ$  azimuth. In this geometry, the d-spacings recorded by detector D1 decrease with the applied stress as they are perpendicular to  $\sigma_1$ , whereas at D2 d-spacing increase slightly as they are parallel to  $\sigma_1$ . A sinusoidal curve can be fitted to these two positions, as shown in **Figure 47**, illustrating the decrease in d-spacing at  $0^\circ$  azimuth, i.e. at detector D1. The data was measured at P61B on MgO, with no heating, peak (111) only.

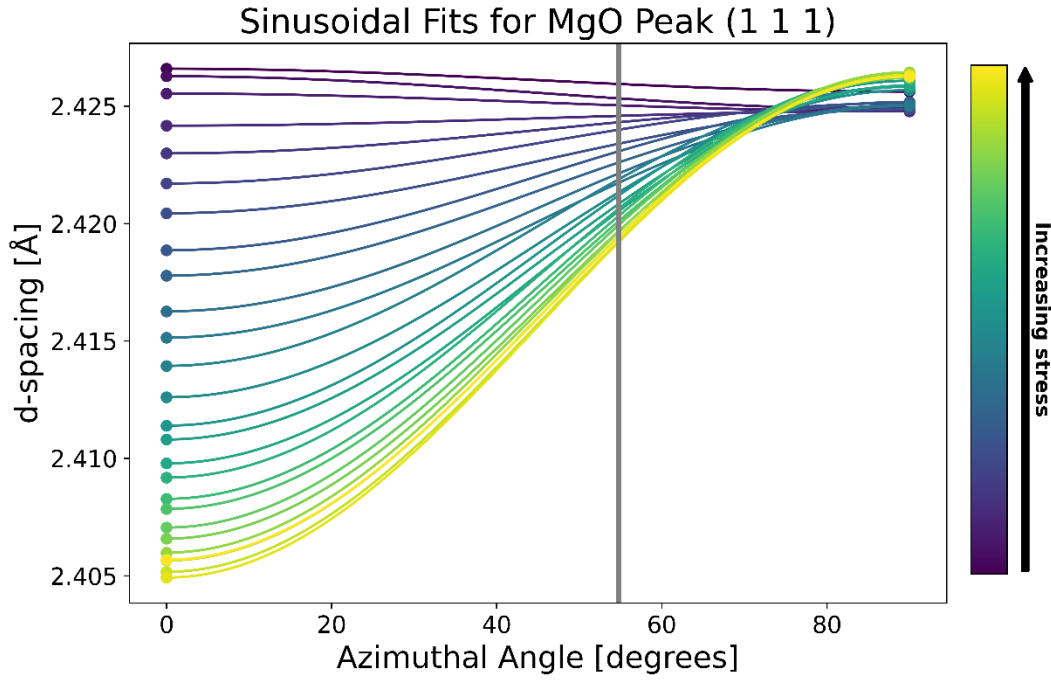


**Figure 47.** An example of the sinusoidal distribution of the d-spacings as measured at detector D1 ( $0^\circ$ ) and D2 ( $90^\circ$ ). The data was measured on MgO undergoing deformation with no heating. The gray vertical line represents the ‘magic angle’ of  $54.74^\circ$ . This defines the d-spacing of the MgO assuming hydrostatic conditions.

Eq. 104 — Eq. 106 describe the sinusoidal function for the case where d-spacings are provided by only two detectors, at azimuthal angles of  $0^\circ$  and  $90^\circ$ .

$$d_{hkl}(\psi) = A \cos(2\psi) + B \quad \text{Eq. 104}$$

$$A = \frac{d_{hkl}(0^\circ) - d_{hkl}(90^\circ)}{2} \quad \text{Eq. 105}$$

$$B = \frac{d_{hkl}(0^\circ) + d_{hkl}(90^\circ)}{2} \quad \text{Eq. 106}$$

## 2. Methods

In **Figure 47** the sample of polycrystalline MgO is being deformed uniaxially and as the stress increases, the d-spacing at the azimuthal angle of  $0^\circ$  shows decreases, while the value at  $90^\circ$  shows a slight increase. The hydrostatic pressure at which the sample is being deformed can be determined by the d-spacing at the ‘magic angle’ (Guignard & Crichton, 2015) azimuth of  $54.74^\circ$ , where the deviatoric contribution to the lattice strain vanishes (Duffy, Shen, Shu, et al., 1999). This is derived by solving for  $\psi$  in this relation:  $(1 - 3 \cos^2(\psi)) = 0$ . For the experiments at P61B, MgO was used as the pressure standard for all runs. The d-spacing of the sinusoidal wave at  $54.74^\circ$  azimuth was used in a 3<sup>rd</sup> order Birch-Murnaghan (3BM) (Birch, 1978) equation of state to calculate the experimental hydrostatic pressure.

$$P(V) = \frac{3B_0}{2} \left[ \left( \frac{V_0}{V} \right)^{7/3} - \left( \frac{V_0}{V} \right)^{5/3} \right] \left\{ 1 + \frac{3}{4} (B'_0 - 4) \left[ \left( \frac{V_0}{V} \right)^{2/3} - 1 \right] \right\} \quad \text{Eq. 107}$$

Where  $P$  is pressure,  $V$  is compressed volume,  $B_0$  is the bulk modulus,  $B'_0$  is the derivative of the bulk modulus with respect to pressure, and  $V_0$  is the 1 bar reference volume (Birch, 1978). Eq. 107 calculates the pressure at room temperature, to which a thermal pressure correction is added (Tange et al., 2009). The equation of state parameters for MgO used in the thermal pressure-corrected 3BM are listed in **Table 5**.

**Table 5.** EOS parameters for MgO used to calculate the hydrostatic pressures in some of the runs.  $V_0$  was calculated from a 1 bar XRD taken of MgO at the start of every experiment.  $V_0$ : reference 1 bar volume;  $K_{T0}$ : reference isothermal bulk modulus;  $\Theta_0$ : reference Debye temperature;  $\gamma_0$ : reference Grüneisen parameter;  $a, b$ : volume-independent adjustable parameters. Values from (Tange et al., 2009).

$V_0$ [ $\text{\AA}^3$ ]	$K_{T0}$ [GPa]	$K'_{T0}$	$\Theta_0$ [K]	$\gamma_0$	$a$	$b$
From XRD	160.64(18)	4.221(11)	761(13)	1.431(14)	0.29(4)	3.5(5)

All XRD patterns were fitted peak-by-peak using Pseudo-Voigt profiles with the software *PDIndexer* (Yusuke, 2010), if the patterns were clean enough for automated sequential analysis, or *PeakPo* (S.-H. Dan Shim, 2022) if they were not and required manual fitting. Since the piezoelectric stress measurement technique determines only the changes in stress, rather than absolute values, the initial deviatoric stress state needs to be normalized. The curve is then offset so the first measurement point begins at this normalized initial stress state. When comparing with XRD-derived stress measurements, since the XRD technique can measure absolute stress, the piezoelectrical stress measurement data was normalized to match the first

## 2. Methods

XRD stress point. This initial stress state is unknown for deformation experiments where XRD was not performed and in those cases, the initial deviatoric stress state is assumed to be 0 MPa. This is quite reasonable if the sample is initially annealed at high temperature to relax stresses prior to deformation.

The samples deformed at P61B are synthetic Mg-Al spinel ( $\text{MgAl}_2\text{O}_4$ ), synthetic MgO, and natural San Carlos olivine ( $\alpha\text{-(Mg,Fe)}_2\text{SiO}_4$ ).

### 2.4.3. P61B anvils and pressure/temperature calibration

Since the anvils used at BGI are tungsten carbide, they would attenuate the x-ray beam almost completely when used at the beamline and under high pressures because the gap between the anvils, sustained by the pyrophyllite gaskets, becomes too small to allow a  $5^\circ$   $2\theta$  diffracted beam angle in the horizontal direction.  $5^\circ$  was chosen because the beamline has Pb X-ray emission lines at 74.97 KeV ( $K_{\alpha 1}$ ), 72.80 KeV ( $K_{\alpha 2}$ ), and 84.94 KeV ( $K_{\beta}$ ) and  $5^\circ$   $2\theta$  placed these in the least intrusive position relative to the sample peaks (Jonnard & Bonnelle, 2011). To overcome the attenuation issue, custom anvils were machined.

Polycrystalline diamond (PCD) is an ideal material choice for this purpose as it has similar or higher strength than WC anvils but because it mainly consists of polycrystalline diamond, it attenuates x-rays much less than WC. For this reason, WD960C wire drawing blanks were purchased from Sumitomo Electric Carbide, Inc. These are polycrystalline diamond wire drawing blanks with a metal binder supported by a pressure fitted outer steel ring. The PCD is  $\sim 92\%$  polycrystalline diamond with the rest being the metal binder. A side view of the anvil is shown in **Figure 48**.

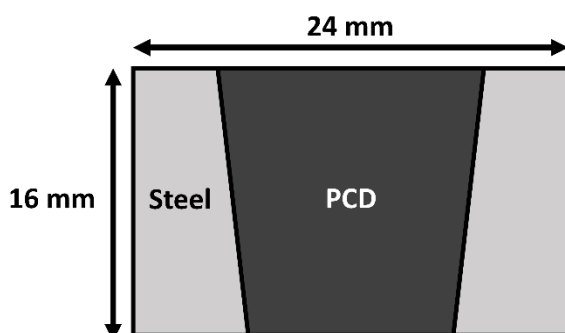


**Figure 48.** The WD960C wire drawing blank, as received from Sumitomo. The outer steel pressure ring and PCD are shown in a cross section. The PCD diameter change through the blank is exaggerated. In reality, it only varies by 3%. The wider diameter of the PCD is 16 mm.

## 2. Methods

The WD960C wire drawing blank had to be machined further into a 15/10 anvil. One end was truncated to a 10 mm square, with the sides cut down at a 45° angle. The Aster-15 LVP press can be rotated along the vertical axis by  $\pm 15^\circ$ . During XRD acquisition, the press is rotated, usually only  $\pm 3^\circ$  around this axis. This rotation allows the x-ray beam to diffract a larger number of crystallites within the sample and improves the pattern quality. To allow for this rotation, the PCD anvils had one side cut down, or ‘shaved off,’ more than the other three sides. The drawing of the final anvil after machining, including this extra cut, is shown in **Figure 49**.

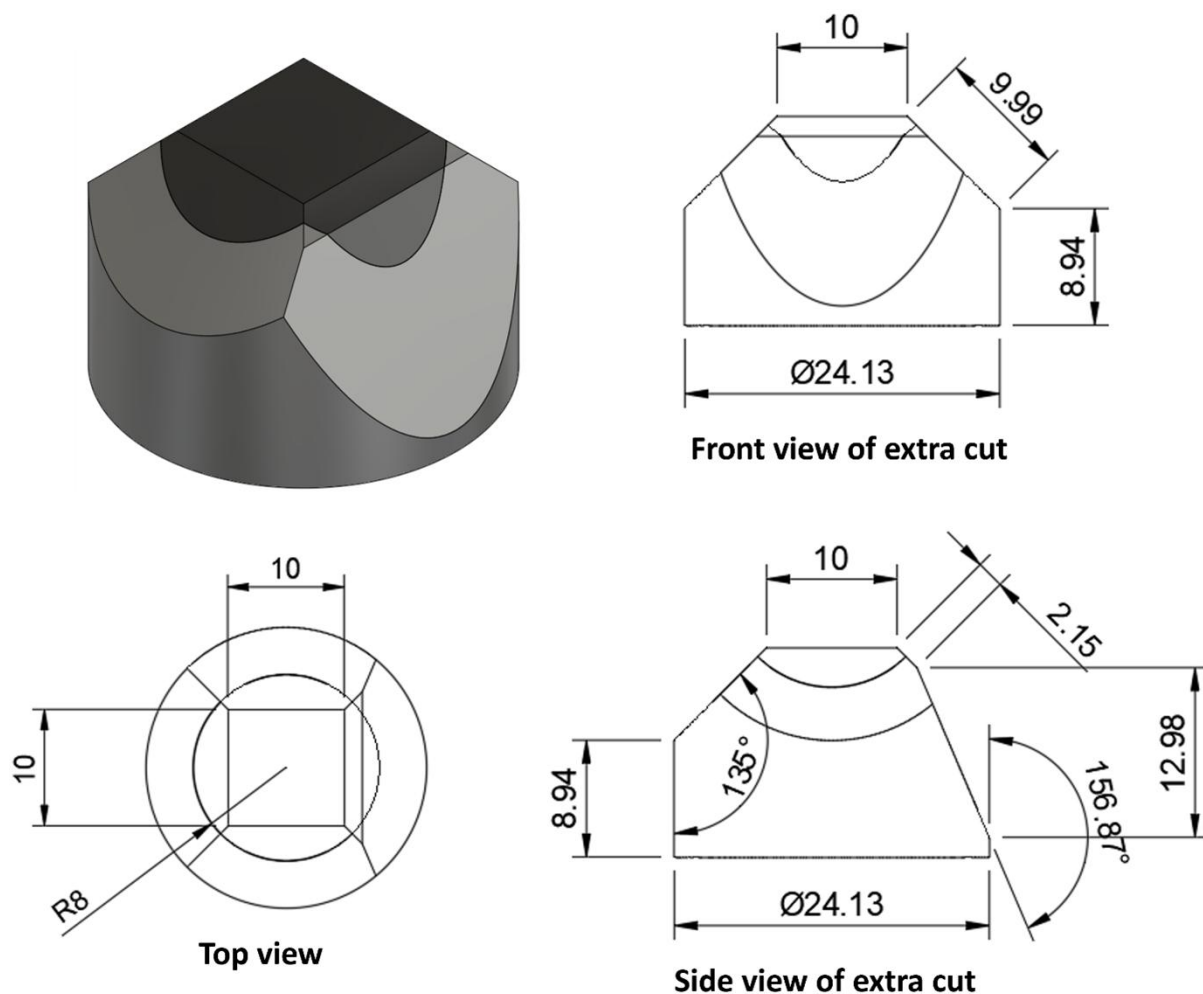


**Figure 49.** Schematic drawing of the final PCD anvil after machining. The darker gray is the PCD and the lighter gray is the pressure fit steel ring. Notice that one side has a deeper side cut to allow for a wider x-ray diffraction angle.

The assembly for P61B required only two of these PCD anvils. The other 4 can be typical WC anvils supplied by Hawedia GmbH. The WC supplied is type ha-co6%, which means it contains 6% cobalt as a binder. The schematic drawing for these anvils is shown in **Figure 50**. These

## 2. Methods

were cut to the same dimensions as the PCD anvil except for the extra side shaved off. The arrangement of the two PCD anvils was chosen to allow for the greatest possible angle of rotation. One was placed upstream of the beam with the shaved-off side facing the beam and the other was placed downstream of the beam with the shaved-off side facing the beam but from the other direction.

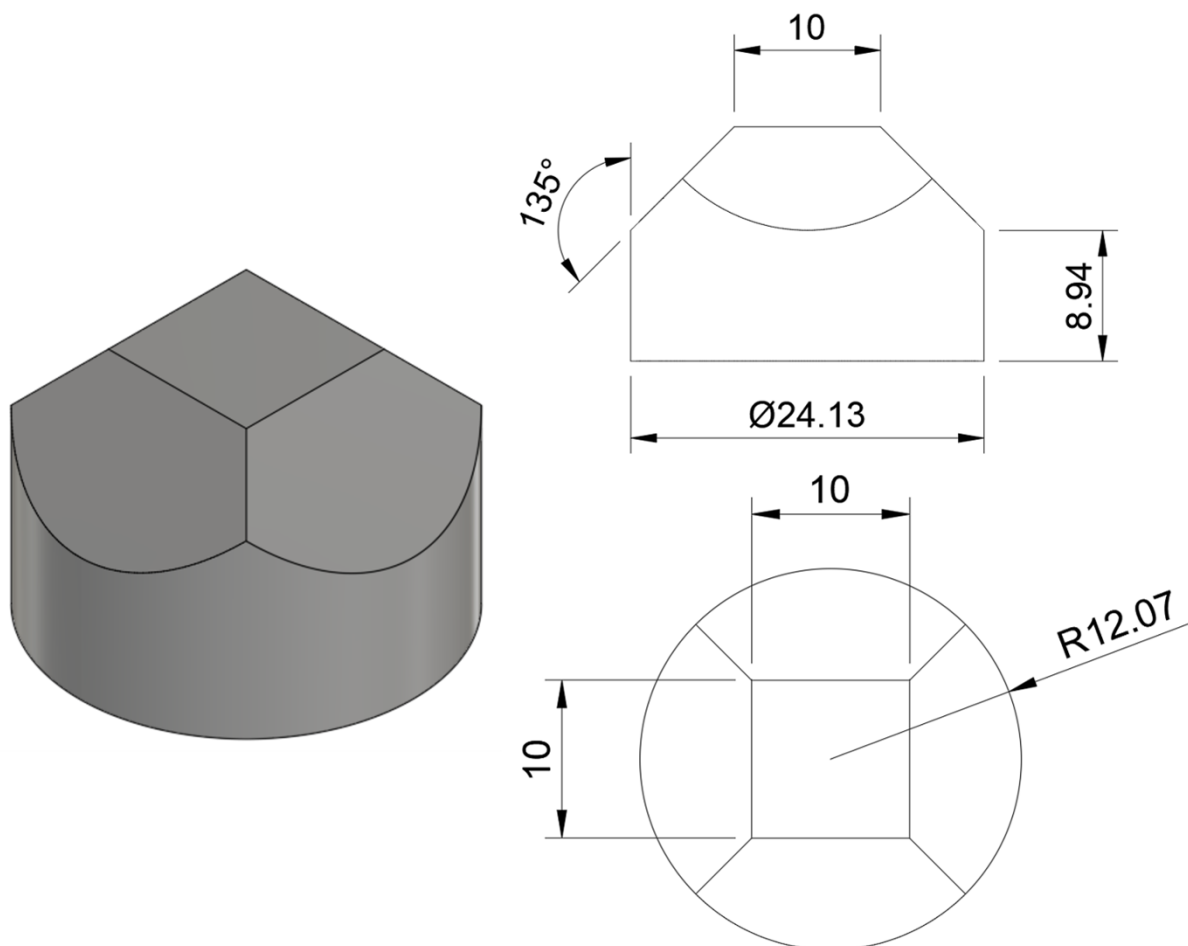


**Figure 50.** Schematic drawing of the WC anvils used for synchrotron experiments. Supplied by Hawedia. Contains 6% cobalt as a binder.

As shown, two PCD anvils are positioned upstream and downstream, allowing for maximum rotational range of the press. The render displays the 1 bar arrangement, where the gaskets are relatively uncompressed. At high pressures, however, the gaskets collapse significantly, and the gaps between the anvils shrink dramatically. Under these conditions, the rotational range is limited to  $\pm 3^\circ$  rotation range only. With the D2 detector placed horizontally at an azimuthal angle of  $90^\circ$  and a  $2\theta$  angle of  $5^\circ$ , the gap at high pressure allows for a minimum  $2\theta$  of  $8^\circ$

## 2. Methods

towards the D2 detector, with less rotation available on the opposite side. The D1 detector, vertically positioned at an azimuthal angle of  $0^\circ$ , is unaffected by the anvil gap.

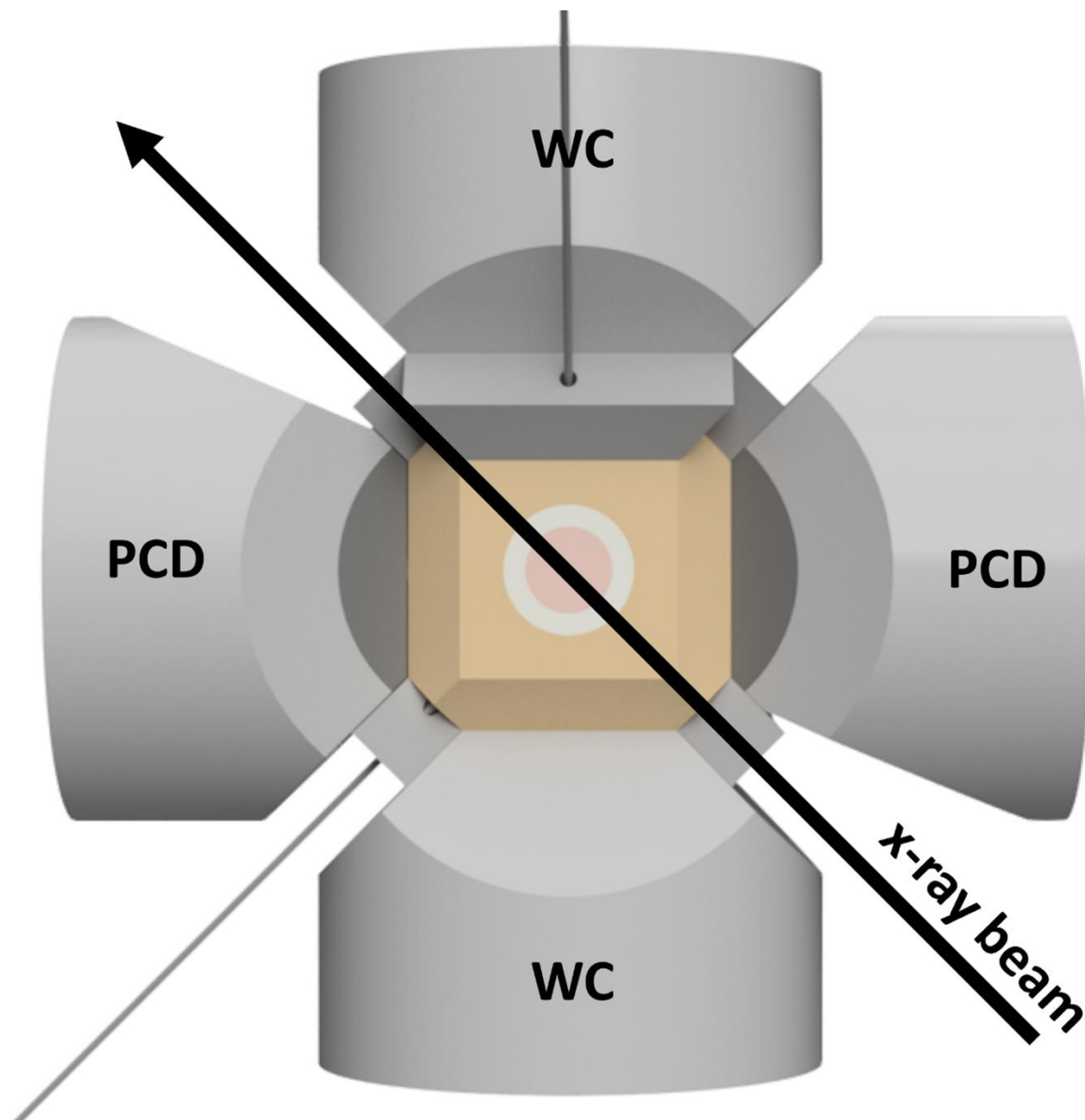


**Figure 51.** An equatorial cross-sectional view of the arrangement of the anvils for the P61B assembly. The x-ray beam is labeled, as well as the materials of the anvils shown. The top and bottom anvil are not shown for clarity. The two thin wires are the piezoelectric wires as they exit the assembly through the gaskets.

Due to the ASTER-15 LVP showing an open circuit anvil-to-anvil resistance of approximately  $20\text{ M}\Omega$ , the anvils were fully covered with polyimide film tape, except for the areas under the gasket and on the front truncation.

## 2. Methods

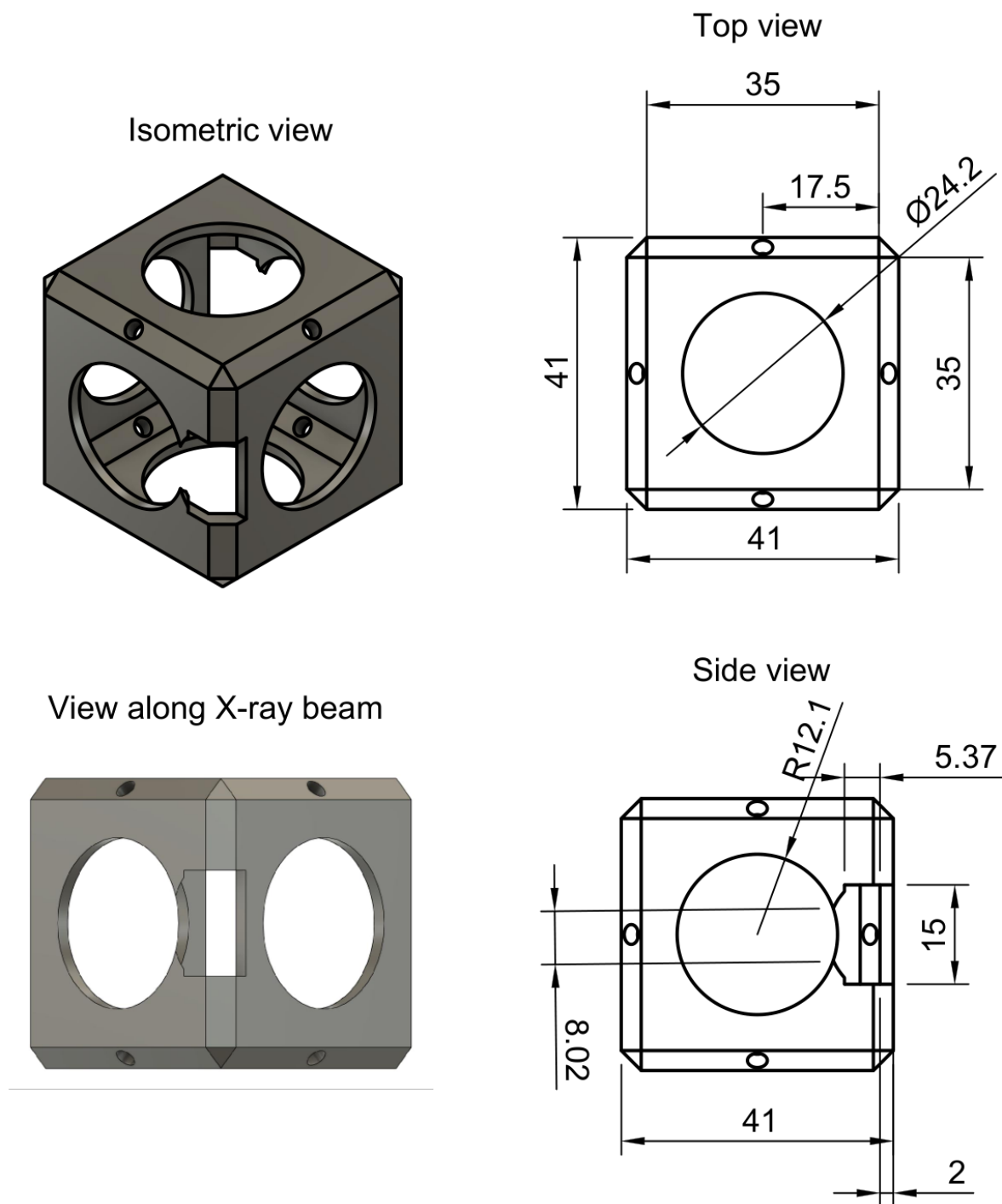


**Figure 52.** Views and drawings of the 3D printed plastic alignment cage for the DESY P61B beamtimes. The slots cut out along the X-ray beam are to limit X-ray absorption. The holes on the edges are for the electrode wires. The wall thickness of the alignment cage is 2 mm. All units shown are in mm.

## 2. Methods

To conduct current for the heating furnace, aluminum foil was placed on the backs of the two WC anvils. The anvils were aligned and held in place using a 3D-printed plastic alignment cage. Since the temperature of the anvils and the alignment cage can exceed 150 °C during heating, stereolithography (SLA) printing with standard resin was chosen to prevent melting, which would occur with a fusion deposition modeling (FDM) printer. The alignment cages were printed using a Phrozen Sonic XL 4K LCD SLA 3D printer with ABS-like resin. Portions of the alignment cage were cut away along the X-ray beam path to avoid shadowing in the radiography image, despite the plastic's low molecular mass and expected low X-ray absorption. The dimensions and design of the alignment cage are shown in **Figure 52**.

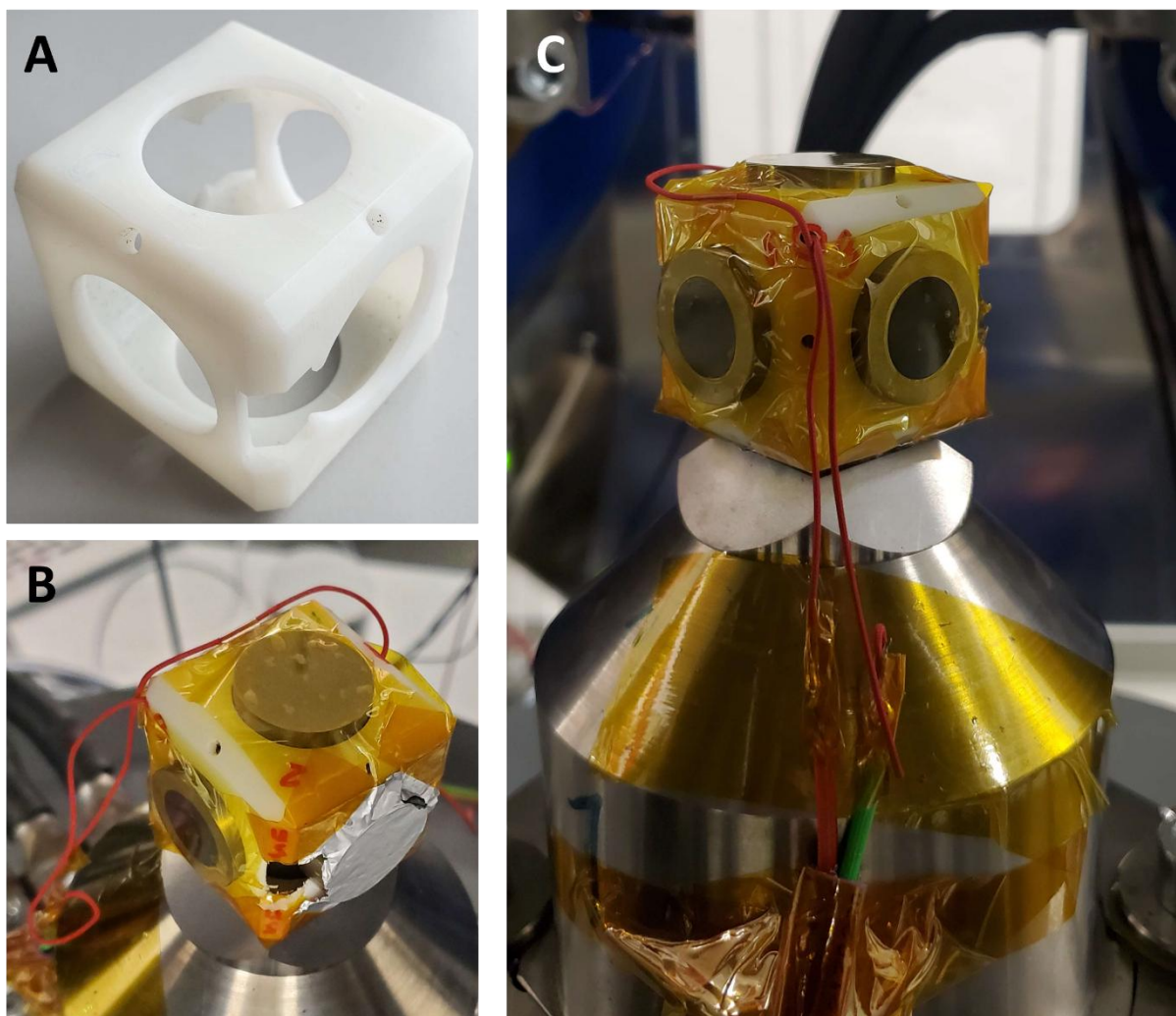


**Figure 53.** Pictures taken of the assembly at the P61B beamtimes at DESY, PETRA-III. (A) shows the SLA resin 3D printed alignment cage with extra holes cut through two opposite edges where the x-ray beam passes through. (B) shows a top view of the completed and ready assembly before compression. The aluminum foil placed on a WC anvil for heating is shown. The two red wires are for the piezoelectric crystal. (C) shows the assembly from a front view.

## 2. Methods

*Two PCD anvils are shown facing the camera. The two red wires, connected to the piezoelectric crystal, are soldered to the wires from the well-shielded cable.*

Pictures of the 3D printed alignment cage and PCD anvils are shown in **Figure 53**. Notice the generous use of polyimide tape on the outside of the anvils to eliminate the low resistance measured between the first stage anvils of the ASTER-15 LVP. The 3D printed alignment cage was found to be re-usable multiple times even though after runs it had slight yellowing and embrittlement due to the elevated temperatures.

Since the ASTER-15 LVP press has a lower maximum force of 5 MN per ram (versus 8 MN for the MAVO press at BGI), the relation of oil pressure to force per ram is different. This had to be corrected. For all experiments, the oil pressure to sample pressure calibration curves were obtained from Sano-Furukawa, A. *et al* (Sano-Furukawa et al., 2014), with calibration experiments conducted using time-of-flight (TOF) neutron diffraction measurements on NaCl. The six-axis press used for the calibration by Sano-Furukawa, A. *et al*, ATSUHIME, is installed at the high-pressure neutron beamline (PLANET) at BL11 of the spallation neutron source of the Materials and Life Science Experimental Facility (MLF) at the Japan Proton Accelerator Research Complex (J-PARC). The exact calibration points were provided by Dr. Sano-Furukawa through private communication. While the XRD experiments contained MgO for *in situ* pressure determination, it was decided to use the Sano-Furukawa *et al* (2014) calibration curves even at the synchrotron. This decision was made to ensure consistency and comparability with the experiments conducted off the beamline at BGI, which also utilized the Sano-Furukawa calibration.

## 2. Methods

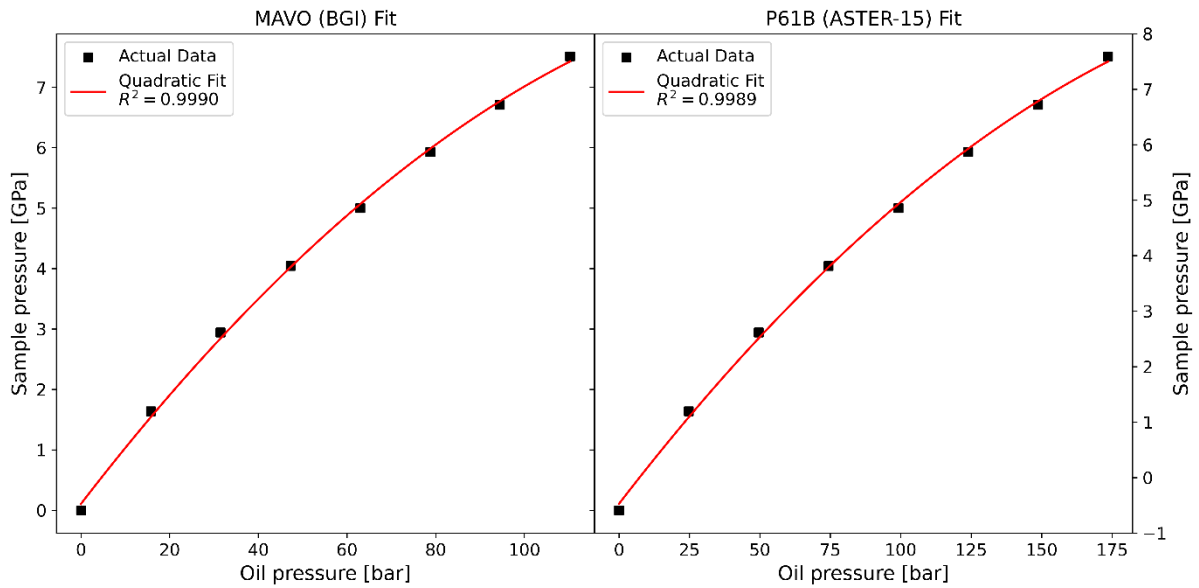


**Figure 54.** Calibration data for the MA6-6 15/10 cubic assembly from Sano-Furukawa, A. et al. (Sano-Furukawa et al., 2014). The curves have been fitted with a quadratic equation and the goodness of fit is shown below them. The left plot is for the MAVO press at BGI and the right plot is for the P61B ASTER-15 press at DESY.

The quadratic equation used to fit both data points is provided in Eq. 108 along with the table of fitting parameters used for both curves. In the equation,  $P_h$  is the sample hydrostatic pressure and  $P_o$  is the ram oil pressure.

$$P_h = a \cdot P_o^2 + b \cdot P_o + c \quad \text{Eq. 108}$$

**Table 6.** Fitting parameters used in Eq. 108 for the MAVO and ASTER-15 press

Press	$a$	$b$	$c$
MAVO (BGI)	$-2.616 \times 10^{-4}$	$9.524 \times 10^{-2}$	$1.062 \times 10^{-1}$
P61B (ASTER-15)	$-1.056 \times 10^{-4}$	$6.049 \times 10^{-2}$	$1.076 \times 10^{-1}$

Since the deformation experiments at the P61B beamline at PETRA-III synchrotron did not contain a thermocouple in the assembly, the temperature versus power relationship that was previously found through calibration runs made using a thermocouple, displayed in **Figure 31**, was used to determine the required power level for heating in watts. Since the power to temperature relation varies with the sample hydrostatic pressure, 2<sup>nd</sup> order surfaces were fit to the sample pressure and heating power to allow for calculation of the expected sample and piezoelectric crystal temperature. This was done for both the MAVO press at BGI and the

## 2. Methods

ASTER-15 press at P61B. The results of these fits, for all four combinations of two presses and two temperature locations, is shown in **Figure 55**.

### Sample pressure and heating power 2<sup>nd</sup> order surface fits to temperature

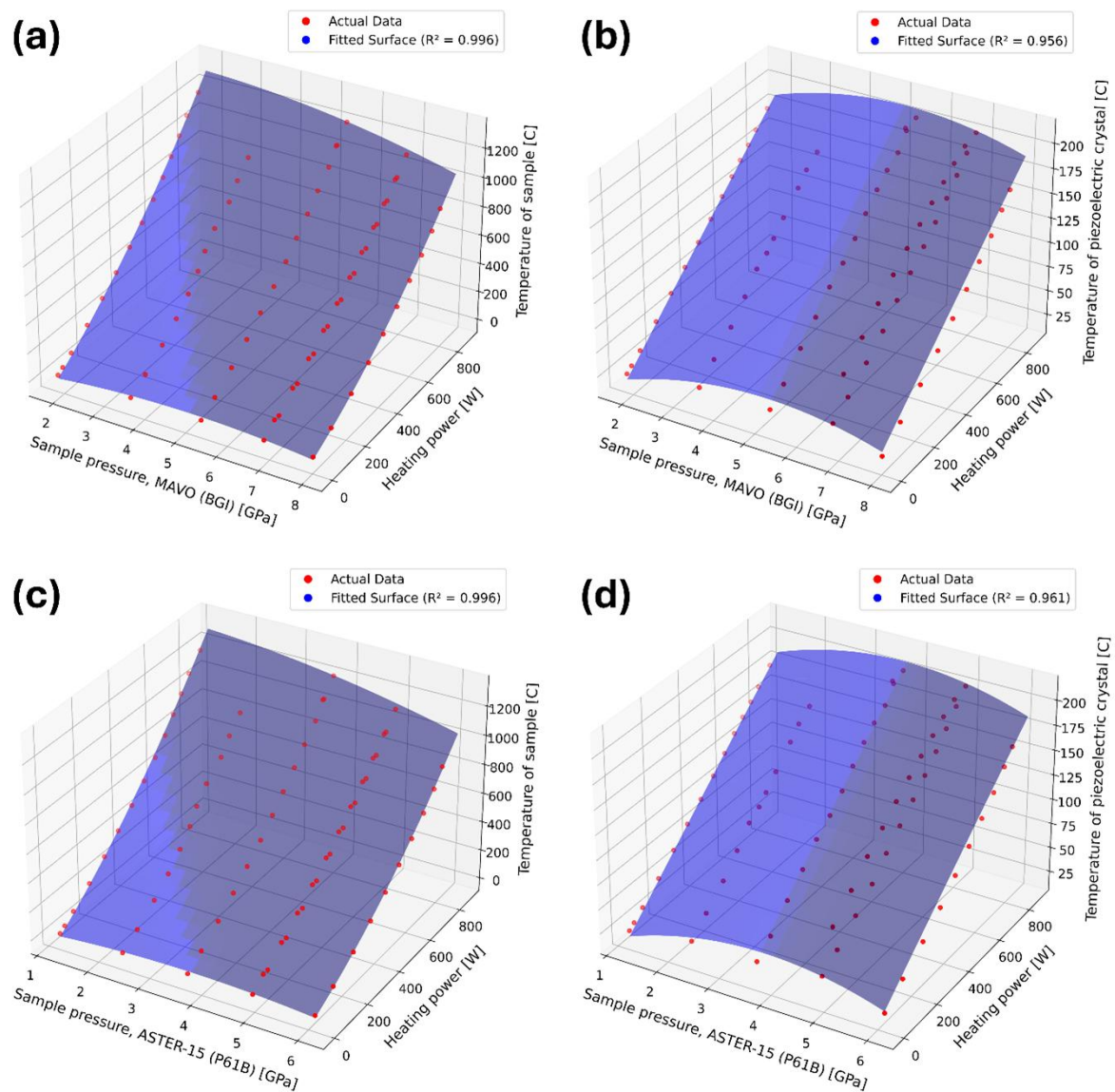


**Figure 55.** The 2<sup>nd</sup> degree surface fits to the power, temperature, and pressure relations derived from calibration experiments at BGI for power/temperature and Sano-Furukawa et al. (Sano-Furukawa et al., 2014) for ram force to sample pressure. (a) is the sample pressure (MAVO, BGI) to sample temperature, (b) is the sample pressure (MAVO, BGI) to piezoelectric crystal temperature, (c) is the sample pressure (ASTER-15, P61B) to sample temperature, and (d) is the sample pressure (ASTER-15, P61B) to piezoelectric crystal temperature.

## 2. Methods

The  $R^2$  of the fit is shown in each legend for all four fits. The generalized equation to fit the surfaces is presented below in Eq. 109.

$$f(x, y) = ax^2 + by^2 + cxy + dx + ey + f \quad \text{Eq. 109}$$

Table 7. The parameters for the 2<sup>nd</sup> order surface fit to the sample hydrostatic pressure for both the MAVO press at BGI and the ASTER-15 press at P61B, and the temperature of the sample and piezoelectric crystal (PZE) are listed below. For all cases,  $y = \text{power [W]}$ .

	$a$	$b$	$c$	$d$	$e$	$f$
$x = \text{P (MAVO) [GPa]}$ $f(x, y) = \text{T (sample) [}^\circ\text{C]}$	$-5.413 \times 10^0$	$5.384 \times 10^{-4}$	$-4.910 \times 10^{-2}$	$5.383 \times 10^1$	$1.129 \times 10^0$	$-8.127 \times 10^1$
$x = \text{P (MAVO) [GPa]}$ $f(x, y) = \text{T (PZE) [}^\circ\text{C]}$	$-2.268 \times 10^0$	$-2.671 \times 10^{-6}$	$-1.026 \times 10^{-3}$	$2.390 \times 10^1$	$1.977 \times 10^{-1}$	$-1.800 \times 10^1$
$x = \text{P (ASTER-15) [GPa]}$ $f(x, y) = \text{T (sample) [}^\circ\text{C]}$	$-6.983 \times 10^0$	$5.300 \times 10^{-4}$	$-6.430 \times 10^{-2}$	$5.180 \times 10^1$	$1.119 \times 10^0$	$-4.991 \times 10^1$
$x = \text{P (ASTER-15) [GPa]}$ $f(x, y) = \text{T (PZE) [}^\circ\text{C]}$	$-3.941 \times 10^0$	$-4.510 \times 10^{-6}$	$-1.361 \times 10^{-3}$	$3.039 \times 10^1$	$1.985 \times 10^{-1}$	$-1.309 \times 10^1$

The parameters  $a, b, c, d, e,$  and  $f$  are presented for each of the four plots in Table 7. The first row represents the surface in **Figure 55** (a), the second row (b), third (c), and fourth row (d). All equations solve for the sample or piezoelectric crystal temperature in  $^\circ\text{C}$ . These equations were used at the beamline to target specific pressures and temperatures. Generally, XRD patterns were integrated for 30 – 60 seconds dependent on a qualitative evaluation of the pattern. Diffraction patterns of the sample to pressure marker, i.e. MgO, ratio was roughly 5:1. In other words, generally 5 XRD patterns of the sample were taken for every 1 MgO diffraction pattern for hydrostatic pressure derivation.

### 2.4.4. Strain measurement at the beamline

At the synchrotron, in situ strain determinations were made possible through x-ray radiography, which imaged the entire deformation column, capturing the full anvil-to-anvil length. Vertical scans were performed before and after deformation, allowing the column to be imaged in sections. These scans were aligned and stitched together based on the vertical positioning of the press, controlled by motor stages, enabling precise strain calculations across both the sample and the assembly components.

However, significant absorption-induced heating by the bright x-ray beam at PETRA-III, particularly when fully opening the slits for imaging, precluded real-time imaging during deformation cycles. This heating caused large and sudden voltage drifts in the signal. Although the exact mechanism remains unclear, one plausible explanation is that high-energy photons,

## 2. Methods

such as x-rays, induce electron emission from metal components in the experimental setup. When high-energy photons strike the surface of a metal, they can eject electrons in a process known as the photoelectric effect (Vartanyants & Zegenhagen, 1999). This occurs when the energy of the incoming photon exceeds the work function of the metal—i.e., the energy required to release an electron from the metal’s surface. The ejected electrons can then accumulate on nearby electrodes or surfaces, generating unintended charge signals that can mimic those produced by the piezoelectric crystal during deformation.

Another contributing factor to the signal drift could be the substantial temperature increase due to x-ray heating, which as discussed previously alters the crystal’s electrical resistivity.

Because of these factors—both the photoelectric effect and temperature-induced signal drift—strain measurements via x-ray radiography were limited to pre- and post-deformation phases

Image analysis involved pixel integration perpendicular to the scanning direction, with logistic function fitting applied to the integrated pixel plot edges, representing the boundaries of different assembly parts within the column as described by Eq. 110.

$$f(x) = \frac{L}{1 + e^{-k(x-x_0)}} + b \quad \text{Eq. 110}$$

$$0 = f(x) - \left(\frac{L}{2} + b\right) \quad \text{Eq. 111}$$

To delineate assembly part boundaries, Eq. 111, simplified to identify the pixel value  $x$  at the curve's half-maximum adjusted for offset  $b$ , was numerically solved for  $x$ . This process, by solving for  $x$ , precisely and consistently marked boundary pixel values between assembly components to eliminate human bias in boundary edge selection. An example of the custom-built software to identify the assembly boundaries is shown in **Figure 56**.

In the top plot the horizontal axis is the pixel value across the deformation column and the vertical axis is the intensity as a result of the integration of pixel brightness. The saw-tooth like pattern in the integrated pattern is due to a brightness gradient in the X-ray image. For each individual image taken as part of the scan, this is visible as a sharp intensity jump. These are artifacts of the X-ray camera and not physical density variations within the sample. To convert pixel values to physical distance, the pixel size of the x-ray radiography camera present at P61B was used, i.e., each pixel is 1.44  $\mu\text{m}$  (Farla et al., 2022).

## 2. Methods

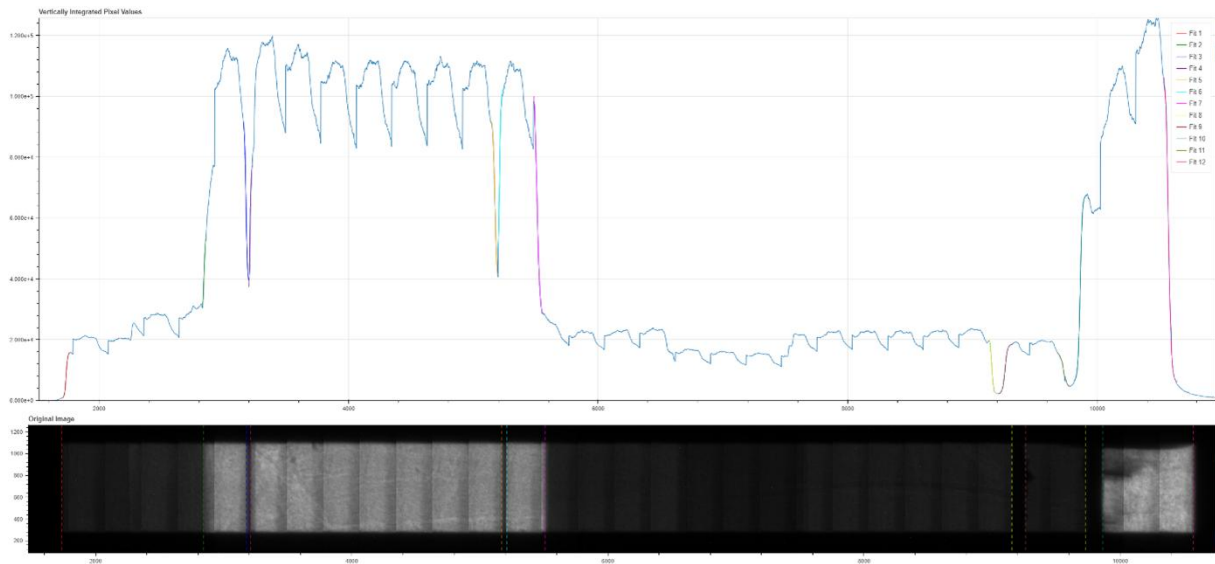


**Figure 56.** A screenshot of the custom-built software, developed by the author, used to fit the boundary edges with logistic functions. The top plot shows, with a blue line, the integrated pixel values of the bottom image. The logistic functions are locally fitted to the rising and falling edges, shown with differently colored lines. On the bottom image, the  $x$  position of each logistic function's half-maximum position is shown with dashed lines. These lines define the part boundaries. The horizontal axis is pixel number and the vertical axis is integrated pixel values on the top plot and vertical pixel count on the bottom image.

For all experiments with pre- and post-deformation x-ray radiography image scans, the strain measurements of each assembly part will be reported using the keys labeled in the image in **Figure 57**.

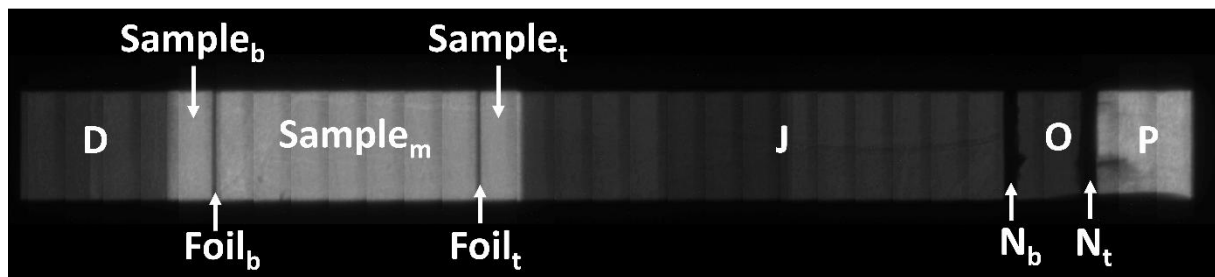


**Figure 57.** An x-ray radiography image of an assembly column at high pressure, with the keys used to label the part strains within the assembly column.  $Sample_m$ , between  $Foil_b$  and  $Foil_a$  in the image, is 3.7 mm in length.

## 2. Methods

**Table 8.** Description of the keys used in labeling the strain measurements of each part, as shown in **Figure 57**.

Key	Part	Material
D	Bottom plug	Porous zirconia
Sample <sub>b</sub>	Bottom sample disk	Sample
Foil <sub>b</sub>	Bottom strain marker	Gold foil
Sample <sub>m</sub>	Sample	Sample
Foil <sub>t</sub>	Top strain marker	Gold foil
Sample <sub>t</sub>	Top sample disk	Sample
J	Top plug	Non-porous zirconia
N <sub>b</sub>	Bottom piezoelectric electrode	Copper
O	Piezoelectric crystal	CTGS
N <sub>t</sub>	Top piezoelectric electrode	Copper
P	Heat sink disk	Diamond

This short-hand labeling is used as a key to represent the specific assembly parts which largely will follow the naming convention described previously in **Table 3**. The full key label descriptions are provided in **Table 8**. All strains calculated are engineering strains according to Eq. 112, where  $L_f$  is the final length and  $L_0$  is the initial length.

$$\varepsilon = \left( \frac{L_f - L_0}{L_0} \right) \cdot 100\% \quad \text{Eq. 112}$$

### 2.5. Brillouin spectroscopy of CTGS at high pressure

A DAC consists of two conical diamonds with the tips flattened to produce two culets, which generally range in diameter from 50 to 500  $\mu\text{m}$ . By pressing the two diamond culets together by tightening the screws of a retainment frame, the area between the two culets is placed under extremely high pressures. As pressure is force over an area, the small area ensures that high pressures can be reached with moderate forces. The pressure chamber between the diamonds is sealed radially with a thick metal foil called a gasket. As the diamonds are pressed together, they extrude the metal gasket and the shear friction between the gasket and the diamonds as well as the tensile strength of the gasket itself seals the high-pressure chamber (Jayaraman, 1983; O'Bannon et al., 2018).

## 2. Methods

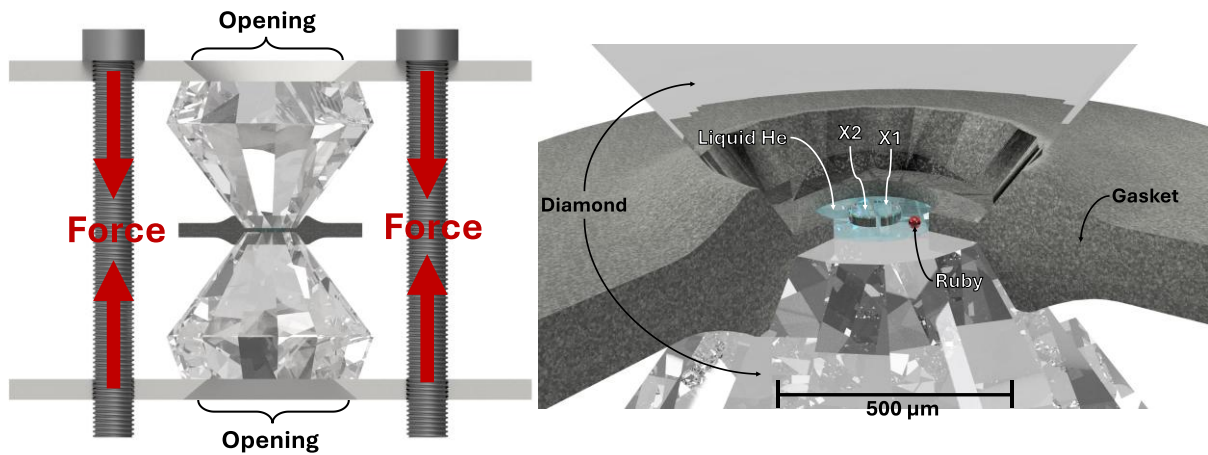


**Figure 58.** Computer renders of the working principle of a DAC on the left and a cross-sectional close-up view of the sample chamber on the right between the diamond culets.

Using a DAC with below 100 µm culets, static hydrostatic pressures beyond that of the center of the Earth are achievable (Dubrovinsky et al., 2012; O’Bannon et al., 2018). For this work, however, since the pressures needed are much lower, diamonds with 500 µm culets were used. The operating principle of the DAC is illustrated in **Figure 58**. The diamonds are pressed together, culet-to-culet, using screws that tighten two opposing frame segments in which the diamonds are fixed. Within the frame holding the diamonds together, an opening is made so that the sample chamber can be viewed through the transparent diamonds. This also allows for optical measurements, such as Raman and Brillouin spectroscopy, to be made, as well as XRD measurements, since diamond has low x-ray absorption (Heismann et al., 2003). The figure also shows a close-up cross-sectional view of the sample chamber on the right. The diamonds are held a few tens of microns apart by the extruded gasket, usually above  $\geq 30$  µm in a 500 µm DAC.

To ensure hydrostatic conditions within the sample chamber and thus eliminate deviatoric stress effects on the sound velocity measurements, helium is loaded into the sample chamber before closing. He was chosen because it remains a liquid up to 11.6 GPa (Zha et al., 2004). Inside the chamber, the two crystal platelets are placed onto the diamond surface and a small crystal of ruby is also added. The wavenumber shift of the ruby R1 luminescence line is commonly used as a pressure standard (Hawke et al., 1974; L. Lei et al., 2013; Yamaoka et al., 2012). By taking fluorescence spectrum of the ruby, the peak can be fitted with a pseudo-Voigt peak and the peak location used to measure the sample chamber pressure during experiments.

## 2. Methods

Raman spectroscopy is similar to Brillouin spectroscopy but measures the optical branches of the dispersion relation curves. Since Eq. 80 has a density term, the density of CTGS is required and was measured at every pressure point with XRD. XRD was also used to determine the exact platelet orientation with respect to the laboratory frame of reference. The XRD patterns were characterized at BGI and the peaks used to calculate the lattice parameters according to Eq. 113 (Powell, 2010; Patterson & Bailey, 2018). These are then used to calculate the unit cell volume using Eq. 114 (Patterson & Bailey, 2018) and thus the density of the crystal using the known chemical formula.

$$\frac{1}{d_{hkl}^2} = \frac{4}{3} \left( \frac{h^2 + hk + k^2}{a^2} \right) + \frac{l^2}{c^2} \quad \text{Eq. 113}$$

$$V = \frac{\sqrt{3}}{2} a^2 c \quad \text{Eq. 114}$$

As mentioned previously, since CTGS has 6 independent elastic stiffness coefficients, two crystal platelets are required to solve the full tensor (Calderon et al., 2007). A CTGS crystal that is typically used in deformation experiments and comes pre-oriented by the manufacturer was utilized for this purpose. Two platelets, labeled X1 and X2 were cut and double-polished from the main, larger crystal. The orientation of the two platelets relative to the parent crystal is shown in **Figure 59**. X2 was chosen to have a normal parallel to the crystals  $x$  direction, and X1 was cut perpendicular to this. The direction of the X1 normal was unknown beyond that it was perpendicular to X2. The platelets were double polished down to 20  $\mu\text{m}$  thickness. It was crucial to ensure that the platelets were thinner than the diamond culet gap, to avoid them bridging the diamond anvils and developing deviatoric stress or in the worst case getting crushed.

## 2. Methods

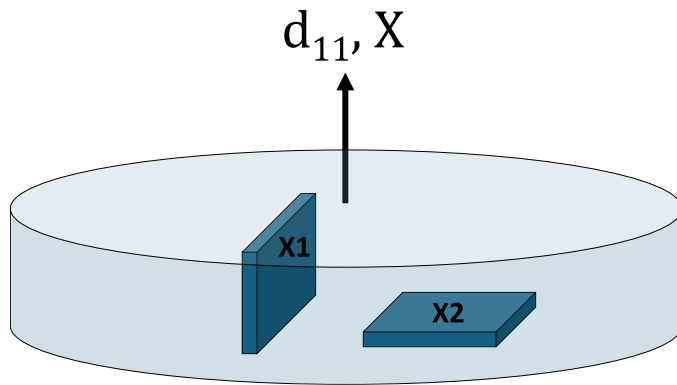


**Figure 59.** Orientation of cuts for the two platelets loaded into the DAC. They are labeled X1 and X2. The  $x$  direction of the crystal they were cut from is labeled, which is the same direction as the  $d_{11}$  piezoelectric vector and the  $a$  lattice parameter.

At this stage, the platelets were too large to load into the gasket chamber of the DAC, which was drilled to a 270  $\mu\text{m}$  diameter. Just as the platelets should not bridge the diamonds, they should also not come into contact with the gasket material to avoid issues of deviatoric stress. The initial irregular 20  $\mu\text{m}$  thick platelets, that were  $> 200 \mu\text{m}$  wide in some directions, were further milled to 100  $\mu\text{m}$  diameter half-circles using a FEI Scios focused ion beam (FIB) with a Ga ion beam, located at BGI. SEM images of the milled platelets for X1 and X2, after milling, as well as an optical microscope image of the two platelets loaded into the sample chamber of the DAC are presented in **Figure 60**. The top two images are of the platelets after ion beam milling and the bottom image is through a microscope. The optical microscope image is before He is loaded, so the DAC is open at 1 bar. After loading and compression, the gasket hole tends to shrink. This is expected and room was left around the crystals to allow for this. The image in **Figure 60** is taken before the ruby crystal was added into the DAC.

Brillouin spectroscopy data was acquired at BGI using the in-house system at 1 bar, and all subsequent higher-pressure spectra were acquired at DESY at the PETRA-III synchrotron in the Laser Laboratory, which is part of the PETRA-III P02.2 Extreme Conditions Beamline (Liermann et al., 2015). A simplified schematic plan of the Brillouin spectroscopy system at DESY is displayed in **Figure 61**, modified from (Speziale et al., 2014). The advantage of the platelet geometry is that the refractive index of the crystal is not required (Kojima, 2022; Polian, 2003; Speziale et al., 2014). Only the scattering angle must be measured and is labeled  $\theta$  in the figure.

## 2. Methods

For each pressure point, the process is as follows. Fluorescence spectrum is first measured on the ruby crystal to determine the chamber pressure 24 hours after the DAC pressure is increased to allow for relaxation of the gasket and diamonds, which can otherwise cause a drift in the pressure. Then, the DAC is placed in the goniometer and the system is aligned, as well as the photon counter channels calibrated. Brillouin spectra are collected on each crystal, X1 and X2, individually at  $10^\circ$   $\chi$  angle increments in the range  $0^\circ - 190^\circ$   $\chi$ . The excitation laser used at both BGI and DESY is an Nd:YVO<sub>4</sub> laser at 532 nm. After Brillouin measurements are performed on both crystals, XRD is collected on X1. This is done both for density determination but also to ensure the crystal orientations within the DAC chamber have not shifted as the crystal lattice orientation must be known when converting velocity curves along  $\chi$  to elastic coefficients. Then, the pressure is increased again to the next pressure point and the process is repeated. Since the hydrostatic pressures in deformation experiments in the LVP do not exceed 6 GPa, Brillouin spectroscopy measurements were made up to 10 GPa. Including 1 bar measurement, a total of 5 pressure points were collected on CTGS. The velocity curves are used to solve for the elastic tensor using Eq. 77—Eq. 80 using a custom routine implemented in OriginPro 2023 (OriginLab Corporation, Northampton, MA, USA). The routine solves for the best fitting elastic tensor using inversion models developed in Buchen (2018) using the OriginPro 2023 project provided by Dr. Johannes Buchen.

## 2. Methods

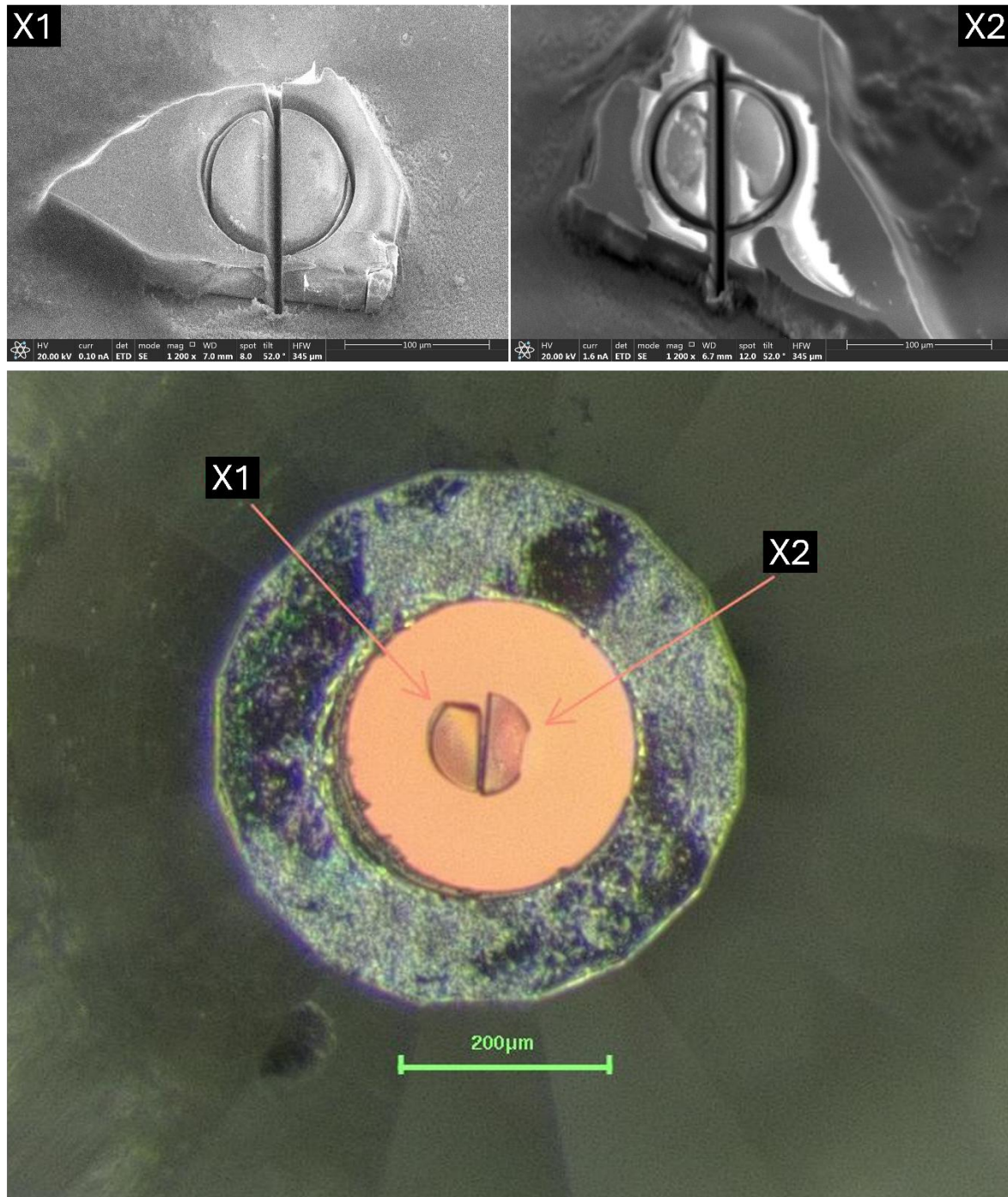


**Figure 60.** The top two images are of the platelets, X1 and X2, taken with the SEM as part of the ion milling process. The larger platelets have been milled into two circular hemispheres each. One hemisphere from both crystals is placed into the DAC chamber as shown in the bottom image, near each other. This image is taken through an optical microscope and is at 1 bar before He loading.

## 2. Methods

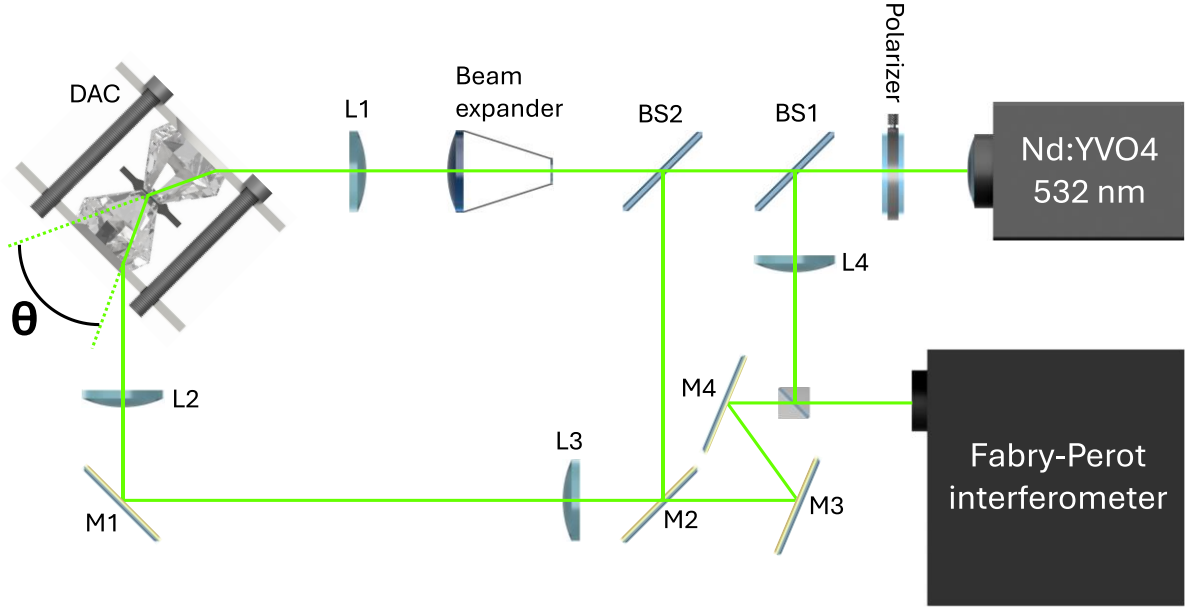


**Figure 61.** The Brillouin spectroscopy setup at DESY.  $L_x$  are lenses,  $M_x$  are mirrors,  $BS_x$  are beam splitters. Also labeled is the scattering angle in the DAC Brillouin setup.

Once the velocity dispersion points along  $\chi$  are collected, the velocity dispersion curves can be numerically fitted by repeatedly solving Eq. 80, in the OriginPro 2023 project functions provided by Dr. Johannes Buchen (Buchen, 2018), and varying the elastic stiffness coefficients. The bulk modulus,  $K$ , can be calculated using the coefficients according to Eq. 115, which is defined for point group 32 for the Voigt bound condition (Calderon et al., 2007; Sin'ko, 2008; Sotnikov et al., 2013; J. Wang et al., 2015).

$$K = \frac{C_{33}(C_{11} + C_{12}) - 2C_{13}^2}{C_{11} + C_{12} + 2C_{33} - 4C_{13}} \quad \text{Eq. 115}$$

Since the hydrostatic pressure within the DAC pressure chamber is known through ruby fluorescence measurements, the data points can be fit with a straight line to provide a first order approximation of the pressure trend. In this way, the pressure dependence of the elastic coefficients as well as the bulk modulus and density are calculated. Finite-strain equations are ultimately used to fit the data, as explained later.

### 2.6. Sample synthesis

The 15/10 MA6-6 cubic assembly used has a sample chamber that is 4 mm high and 4 mm in diameter. To be able to measure the sample strain in the x-ray diffraction experiments using x-

## 2. Methods

ray radiography, a sharp density contrast is necessary within the sample. To achieve this, the sample consisted of three pieces separated by 2  $\mu\text{m}$  thick gold foil, 4 mm in diameter. The bottom and top sample pieces were 0.5 mm tall, 4 mm in diameter. They were precisely cut to achieve high parallelism between the faces. The middle sample was 3 mm high. The total length thus was 4 mm. The smaller 0.5 mm tall samples were placed to allow for a better contrast ratio since the  $\text{ZrO}_2$  ceramic rods in contact with the sample are denser and thus darker in X-ray radiography images, approaching the absorption of gold when imaged. If the sample becomes tilted during deformation it can result in large strain errors and thus the strain markers are made thin so tilting is visible when viewed edge-on.

### 2.6.1. MgO

The MgO samples were synthesized from 99.99% purity MgO powder (CAS-Nr: 1309-48-4) supplied by Feinchemikalien und Forschungsbedarf GmbH (ChemPur). To sinter the powder, it was loaded into a simple 15/10 cubic assembly and pumped up to 3 GPa of pressure. After dwelling for 15 minutes it was pumped back to ambient pressure. No heating was used as the MgO powder sintered adequately. SEM analysis of the sintered product confirmed an average grain size, claimed by the manufacturer, of 1.5  $\mu\text{m}$ . For the calculation of stress in the MgO sample during deformation, the elastic stiffness coefficients listed in **Table 9** were used in the formulation from Singh et al. (Singh et al., 1998).

**Table 9.** Elastic stiffness coefficients used to calculate the stress of MgO deformation experiments as well as the pressure derivative and second derivative (Yoneda, 1990).

	$M$ GPa	$(\partial M/\partial P)_T$	$(\partial^2 M/\partial^2 P)_T$ GPa <sup>-1</sup>
$C_{11}$	297.8	8.76	-0.03
$C_{12}$	95.1	1.81	0.02
$C_{44}$	155.8	1.31	-0.09

### 2.6.2. Mg-Al Spinel

Mg-Al spinel ( $\text{MgAl}_2\text{O}_4$ ) was synthesized by mixing approximately equimolar amounts of 99.99% purity MgO (CAS-Nr: 1309-48-4) and  $\alpha$ - $\text{Al}_2\text{O}_3$  (CAS-Nr: 1344-28-1) oxide powders (Feinchemikalien und Forschungsbedarf GmbH; ChemPur). For synchrotron experiments, small grain sizes are preferred as more crystallites can be diffracted along the beam path, resulting in sharper peaks. To ensure that the sintering process limited grain growth, a non-stoichiometric  $\text{MgO}:x\text{Al}_2\text{O}_3$  molar ratio of  $x = 0.95$  was employed. The slight MgO excess has

## 2. Methods

been shown previously to densify quickly with minimal grain growth during the high-temperature sintering process (Ting & Lu, 1999).

The mixture was ground with acetone in a mortar and pestle for a minimum of 1 hour. After the acetone was fully evaporated, it was cold pressed in a hydraulic press at 15 MPa for 2 minutes. Then, the fragile pellets were placed in an open-air furnace inside a Pt crucible at 1600 °C for 15 minutes. This sintered them into a hard ceramic. To ensure full reaction, the pellets were crushed down to powder and ground, cold pressed, and sintered at 1600 °C again for a total of three cycles. Afterwards, a small piece was ground to powder again, and powder x-ray diffraction measurements were made, which confirmed it to be Mg-Al spinel with a small amount of excess MgO, consistent with the composition. SEM BSE imaging showed the grain size of the resultant ceramic to be between 1 – 3  $\mu\text{m}$ . The sintered blocks were then cored and prepared into three pieces for the experimental assembly, as described previously.

**Table 10.** Elastic stiffness coefficients used to calculate the stress of  $\text{MgAl}_2\text{O}_4$  deformation experiments as the pressure derivative and second derivative (Yoneda, 1990).

	$M$ GPa	$(\partial M/\partial P)_T$	$(\partial^2 M/\partial^2 P)_T$ GPa <sup>-1</sup>
$C_{11}$	282.9	5.59	-0.65
$C_{12}$	155.4	5.69	-0.64
$C_{44}$	154.8	1.44	-0.19

### 2.6.3. San Carlos olivine

The sample of San Carlos olivine were privately collected from San Carlos, Arizona. The collected crystals were subsequently carefully selected and separated under a microscope for visual purity and color to ensure minimal pyroxene content. The crystals were then ground into a powder in a mortar and pestle for a minimum of 1 hour and subsequently placed into a ball mill for 30 minutes at 30 Hz using a tungsten carbide crucible and spheres. The olivine powder was loaded into a 5 mm diameter platinum capsule which was then welded shut. The capsule was placed into a 3/4" NaCl piston cylinder assembly and pumped up to 700 MPa of pressure in the piston cylinder apparatus located at BGI. Once at pressure, it was heated to 1200 °C for 3 hours with a graphite furnace, before quenching rapidly. The piston cylinder was then pumped down to ambient pressure over a period of 12 hours, to avoid cracking of the sample. Nonetheless, about 1/3<sup>rd</sup> of the recovered samples had too many cracks to be usable. The platinum capsule was removed from the NaCl assembly and carefully cut open, after which the sintered San Carlos olivine was cut into three pieces for the assembly, as described before.

## 2. Methods

The Singh *et al.* formulation for calculating deviatoric stress from XRD peak positions as described previously by Eq. 4–Eq. 6 employs Reuss and Voigt shear moduli terms,  $G_r(hkl)$  and  $G_v(hkl)$ , that are calculated using equations that are specific for each crystal system. The cubic crystal system equations for both were provided previously in Eq. 7–Eq. 9. Since olivine is orthorhombic, for this system, the Reuss condition shear modulus is defined in Eq. 116. The Voigt condition shear modulus was not employed as iso-stress conditions were assumed within the assembly deformation column.

$$[2G_r(hkl)]^{-1} = \frac{1}{2} \{ -(S_{12} + S_{13} + S_{23}) + l_1^2(S_{23} - S_{11}) + l_2^2(S_{13} - S_{22}) + l_3^2(S_{12} - S_{33}) + 3[l_1^4 S_{11} + l_2^4 S_{22} + l_3^4 S_{33} + l_1^2 l_2^2 (2S_{12} + S_{66}) + l_2^2 l_3^2 (2S_{23} + S_{44}) + l_3^2 l_1^2 (2S_{13} + S_{55})] \} \quad \text{Eq. 116}$$

$$l_1 = \frac{hd(hkl)}{a}, l_2 = \frac{kd(hkl)}{b}, l_3 = \frac{ld(hkl)}{c}$$

In the equation,  $a$ ,  $b$ , and  $c$  are the lattice parameters, which for orthorhombic crystal systems are calculated with Eq. 117. Since there are three unknowns ( $a$ ,  $b$ ,  $c$ ) in the equation, a minimum of three peaks must be fitted for them to be determined.

$$\left( \frac{1}{d(hkl)} \right)^2 = \frac{h^2}{a^2} + \frac{k^2}{b^2} + \frac{l^2}{c^2} \quad \text{Eq. 117}$$

The elastic constants reported by Mao *et al.* (Mao et al., 2015) were used, as listed in **Table 11**. The elastic stiffness coefficient was calculated at the particular pressure and temperature of interest, to produce an orthorhombic elastic matrix, which was then inverted to find the elastic compliance coefficients. These are used for each data point to calculate the stress, as detailed in Eq. 116.

**Table 11.** Elastic coefficients ( $M$ ), as well as the first and second pressure derivatives and the first temperature derivative of the elastic coefficients (Mao et al., 2015) of San Carlos olivine.

	$M$ GPa	$(\partial M / \partial P)_T$	$(\partial^2 M / \partial^2 P)_T$ GPa <sup>-1</sup>	$(\partial M / \partial T)_P$ GPa/K
$C_{11}$	320.2(19)	7.5(2)	-0.240(8)	-0.033(3)
$C_{22}$	196.5(10)	5.5(1)	-0.089(4)	-0.028(3)
$C_{33}$	232.3(8)	5.4(1)	-0.080(5)	-0.032(4)
$C_{44}$	63.2(4)	2.0(1)	-0.099(4)	-0.010(2)
$C_{55}$	76.6(5)	2.0(1)	-0.140(5)	-0.010(2)
$C_{66}$	79.7(7)	2.4(1)	-0.122(6)	-0.019(3)
$C_{12}$	71(2)	3.8(1)	0.077(4)	-0.015(2)

### 3. Results

$$\begin{array}{c|c|c|c|c} C_{13} & 71(1) & 3.8(2) & 0.010(2) & -0.009(2) \\ C_{23} & 76(1) & 3.5(2) & -0.059(5) & -0.013(2) \end{array}$$

#### 2.6.4. Single crystal MgO and Fo

The samples consisted of lab-synthesized single crystals of MgO and forsterite ( $\text{Mg}_2\text{SiO}_4$ ), pre-oriented by the manufacturer, Sigma-Aldrich. Cores from these samples were made, 4 mm in diameter and 4 mm high. The top and bottom were polished and checked for parallelism to within  $\pm 1^\circ$ . The orientations provided by the manufacturer were used to orient both types of crystal such that the deformation axis was in the crystal  $\langle 100 \rangle$  direction.

### 3. Results

#### 3.1. San Carlos olivine, MgO, and spinel deformation at synchrotron

Two beamtimes were completed at the large volume press P61B beamline, of the PETRA-III synchrotron, DESY. In each run the assembly was deformed multiple times under a series of different conditions. The run was stopped once the piezoelectric crystal degraded, or the resistance dropped outside of what could be compensated with the dial on the front of the charge integrator. At very large voltage drifts, even when the voltage fitting and correction routine is employed afterwards, the signal is lost to capacitor discharge noise.

For all runs, the assembly was deformed using the vertically oriented rams, 1 and 2. Each deformation cycle consisted of pre-heating to relax the deviatoric stresses at 800 °C for a minimum of 20 minutes in the case of the San Carlos olivine and MgO, and 1000 °C in the case of the Mg-Al spinel. This was followed by a triaxial or simple shear compression deformation at a specific anvil advancement rate for a specified number of minutes. Once the compression deformation was completed, a triaxial tension deformation at the same temperature was applied to the sample that consisted of rams 1 and 2 retreating backwards to equal positions, as measured by the position encoders on the back of the rams. This was followed by static heating to anneal again for a minimum of 20 minutes to prepare for the next deformation cycle.

### 3. Results

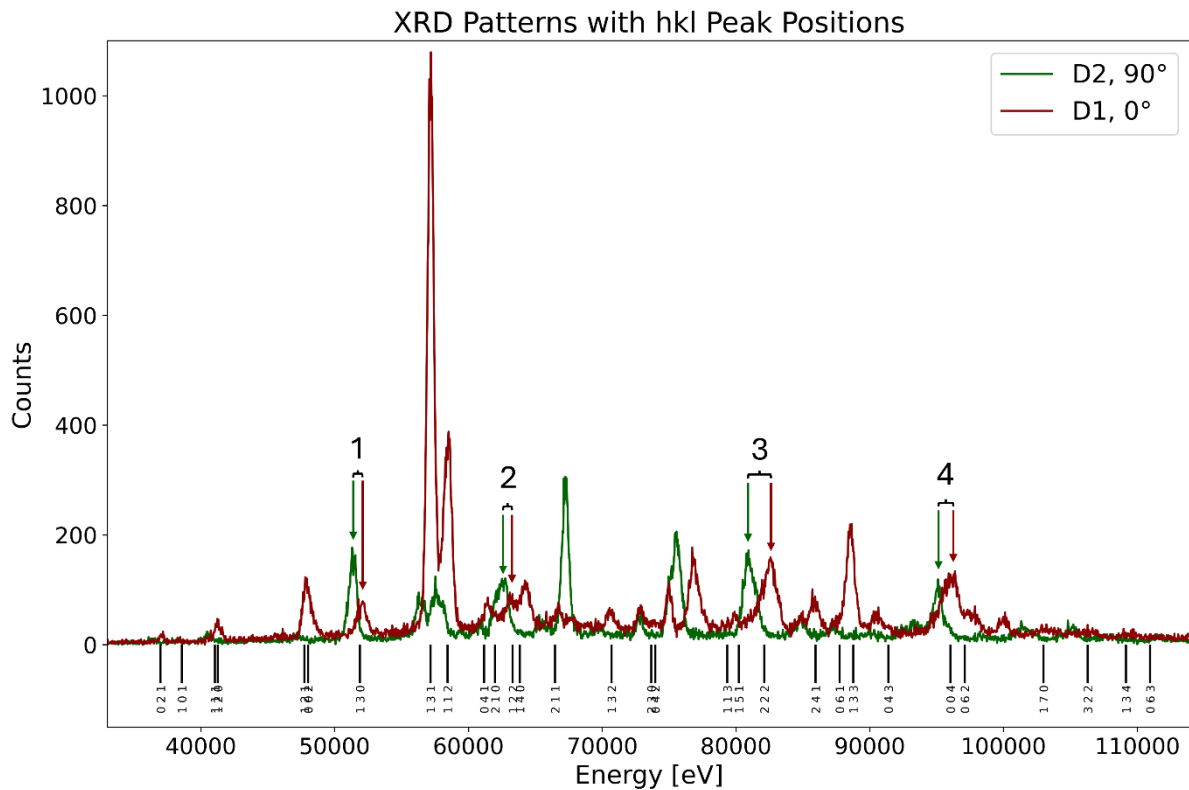


**Figure 62.** An example XRD pattern collected on stressed San Carlos olivine. The patterns from both detectors are shown overlain. The  $(hkl)$  peaks fitted to D1 to measure the XRD stress are shown below the patterns only, with the  $(hkl)$  Miller indices labeled for each. The same fitting was done for D2 as well, not shown in this figure. Shifts in a selected subset of peaks between D2 and D1 are labeled with 1, 2, 3, and 4.

In **Figure 62** an example XRD pattern collected on San Carlos olivine is plotted. Both detectors, with their azimuthal angles labeled, recorded patterns that are offset, due to a stress of approximately 630 MPa in this instance. The black lines below the patterns mark the locations of the fitted San Carlos olivine peaks, aligned with the D1 pattern. A subset, for illustrative purposes, of 4 shifted peaks are labeled in the figure. Peak shift 1 is for lattice plane (130), 2 for (122), 3 for (222), and 4 for (004). Not all peaks labeled below the patterns with the vertical bars in **Figure 62** were able to be fitted for all patterns. However, from the complete list of peaks, each pattern had no more than three peaks that could not be fitted. As is visible, the two patterns have peak positions offset compared to each other. This is due to the stress in the sample and this offset is used to calculate the microstrain, and thus the stress in the San Carlos olivine.

### 3. Results

#### 3.2. San Carlos olivine deformations with XRD

##### 3.2.1. Linear compression deformation on San Carlos olivine

It has been reported that forsterite stress development during deformation has a strong correlation with temperature, especially starting above 1000 °C with a rapid drop in strength at 1200 °C (Darot & Gueguen, 1981; Thieme et al., 2018). To explore this weakening and confirm the ability to measure it with the piezoelectric method, deformation experiments were undertaken at high-pressure and -temperature. A series of three deformations, ranging between 780 – 1180 °C in a triaxial compression direction were chosen.

**Table 12.** Run table of three linear compression deformations on San Carlos olivine at varying sample temperatures. The temperature errors are estimated to be  $\pm 50$  °C.

Cycle	Oil pressure [bar]	Sample pressure [GPa]	Heating power [W]	Sample temperature [°C]	Piezoelectric temperature [°C]	Anvil rate [ $\mu\text{m}/\text{min}$ ]	Deform time [min]
C1	40	2.4	580	780	150	-4.3	100
C2	40	2.4	710	990	170	-4.3	100
C3	40	2.4	820	1180	190	-4.3	100

San Carlos olivine samples were deformed at a constant anvil advancement rate at different temperatures. As described, anvil 1 and 2, the vertical anvils, are set to advance inwards at a constant rate. To keep the sample chamber volume as close to constant as possible during deformation, the hydrostatic oil pressure was reduced by 10% for all rams over the deformation period. For example, if deformation begins at 40 bar of oil pressure, the PLC is programmed to reduce it to 36 bar at the end of the deformation period. In this way, the non-advancing rams 3, 4, 5 and 6 are allowed to relax outwards.

### 3. Results

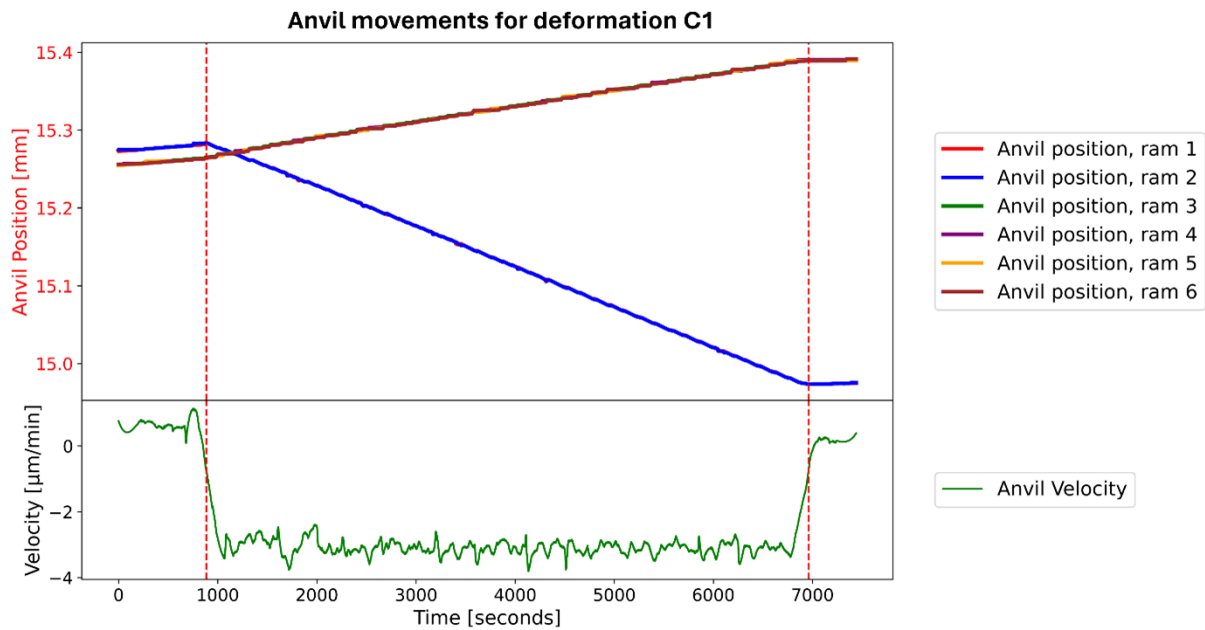
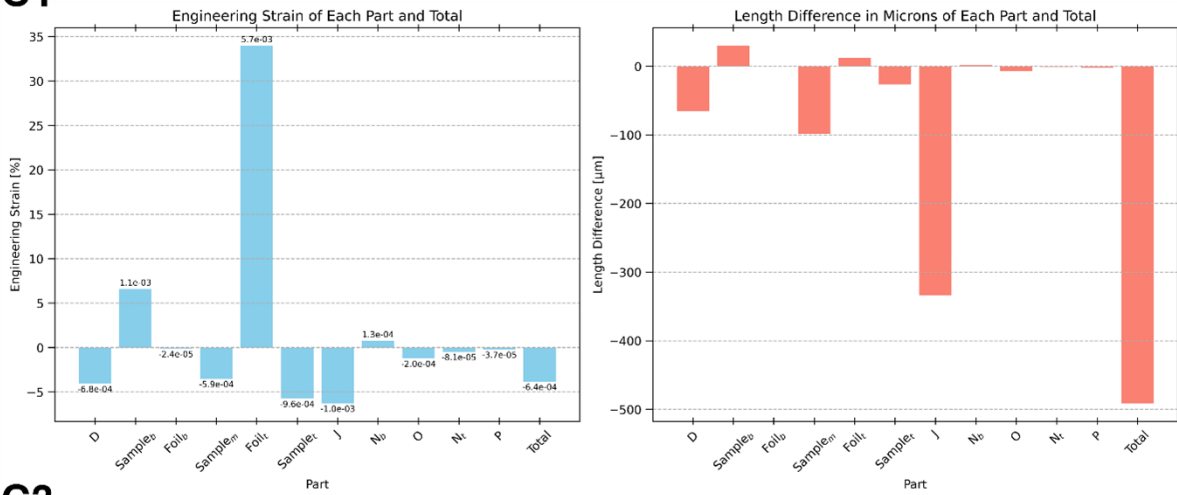


**Figure 63.** Anvil movements of deformation C1. The other deformations, C2 and C3, are similar to this. The top plot shows the anvil positions over time and the bottom the anvil velocity. The velocity of anvil 1 is plotted. The red vertical dashed lines mark the beginning and end of the deformation cycle. The elapsed time has not been normalized to the start of deformation.

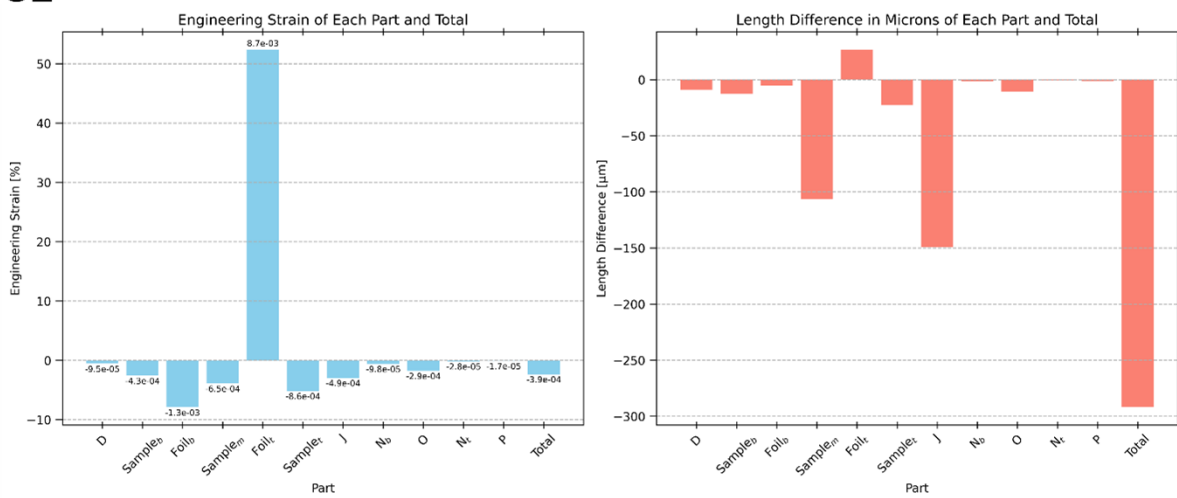
The anvil displacements of the three deformation cycles reported in **Table 12** are all similar to those shown for C1 in **Figure 63**. The top plot shows the anvil displacement, with the beginning and end of deformation marked with vertical red dashed lines. Due to the geometry of the position encoder on the rams, a decrease in anvil position value represents a movement inwards into the sample chamber. As can be seen, while anvils 3, 4, 5, and 6 are allowed to relax outwards, the movement is not sufficient to sustain a constant sample chamber volume during deformation. Anvil 1 and 2, with their lines overlain on top of each other, shows how they are moving inwards in position at a constant velocity. This velocity is shown in the bottom half of **Figure 63**. This velocity will be shown on all plots and represents the anvil velocity of anvil 1. During a compression deformation, the inwards anvil displacement velocity is negative and during deformation in tension, or outwards retreat of the anvil, it is positive. The velocity has been smoothed with a Savitzky-Golay filter with a window length of 403 and polynomial order 3. This was applied because the velocity measurements are inherently noisy due to the stepped movements of the anvils.

### 3. Results

#### C1



#### C2



#### C3

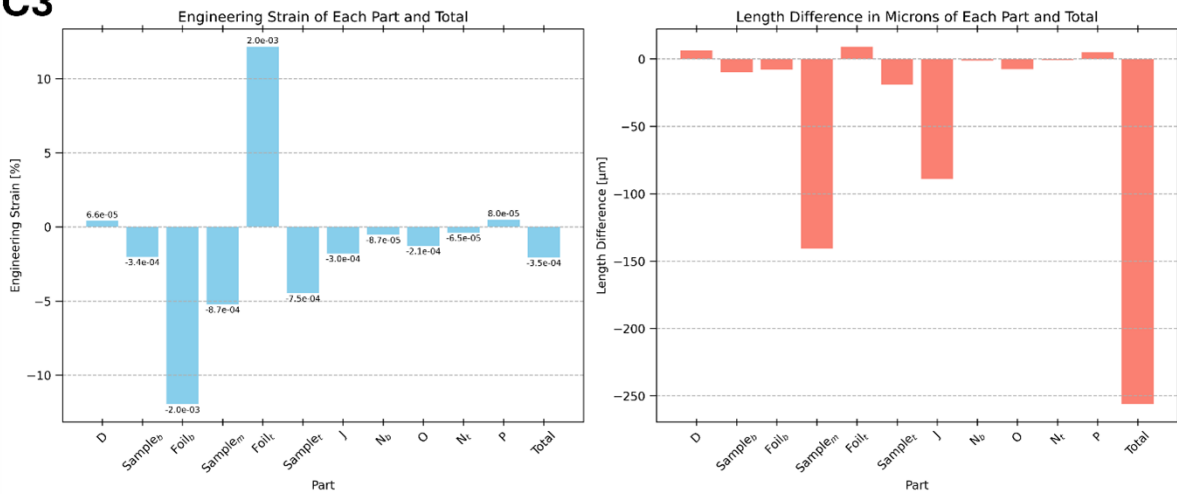


**Figure 64.** The measured strains of C1, C2, and C3. Each deformation strain plotted on the left side is the engineering strain and on the right side the length difference in microns. Both are calculated based on the x-ray radiography images of before and after deformation of the

### 3. Results

*assembly parts. The engineering strain bar plots also list the calculated strain rates for each part at the end of each bar. The units are  $s^{-1}$ .*

Strain was measured within the full deformation column using radiometry images made before and after deformation for these three experiments, as shown in **Figure 64**. For each deformation, the engineering strain and micron length difference has been plotted on the left and right sides of the figure respectively.

### 3. Results

#### Average lattice microstrains from D1 (0°) and D2 (90°)

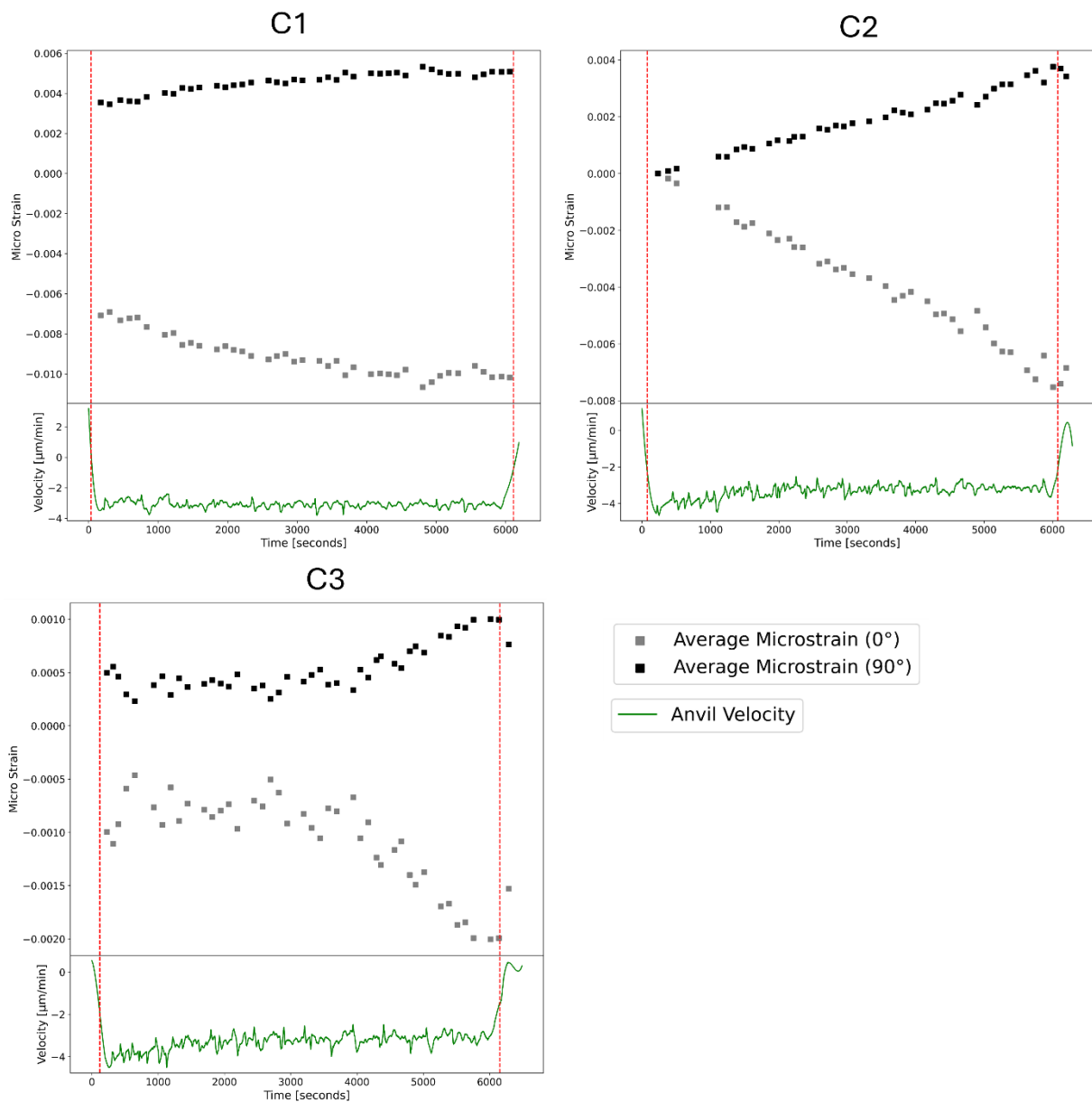


**Figure 65.** Averaged lattice microstrains as measured by the D1 and D2 detectors, for C1, C2, and C3, showing the clear splitting in the average lattice plane microstrain caused by deviatoric stress.

In **Figure 65**, the lattice microstrains measured with each XRD pattern during the deformation of all three experiments are plotted by detector. The microstrain from each fitted peak was averaged. As can be seen for all three compression deformation experiments, a clear splitting is visible in the microstrain behavior, confirming that the sample was under stress and the stress did increase with the sample macroscopic strain.



### 3. Results

experiment is shown with the piezoelectric method derived deviatoric stress plotted together in **Figure 66**.

#### XRD and piezoelectric method measured deviatoric stress with hydrostatic pressure

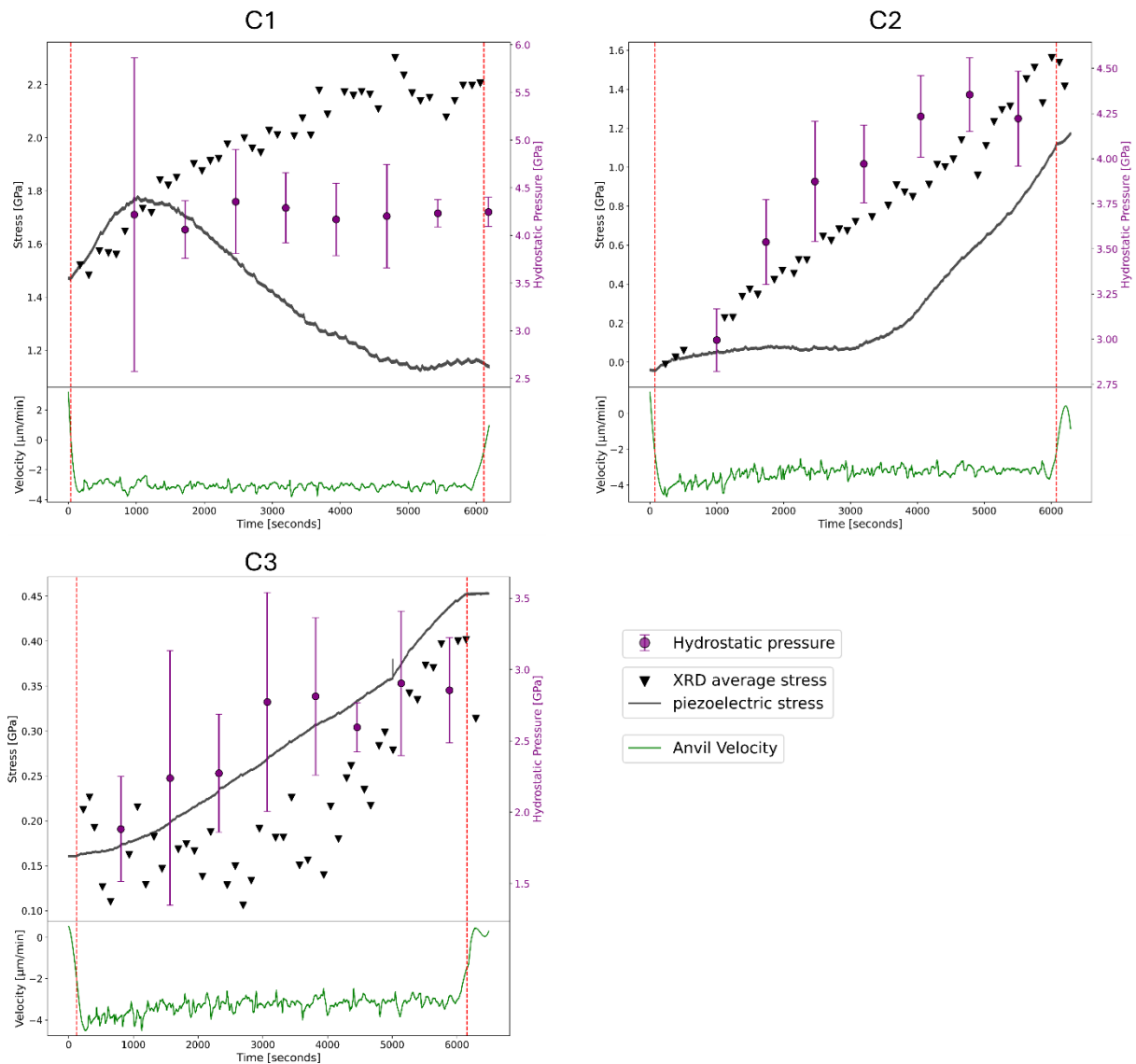


**Figure 67.** The averaged XRD measured stress with the piezoelectric stress. Additionally, the hydrostatic pressure during the experiment is shown, as measured using the MgO sleeve around the sample.

Finally, by averaging the stresses calculated from each (hkl) peak, it's possible to compare the piezoelectric and XRD stresses more precisely with the added hydrostatic pressure as measured by the MgO sleeve that was placed around the sample. These are shown in **Figure 67**.

### 3. Results

To account for potential deviatoric stress effects on the MgO, the hydrostatic pressure was calculated using the d-spacings derived at the azimuthal ‘magic angle’ which is theoretically the d-spacing from hydrostatic pressure effect only. The temperature used in the hydrostatic pressure calculations was assumed to be the same as the sample temperature since the MgO sleeve is inside of the graphite furnace. The results are relatively close between the piezoelectric and XRD stress measurement techniques apart from a clear difference in C1.

The assumption is that, while CTGS has not yet been shown to undergo ferroelastic switching, theoretically, since it has the same space group as  $\alpha$ -quartz, there should be a stress condition that causes a ferroelastic switch. The results of C1 follow the expected trend of a ferroelastic switch in CTGS. The trend reverses smoothly and does not reverse again through the whole experiment. If the stress measured by the piezoelectric method in C1 is mirrored across the line where the switch happens, at roughly 1000 seconds in the experiment, the final measured stress is, on a relative scale, similar to the XRD stress. This is expected of a ferroelastic switch. The switch only reverses the sign of  $d_{11}$  but does not alter the absolute value of it. Therefore, the stress measured should be equal but reversed in sign, as the figure shows.

#### 3.2.2. Linear tension deformation on San Carlos Olivine

After each compression deformation, i.e., where anvils 1 and 2 advance into the sample, tensile deformation was performed where the anvils were retracted back to assume equal positions with anvils 3, 4, 5, and 6. As these resulted in an interesting test regime where stresses dropped over the deformation cycle, piezoelectric as well as XRD stress measurements were also recorded for most cycles. **Table 13** shows the conditions of tensile deformation cycles.

**Table 13.** Run table of five linear tension deformations on San Carlos olivine at varying sample temperatures and two hydrostatic pressures. The temperature errors are estimated to be  $\pm 50$  °C.

Cycle	Oil pressure [bar]	Sample pressure [GPa]	Heating power [W]	Sample temperature [°C]	Piezoelectric temperature [°C]	Anvil rate [ $\mu\text{m}/\text{min}$ ]	Deform time [min]
T1	36	2.1	580	780	150	+4.3	12.75
T2	36	2.1	710	990	170	+4.3	100
T3	36	2.1	820	1190	190	+4.3	100
T4	56.4	3.2	710	960	180	+10.0	33
T5	36	2.1	460	590	120	+10.0	28

T1 was planned to be a 100 minute tension experiment like T2 and T3, however the PETRA-III beam dropped after 12.75 minutes and the experiment had to be stopped as no more XRD could be collected. As with compression experiments, the PLC is programmed to increase the oil pressure during the tension deformation. For example, at 36 bar, over the tension

### 3. Results

deformation period, the oil pressure was programmed to increase to 40 bar. Once again, this was done to keep the sample chamber volume more constant.

As an example, the anvil positions of T2 are plotted in **Figure 68**. Compared to **Figure 63**, it can be seen that anvil positions of ram 1 and 2 are now increasing over the deformation cycle time. Also, the other anvils do move in, albeit less than anvils 1 and 2, over the same period. Even though they do not reach the same anvil position at the end of deformation, according to the PLC they are back in their starting position. It is not entirely clear why the PLC does not do so. According to the manufacturer, the PLC attempts to equalize the anvil positions, not the oil pressure, so it would be expected that the anvil positions match in distance. The anvil velocity has the same smoothing algorithm applied as in the previous deformations.

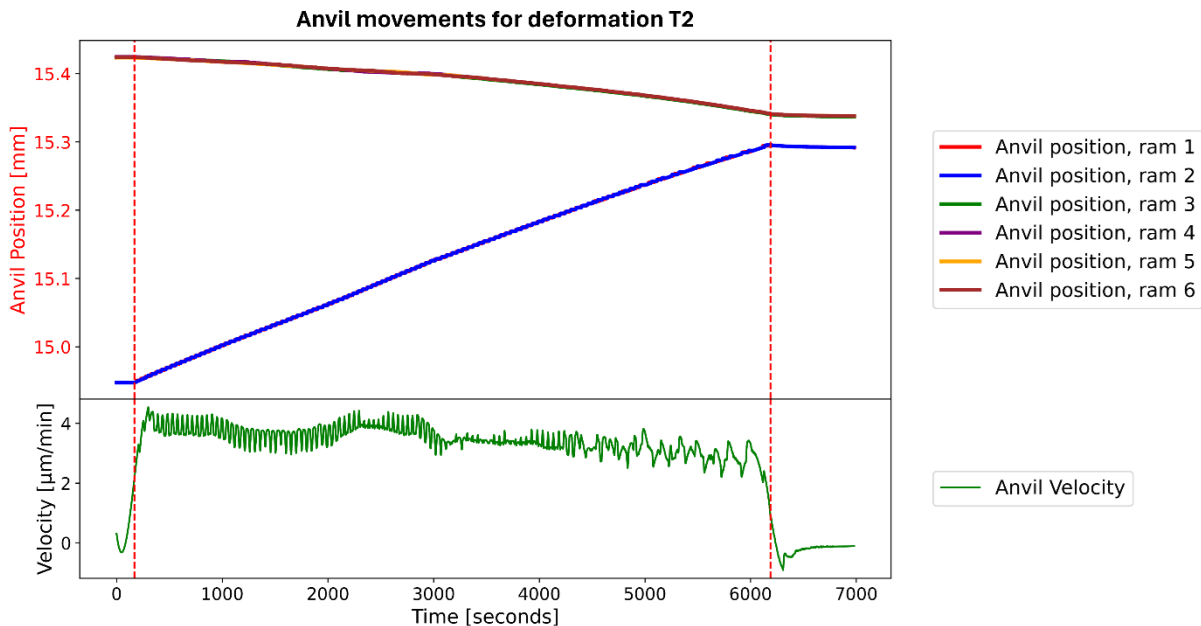
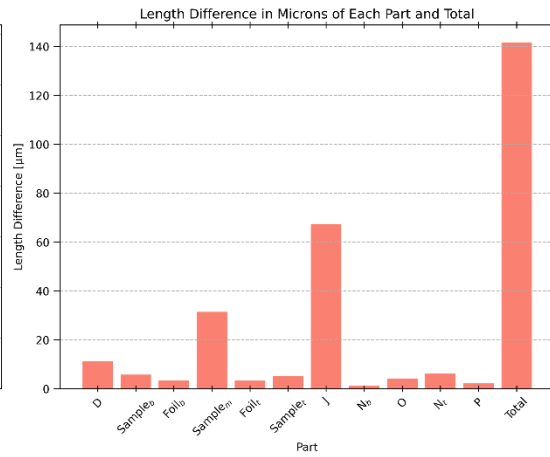
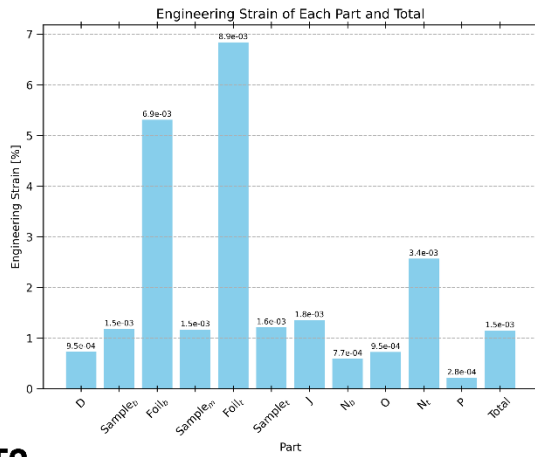


**Figure 68.** Anvil movements of tension deformation T2. The top plot shows the anvil position over time and the bottom the anvil velocity. The velocity of anvil 1 is plotted. The red vertical dashed lines mark the beginning and end of the deformation cycle. The elapsed time has not been normalized to the start of deformation.

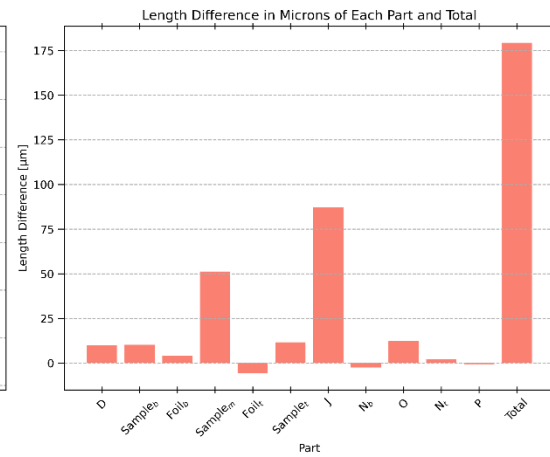
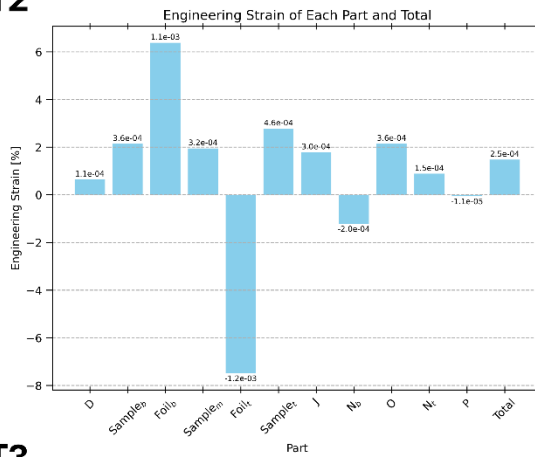
Pre- and post-deformation x-ray radiography images were taken for T1, T2, T3, and T5. None were taken for T4. The strains, strain rates, and micron differences are shown in **Figure 69**. As before, the left side plots are of the engineering strain with the calculated strain rate and the right side of the actual difference in microns.

### 3. Results

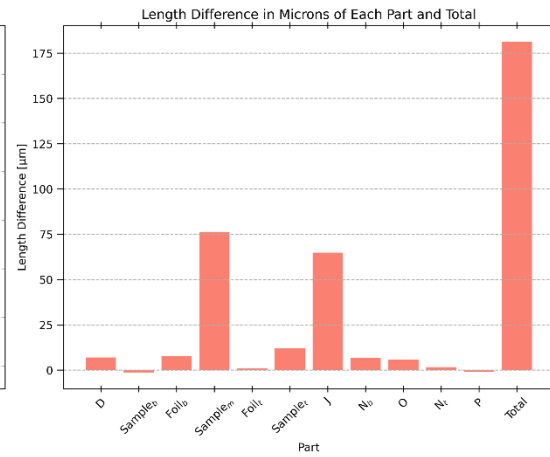
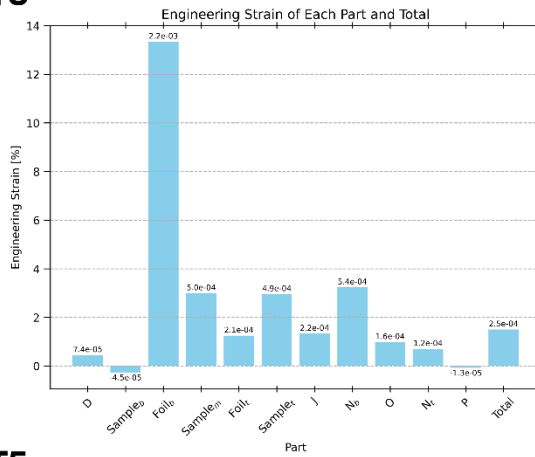
#### T1



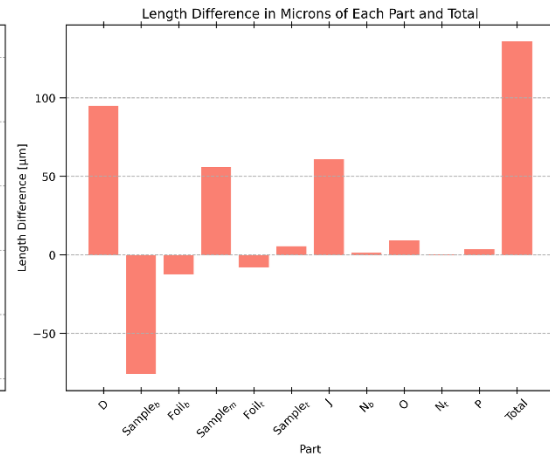
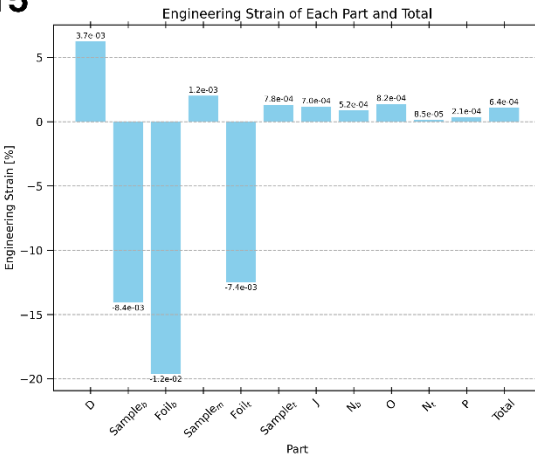
#### T2



#### T3



#### T5



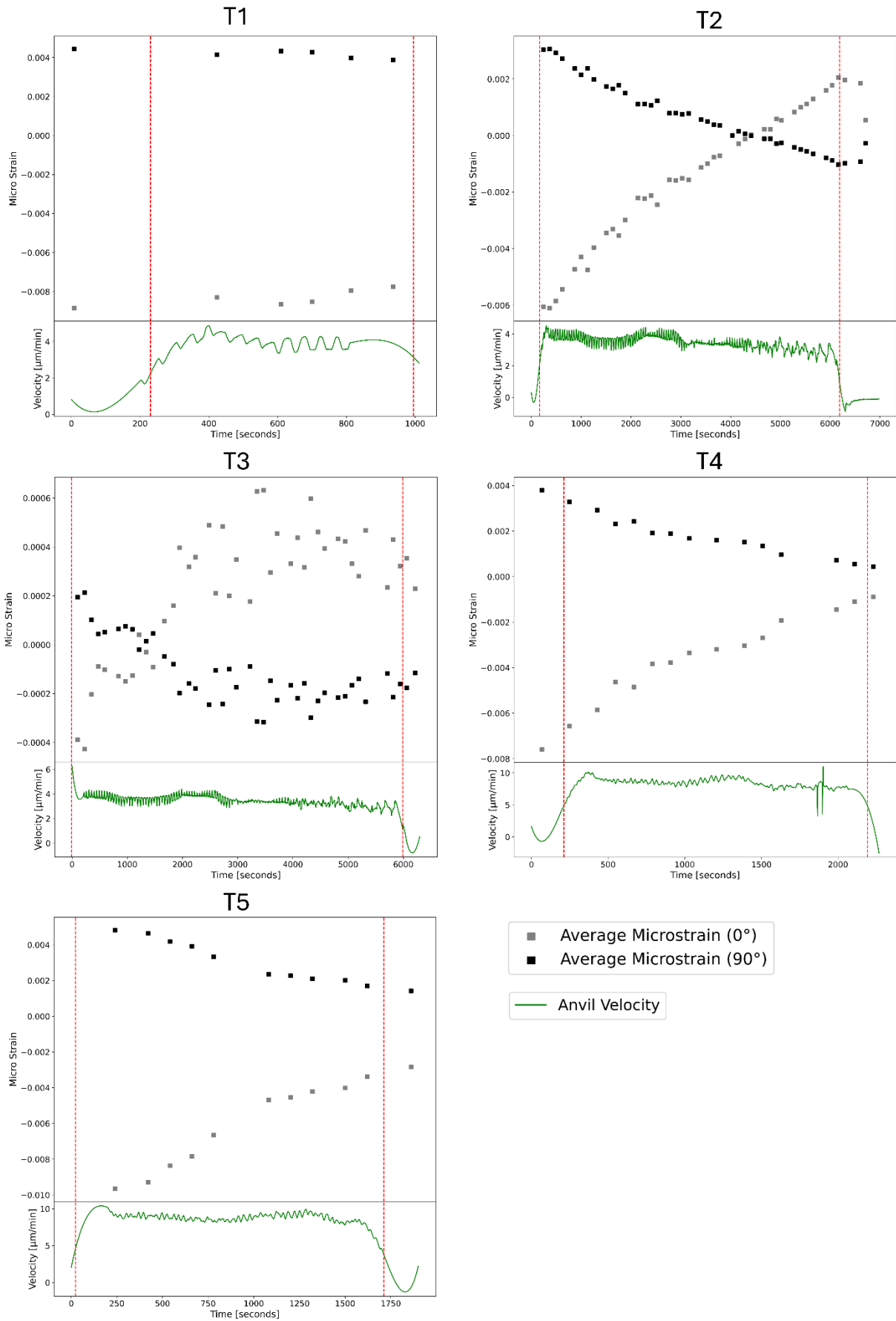
### 3. Results

**Figure 69.** *The measured strains of T1, T2, T3, and T5. Each tension deformation strain plotted on the left side is the engineering strain and on the right side the length difference in microns. Both are calculated based on the x-ray radiography images of before and after deformation of the assembly parts. The engineering strain bar plots also list the calculated strain rates for each part next to the end of each bar. The units are  $s^{-1}$ .*

Just as with the compression deformation experiments, the lattice microstrains are plotted in **Figure 70**. The high temperature experiments start with a smaller lattice microstrain as expected. After a compression deformation, the sample is kept at high-temperature and a short period of 5 – 10 minutes is required to prepare for the following tension experiment. Stresses have time to relax in this period if the temperature is high enough for dislocations to be mobile enough to relax the crystal lattice. T2, for example, has a 300 MPa overshoot at the end of the deformation implying that 300 MPa of stress was relaxed after the compression deformation experiment. In the case of T3, the compression stress in the sample at the beginning, at roughly 100 MPa, is reversed past the zero point within the first 1000 seconds and then goes into a creep flow in tension for the rest of the deformation. Apart from that, as expected, at higher temperatures the olivine is weaker and thus the compression deformation before the tension deformation resulted in smaller stresses overall being imparted on the sample.

### 3. Results

#### Average lattice microstrains from D1 (0°) and D2 (90°)



### 3. Results

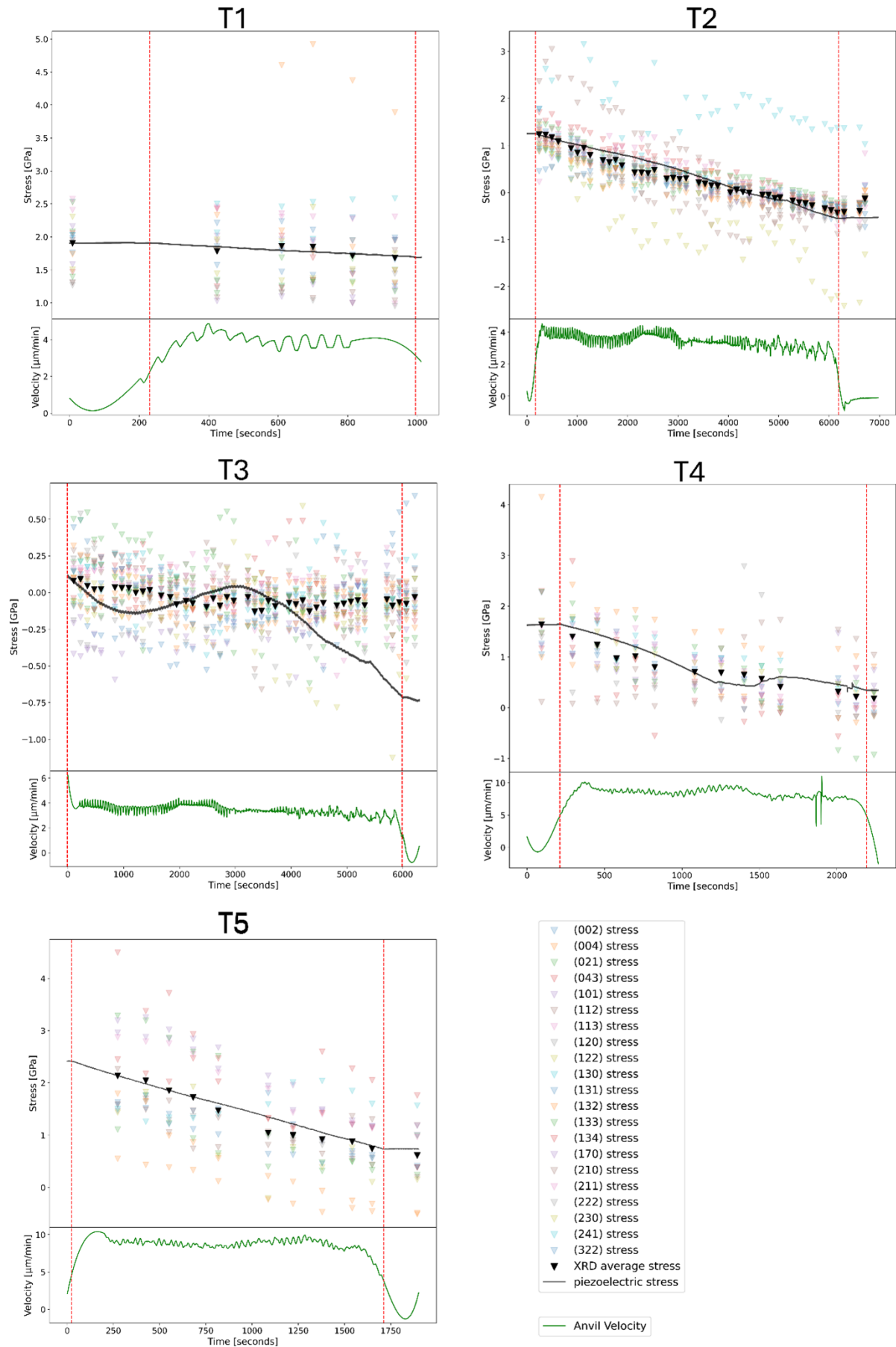
**Figure 70.** *Averaged lattice microstrains during tensile cycles as measured by the D1 and D2 detectors, for T1, T2, T3, T4, and T5. The lattice strains from the two detectors approach zero together, showing a clear decrease in the deviatoric stress in the sample.*

Tensile experiment cycles are shown with both the XRD and piezoelectric determined deviatoric stress in **Figure 71**. Additionally, the averaged XRD stress, acquired by averaging all the stresses from the reflections from the lattice planes, is shown alongside the piezoelectric method stress measurement and the MgO pressure marker hydrostatic pressure. Some of the experiments, being shorter, did not allow as many MgO measurements. The same process as the compression experiments was applied to the MgO to ensure the lattice microstrain induced by deviatoric stress was not considered in the hydrostatic pressure calculations.

The experiment T3, as seen in **Figure 71**, recorded an oscillation in the CTGS piezoelectric stress with a wavelength of about 3000 – 4000 seconds. Of note is that this was also the highest temperature experiment in this series, with the sample heated to 1190 °C. Consequently, the piezoelectric crystal was higher in temperature at 190 °C. In general, from previous experience, these higher temperature experiments sometimes record oscillatory stress. This could be because of ferroelastic switching, but it could also be from unknown effects due to the high amount of current passing through the furnace. The piezoelectric crystal, since it outputs current on the order of a few microamps, is highly sensitive to current noise. Even with a DC heater, as was used in all these experiments, the graphite furnace requires an exceptionally high amperage to heat. Any kind of noise or instability in the heating current could induce current noise. Unfortunately, it is not straightforward to determine the source of the oscillation in the signal. However, it is trivial to detect this noise but not trivial to treat the data later to correct for it and remove it so the experiment would have to be abandoned.

### 3. Results

#### XRD and piezoelectric method measured deviatoric stress



### 3. Results

**Figure 71.** Deviatoric stress, as measured with both XRD and the piezoelectric method, is shown for five tension deformation experiments. See **Figure 66** for explanation of symbols.

### 3. Results

#### XRD and piezoelectric method measured deviatoric stress with hydrostatic pressure

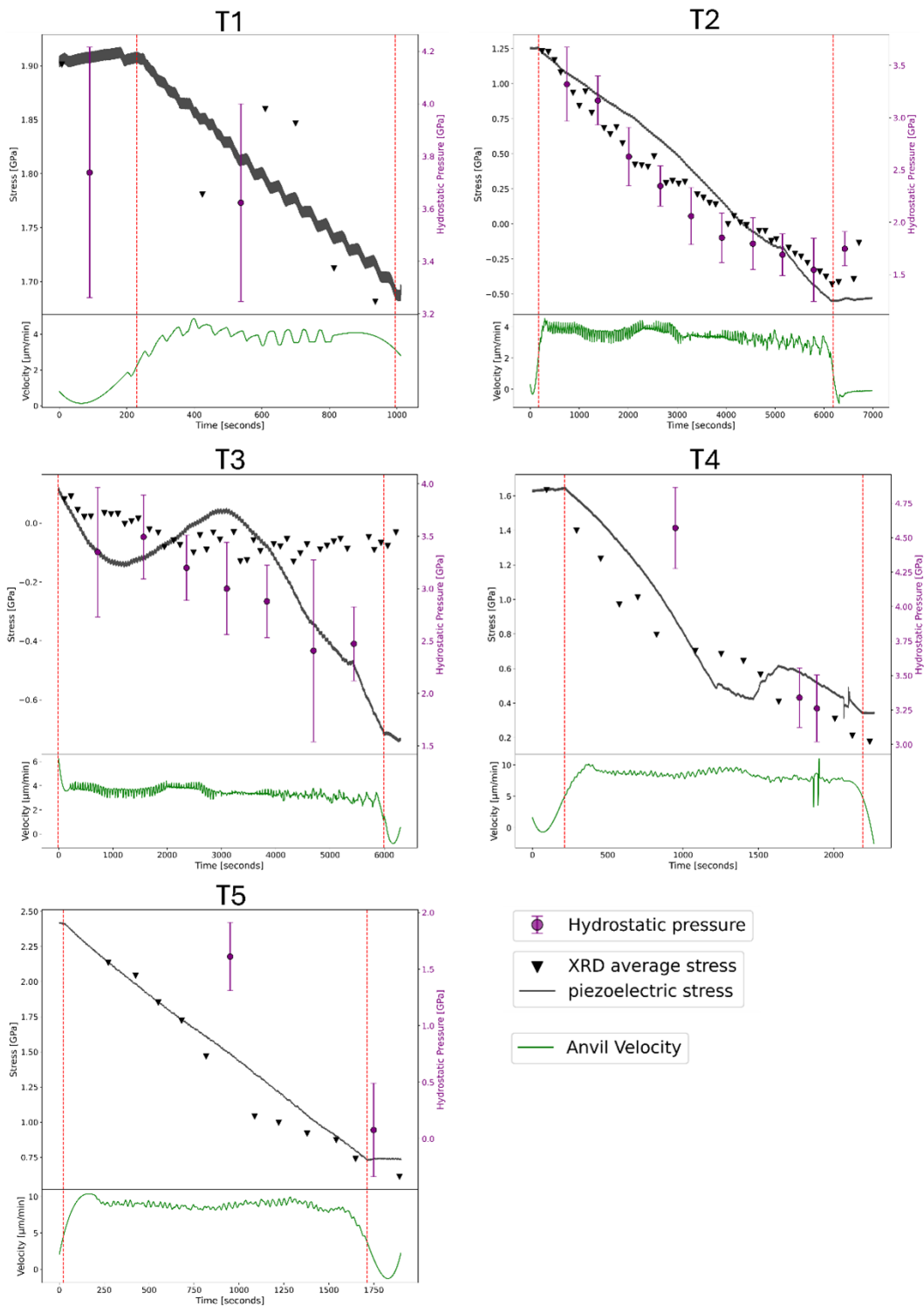


**Figure 72.** The averaged XRD measured stress with the piezoelectric method stress. Additionally, the hydrostatic pressure during the experiment is added, as measured by the MgO sleeve around the sample.

### 3. Results

#### 3.2.3. Stepped deformation of San Carlos olivine

To verify that the piezoelectric crystal is sensitive to strain rate changes, especially after the sample reaches steady-state creep, three deformation experiments in compression were undertaken where the strain rate was increased in stages. The experiments began with a slower strain rate which was increased to a higher strain rate, in either two or three steps. The change in strain rate is abrupt and the piezoelectric crystal should, therefore, detect a relatively sudden increase in stress. As before, these experiments were heated at several different temperatures.

**Table 14.** Run table of three stepped compression deformation cycles on San Carlos olivine at varying sample temperatures and two pressures. The temperature errors are estimated to be  $\pm 50$  °C. The cycles are listed in the order in which they were run.

Cycle	Oil pressure [bar]	Sample pressure [GPa]	Heating power [W]	Sample temperature [°C]	Piezoelectric temperature [°C]	Anvil rate [ $\mu\text{m}/\text{min}$ ]	Deform time [min]
SR1	60	3.4	710	950	180	-1.9, -6.3	53, 16.8
SR2	40	2.4	460	590	130	-1.6, -2.8, -6.1	20, 20, 20
SR3	40	2.4	710	990	170	-1.6, -2.8, -6.1	20, 20, 20

The run cycles with this anvil movement are listed in **Table 14**. The difference between these and the previous compression and tension experiments is that in the stepped deformation there are multiple anvil advancement rates, with the total deformation time for each anvil advancement rate provided. The change in anvil rates were programmed into the LVP PLC and thus there is no pause in time between each stage.

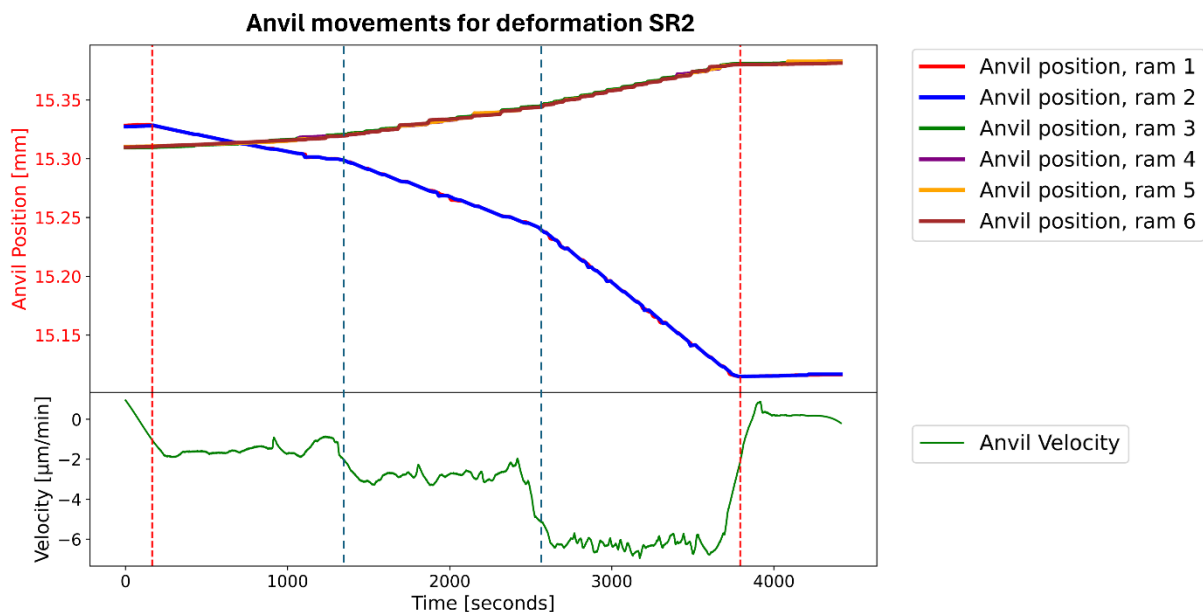


**Figure 73.** Anvil movements of a stepped deformation, SR2, illustrating the change in strain rate. The plot is similar to the previous plots of anvil advancement but in this case the strain

### 3. Results

*rate changes have been marked with a dashed blue line. This one, as is described in **Table 14**, consisted of three strain rate stages, each of 20 minutes in length.*

The stepped deformation strain rates are shown in **Figure 73**. Once again, rams 1 and 2 are advanced inwards, into the sample chamber, for compression experiments. In this case, the change in slope at each vertical blue dashed line indicates the strain rate change, and the anvil velocity is shown at the bottom of the plot. For these deformation cycles, no pre- and -post deformation x-ray radiography images were taken of the sample column, so no strain was measured on the sample. Because radiography images cannot be taken during a deformation and the strain rate varies with these experiments, a pre- and post- deformation radiography image would not allow for calculation of strain rate or even strain for each phase, only the total, and to save time it was decided to skip the radiography imaging.

### 3. Results

#### Average lattice microstrains from D1 (0°) and D2 (90°)

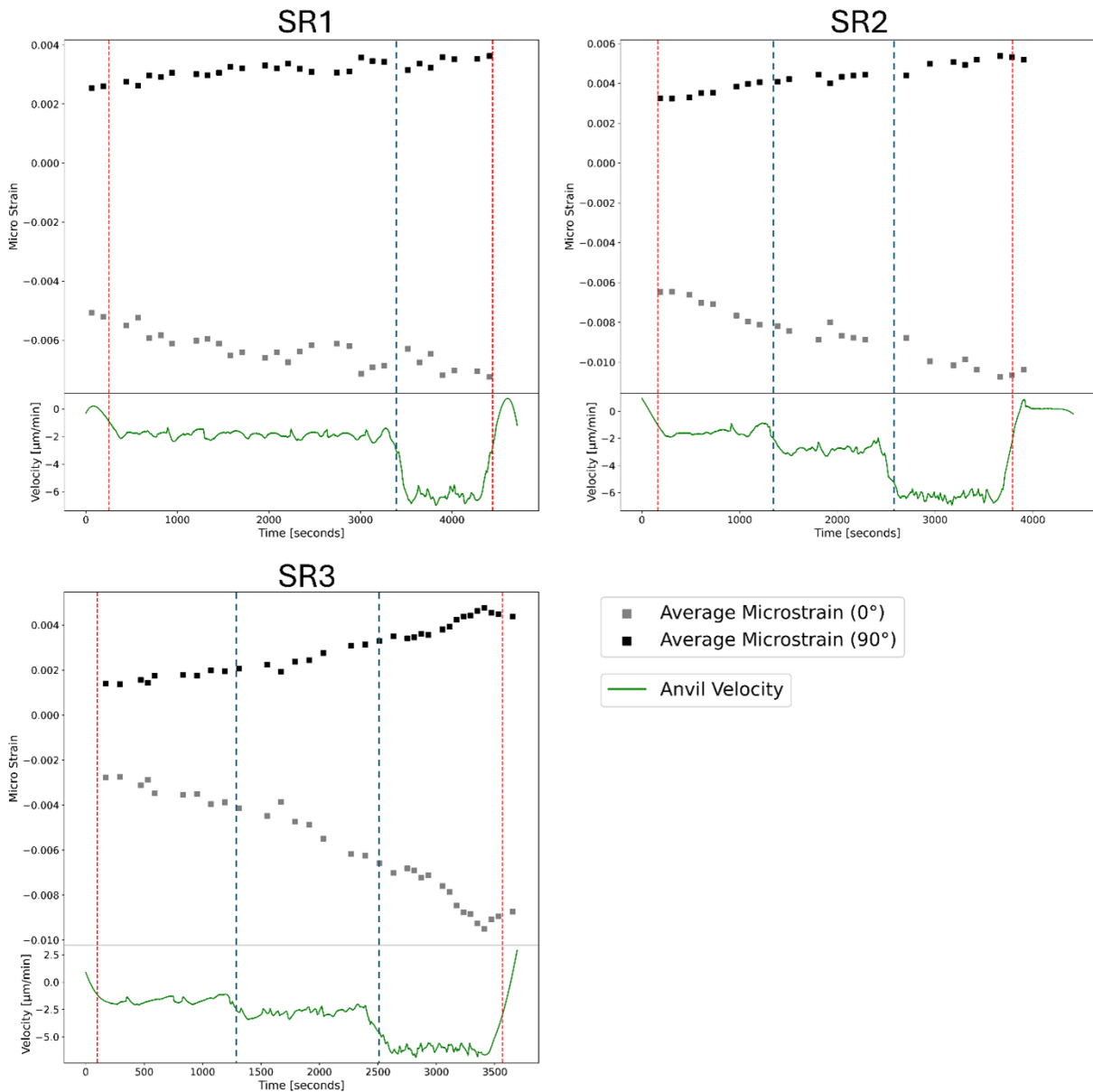


**Figure 74.** The average lattice micro strains from each fitted (hkl) lattice plane are plotted for each stepped deformation experiment. Detector D1 and D2 are plotted separately.

**Figure 74** displays the average microstrain as derived from the fitted (hkl) peaks. As before, most experiments did not start with only hydrostatic stress. All show some initial deviatoric stress. This would not be captured in the piezoelectric stress measurements, however with high enough temperature and long enough heating, it can of course be assumed to be at zero and thus set a starting point. As long as the temperature is kept constant, the integrated voltage can keep track of the current absolute stress from the crystal.

### 3. Results

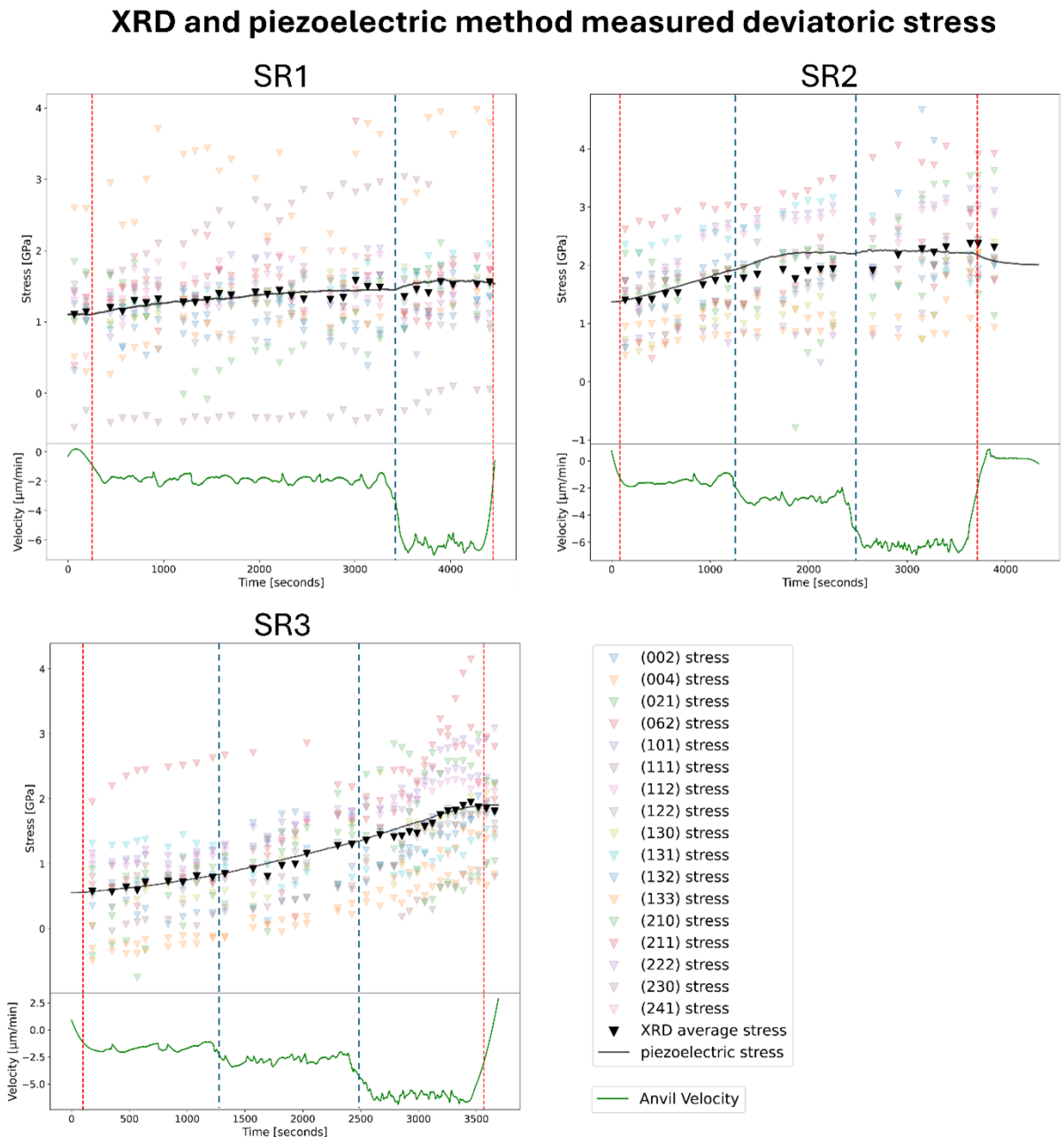


**Figure 75.** The stress, as measured by all fitted XRD peaks as well as the piezoelectric method. See previous captions for explanation.

The plots in **Figure 75** compare the stresses measured with the XRD and piezoelectric methods. Once again, the large spread in stresses measured by individual lattice plane peaks from the XRD pattern entirely contains the piezoelectric stress curves. As expected, each increase in anvil advancement rate causes an increase in the stress in both the piezoelectric stress curve and the XRD stress.

### 3. Results

#### XRD and piezoelectric method measured deviatoric stress with hydrostatic pressure

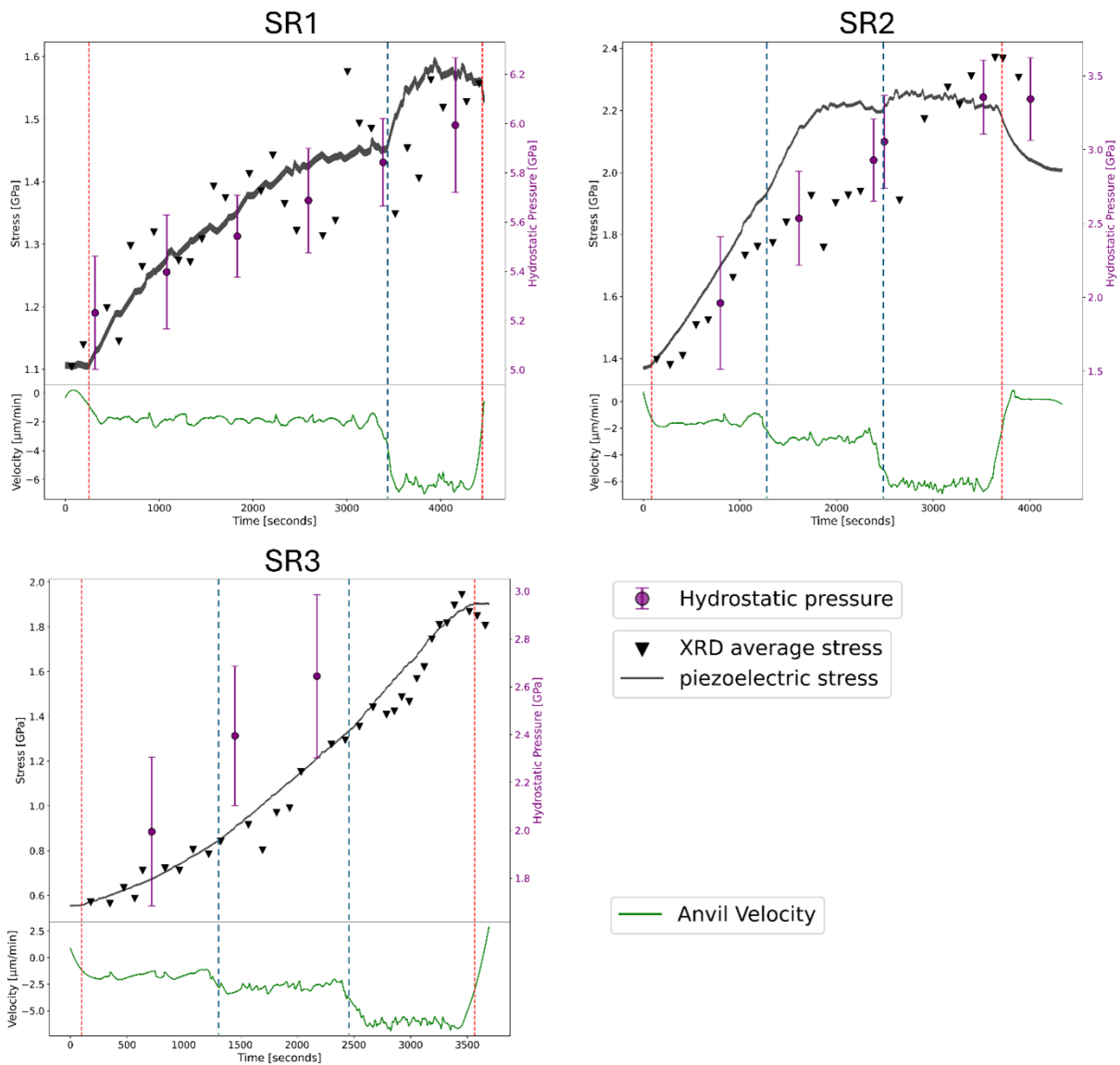


**Figure 76.** The averaged XRD measured stress with the piezoelectric stress overlain. Additionally, the hydrostatic pressure as measured with MgO is added.

The stepped deformation experiments show the rapid response of the piezoelectric crystal to the strain rate. When the anvil advancement rate is increased, the crystal measures an almost instant increase in stress. Since the crystal is closer to the anvil than the sample and is coupled to it through a diamond disk, it logically follows that it would react quickly to a change in stress from the anvils.

It is essential to delineate the transition between the elastic and creep regimes. Initially, the material exhibits a linear, elastic response to applied stress, characterized by a proportional increase in strain. This behavior adheres to Hooke's Law, where the stress  $\sigma$  is directly

### 3. Results

proportional to the strain  $\varepsilon$ , expressed as  $\sigma = E \cdot \varepsilon$ , with  $E$  being the Young's modulus of the material (Dixon & Durham, 2018; Wallis et al., 2020). During this phase, the olivine's internal structure resists deformation, and the energy is stored elastically. As the strain continues to increase, the material reaches a yield point, beyond which it enters the creep regime. In this regime, the stress no longer increases with strain; instead, the material begins to flow plastically.

The creep behavior can be described by the Norton-Bailey law, which relates the creep strain rate  $\dot{\varepsilon}$  to the applied stress, given by  $\dot{\varepsilon} = A \cdot \sigma^n \cdot t^m$  where  $A$ ,  $n$ , and  $m$  are temperature dependent material constants that are generally independent of stress, and  $t$  is time (Liang et al., 2020; May et al., 2013). The transition to the creep regime signifies that microstructural mechanisms, such as dislocation glide or grain boundary sliding, have become dominant, allowing the olivine to deform plastically under constant stress.

Upon stepping up the deformation rate, the material momentarily reverts to an elastic state, exhibiting a linear increase in stress with strain. This is indicative of the piezoelectric crystal's rapid response to the altered strain rate, as it immediately registers the increased stress imposed by the advancing anvils. However, this elastic behavior is transient, and as the strain accumulates, the material once again settles into a creep regime. The stress plateaus, reflecting olivine's capacity to accommodate the additional strain through plastic flow without a corresponding rise in stress (Wallis et al., 2020).

#### 3.2.4. Oscillation deformation of San Carlos olivine

Since piezoelectric crystals tend to have a hysteresis loop of voltage output versus lattice microstrain, especially at higher temperatures and with repeated strains (Bertagnolli et al., 1979; Damjanovic & Demartin, 1996), deformation experiments were undertaken at a variety of temperatures to test the repeatability of stress measurements. The objective was to determine whether there is a degradation or an increase in drift from the piezoelectric crystal signal during repeated compression and tension deformation oscillations. XRD patterns were taken during the deformation. To increase the XRD stress measurement temporal resolution, no MgO XRD patterns were taken for hydrostatic pressure measurements.

The typical deformation oscillation consisted of a constant anvil rate for a specified number of minutes, followed by a reversal of the anvils at the same rate and for the same amount of time. Then, another oscillation is started immediately with compression and followed again by tension. This is repeated for either two or four total oscillations. The run table for these experiments is provided in **Table 15**.

### 3. Results

**Table 15.** Run table of five oscillation deformations on San Carlos olivine at varying sample temperatures. The temperature errors are estimated to be  $\pm 50$  °C. The number of oscillation cycles is in the Osc. cycles column. The anvil direction reverses for each oscillation, so the anvil rate is positive and negative. The last column is the deformation time per cycle, which includes a compression and tension deformation pair.

Cycle	Oil pressure [bar]	Sample pressure [GPa]	Heating power [W]	Sample temperature [°C]	Piezoelectric temperature [°C]	Osc. cycles	Anvil rate [ $\mu\text{m}/\text{min}$ ]	Deform time per cycle [min]
OS1	36	2.1	580	780	150	4	$\pm 5.0$	8
OS2	36	2.1	580	780	150	4	$\pm 20.0$	8
OS3	36	2.1	820	1190	190	4	$\pm 20.0$	8
OS4	36	2.1	820	1190	190	2	$\pm 30.0$	16
OS5	36	2.1	0	23	23	2	$\pm 20.0$	8

The anvil rate for compression, i.e. anvil advancement, is positive and negative for tension, i.e. retraction. Five cycles of deformation were accomplished. The anvil deformation rates were varied as well to test if the total strain imposed on the crystal potentially has any effect on the hysteresis. Note that the oscillations were pre-programmed into the PLC so that the press immediately reversed advancement rates for each cycle so as not to allow a recovery period in the crystal.

### 3. Results

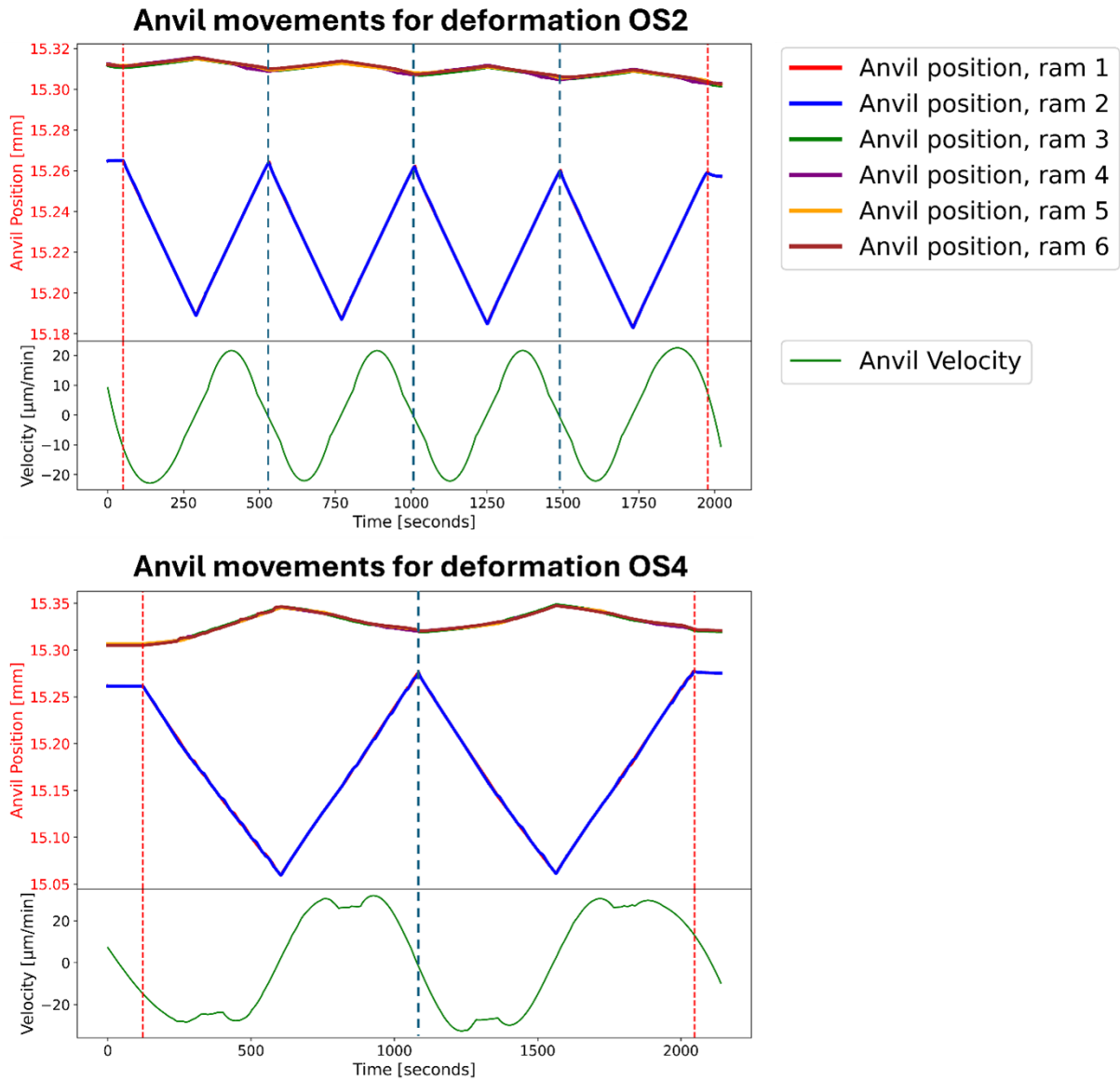


**Figure 77.** Anvil movements of two cyclical deformation experiments. Experiment OS2 and OS4 are illustrated in the top and bottom plot respectively. OS2 consists of an experiment with four deformation cycles and OS4 of two deformation cycles. The anvil velocities are also shown below. The velocities seem sinusoidal and overly smooth because of the Savitzky-Golay filter applied to remove the noise. In actuality, the velocities match with the cycles accurately. Blue vertical dashed lines mark the full cycles.

Two cycles, OS2 and OS4, are illustrated in **Figure 77**. The top plot, OS2, shows the anvil movements during a four-oscillation deformation. Each cycle is defined by a return to the initial anvil positions, so each consists of a compression and a tension strain rate. These points are marked with blue vertical dashed lines. The anvil velocity may at first glance seem offset from the actual anvil movements, but this is only a result of the Savitzky-Golay filter applied to

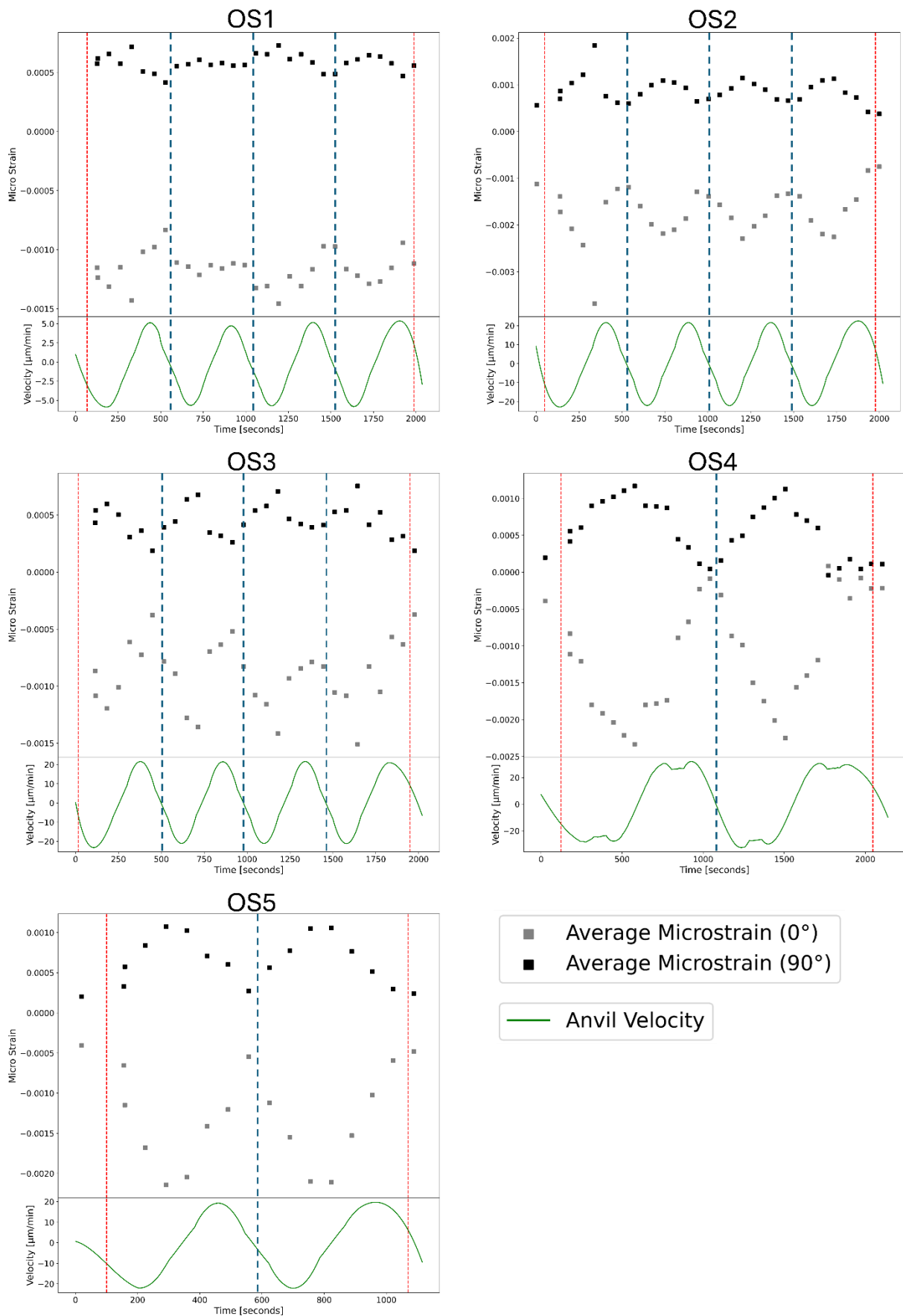
### 3. Results

remove the high-frequency noise from the anvil velocity data. The window size of 401 seconds used in the filter coupled with the shorter deformation cycles obscures the point at which velocities were reversed. Apart from the minima and maxima of the anvil positions due to the varying strain rates and deformation duration, the other cyclical deformation experiments are similar in appearance.

For these experiments, no x-ray radiography images were taken of the deformation column before and after the experiments. Thus, no strain measurements are possible. The averaged microstrains from each fitted San Carlos olivine peak are shown in **Figure 78**. Apart from OS4 and OS5, all the cyclical deformation experiments begin at a positive deviatoric stress. This can be seen by the splitting of the D1 (azimuth  $0^\circ$ ) and D2 (azimuth  $90^\circ$ ) microstrains already at the start of deformation. Even so, the cyclical anvil movements are clearly recorded in the lattice microstrains and in OS4 there is enough strain rate in a full cycle to bring the deviatoric stress to roughly zero.

### 3. Results

## Average lattice microstrains from D1 (0°) and D2 (90°)



### 3. Results

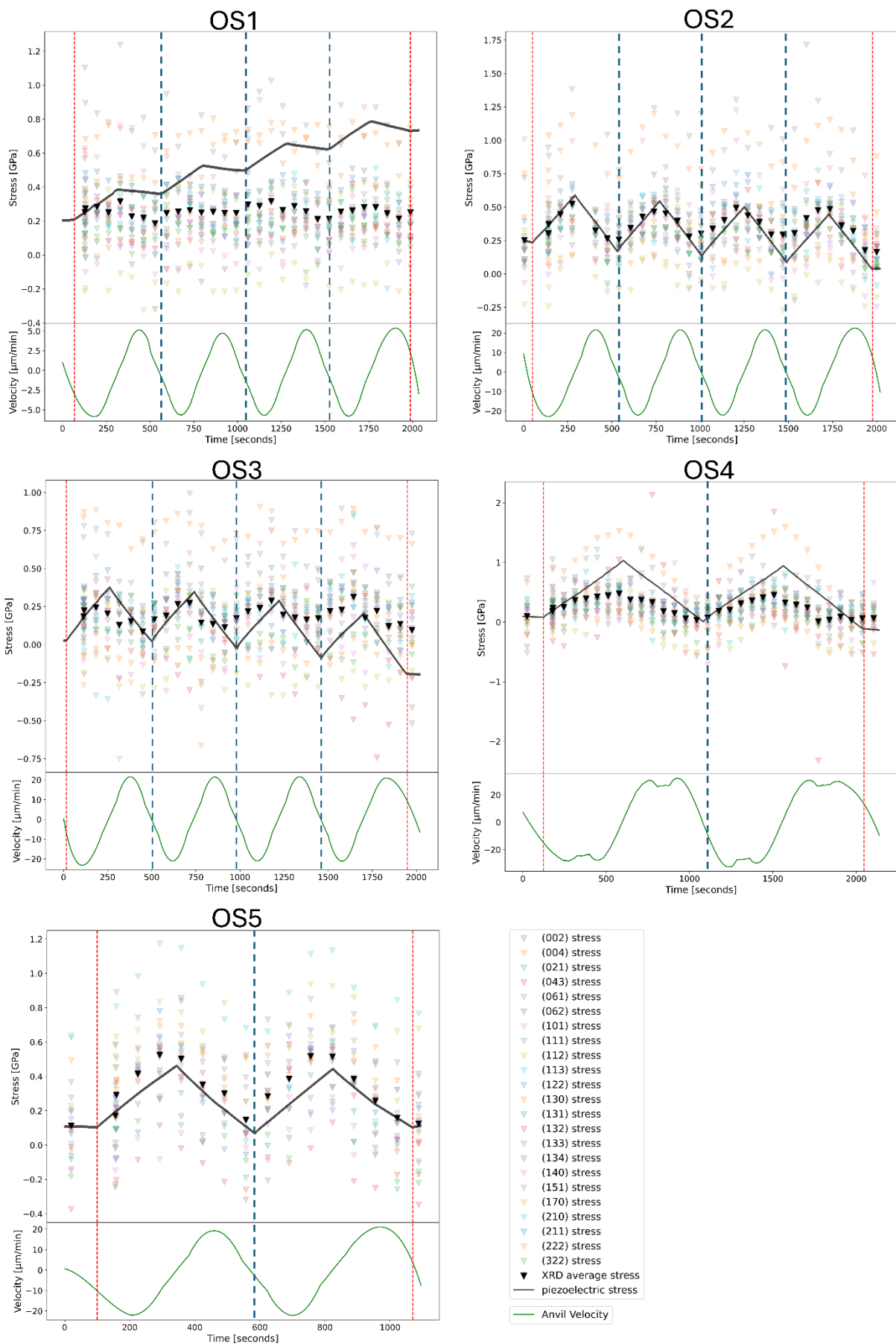
**Figure 78.** *Averaged lattice microstrains as measured by the D1 and D2 detectors for the cyclical deformation experiments. Blue vertical dashed lines mark cycles.*

**Figure 79** overlays the calculated XRD stress and measured piezoelectric method stress once again. The large spread of each peak's fitted stress, in particular (140) and (151) in OS1, OS2, and OS3, shows the issue with the wide range of stresses measured by each peak in XRD. Although, with the large number of peaks fitted the averaged XRD stress, plotted with black triangle markers, still forms a clear cyclical signal. In comparison, the piezoelectric-determined stress, also displays this cyclical nature. However, the piezoelectric stress is much sharper and shows an immediate response in the signal to direction reversals in anvil movement.

Deformation OS1 has a drift in the piezoelectric-determined stress that the fitting method used in all experiments did not remove. Each tension portion seems to have not reversed the signal completely, leading to an almost linear upwards drift in stress. The other experiments do not display the same issue. The piezoelectric method, having much higher temporal resolution, records sharp stress changes when the anvils stop and reverse while the XRD measured stress does not, following a smoother transition, especially visible in OS4. Apart from the fact that each XRD measures in fact an average stress over the period of the XRD exposure time, another reason could be that the piezoelectric crystal is coupled to the deformation anvil through a 1 mm thick diamond disk. Therefore, any application of force from the anvil is immediately recorded in the current signal while the sample lags behind due to frictional losses and strain accommodated by the other assembly parts.

### 3. Results

#### XRD and piezoelectric method measured deviatoric stress



### 3. Results

**Figure 79.** Stresses as measured with both the XRD and piezoelectric method. The XRD stresses from every fitted peak are shown (triangles). The average XRD-determined stresses are shown as black triangles. The black line is the stress as measured by the piezoelectric method.

#### 3.3. Linear compression and tension deformations on $\text{MgAl}_2\text{O}_4$ spinel at room temperature with XRD

**Table 16.** The isentropic bulk modulus ( $K_{S0}$ ) in GPa of the samples deformed. (Mao et al., 2015)<sup>a</sup>, (Yoneda, 1990)<sup>b</sup>.

	$K_{S0}$ [GPa]
San Carlos olivine	129.8(9) <sup>a</sup>
$\text{MgAl}_2\text{O}_4$ spinel	197.9(2) <sup>b</sup>
MgO	162.7(2) <sup>b</sup>

$\text{MgAl}_2\text{O}_4$  spinel was chosen as a test material because it has a higher bulk modulus and yield strength than olivine (Hansen et al., 2019; Palmour et al., 1963; Rufner et al., 2014; Sokol et al., 2017). Initially, heating issues caused sudden and drastic drops in resistance across the piezoelectric crystal, prompting a shift to room temperature experiments although heating could still be used to relax the sample stresses before and between measurements.

Despite the predominantly brittle nature of deformation at room temperature, the deformation of a higher bulk modulus material provides a useful test because it results in higher stresses being supported within the sample before failure. The bulk moduli of all three materials tested in this thesis are listed in **Table 16**. Because the piezoelectric crystal generates a charge separation proportional to the elastic compression of the crystal, there is a maximum limit to how much stress it can measure before the deformation induces inelastic strain, which is not measured by the crystal.

In other words, there is a plateau to the maximum measurable stress. This behavior is akin to how stresses are measured with XRD, as it can only do so through the elastic microstrain of the lattice. If the sample has a higher yield strength than the piezoelectric crystal, the stress measured by the crystal would plateau once the crystal's yield strength is reached. The charge trend under these conditions would appear identical to the charge trend for the sample creeping, where stress does not increase proportionally with strain.

To better characterize if this limit is of concern in a typical deformation experiment,  $\text{MgAl}_2\text{O}_4$  spinel was deformed at room temperature and high pressure above 2 GPa to generate high stresses within the sample. These experiments were done at the P61B beamline at the PETRA-

### 3. Results

III synchrotron in DESY, Hamburg. Different deformation rates and times were used to determine if plastic creep could be achieved in the sample and if the piezoelectric crystal records the yield strength of the sample at this point.

**Table 17.** Run table of three linear compression and two linear tension deformations on  $MgAl_2O_4$  spinel at room temperature.

Cycle	Type of deformation	Oil pressure [bar]	Sample pressure [GPa]	Anvil rate [ $\mu\text{m}/\text{min}$ ]	Deform time [min]
C4	Compression	45.0	2.6	6.7	44.4
C5	Compression	45.0	2.6	4.4	66.7
C6	Compression	45.0	2.6	2.9	100.0
T6	Tension	40.5	2.4	6.7	44.4
T7	Tension	40.5	2.4	4.4	66.7

**Table 17** lists the experiments on  $MgAl_2O_4$  spinel. A pair of compression and tension phases forms a ‘cycle’. Between cycles, the sample was heated to 1000 °C for up to one hour to relax the sample and reduce stresses to zero. The last tension deformation failed as the platinum wire on the crystal, passing through the assembly, ‘pinched’ off.

**Figure 80** has all the lattice microstrains of the deformation experiments plotted, averaged for all the fitted peaks. As is clear, the compression experiments successfully started with close to zero stress in the sample. Additionally, immediately retracting the anvils after a compression deformation, to induce a tension deformation, successfully brought the lattice microstrains back close to zero. The stress hysteresis in  $MgAl_2O_4$  spinel is minimal at room temperature.

As with the San Carlos olivine experiments, the full deformation column was imaged using x-ray radiography before and after every deformation. The measured engineering strain and length difference in microns has been calculated and shown in **Figure 81**. While once again the anvil rate and deformation time programmed into the PLC is not a completely accurate measure of the actual sample shortening or lengthening measured, the strain rate is at least proportionally increasing with increased anvil rate.

The anvil rate and deformation time were both adjusted in each deformation cycle to result in a total shortening or lengthening of the sample of 300  $\mu\text{m}$ . As can be seen by the right-handed plots in **Figure 81**, the total strain of the sample was less than this. The total engineering strain of the deformation column does match closest to the strain of the sample, labeled  $\text{Sample}_m$  in the left side plots.

### 3. Results

Once again, some of the foils (Foil<sub>b</sub>, Foil<sub>t</sub>, N<sub>b</sub>, N<sub>t</sub>) and shorter sample disks (Sample<sub>b</sub>, Sample<sub>t</sub>) show unreasonable amounts of strain. This most likely results from a tilting or misorientation of the materials and is not due to actual strain. Since these parts are thin and 4 mm in diameter, even a small angle of misorientation, when imaged edge-on, would result in the material appearing to be much thicker. The total strain measured is closest to the Sample<sub>m</sub> strain, which is the 3 mm length sample that is under investigation. This at least suggests that with both San Carlos olivine and MgAl<sub>2</sub>O<sub>4</sub> spinel, the strain measured by the position encoders on the anvils could be used as a reasonable measurement of the sample strain, after correction for the anvil strain itself.

### 3. Results

#### Average lattice microstrains from D1 (0°) and D2 (90°)

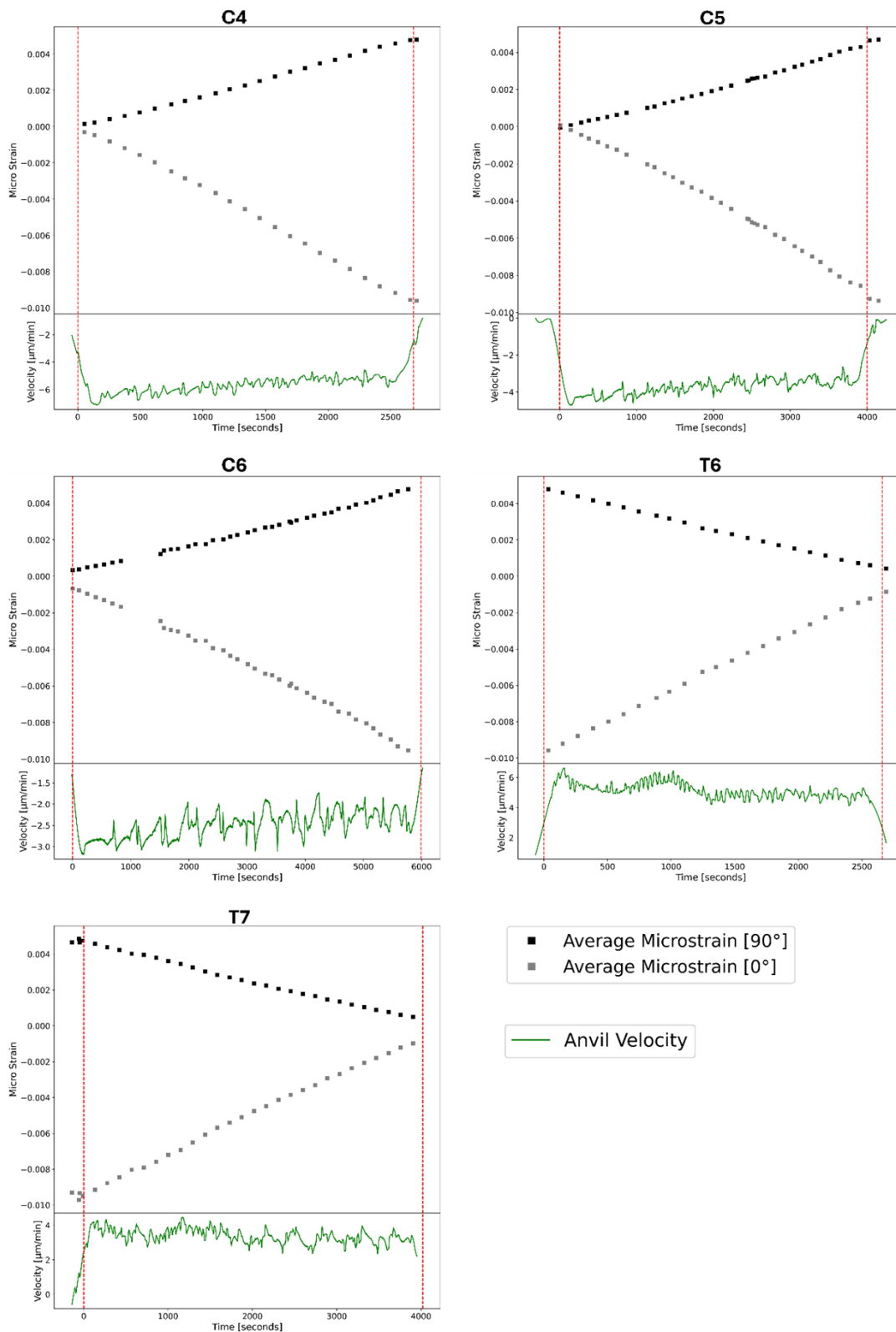


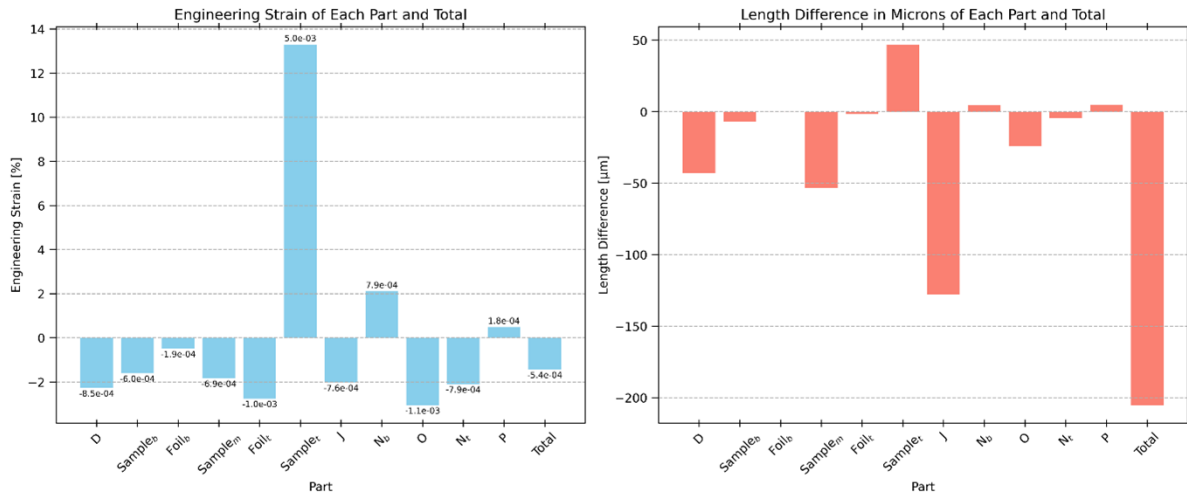
**Figure 80.** Averaged lattice microstrains as measured by the D1 and D2 detectors, for C4, C5, C6, T6, and T7. In this case, the lattice strains begin and end close to zero with each experiment.

### 3. Results

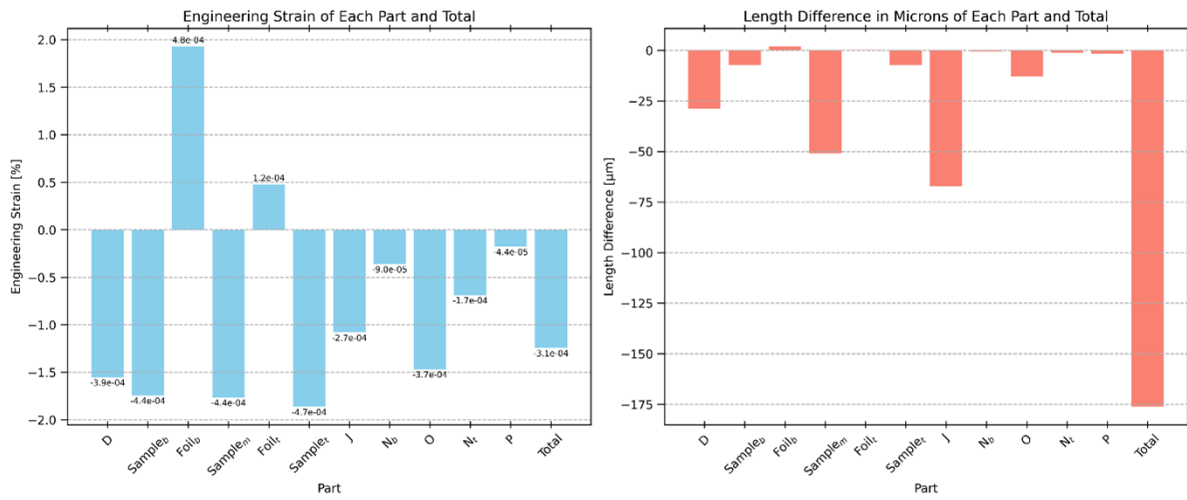
*This exemplifies adequate stress recovery from the sample, with little to none being relaxed between the deformations.*

### 3. Results

#### C4 Strain measurements of $MgAl_2O_4$ spinel



#### C5



#### C6

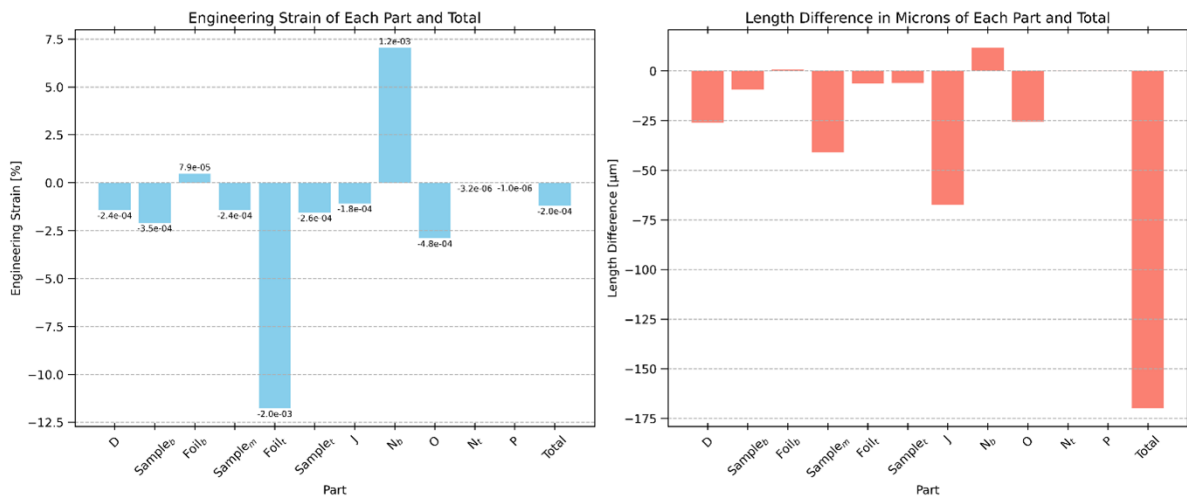


**Figure 81.** The measured strains of C4, C5, and C6. On the left side are the engineering strain measurements and on the right side the length difference in images. The engineering strain bar

### 3. Results

plots also list the calculated strain rates for each part at the end of the bars. The units for these are  $s^{-1}$ .

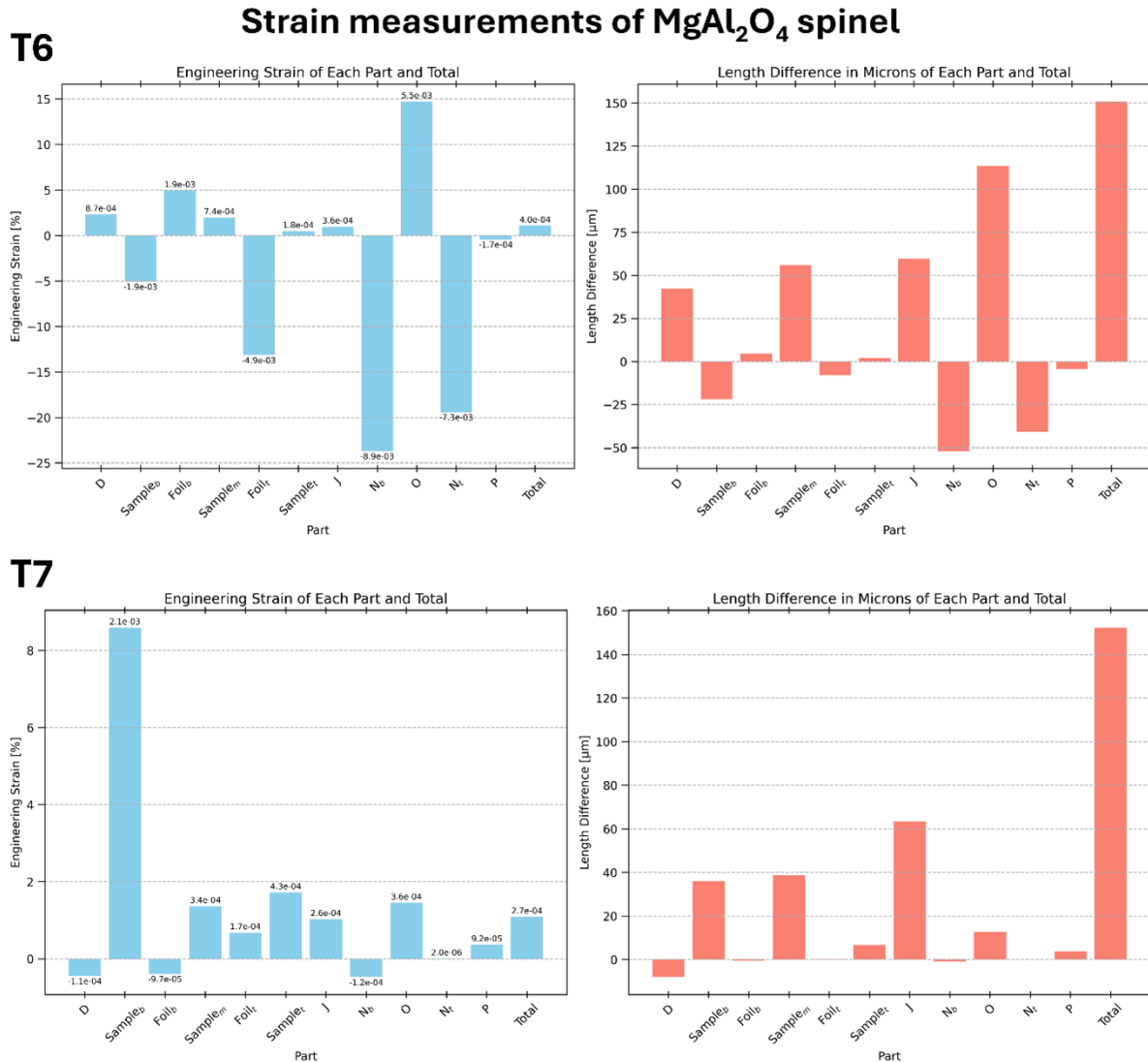


**Figure 82.** The measured strains of T6 and T7. Each tension deformation engineering strain is on the left side and the length difference of each part on the right side. The engineering strain bar plots also list the calculated strain rates for each part at the end of the bars. The units for these are  $s^{-1}$ .

The calculated stresses using both XRD and piezoelectric method are plotted in **Figure 83**. As expected, the deviatoric stresses increase to substantially higher levels as compared to the high-temperature olivine experiments. The average XRD measured stress in the spinel reaches above 4 GPa, higher even than the confining pressure. For these experiments, no XRD was taken of

### 3. Results

the MgO sleeve around the sample to calculate the hydrostatic pressure. However, using the equation of state of  $\text{MgAl}_2\text{O}_4$  spinel (Yoneda, 1990) and the d-spacing at the azimuthal angle of  $54.74^\circ$ , the hydrostatic pressure did not exceed 3 GPa at any point during deformation.

Even at very high deviatoric stresses, the CTGS piezoelectric crystal continues to register increasing stress. However, during deformation runs C4, C5, and C6, a discrepancy arises in the latter half of each experiment, where the XRD measurements and the stress recorded by the CTGS sensor begin to diverge. One plausible reason for this could be that the CTGS crystal itself is approaching its elastic limit. Since the piezoelectric crystal can only generate a signal when it is elastically deforming, reaching this limit could lead to the observed reduction in stress accumulation rates, indicating the onset of inelastic, permanent deformation in the CTGS crystal.

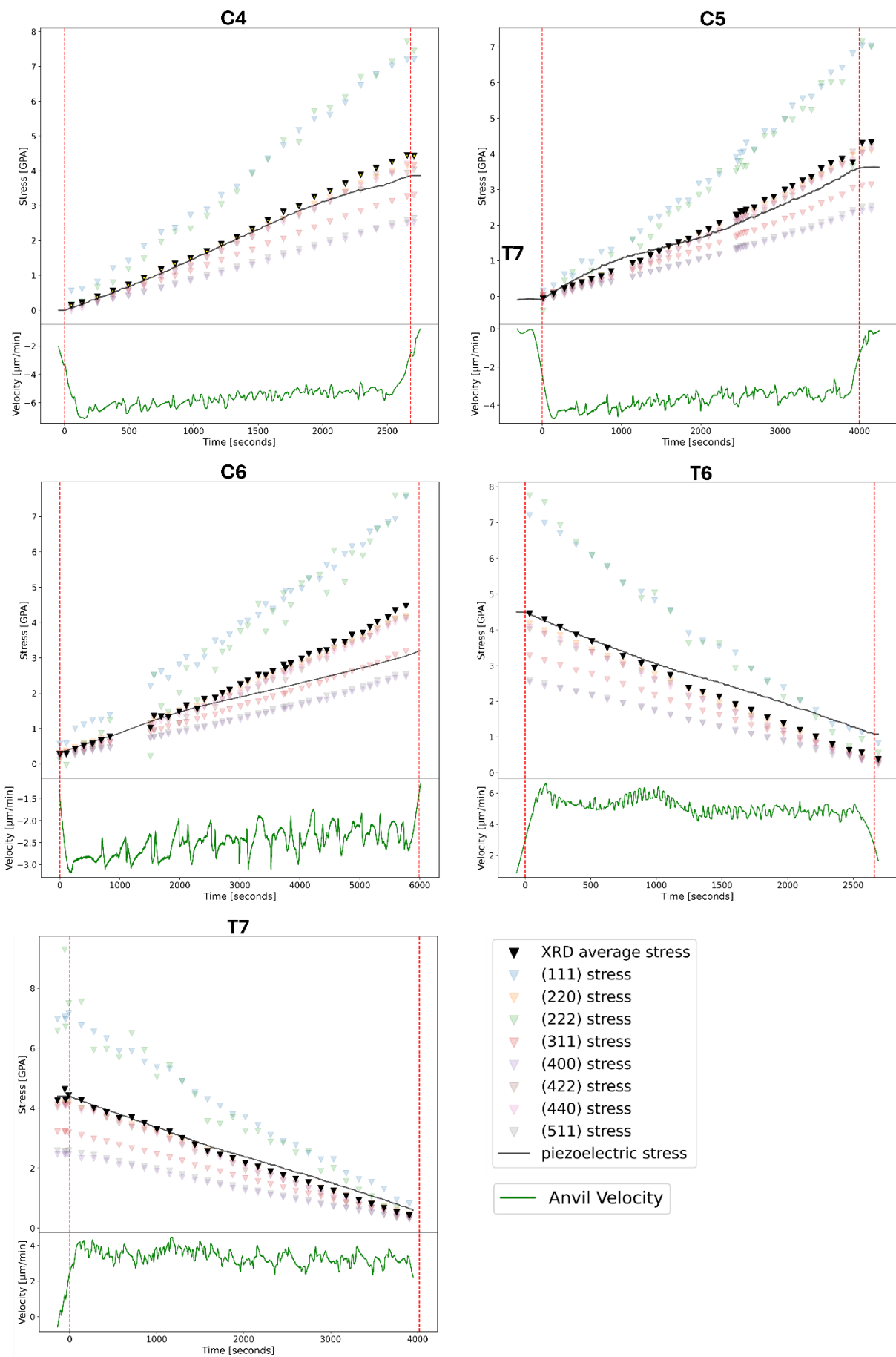
This decrease in the rate of stress accumulation is consistently observed at around 2 GPa of deviatoric stress in each experiment. To confirm whether this threshold corresponds to the elastic limit of the CTGS crystal or whether it may be due to inaccuracies in the XRD stress measurements, further experimental investigation is necessary.

Despite these discrepancies, the XRD measurements of spinel continue to show a linear increase in stress throughout the deformation, suggesting that spinel remains within its elastic regime and has not undergone significant inelastic deformation. The piezoelectric signals recorded in these room-temperature experiments also display greater stability and fewer issues with signal oscillation or ferroelastic switching compared to the high-temperature experiments conducted on San Carlos olivine. While the high-temperature experiments confirm that piezoelectric stress measurements can be effectively performed at elevated temperatures, the room-temperature experiments on spinel demonstrate that the technique provides more accurate and precise measurements under these conditions.

The 2 GPa stress limit observed could indicate that the CTGS crystal is reaching its elastic limit, or it may reflect inaccuracies in the XRD technique. Nevertheless, at higher temperatures, where materials tend to soften, this stress limit is unlikely to present a significant issue under real-world geological conditions.

### 3. Results

#### XRD and piezoelectric method measured deviatoric stress



### 3. Results

**Figure 83.** Deviatoric stresses as measured with both the XRD and piezoelectric method on  $MgAl_2O_4$ . The three (C4, C5, C6) compression experiments and the three tension experiments are shown. The bottom plot shows the anvil velocity.

#### 3.4. Linear compression and tension deformations on MgO at room temperature with XRD

After  $MgAl_2O_4$  spinel, polycrystalline MgO was deformed. Identical sample pressures, anvil rate, and deformation times were applied as in the spinel experiments.

**Table 18.** Run table of three linear compression and three linear tension deformations on MgO at room temperature.

Cycle	Type of deformation	Oil pressure [bar]	Sample pressure [GPa]	Anvil rate [ $\mu\text{m}/\text{min}$ ]	Deform time [min]
C7	Compression	45.0	2.6	6.7	44.4
C8	Compression	45.0	2.6	4.4	66.7
C9	Compression	45.0	2.6	2.9	100.0
T8	Tension	40.5	2.4	6.7	44.4
T9	Tension	40.5	2.4	4.4	66.7
T10	Tension	40.5	2.4	2.9	100.0

Once again, all the deformation cycles of MgO listed in **Table 18** were at room temperature. In this case, unlike the  $MgAl_2O_4$  spinel deformation, the last tension experiment was successful (T10). After each pair of compression and tension deformation cycles, the sample was heated to 1000 °C for 30 minutes to relax stresses. Unfortunately, this was not adequate to completely relax the stresses as can be seen in **Figure 86**.

The lattice microstrains indicate that each compression deformation cycle started with residual tensional stress. This tensional stress, visible in the microstrain plot, gradually decreased, passing through a point of zero stress, and then transitioned into positive compressional stress. Additionally, although as in the previous deformation of spinel, no heating was used before the tension deformation, substantial stress hysteresis is present in MgO. The lattice microstrains always crossed during the deformation and reversed.

The plots of the measured strain also exemplifies the weaker nature of MgO as compared to the spinel. Both the engineering strain and the absolute micron difference in the sample length,  $\text{Sample}_m$ , are larger with the MgO sample compared to the spinel sample. The slowest compression deformation, C9, shows an anomalous decrease in length of the  $ZrO_2$  plug at the

### 3. Results

bottom of the assembly (D). It is unclear why the zirconia plug shortened more than usual during this deformation experiment.

### 3. Results

## Strain measurements of MgO

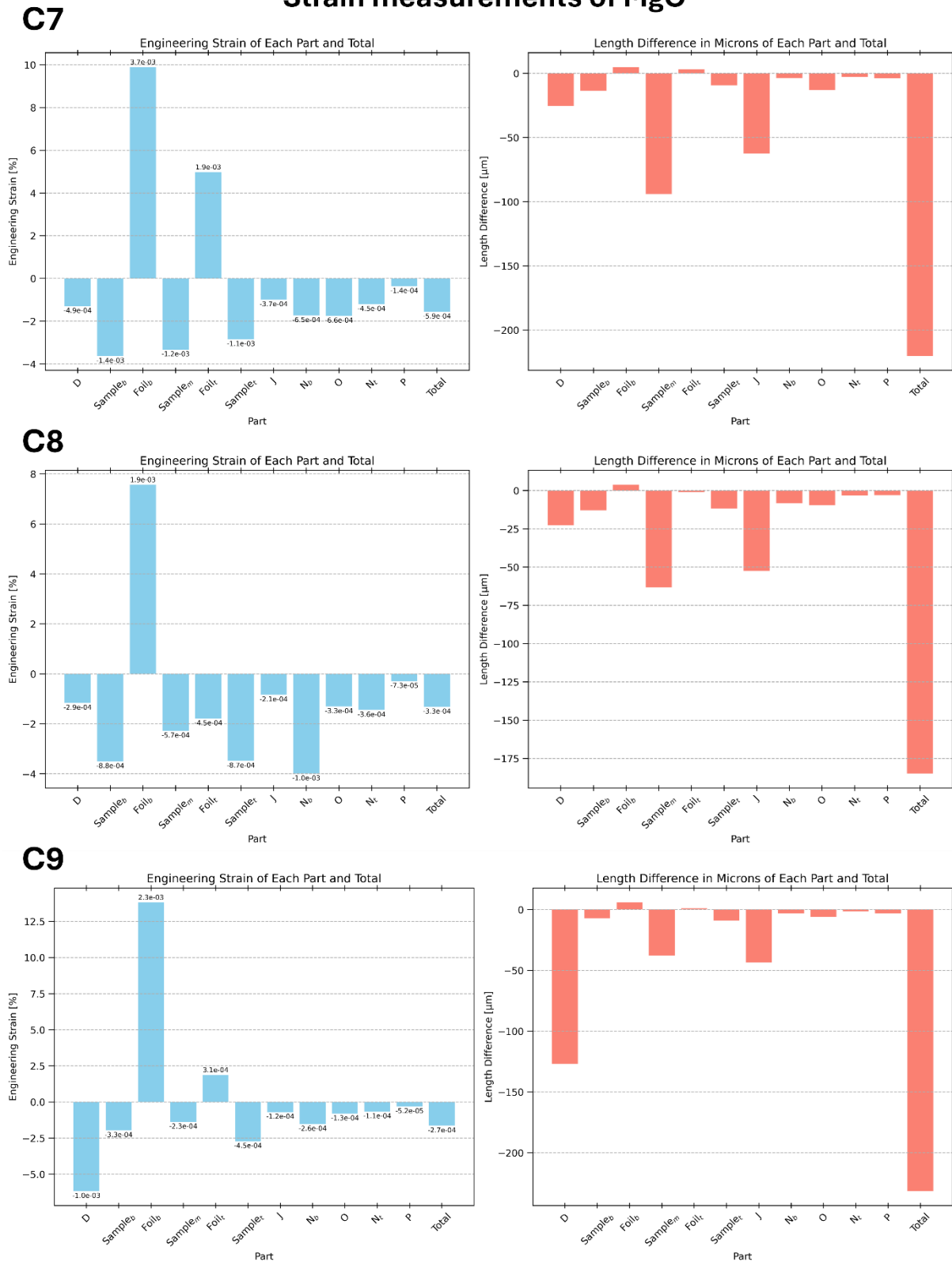
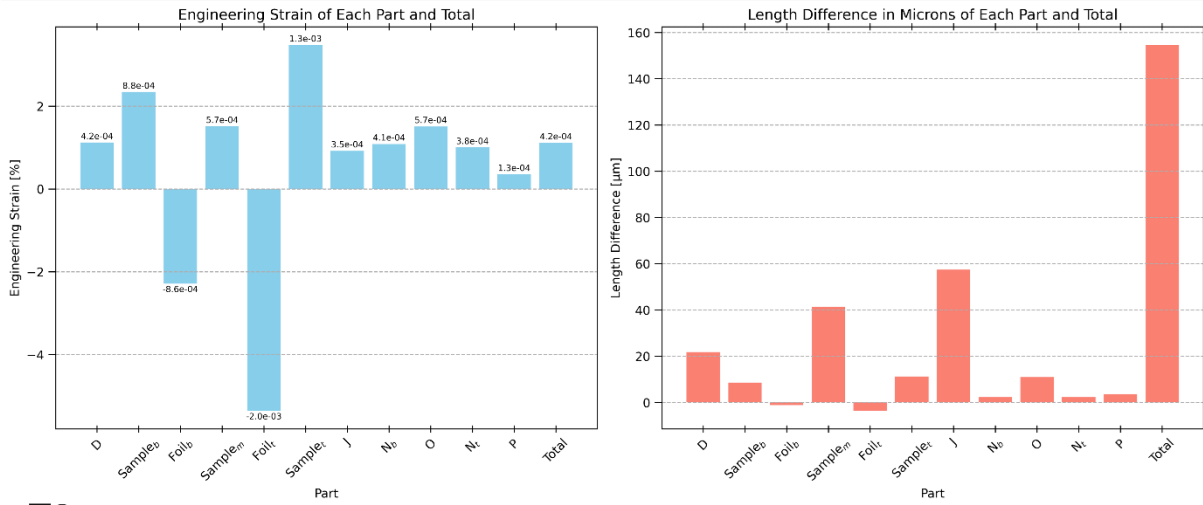


**Figure 84.** Compression strains for C7, C8, and C9 on MgO. Displayed are the engineering strain (left) and length change in microns (right), derived from x-ray radiography pre- and post-deformation. Strain rates are indicated adjacent to each bar, with units in s<sup>-1</sup>.

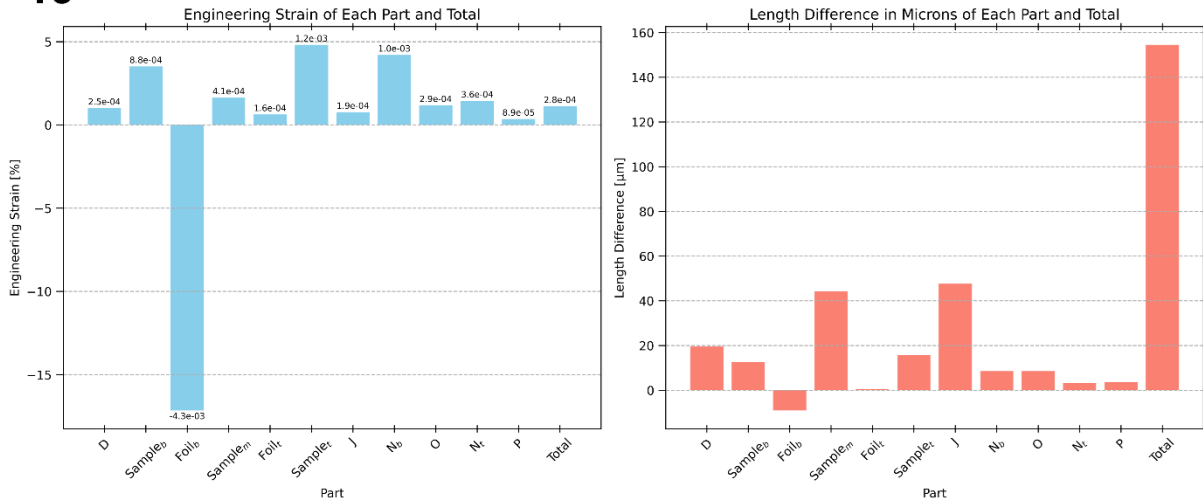
### 3. Results

## Strain measurements of MgO

T8



T9



T10

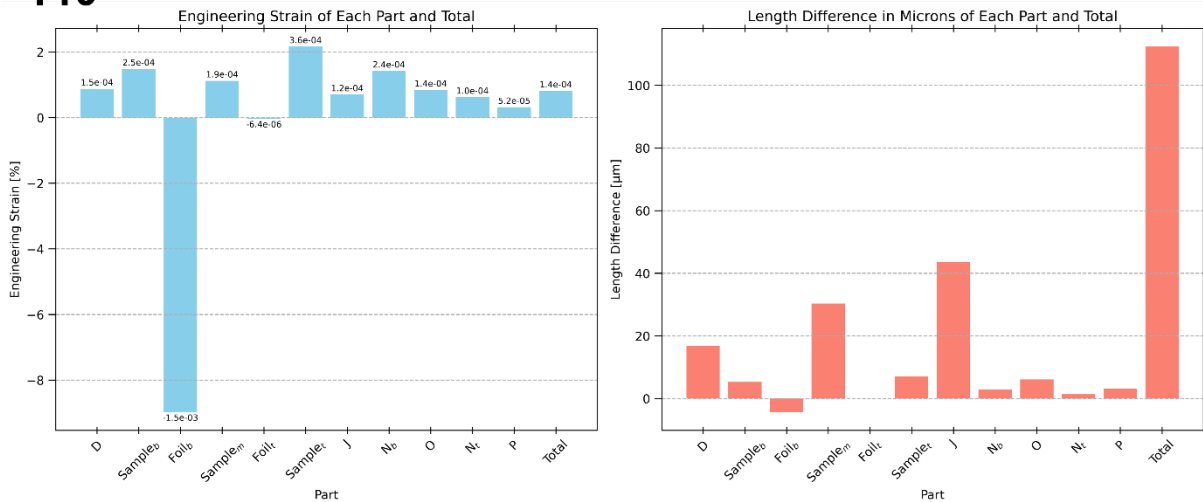


**Figure 85.** Tension strains for T8, T9, and T10. Engineering strain (left) and micron-scale length change (right) are presented, based on x-ray radiography before and after tensioning. Strain rates are denoted beside each corresponding bar, in  $s^{-1}$ .

### 3. Results

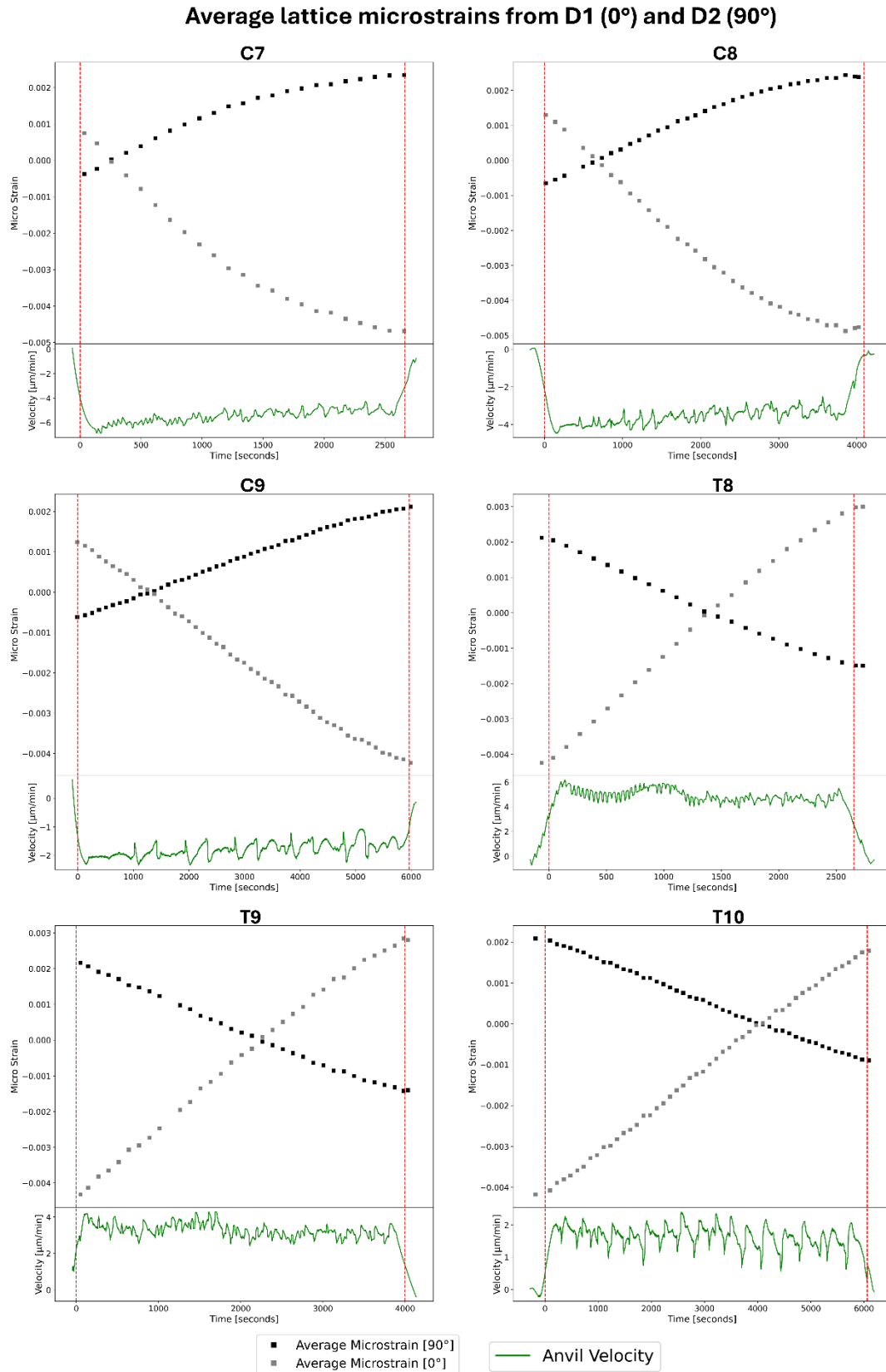


**Figure 86.** Averaged lattice microstrains for C7, C8, C9, T8, T9, and T10, as detected by D1 and D2. Notably, microstrains ‘overshoot’ and switch positions, indicating a significant

### 3. Results

*relaxation of stress between experiments on MgO, contrary to the convergence towards 0 observed in previous deformations on MgAl<sub>2</sub>O<sub>4</sub>.*

The MgO sample strain,  $\text{Sample}_m$ , increased consistently with an increasing rate of anvil movement. This is not entirely expected as the anvil rates and deformation time were specifically chosen to result in the same total strain for all cycles. The fact that the strain on the sample is larger even though the total deformation column strain is roughly equal between each experiment can be explained by the plots in **Figure 87**.

The higher anvil movement rate experiment, C7, reaches a higher final stress state in the MgO as compared to the slower C8 or slowest C9. In all cases, the stress, measured both from XRD and the piezoelectric method, is close to linear to about 2.5 GPa. Beyond this point, plastic flow begins and the stress increases at a slower pace with increasing strain. Both C7 and C8, beyond 2.5 GPa of deviatoric stress, show this flattening of the strain-stress curve. The piezoelectric method also follows the same pattern.

The piezoelectric signal in C7 has two kinks in it because in this experiment the voltage drift was larger than usual. The two kinks are when the voltage drifted past the integrating capacitor limit of 10 V. At this voltage, referring to **Figure 38**, the integrator closes switch  $S_2$  which discharges the capacitor back to 0 V and begins integrating the charge again. At this point, the voltage has been reset to 0 V.

In most deformation experiments, the voltage drift is low enough that the reset point at either -10 V or +10 V is never reached. Previous experience with the charge integrator has shown that at the 'reset' point of 0 V, the capacitor charging rate is not linear. It tends to flatten at the high end of the voltage range and is steeper at the lower end of the voltage range. This is why in C7 the piezoelectric stress before the kink, where it is approaching either +10 V or -10V, has a smaller slope and once it resets to 0 V, the slope is briefly steeper, forming a humped shape. As most experiments did not have drift enough to reach the limits, no further work was done to find the source of this nonlinear voltage increase.

### 3. Results

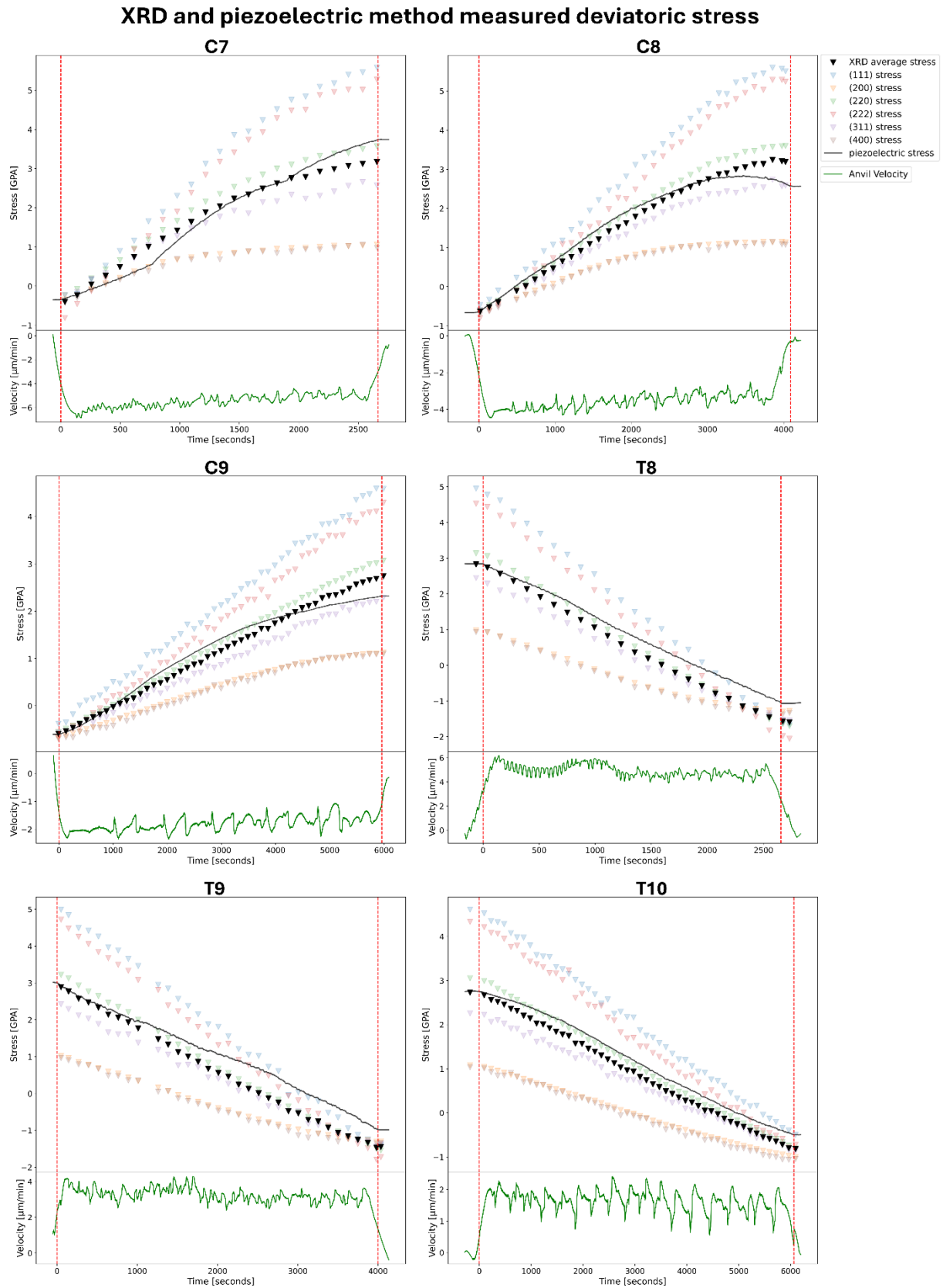


**Figure 87.** Deviatoric stresses measured via XRD and piezoelectric methods for MgO. Showcased are the compression (C7, C8, C9) and tension (T8, T9, T10) experiments. The lower graph illustrates the anvil velocity for each run.

### 3. Results

As with  $\text{MgAl}_2\text{O}_4$  spinel experiments, tension i.e. deformation through anvil retraction, was also conducted. The three runs, T8, T9, and T10 all behaved well and the piezoelectric stress closely matches the XRD measured stress. Even at the higher stresses of over 2 GPa, no plateau in stress was seen. The results seem reasonable. None reached the flow strain regime and thus the stresses are largely linear through the whole deformation cycle. In general, it was found that the piezoelectric stress measurement method was consistently more stable, precise, and easier to work with during tensile deformation.

#### 3.5. Single crystal MgO and Fo deformation in the creep regime

Single crystal deformation experiments at high pressures and temperatures, as opposed to polycrystalline samples allow specific slip planes to be targeted. In previous high pressure experiments on single crystals, stresses were measured by including powdered materials within the same deformation column and using XRD microstrain determinations (Girard et al., 2012). This is necessary because high pressure deformation devices do not allow the single crystal samples themselves to be rotated as in single crystal X-ray diffractometry. The piezoelectric method, however, allows such measurements to be performed away from a beamline. Several previous studies have been performed on MgO and forsterite single crystals to measure the stress and strain relations at various hydrostatic pressures and temperatures and at different orientations of the single crystals to the direction of deviatoric stress. (Darot & Gueguen, 1981; Demouchy et al., 2009; Girard et al., 2012; Mei et al., 2008; Raterron et al., 2007).

Single crystal studies, that have generally been performed with the Patterson or Griggs apparatus, can be used to evaluate the piezoelectric method as the effects of grain size and grain boundary effects are eliminated. To compare with previous studies, MgO and forsterite single crystals were deformed with the piezoelectric crystal as the stress sensor at high pressure and temperature. The deformation experiments are shown in **Table 19**. These experiments were undertaken with the MAVO LPQ7-2400-100 press present at BGI using the MA6-6 15/10 cubic piezoelectric assembly described previously in section 2.2.1.

***Table 19.** Results of deformation experiments on single crystals, forsterite and MgO, with  $\sigma_1$  along [100]. The experiments indicated in bold reached the creep regime, i.e., flow stress. Otherwise, the maximum  $\sigma$  provided is right at the end of deformation as opposed to sometime*

### 3. Results

before the end of deformation for the bolded rows. All experiments are at a strain rate of  $5 \times 10^{-5} \text{ s}^{-1}$  (7.2  $\mu\text{m}/\text{min}$  anvil advancement rate) for 55.55 minutes.

Forsterite single crystal [100]			
Oil pressure [bar]	Sample pressure [GPa]	Temperature [°C]	Maximum $\sigma$ [MPa]
15.3	1.5	800	1779
15.3	1.5	1000	1554
15.3	1.5	1200	1280
15.3	1.5	1300	1156
24.1	2.3	600	1960
24.1	2.3	800	1704
24.1	2.3	1000	1531
<b>24.1</b>	<b>2.3</b>	<b>1200</b>	<b>1368</b>
<b>24.1</b>	<b>2.3</b>	<b>1300</b>	<b>1175</b>
33.4	3.0	600	1375
33.4	3.0	800	1545
33.4	3.0	1000	1590
<b>33.4</b>	<b>3.0</b>	<b>1200</b>	<b>1552</b>
<b>33.4</b>	<b>3.0</b>	<b>1300</b>	<b>1343</b>
MgO single crystal [100]			
Oil pressure [bar]	Sample pressure [GPa]	Temperature [°C]	Maximum $\sigma$ [MPa]
<b>15.3</b>	<b>1.5</b>	<b>800</b>	<b>750</b>
<b>15.3</b>	<b>1.5</b>	<b>1000</b>	<b>481</b>
<b>15.3</b>	<b>1.5</b>	<b>1200</b>	<b>217</b>
<b>15.3</b>	<b>1.5</b>	<b>1300</b>	<b>99</b>
24.1	2.3	600	1377
<b>24.1</b>	<b>2.3</b>	<b>800</b>	<b>1060</b>
<b>24.1</b>	<b>2.3</b>	<b>1200</b>	<b>578</b>
<b>24.1</b>	<b>2.3</b>	<b>1300</b>	<b>364</b>
33.4	3.0	600	1666
33.4	3.0	800	1449
33.4	3.0	1000	1417
<b>33.4</b>	<b>3.0</b>	<b>1300</b>	<b>409</b>

Since X-ray radiography could not be used to measure the actual strain rate on the sample, the strain rate was calculated from the anvil position encoders on the press. As was seen from the XRD experiments, the sample strain is generally less than that recorded by the encoders. Analyzing the sample height after deformation is not necessarily feasible as during decompression the samples often crack, leaving large joints throughout, and sometimes the samples even crumble. This makes the sample length determination after some experiments inaccurate.

Thus, an approximation for strain rate was made assuming that all anvil movement is applied to sample shortening. The strain rate discrepancy between that assumed and the true strain rate

### 3. Results

on the sample is likely to be inaccurate only by a factor of 2 or 3. The estimate comes from experiments conducted at the synchrotron with the same assembly showing that the calculated strain rate on the whole assembly only varies by factors of 2 – 3 from the strain rate on the sample.

To determine whether the stress became constant, i.e., the sample is in a creep regime, the maximum stress was found and if this occurred before the end of deformation, as opposed to directly at the end of deformation, the sample was assumed to be in a creep regime. These specific deformation experiments, where a creep state was reached, are indicated in the run table (**Table 19**) in bold. As expected, the highest temperature deformation experiments as well as those at lower pressures are more likely to reach a creep state within the deformation time. The only exception is the forsterite sample, where the lowest pressure run at 1.5 GPa never reached an expected creep state.

### 3. Results

#### Deformation of single crystal forsterite

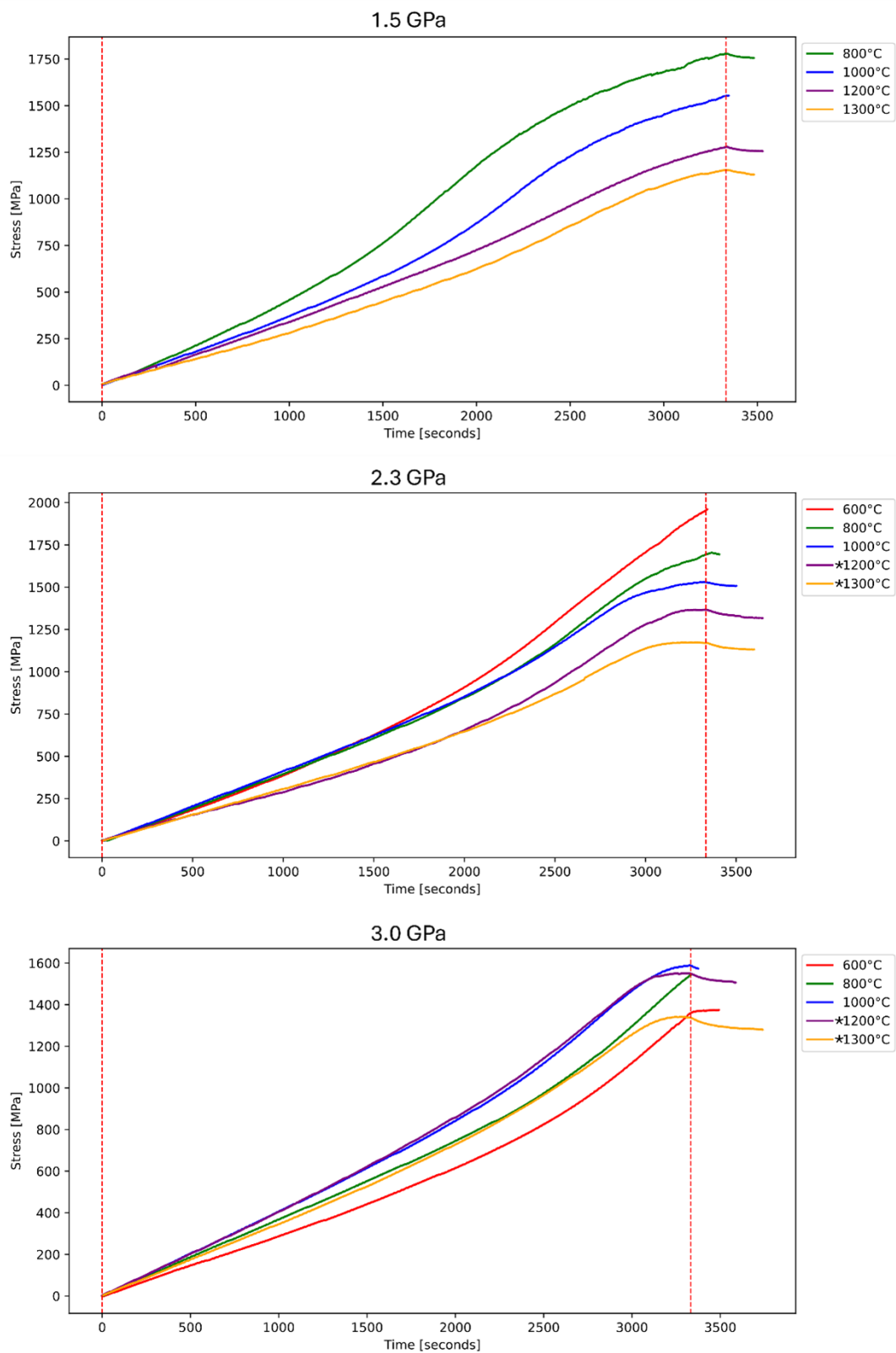


**Figure 88.** Stress, as measured with the piezoelectric method using CTGS as the piezoelectric crystal, of synthetic single crystal forsterite. Each separate plot is at a different hydrostatic pressure and each curve corresponds to a different temperature. The red, vertical dashed lines

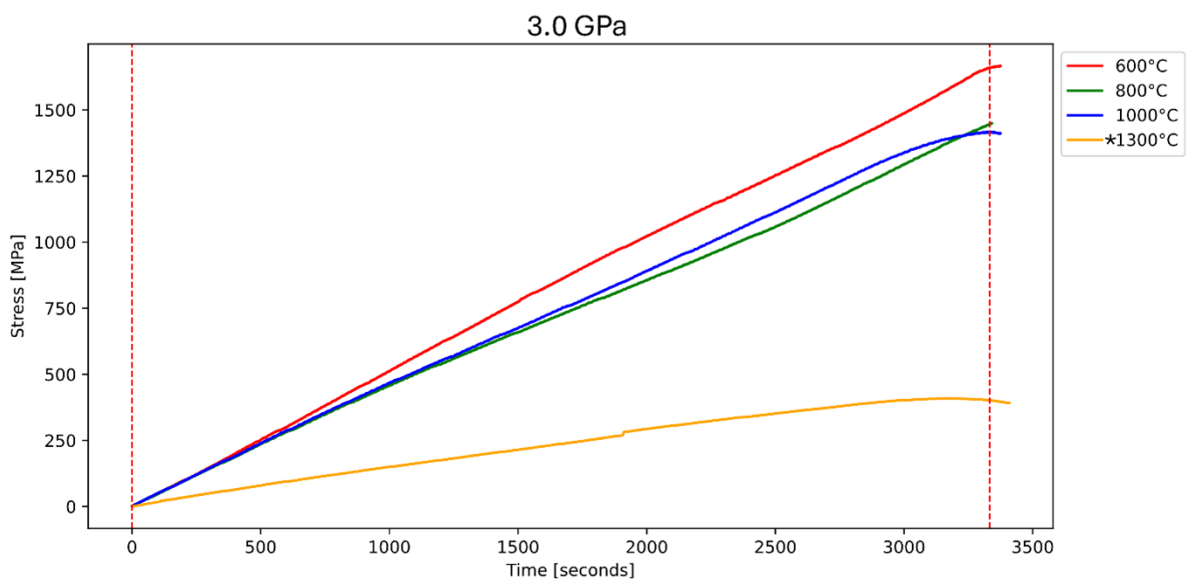
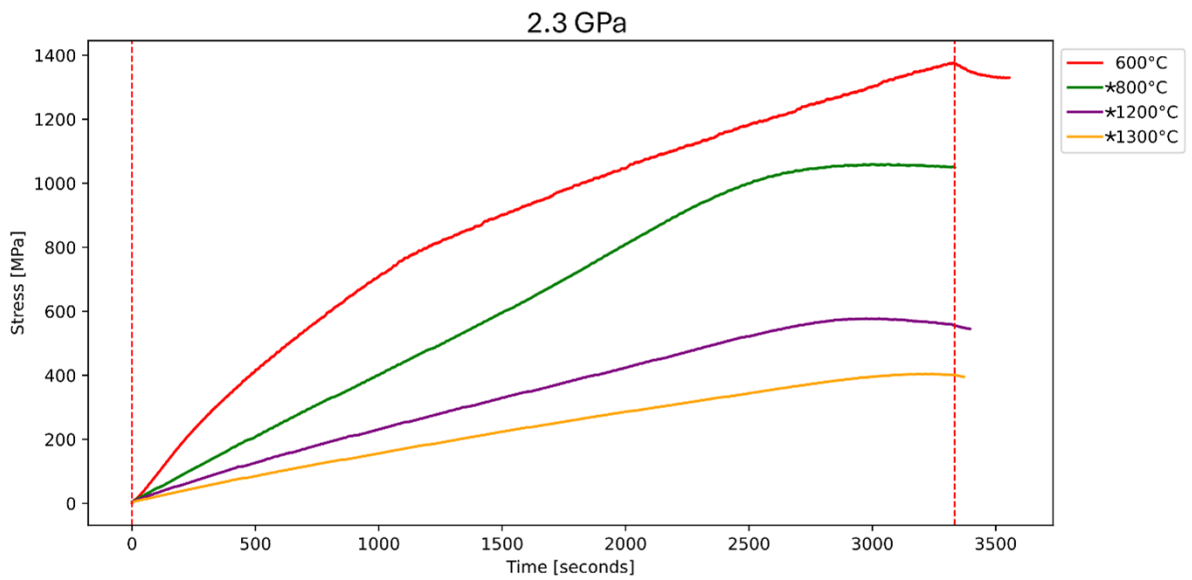
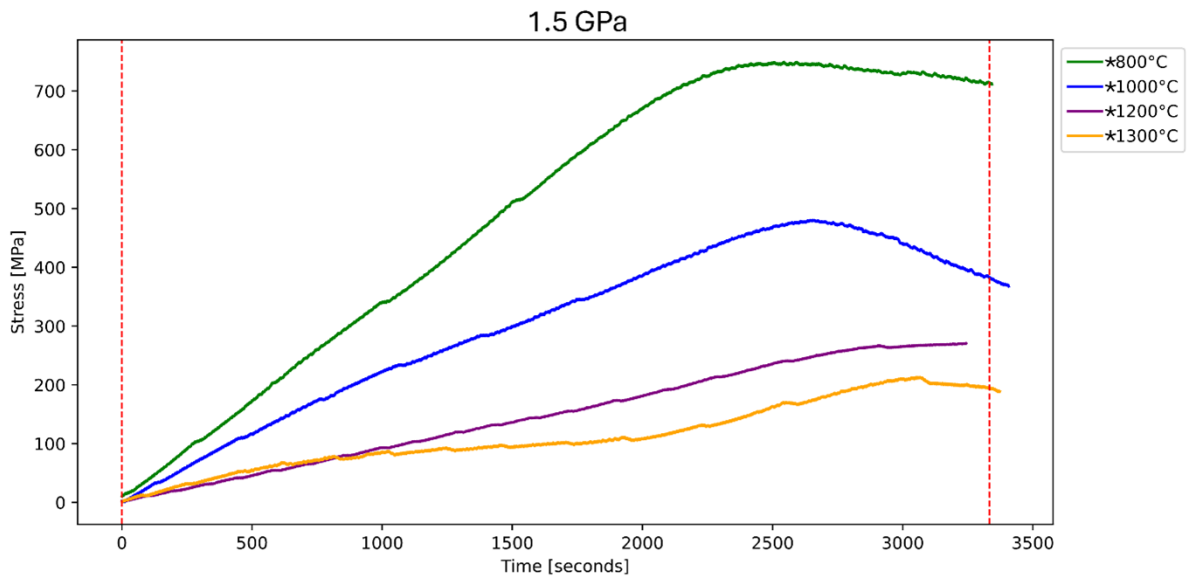
### 3. Results

*represent the start and end of deformation, respectively. In the legend, the star indicates deformations that reached creep.*

The results of stress measurements on the single crystal forsterite deformation are presented in **Figure 88**. The experiments that passed the yield strength and reached a creep flow state are indicated with a star in the legend. Consistent behavior is found where the yield stress becomes larger with decreasing temperature and increasing pressure which is expected to happen, as predicted by the power law creep equation. Since the activation volume is not expected to be negative in materials, the flow stress would increase with increasing pressure. Additionally, since the temperature is in the denominator of the exponential, a decreasing temperature would increase stress.

### 3. Results

## Deformation of single crystal MgO



### 3. Results

**Figure 89.** Stress, as measured using CTGS piezoelectric crystals, of synthetic single crystals of forsterite. Each separate plot is at a different hydrostatic pressure and each curve corresponds to a different temperature. The red, vertical dashed lines shows the start and end of deformation, respectively.

The MgO results are provided in **Figure 89**. In this case, MgO shows much more dramatic softening with temperature compared to forsterite, in addition to lower strength at all temperatures. As expected, a creep regime is entered more consistently at a lower temperature than for forsterite. Once again, the deformation experiments that were judged to have entered a creep regime are indicated with a star in the legend. For the run at 1.5 GPa and 1300 °C, the actual creep is taken not at the maximum stress, but before it at roughly 2000 seconds. This is because this region shows a marked flattening before a slow increase and then another flattening. This earlier region is taken as the first creep regime before some strength hardening takes place with increasing strain and there is another increase in stress.

#### 3.6. Raman spectroscopy of CTGS

A search of literature did not reveal any studies on the Raman spectrum of CTGS crystals. The unit cell of CTGS contains only one formula unit ( $Z=1$ ) and thus 23 atoms. Since each atom has 3 degrees of freedom, the total degrees of freedom are  $3 \times 23 = 69$ , and subtracting the 3 translational modes as well as the three rotational modes, the total number of vibrational or phonon modes for CTGS is 63. The positions and coordinates of the CTGS crystal, based on the point group 32 and space group P321, are provided in **Table 20** based on atomic positions (Ai et al., 2024; Kitaura et al., 2022; Lan et al., 2005).

**Table 20.** Positions and coordinates of atoms in the unit cell of CTGS crystal (Kitaura et al., 2022).

atom	Wyckoff position	symmetry	coordinates
1Ta	1a	32	(0,0,0)
2Si & 2O	2d	3	$(1/3, 2/3, z), (2/3, 1/3, -z)$
3Ca	3e	2	$(x, 0, 0), (0, x, 0), (-x, -x, 0)$
3Ga	3f	2	$(x, 0, 1/2), (0, x, 1/2), (-x, -x, 1/2)$
12O	6g	1	$(x, y, z), (-y, x - y, z), (-x + y, -x, z),$ $(y, x, -z), (x - y, -y, -z), (-x, -x + y, -z)$

In point group 32, the character table of the irreducible representation can be reduced using factor group theory to:

### 3. Results

$$6g: 3A_1 + 3A_2 + 6E$$

$$3f: 1A_1 + 2A_2 + 3E$$

$$3e: 1A_1 + 2A_2 + 3E$$

$$2d: 1A_1 + 1A_2 + 2E$$

$$1a: 0A_1 + 1A_2 + 1E$$

The irreducible representation of the lattice vibrational modes of CTGS crystal is obtained as

$$10A_1 + 13A_2 + 23E$$

So, for the above result there are a total of 69 normal vibrational modes, consistent with the actual number of atoms. Removing the three acoustical modes  $1A_2 + E$  there are 66 principal vibrational modes (Lan et al., 2005).

Now, according to the character table of point group 32, the Raman (R) active and infrared (IR) active optical phonon modes at the first Brillouin zone center can be assigned as

$$\Gamma_{vib} = 10A_1(R) + 12A_2(IR) + 22E(R, IR)$$

The irreducible  $A_1$  and  $A_2$  denote the one-dimensional symmetry species which end up corresponding to 10 Raman and 12 IR active optical phonon modes respectively. As for E, the irreducible representation denotes that two-dimensional symmetry species correspond to 44 vibrational modes. Thus, there are no more than 54 theoretically observable Raman peaks and 34 IR reflection bands. This is the same as CNGS ( $\text{Ca}_3\text{NbGa}_3\text{Si}_2\text{O}_{14}$ ) and LGS crystals (Lan et al., 2005; Lu et al., 2004).

Further calculation of specific Raman active optical phonon modes would require density-functional theory (DFT) calculations, which are beyond the scope of this work. However, to further understand the piezoelectric material and aid with identification of CTGS crystals after experiments to determine if they were damaged or amorphized, a Raman spectrum was collected on CTGS using a 532 nm excitation laser. A total of 37 minutes of exposure time with a laser power of 500 mW was employed with measurements on 5 different spots on the same CTGS crystal. The counts were then summed into a single Raman spectrum after manual verification to ensure that, at least visually, the spectra did not contain errant peaks not present in the others. Even at the high power of 500 mW, no damage was visible after a careful microscopic analysis of the heating spots.

### 3. Results

After collection and summation, the software Fityk (Wojdyr, 2010) was used to fit the peaks in the data. An initial background subtraction using a spline was conducted by visually placing fit points between the peaks. Afterwards, Voigt peaks were used to fit the data through manual peak placement and then running the fit routine in Fityk. A minimal number of peaks were first placed and then fitted, and any large asymmetry in the fitted peaks identified through the residuals were used to place additional, smaller peaks to account for peak asymmetry. All efforts were made to keep the number of peaks to a minimum.

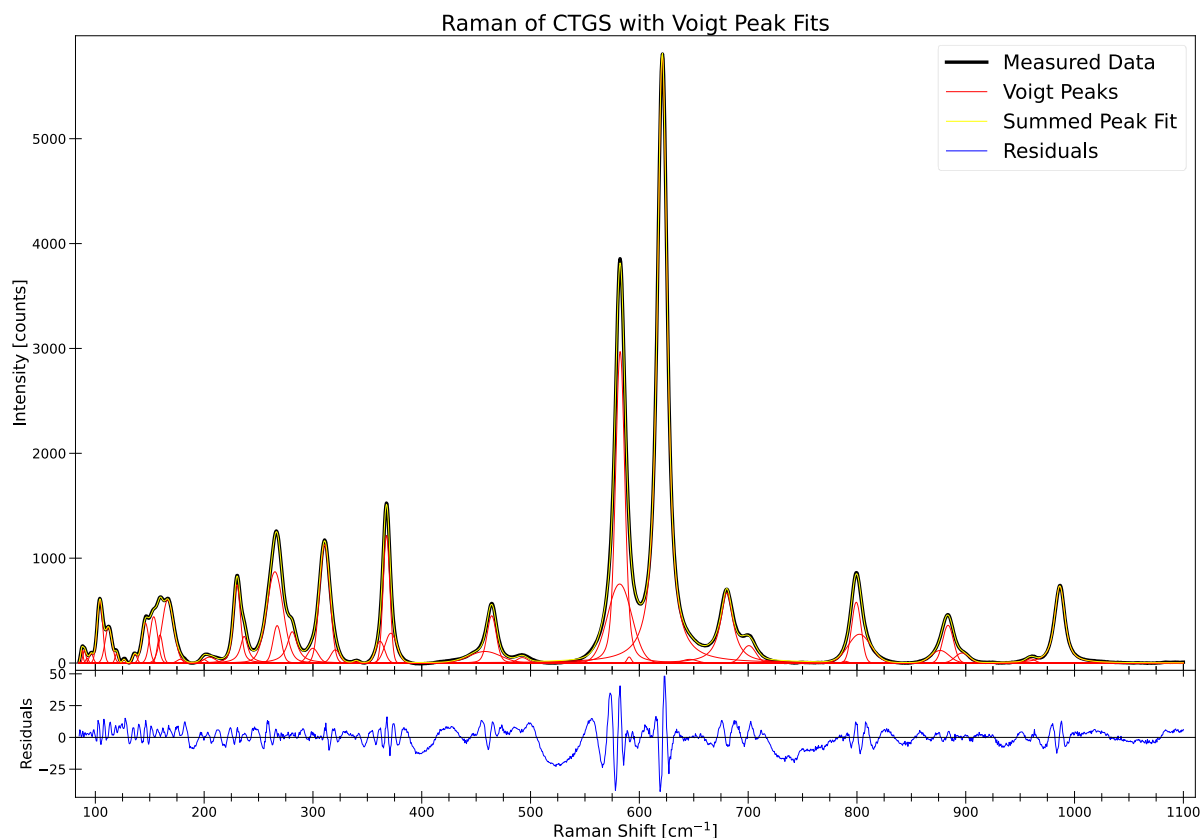


**Figure 90.** The original measured data, after background subtraction, in black with the Voigt peaks that were fit in red and the summed peaks in yellow, overlaid over the original data. The residual is plotted below in the blue line.

**Figure 90** plots the original data as measured in black, with the summed Voigt peaks overlaid in a thin, yellow line. The individual Voigt peaks are plotted in red with the residuals shown below the plot. As can be seen, the relatively heavier atoms in CTGS, specifically Ta, increase the low Raman shift complexity. In Raman spectroscopy, the intensity and position of peaks are influenced by the mass of the atoms involved (Patterson & Bailey, 2018; Scarponi et al., 2017). Heavier atoms, such as tantalum (Ta) and gallium (Ga) in CTGS, have lower vibrational

### 3. Results

frequencies due to their greater inertia. This results in Raman shifts that occur at lower frequencies as compared to, for example,  $\alpha$ -quartz, as well as most typical and common Earth minerals since they tend to largely contain lower mass atoms.

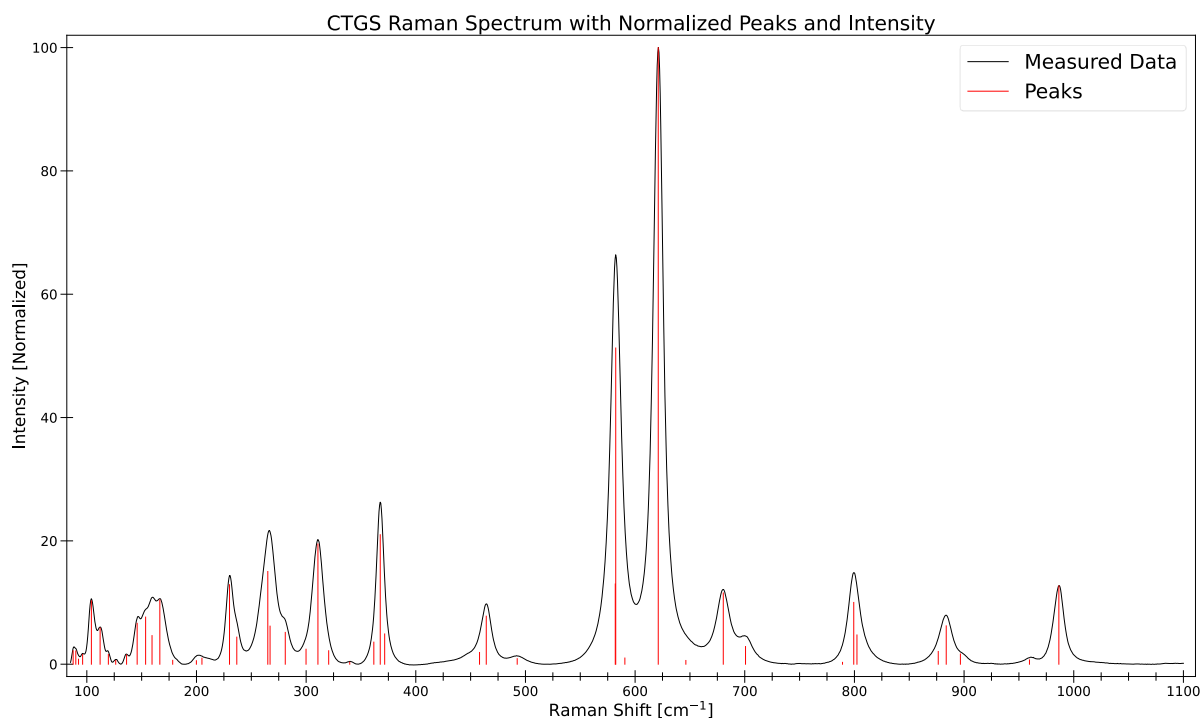


**Figure 91.** The directly measured data, with background subtraction, and the peaks fit with Voigt functions. Both the Raman counts and peak heights were normalized to 100.

The measured data with the peak locations derived from the Voigt profile fits, both normalized to an intensity of 100, are displayed in **Figure 91**. As can be seen, the number of peaks in the low Raman shift range are higher than most abundant natural minerals owing to the high atomic mass ions in CTGS, as expected. The lowest Raman shift that could be measured was 85 cm<sup>-1</sup>. The expectation is that more peaks are present below this range, but the Raman system was not capable of measuring closer to the Rayleigh scattering peak.

All the peaks are listed in **Table 21**. While most of the peaks listed are likely present, some of the low intensity but large FWHM peaks are possibly over-fitted or a result of noise. The table can be used to accurately recreate the measured Raman spectrum. A total of 46 peaks were fit, less than the maximum possible 54 peaks predicted theoretically.

### 3. Results

**Table 21.** All Raman peaks of CTGS derived from Voigt profile fits. The center position, relative intensity (normalized to 100), and full-width half-maximum (FWHM) of each peak for both the Gaussian and Lorentzian profiles are listed in ascending order of center position.

Center [cm <sup>-1</sup> ]	Relative intensity	Gaussian FWHM [cm <sup>-1</sup> ]	Lorentzian FWHM [cm <sup>-1</sup> ]	Center [cm <sup>-1</sup> ]	Relative intensity	Gaussian FWHM [cm <sup>-1</sup> ]	Lorentzian FWHM [cm <sup>-1</sup> ]
87.53	2.18	2.687	3.099e-07	320.56	2.18	9.463	0.437
89.95	2.15	3.103	1.111e-04	339.77	0.31	5.046	-3.054e-02
92.44	0.81	2.889	8.063e-08	361.73	3.58	9.791	2.071e-06
96.17	1.58	4.261	1.754e-04	367.58	21.00	7.182	-1.476e-10
104.16	10.28	6.072	-2.602e-08	371.62	4.91	12.774	3.236e-08
112.11	5.88	7.504	1.093e-04	458.12	1.90	34.041	2.037e-07
119.64	1.58	3.518	-4.403e-05	464.26	7.78	8.696	2.443
126.34	0.61	3.152	4.676e-07	492.48	0.90	11.669	-9.632e-08
136.25	1.50	4.671	1.780e-06	581.89	13.01	26.080	-5.250e-06
145.91	6.63	7.592	2.824e-06	582.35	51.28	8.030	3.392
153.62	7.64	8.218	-3.283e-06	590.64	1.00	4.505	-1.093e-04
159.46	4.63	5.775	4.883e-06	621.10	100.00	4.359	9.064
166.58	10.42	12.520	-3.780e-06	646.25	0.60	15.727	7.859e-05
178.32	0.63	7.601	-6.325e-06	680.39	11.55	0.345	13.961
199.91	0.56	5.658	2.093e-05	700.68	2.86	14.642	-5.146e-06
204.98	0.98	12.006	-3.407e-06	789.15	0.30	5.773	-3.039e-02
230.13	12.89	5.688	3.253	799.38	10.02	10.197	-1.954e-05
236.76	4.39	1.233	8.074	802.30	4.74	24.598	7.359e-08
265.05	15.03	16.177	2.532	876.45	2.07	19.283	1.564e-06
267.10	6.17	8.241	1.153	883.73	6.21	11.578	1.179e-07
280.96	5.16	1.739	10.822	896.65	1.65	15.070	9.906e-06
299.91	2.43	11.231	-0.429	959.65	0.69	9.590	-1.684e-05
310.76	19.49	11.058	0.018	986.42	12.68	5.708	8.269

Previous work has been done on CNGS crystals to determine Raman peaks. First, Raman spectrum was collected and then ab-initio molecular orbital calculations were done. CNGS is identical structurally to CTGS except the Ta is replaced with Nb. Although not directly comparable since the atomic masses are different, the assignment for the other atoms within the structure that are identical can be compared more closely, listed in **Table 22**.

### 3. Results

**Table 22.** Raman peaks calculated with *ab-initio* orbital calculations and assignment to specific vibrational modes (Lan et al., 2005) compared to the closest peak fit on CTGS in this study. Peaks not clearly seen in CTGS are omitted.

Frequency		Assignment
Calculated for CNGS [cm <sup>-1</sup> ]	Observed in CTGS [cm <sup>-1</sup> ]	
147	146	GaO <sub>3</sub> -Ca-SiO <sub>3</sub> bending
161	168	GaO <sub>3</sub> -Ca-SiO <sub>3</sub> stretching
178	-	GaO <sub>3</sub> -Ca-SiO <sub>3</sub> bending
227	230	GaO <sub>3</sub> -O-GaO <sub>3</sub> bending
241	237	GaO <sub>3</sub> -O-SiO <sub>3</sub> stretching
242	237	GaO <sub>3</sub> -O-SiO <sub>3</sub> stretching
270	265	GaO <sub>3</sub> -O-GaO <sub>3</sub> stretching
282	281	GaO <sub>3</sub> -O-SiO <sub>3</sub> stretching
313	311	SiO <sub>4</sub> -Ca-SiO <sub>4</sub> stretching
333	-	Ga-O stretching
377	368	O-Ca-O stretching
442	-	GaO <sub>3</sub> -Ca-SiO <sub>3</sub> stretching
458	464	O-Ga-O bending
581	582	O-Si-O bending
618	621	O-Ga-O stretching
656	-	O-Ga-O stretching
673	680	Ga-O stretching
688	701	Si-O stretching
727	-	Si-O stretching
768	799	Si-O stretching
866	876	O-Si-O stretching
974	986	Si-O stretching

#### 3.7. Brillouin spectroscopy results

The Brillouin spectra were fit using Brillouin Win1024 (Sinogeikin et al., 2006). A systematic fit using Gaussian or Voigt profiles is generally not possible since the Brillouin signal counts are low for most spectra. This low signal count is inherent to Brillouin spectroscopy due to several factors. Firstly, Brillouin scattering is a relatively weak phenomenon as it involves the interaction of light with acoustic phonons, which are low-energy excitations within the material. Consequently, the intensity of the scattered light is significantly lower compared to other scattering processes such as Raman scattering.

Furthermore, the experimental setup for Brillouin spectroscopy often involves narrow-bandwidth lasers and high-resolution interferometers, which, while necessary for resolving the small frequency shifts associated with acoustic phonons, also contribute to the low signal counts.

### 3. Results

The efficiency of the detection system and the intrinsic properties of the sample, such as its transparency and acoustic properties, can further limit the intensity of the Brillouin signal. Due to these intrinsic limitations, fitting a Gaussian or Voigt profile to the spectra is generally not feasible.

The low signal-to-noise ratio (SNR) means that the peaks corresponding to the Brillouin shifts are often weak and broad, making it challenging to distinguish them from the background noise. This difficulty is compounded when working with materials that inherently produce weaker Brillouin signals or when operating under conditions that further reduce signal strength, such as high-pressure environments. The low counts observed in Brillouin spectroscopy data typically follow a Poisson distribution, which describes the probability of a given number of scattered photons being detected in a fixed interval (Dil & Brody, 1976). This distribution is characterized by the variance being equal to the mean, highlighting the random nature of the low-count events.

Error was estimated as the ratio between the amplitude variation of the noise to the peak height. To convert this ratio to an error, a series of 20 Brillouin spectra collected continuously on the same crystal were fit manually. The SNR of each fit along with the error in the velocities between them were used to define an error function that relates the SNR to a velocity error. This was used on each velocity fit on CTGS to calibrate the researcher's manual fitting error.

To ensure the quality of the fit, a Voigt profile was first fit to the central, elastic peak. Following this, the Stokes and Anti-Stokes peaks for each velocity were fit. The average channel positions of these fits were then compared to the channel position of the central elastic peak. If the average channel position differed by more than one channel from the central peak's position, the fitting process was refined for greater precision. An example spectrum of one data point is shown in **Figure 92**.

### 3. Results

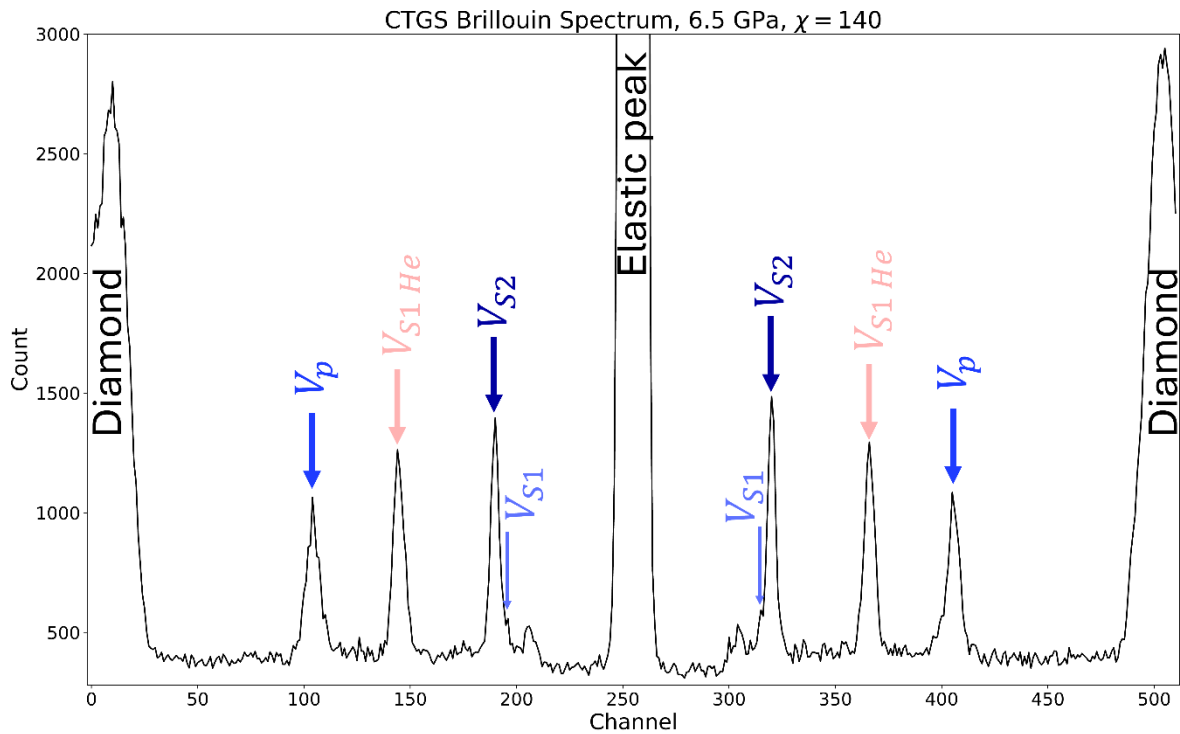


**Figure 92.** Example of a Brillouin spectra on CTGS. This was collected at 6.5 GPa on XI at  $\chi=140^\circ$ . The velocity peaks of the sample as well as the diamond and He are labeled. The central peak is the Rayleigh scattering, or elastic peak.

The final fits to the velocity dispersion curves are detailed in **Figure 93**. Also included in the plots are the velocities of the liquid He  $V_{S1}$  and  $V_{S2}$ . These peaks do not shift with  $\chi$  as liquids are isotropic. Since the He peaks were prominent, no CTGS velocity peaks could be fit if they shifted too close to them. Fortunately, the He peaks did not dramatically hinder fitting for any pressure point. The liquid He velocities were acquired from literature reported data (Hanayama & Kimura, 1995) up to 3 GPa and fit with a simple power law equation and extrapolated to 9.8 GPa. The He peaks indeed appeared in the expected position according to the equation.

### 3. Results

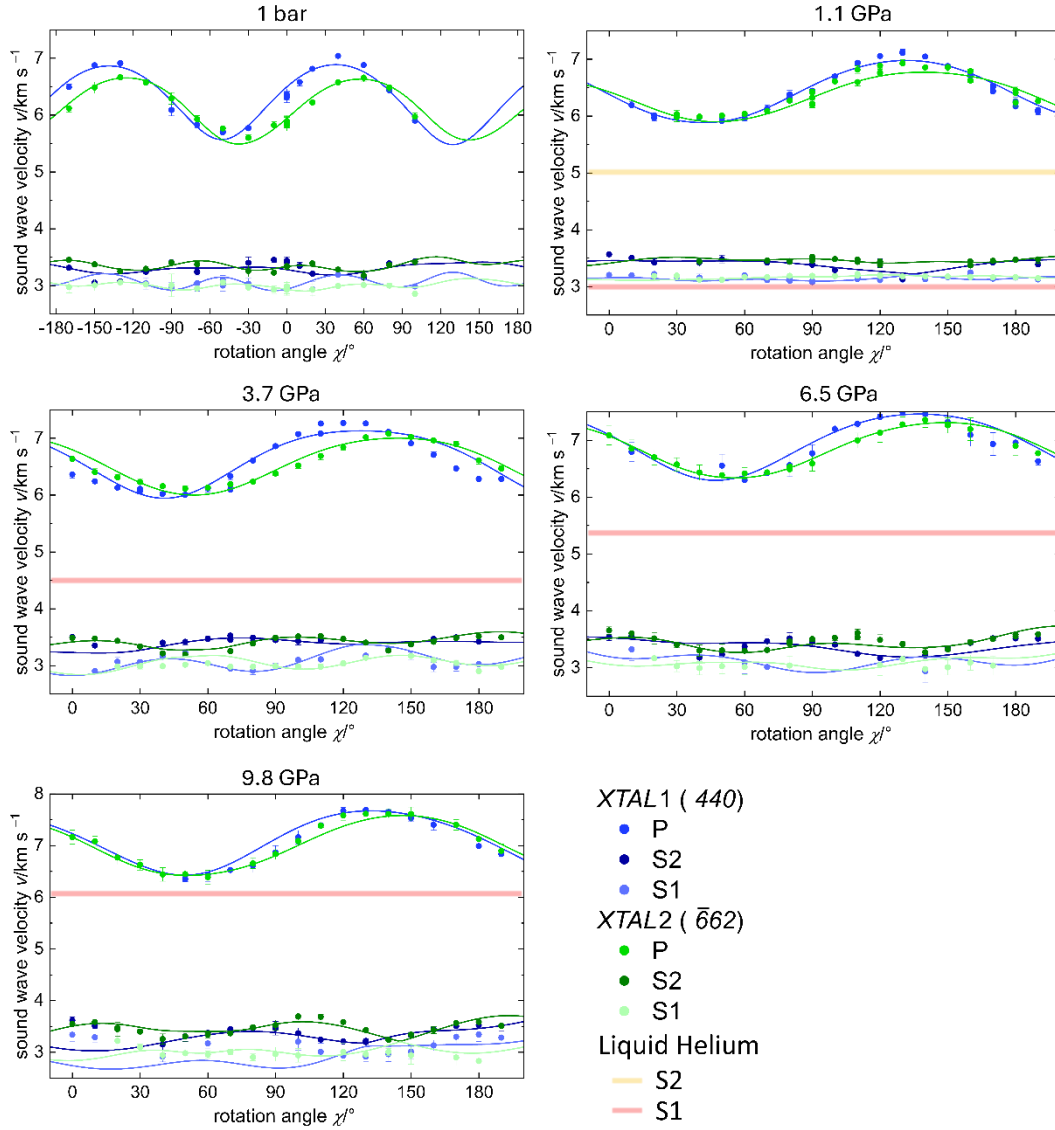


**Figure 93.** Velocity dispersion curves with  $\chi$  angles are plotted for each pressure point measured on CTGS. The directly fitted points are plotted with the curves fitted to each in the same color.  $V_p = P$ ,  $V_{S2} = S2$ ,  $V_{S1} = S1$ . The  $\chi$  angle range in the 1 bar plot is different because it was measured at BGI. The rest were measured at DESY. Also added are the liquid He  $V_{S2}$  and  $V_{S1}$  peak locations for each pressure point.

After fitting the velocity dispersion curves by numerically solving Eq. 80, solutions for the 6 independent elastic stiffness coefficients ( $C_{11}$ ,  $C_{33}$ ,  $C_{44}$ ,  $C_{12}$ ,  $C_{13}$ ,  $C_{14}$ ) were derived. The elastic coefficient  $C_{66}$  is not independent and is instead calculated, according to the tensor in Eq. 81, with the formula  $\frac{1}{2}(C_{11} - C_{12})$ .

### 3. Results

Pressure GPa	Unit cell volume $\text{\AA}^3$	Density $g/cm^3$	$C_{11}$ GPa	$C_{33}$ GPa	$C_{44}$ GPa	$C_{12}$ GPa	$C_{13}$ GPa	$C_{14}$ GPa	$C_{66}$ GPa	$K$ GPa
0.0	282.86(73)	4.641(12)	140.6(1.3)	219.5(1.3)	47.49(34)	36.6(1.5)	93.7(1.0)	-0.30(31)	52.00(48)	88.4(1.6)
1.1(1)	281.12(47)	4.670(8)	161.5(2.1)	233.1(3.1)	49.35(30)	49.1(2.1)	100.3(1.3)	1.41(16)	56.20(32)	105.1(2.0)
3.7(1)	273.18(92)	4.805(16)	169.4(2.5)	245.7(2.9)	53.26(49)	63.5(2.8)	121.0(1.8)	-1.13(32)	52.89(65)	116.2(3.0)
6.5(1)	269.1(1.1)	4.878(19)	194.6(2.2)	274.6(2.0)	55.58(50)	78.1(2.6)	135.8(2.6)	-0.59(72)	58.29(70)	136.4(2.4)
9.8(1)	260.0(1.0)	5.050(19)	206.9(3.8)	298.8(2.0)	51.80(60)	88.7(4.3)	159.9(2.8)	-5.15(70)	59.5(1.0)	146.6(5.5)
	$\frac{\partial V}{\partial P}$	$\frac{\partial \rho}{\partial P}$	$\frac{\partial C_{11}}{\partial P}$	$\frac{\partial C_{33}}{\partial P}$	$\frac{\partial C_{44}}{\partial P}$	$\frac{\partial C_{12}}{\partial P}$	$\frac{\partial C_{13}}{\partial P}$	$\frac{\partial C_{14}}{\partial P}$	$\frac{\partial C_{66}}{\partial P}$	$\frac{\partial K}{\partial P}$
	$\text{\AA}^3/\text{GPa}$	$g/cm^3\text{GPa}$	$\text{GPa}/\text{GPa}$	$\text{GPa}/\text{GPa}$						
	-2.354(80)	0.0417(15)	7.310(62)	8.130(18)	0.711(20)	5.791(38)	6.778(16)	-0.548(16)	0.554(25)	5.734(53)

**Table 23.** Material properties derived from Brillouin spectroscopy of CTGS at different pressures. All measurements are at room temperature. Pressure was calculated from fluorescence spectroscopy of the ruby crystal placed inside the DAC pressure chamber. The unit cell volume, density, elastic stiffness coefficients, and calculated bulk modulus

## 4. Discussion

All the pressures points are listed in **Table 23**. For each pressure point, the unit cell volume, crystal density, elastic stiffness coefficients, and bulk modulus are provided. The change in pressure for each parameter is also provided in the table. These were calculated by fitting a straight line to each parameter against the hydrostatic pressure and the slope of this line is then taken as the derivative of the parameter with pressure of each.

## 4. Discussion

### 4.1. San Carlos olivine deformation with XRD

As olivine is the predominant mineral in the Earth's upper mantle, it plays a crucial role in determining seismic anisotropy and mantle convection through its deformation behavior. Of particular interest is the asthenosphere, where there is a notable reduction in strength compared to the overlying lithosphere. This strength reduction is essential for plate tectonics, as it allows the rigid lithospheric plates to mechanically decouple from the underlying mantle, creating a 'lubricating' layer that facilitates plate movements (Hirth & Kohlstedt, 2003). **Figure 94** illustrates the strength envelopes for both oceanic and continental lithospheres at a constant strain rate of  $10^{-15} \text{ s}^{-1}$ . The strength envelopes for quartzite in the continental lithosphere are plotted according to flow laws from (Gleason & Tullis, 1995; Kronenberg & Tullis, 1984; Luan & Paterson, 1992).

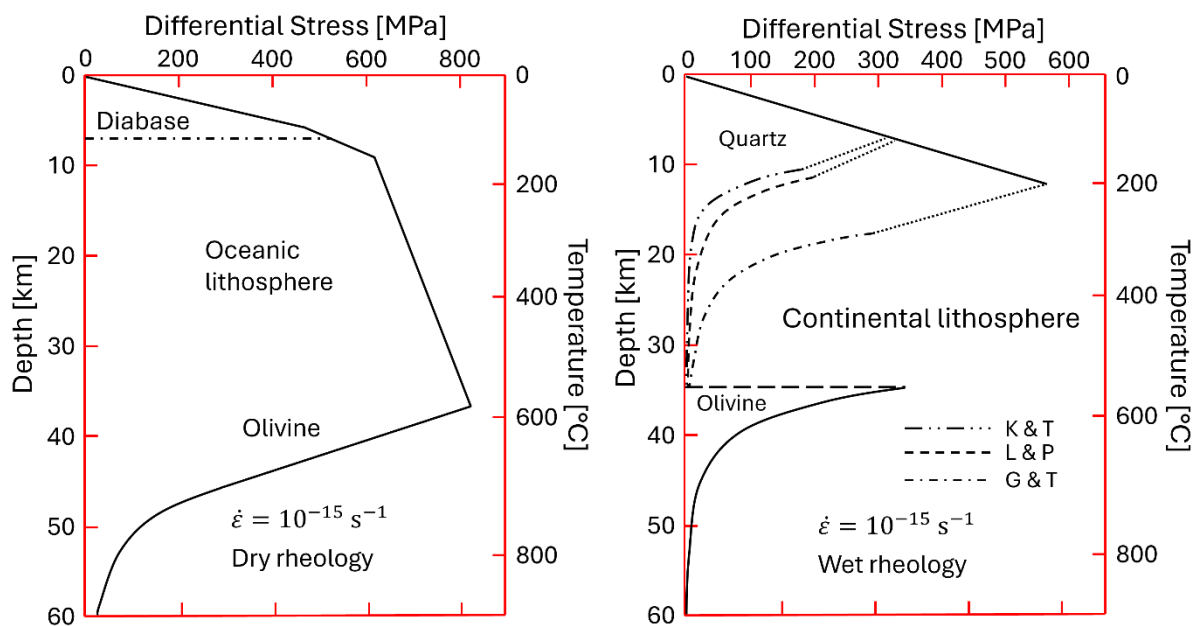


**Figure 94.** Schematic illustration of the strength envelopes for oceanic lithosphere (left) and continental lithosphere (right) at a constant strain rate of  $10^{-15} \text{ s}^{-1}$ . The quartzite strength

#### 4. Discussion

*envelopes in the continental lithosphere are based on flow laws from K & T (Kronenberg & Tullis, 1984), L & P (Luan & Paterson, 1992), and G & T (Gleason & Tullis, 1995). Figure modified from (Kohlstedt et al., 1995).*

Several factors have been proposed to explain the drop in olivine strength at the asthenospheric depths. Partial melting is a significant factor, but it alone cannot account for the dramatic increase in weakness without unrealistically high melt percentages (Demouchy et al., 2013; S. Karato, 2010; Kohlstedt et al., 1995). The complexity deepens with findings that olivine strength is significantly influenced by grain size, oxygen fugacity, and water content (Boioli et al., 2015; Demouchy et al., 2013; Hansen et al., 2019; Jain et al., 2018; Wallis et al., 2020). Furthermore, the region is not composed solely of olivine but includes pyroxenes as well. The sudden decrease in strength in the asthenosphere is likely due to a combination of these factors.

To accurately determine the precise conditions and mechanisms behind this low strength, extensive deformation experiments are required. These experiments should be conducted under high pressure and temperature conditions and involve multiphase mixtures to simulate the mantle environment accurately. Currently, above approximately 0.5 GPa, XRD is required for accurate stress state estimates during deformation at high temperature. However, limited beamline availability has constrained the exploration of variable space for olivine. Establishing the relationship between olivine strength and various conditions would benefit from a method to measure stress at higher pressures without relying on XRD. The piezoelectric method presents a promising alternative.

An extensive exploration of this variable space for olivine strength is beyond the scope of this thesis. However, some stress data from San Carlos olivine, deformed during piezoelectric method testing, can be compared to literature results. The grain size of the San Carlos olivine starting material was estimated to range between 5-15  $\mu\text{m}$ , based on scanning electron microscopy (SEM) secondary electron imaging. While the water content was not measured, the olivine was hot-pressed under nominally anhydrous conditions. No specific attempts were made to control oxygen fugacity in these experiments.

Two San Carlos olivine deformation experiments, labeled SR1 and SR2 and detailed in **Table 14**, appeared to reach a creep state. During these deformation experiments, the piezoelectric crystal voltage exhibited a plateau, indicating a region where voltage did not increase with further strain. These regions are highlighted with red boxes in **Figure 95**. Within each boxed

## 4. Discussion

region, piezoelectric voltage measurements were averaged to calculate the average stress. Hydrostatic pressure was derived from the closest MgO pattern. As no X-ray radiography images were taken before and after these deformations, direct strain rate measurements were not available. Consequently, sample strain rates were extrapolated from previous deformations (C1, C2, and C3) using known anvil rates and temperatures. This data, provided in **Table 12** and **Figure 28**, allowed for reasonable strain rate calculations for the subregions of SR1 and SR2.

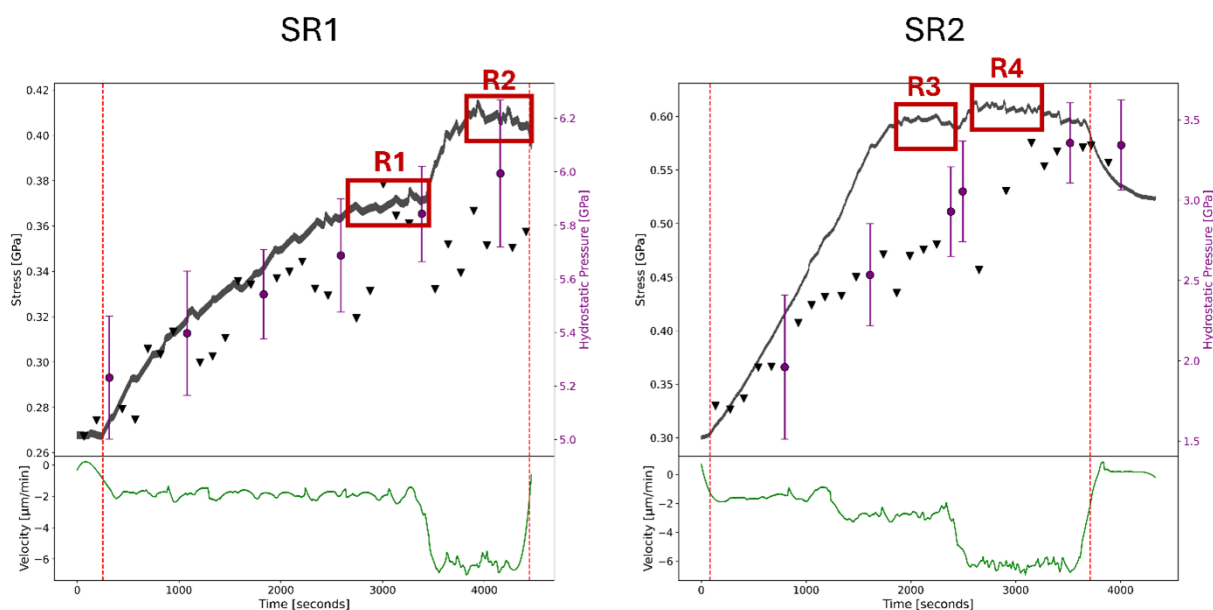


**Figure 95.** Stress and hydrostatic pressure data for the SR1 and SR2 deformation experiments on San Carlos olivine. The red boxes indicate regions (R1 to R4) where the piezoelectric voltage plateaued, suggesting entry into a creep regime. Stress is plotted against time, with hydrostatic pressure data shown alongside. Anvil velocity data is presented at the bottom to provide context for the deformation process.

The values obtained from SR1 and SR2 are listed in **Table 24**. Initially, the intent was to compare the data with the classical power law creep equation (Eq. 123). However, at the lower temperatures used in SR1 and SR2, the power law creep equation does not hold, and the parameters reported in the literature for these temperatures yield unreasonably high stresses, as displayed in **Figure 96**. The two vertical lines, placed at 863 K and 1223 K, predict stresses well above 10 GPa with most reported literature parameters.

#### 4. Discussion

**Table 24.** Experimental parameters from regions R1 – R4 in SR1 and SR2 from **Figure 95**.

	$\sigma$ [MPa]	Temperature [K]	Pressure [GPa]	Strain rate [ $\times 10^{-4} \text{ s}^{-1}$ ]
R1	$1.446(8) \times 10^3$	1223	5.8	2.9
R2	$1.577(7) \times 10^3$	1223	6.0	9.5
R3	$2.214(7) \times 10^3$	863	2.9	1.6
R4	$2.249(7) \times 10^3$	863	3.4	3.4

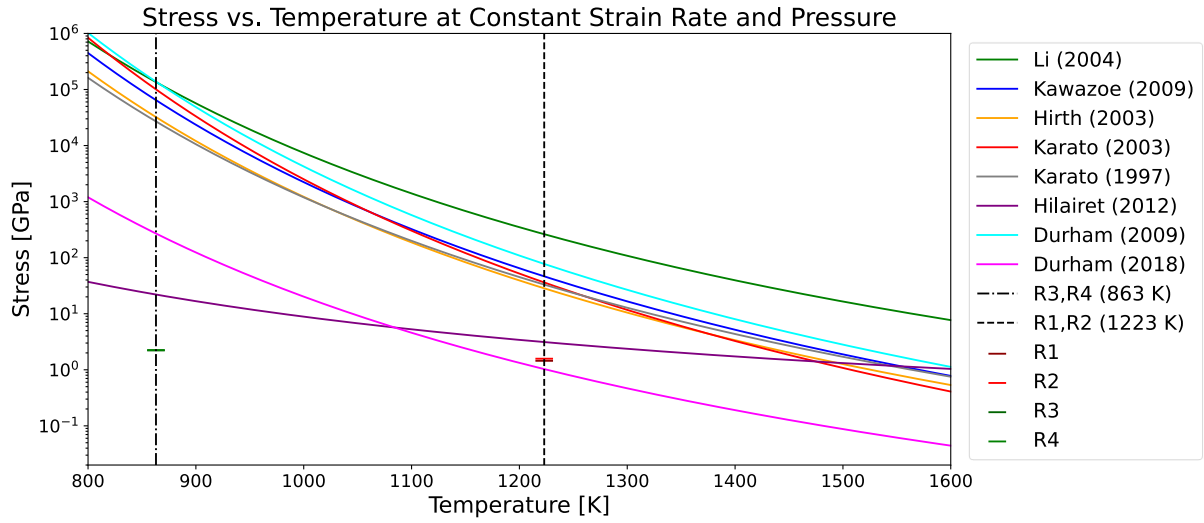


**Figure 96.** Curves calculated using the power law creep equation (Eq. 123) from parameters as reported in literature. The strain rate and hydrostatic pressure are kept constant at  $10^{-5} \text{ s}^{-1}$  and 5 GPa respectively. Also shown with the two black vertical lines are the temperatures at which the R1 – R4 subregions were deformed and with horizontal lines each point. (Dixon & Durham, 2018; Durham et al., 2009; Hilairet et al., 2012; Hirth & Kohlstedt, 2003; S. Karato & Rubie, 1997; S.-I. Karato & Jung, 2003; Kawazoe et al., 2009; L. Li et al., 2004)

Instead of power law creep, a different deformation mechanism, obstacle/Peierls' stress-limited dislocation creep, is active at these lower temperatures (Katayama & Karato, 2008; Raterron et al., 2004). Therefore, this creep regime is best described by Eq. 118 (Raterron et al., 2004).

$$\dot{\epsilon} = \dot{\epsilon}_0 \exp \left( - \frac{F_0 \left[ 1 - \left( \frac{\sigma}{\tau} \right)^p \right]^q}{RT} \right) \quad \text{Eq. 118}$$

#### 4. Discussion

In this equation,  $\dot{\epsilon}_0$  represents a pre-exponential constant. The stress dependence,  $\sigma$ , is captured in the exponential term, which depends on  $F_0$ , the free energy needed for dislocations to overcome barriers, also known as the activation energy, and  $\tau$ , the maximum glide resistance, representing the Peierls' stress. The parameters  $p$  and  $q$  are fitting constants, typically within the ranges  $0 \leq p \leq 1$  and  $1 \leq q \leq 2$  (Frost & Ashby, 1982; Poirier, 1985). Notably, this equation does not include an activation volume. Instead, the influence of pressure on olivine rheology is indirectly accounted for through  $\tau$ , since higher pressure is expected to increase the Peierls' stress (Raterron et al., 2004). The results of this study measure a higher stress than predicted by Raterron et al. (2004). One potential explanation is provided in **Figure 99** and the text that discusses it below.

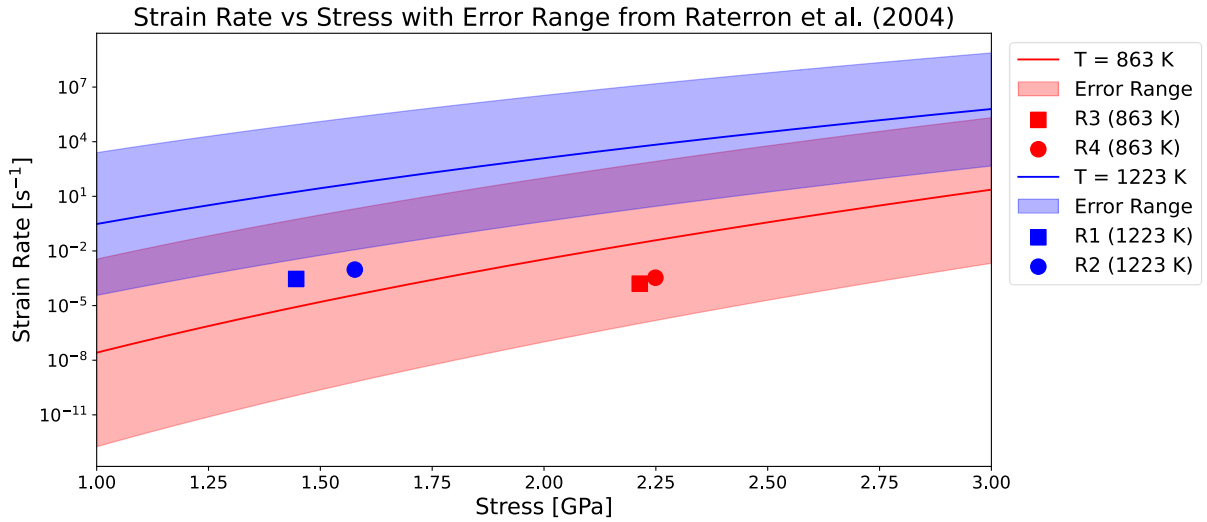


**Figure 97.** Curves and error bands from Raterron et al. (2004) compared to the regions R1 – R4 from this study, shown as a square and circle. Red is calculated at 863 K, blue at 1223 K.

More recently, efforts have been made to unify the description of olivine rheology under varying temperature and stress conditions. Gouriet et al. (2019) proposed a unified creep law that effectively models the transition between power law and exponential flow behaviors in olivine. This law is particularly useful for describing deformation over a wide range of mantle conditions. Their work introduced a new exponential equation that accounts for both low and high stress regimes, which can be expressed as shown in Eq. 119 (Gouriet et al., 2019)

$$\dot{\epsilon} = A \left( \frac{\sigma}{\mu} \right)^n \exp \left( - \frac{Q(\sigma)}{RT} \right) \quad \text{Eq. 119}$$

#### 4. Discussion

In this equation, the newly introduced symbol,  $\mu$ , is the shear modulus.  $Q(\sigma)$  is the stress-dependent activation enthalpy, which is further defined by Eq. 120.

$$Q(\sigma) = Q_0 \left( 1 - \left( \frac{\sigma}{\tilde{\sigma}} \right)^p \right)^q \quad \text{Eq. 120}$$

$Q_0$  is the zero-stress activation enthalpy,  $\tilde{\sigma}$  is the mechanical resistance parameter, and  $p$  and  $q$  are once again fitting parameters. They derived specific values for these parameters through a detailed analysis of experimental data and numerical simulations. The best for olivine rheology was obtained with the following parameters:  $Q_0 = 460 \times 10^3$  J/mol,  $p = 1.52$ , and  $q = 2.00$ , with the stress exponent  $n = 2.95$ . The shear modulus  $\mu$  was taken as 80 GPa, as suggested by their simulations. The final unified exponential law for olivine creep is expressed as:

$$\dot{\epsilon} = 1.7 \times 10^{16} \left( \frac{\sigma}{8.0 \times 10^4 \text{ MPa}} \right)^{2.95} \times \exp \left( \frac{-460 \times 10^3}{RT} \left( 1 - \left( \frac{\sigma}{\tilde{\sigma}} \right)^{1.52} \right)^2 \right) \quad \text{Eq. 121}$$

Eq. 121 covers a wide temperature range of 200 K to 1700 K. The only parameter left to determine is  $\tilde{\sigma}$  which is sensitive to the hydrostatic confining pressure. However, due to the limited number of data points available (only four from the current study), a single value for  $\tilde{\sigma}$  is determined numerically for all data points collectively, rather than solving for different pressures separately. The result is  $\tilde{\sigma} = 5486$  MPa. The strain rate is calculated and compared to the measured strain rate in **Figure 98**. As might be expected, the result is quite good and close to the 1:1 line.

## 4. Discussion

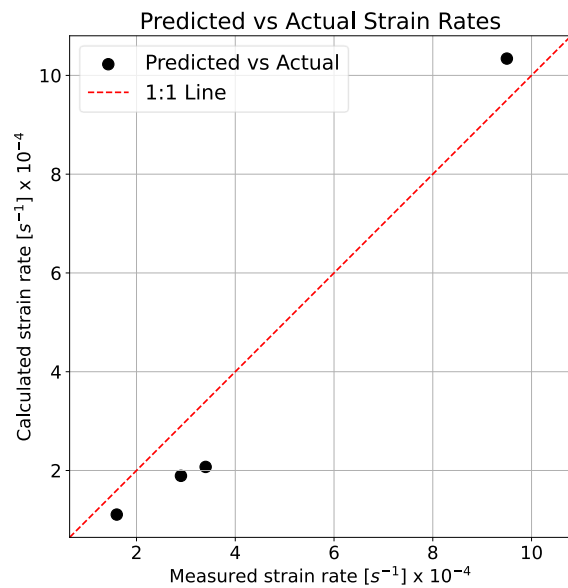


**Figure 98.** The result of fitting the experimental data R1 – R4 with Eq. 121. The calculated strain rate on the vertical axis is compared to the measured strain rate on the horizontal axis. The 1:1 red dashed line reflects an ideal fit.  $\tilde{\sigma} = 5486$  MPa.

Finally, inputting  $\tilde{\sigma} = 5486$  MPa into Eq. 121, a curve can be derived to describe the temperature effect on the flow stress. This is shown with the black curve in **Figure 99**. Along with the study data and fit, a selection of previous literature data has also been plotted. These have not been fit to or corrected with any kind of equation. They are the direct data reported by the studies. While a large part of the scattering is due to different pressures and strain rates, there is good agreement in general with the measurements from this study. Of particular interest is the sudden drop in stress in the Raterron et al. (2004) data at around 750 K. This data was compared directly with R1 – R4 in **Figure 97** which showed a consistently higher stress. As the study temperatures compared at (863 K, 1223 K) are above the sudden stress drop in Raterron et al. (2004), it could be that if the lower temperature data was projected to the higher temperature, the results would fit quite well.

## 4. Discussion

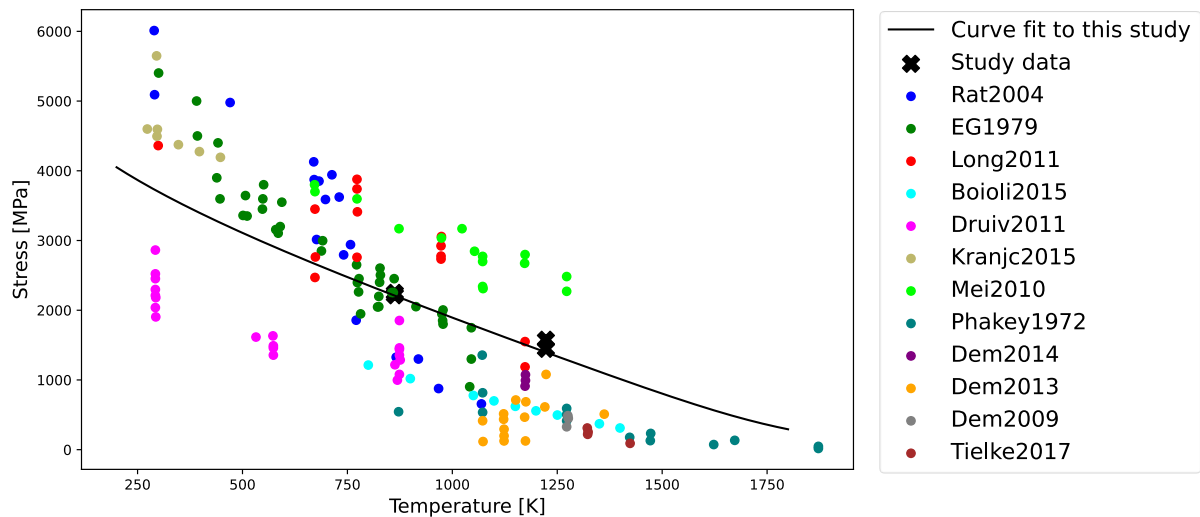


**Figure 99.** A selection of equivalent stresses versus temperature of mechanical data of olivine (Fo90). Modified from (Gouriet et al., 2019). The raw reported data only is plotted, not the creep laws normalized to pressure or strain rate. Also, in black crosses, are the four R1 – R4 data points from this study and the derived equation (Eq. 121) with  $\bar{\sigma} = 5486$  MPa. Rat2004 = (Raterron et al., 2004); EG1979 = (Evans & Goetze, 1979). Long2011 = (Long et al., 2011); Boioli2015 = (Boioli et al., 2015); Druiv2011 = (Druiventak et al., 2011); Kranjc2015 = (Skemer et al., 2015); Mei2010 = (Mei et al., 2010); Phakey1972 = (Phakey et al., 1972); Dem2014 = (Demouchy et al., 2014); Dem2013 = (Demouchy et al., 2013); Dem2009 = (Demouchy et al., 2009); Tielke2017 = (Tielke et al., 2016).

The piezoelectric method thus accurately measures stresses not only when compared to direct XRD measurements but also when compared to previously reported results on olivine.

### 4.2 Anvil position discrepancy

During the deformation experiments at the PETRA-III synchrotron at the P61B beamline, a systematic discrepancy between the anvil movement distance as recorded with the position encoder compared to the radiography images was observed. The experiments that had pre- and post- deformation radiography images are C1, C2, C3, T2, T3, and T5. T1 is omitted because the beam went down during that experiment and the deformation had to be paused which allowed some relaxation time.

If the programmed anvil advancement rate, in  $\mu\text{m}/\text{min}$ , is multiplied by the deformation elapsed time, the total anvil movement distance is found in  $\mu\text{m}$ . The results for the compression and tension deformation experiments that do have measurable strain are listed in Table 25. Also provided is the assumed anvil temperature which is actually the piezoelectric crystal calibrated

#### 4. Discussion

temperature. However, because the crystal is in contact with the anvil through a 1 mm thick diamond disk and diamond has very high thermal conductivity, the anvil can be assumed to be at least close to the same temperature.

*Table 25. Strain measurements from the press encoder and the radiography images for three compression and three tension deformation experiments. The ratio encoder/radiography is also given. Also provided is the piezoelectric crystal temperature for each deformation.*

Cycle	Encoder measured [ $\mu\text{m}$ ]	Radiography measured [ $\mu\text{m}$ ]	Ratio	Anvil temperature [ $^{\circ}\text{C}$ ]
C1	860	489	1.759	150
C2	860	286	3.007	170
C3	860	253	3.399	190
T2	860	183	4.699	170
T3	860	181	4.751	190
T5	560	140	4.000	120

As the table shows, the discrepancy is consistently 2 – 4 times larger than the measured length difference from the x-ray radiography images for both the compression and tension experiments. The reason for this discrepancy is currently unknown. A trend does appear when considering the experiment temperature. By plotting the piezoelectric crystal temperature against the ratio, **Figure 100**, a clear trend emerges.

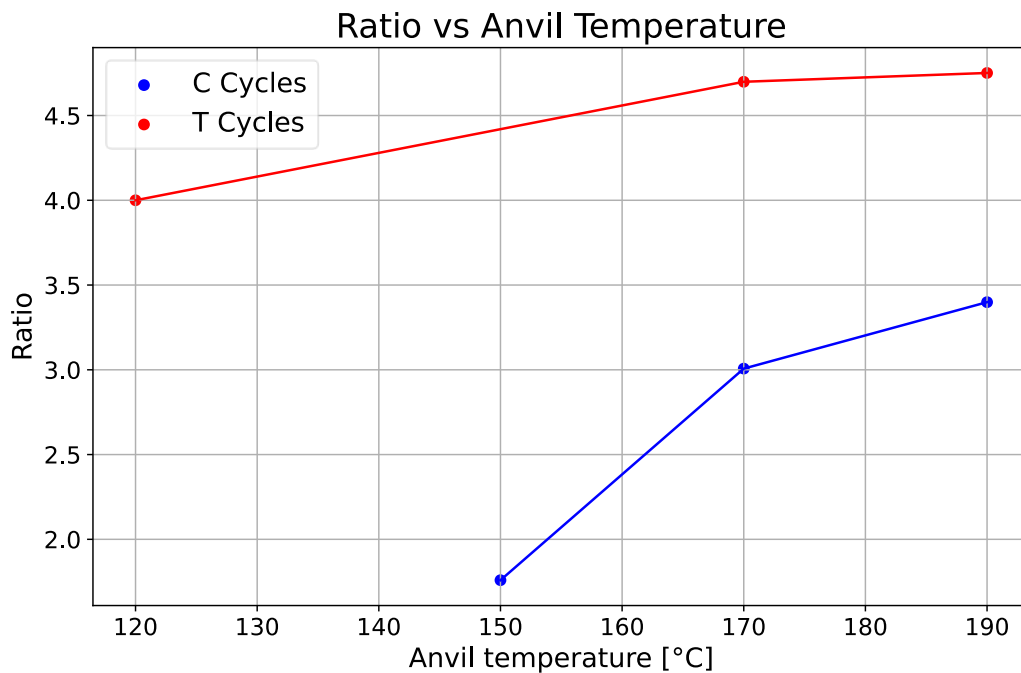


**Figure 100.** The piezoelectric crystal temperature, used as an analogue for the anvil temperature, plotted against the error ratio of the anvil movements between the encoder and

#### 4. Discussion

*radiography measured assembly strain. C cycles are compression deformation experiments, and T are tension.*

There is a positive correlation between the temperature and the error ratio. Also, the compression deformation experiments have a consistently higher error ratio than the tension experiments. It seems that higher temperatures increase the error for both.

The frame bending calibration should correct for outwards buckling of the steel supports that hold the rams in place as they increasingly apply larger force to the assembly, essentially attempting to push outwards against the middle. As previously detailed in section 2.1.2, the frame bending calibration involves measuring the anvil-to-anvil face distance at various oil pressures using a copper polyhedron placed between the anvils. This allows for the determination of specific corrections for each ram based on their individual oil pressures. During deformation experiments, each ram adjusts its reported position using these calibrated distances, rather than relying solely on direct distance measurements from the encoder. Consequently, the actual position used for calculations is based on the calibrated position, which corrects for potential errors caused by frame bending. Therefore, any discrepancies observed in the measurements are not due to frame bending but are likely the result of other factors. Even if frame bending errors do contribute, when looking at **Figure 23**, even at 70 bar oil pressure, the correction amount is no more than 20  $\mu\text{m}$  which is far too small to account for the missing strain.

The frame bending calibration ensures that the anvil-to-anvil face distance is accurately measured, thus eliminating frame bending as a source of error. However, an important aspect is missing when doing frame bending calibrations: the temperature. The calibrations are done at room temperature. It is possible that at high temperatures the frame bending calibration would change. The only press components that appreciably heat up above 100 °C during heating are the first stage and second stage anvils. However, after a heating experiment of more than one hour, all six rams feel noticeably warm to the touch. It could be that heating plays a major role in the discrepancy either because the oil is warmer or the tool steel of the ram itself is warmer which would decrease the Young's modulus and allow for more elastic strain. Of course, the thermal expansion would unintuitively actually increase the size of the steel, but the trend from **Figure 100** seems clear.

## 4. Discussion

The position encoder is attached to the ram itself on the back-face and extends through the cylinder to the back. The distance measurement it records is based on the back of the 1<sup>st</sup> stage anvil. Apart from a small WC insert on the front of the anvil, the majority of the anvil body is hardened tool steel. The exact steel alloy is unknown, but taking a typical value of 200 GPa for the Young's elastic modulus (Wang et al., 2013) of hardened tool steel at the typical anvil temperature during heating of roughly 150 °C, the elastic shortening in the anvil can be calculated according to Eq. 122, where  $\Delta L$  is the shortening,  $F$  the force,  $L$  the initial length,  $A$  the cross-sectional area, and  $E$  Young's modulus.

$$\Delta L = \frac{F \cdot L}{A \cdot E} \quad \text{Eq. 122}$$

The diameter of the tool steel part of the 1<sup>st</sup> stage anvil is 50 mm, length 120 mm. Taking a starting oil pressure on stage 1 and 2, before deformation, of 40 bar, to advance the anvils they typically rise to 70 bar at the end of most of the deformation experiments. Converting this to a difference in force on the anvil between the start and end of deformation, the additional force is 250 kN per ram for ASTER-15. With these parameters in Eq. 122, a total calculated elastic shortening of the tool steel is 76  $\mu\text{m}$ , per anvil. Thus, with both anvil 1 and 2 shortening by this amount, it can be expected that roughly 152  $\mu\text{m}$  of total deformation shortening is accommodated by the elasticity of the tool steel.

At 4.3  $\mu\text{m}/\text{min}$  advancement rate for 100 minutes, typical of the deformations in these experiments, 430  $\mu\text{m}$  of total advancement is expected. Since this is per anvil, with two anvils advancing this distance into the central space, a total shortening of 860  $\mu\text{m}$  is expected to be measured with radiography before and after deformation. Taking the highest temperature experiment in the compression deformation experiment C3, the total shortening of the full sample column measured with radiography imaging is  $\sim 250 \mu\text{m}$ . Thus, by subtracting both from the total anvil advancement,  $860 \mu\text{m} - 152 \mu\text{m} - 250 \mu\text{m} = 458 \mu\text{m}$ , over half of the shortening is still 'missing' from the strain measurements.

A small amount would further be taken up by elastic deformation of the tungsten carbide anvils, but this would be negligible compared to the other sources. Although this isn't enough to compensate for the missing strain, it does seem clear that higher temperatures do increase the missing strain.

### 4.3. Single crystal deformation without XRD

An important first order analysis of a deformation experiment comes from an examination of the shape of the stress-strain curve. Few studies report the direct stress-strain curve, but some

#### 4. Discussion

data does exist for single crystal olivine, or Fo. In **Figure 101** the shape of the stress-strain curves obtained in this study for single crystal Fo at 1.5 GPa, can be compared to similar data obtained for single crystal olivine at 300 MPa. The literature data continues past 10% strain but was cut off at this point since the study data was only deformed to 10% strain.

single crystal Fo, 1.5 GPa deformation compared to literature

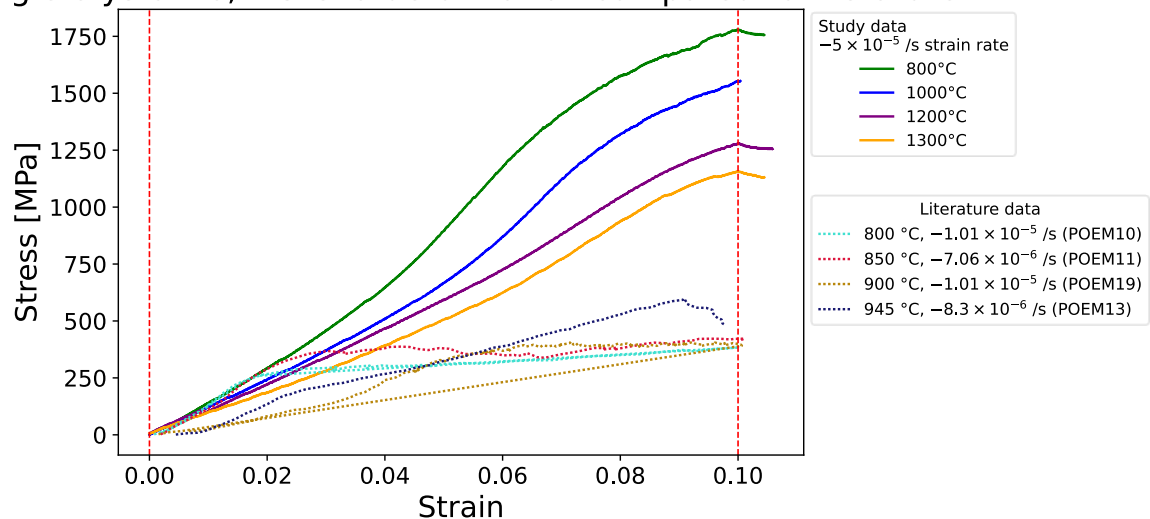


**Figure 101.** Stress versus strain data for the Fo 1.5 GPa single crystal deformation shown again but with the curves from literature plotted on the same scale. The literature data is from (Demouchy et al., 2013) at 300 MPa of confining pressure in a Patterson-type apparatus with a gas-medium. Stress was measured in situ. Temperature, strain rate, and run number are provided in the legend.

Clearly, the stresses are lower overall as compared to this study data. However, this is expected. The confining pressure in this study is 5 times higher (1.5 GPa) compared to the literature data at 0.3 GPa (Demouchy et al., 2013). Overall, a similar pattern of a linear initial increase followed by a steepening and then a slow flattening and plateauing towards the end is visible in both sets of curves.

While more studies have been conducted on the creep of single crystals at ambient conditions (Amodeo et al., 2018), high pressure studies are sparser. Nevertheless, forsterite and MgO were chosen as some studies do exist on these minerals. Since the creep stress is dependent on pressure, temperature, and strain rate, a direct comparison between data points collected in this and previous studies is not possible. Because of this, the equation for power law creep is used to interpolate between the exact experimental conditions (Poirier, 1985).

#### 4. Discussion

$$\dot{\epsilon}(\sigma, T, P) = A\sigma^n \exp\left(-\frac{E^* + PV^*}{RT}\right) \quad \text{Eq. 123}$$

Where  $\dot{\epsilon}$  is the strain rate,  $\sigma$  the creep stress,  $A$  the pre-exponential term,  $T$  the absolute temperature,  $P$  the hydrostatic pressure,  $E^*$  the activation energy,  $V^*$  the activation volume,  $R$  the gas constant, and  $n$  the stress exponent. By measuring the pressure, temperature, creep stress, and strain rate during the deformation experiment, the values for  $A$ ,  $Q$ ,  $E^*$  and  $V^*$  can be obtained for the material.  $n$  depends on the type of creep. At low stresses, creep is partially controlled by transport of matter by diffusion, and  $n = 1$  or  $2$ . At increased stresses, recovery-creep processes controlled by Weertman creep is dominant with  $n \approx 3$  to  $5$  (Poirier, 1985).

At typical laboratory-obtainable stress and strain rates, the power law equation describes creep quite well and thus this was chosen to model the single crystal forsterite and MgO data. Due to the single strain rate that all data was measured at as well as the relatively lower precision and accuracy in the strain rate measurements, all four parameters are not well constrained. To simplify the fitting process,  $n = 3$  was assumed for each fit and not allowed to vary. This is a reasonable value for high-temperature dislocation glide or climb-controlled dislocation creep of both MgO and forsterite (Amodeo et al., 2018; Mei et al., 2008; Wilshire, 1995).

Only the deformation experiments that passed the yield point and entered the creep regime were fit to the power law equation. In this regime, the crystal is deforming at approximately constant stress, at least until strain hardening begins to increase the stress. This creep regime is defined as the flow stress of the sample at a given set of environmental conditions and strain rate (Hansen et al., 2019).

**Table 26.** The result of power law creep fitting of data from this study, compared to literature data on both single crystal forsterite and single crystal MgO. The crystallographic compression direction is listed as well. The superscript  $f$  indicates a parameter that is fixed and not allowed to vary. The forsterite fit range for this study fit is 2.3 – 3.0 GPa and 1473 – 1573 K while for Raterron et al. (2007) it is 3.0 – 7.5 GPa and 1377 – 1677 K. In the MgO case, the fit range in this study is wider at 1.5 – 3.0 GPa and 1073 – 1573 K and for Mei et al. (2008) it is 1.5 – 10.0 GPa and 1350 – 1573 K.

Single crystal forsterite					
Source	$\sigma_1$ direction <hkl>	$A$ [s <sup>-1</sup> · Pa <sup>-n</sup> ]	$n$	$E^*$ [kJ/mol]	$V^*$ [cm <sup>3</sup> /mol]
This study	<100>	$1.9 \times 10^{-29}$ $\pm 2.0 \times 10^{-30}$	$3^f$	$67 \pm 24$	$6.5 \pm 4.5$

#### 4. Discussion

Raterron <i>et al.</i> (2007)	<110>	$1.5 \times 10^{-24}$	$2.6 \pm 0.3$	$112 \pm 40$	$3.0 \pm 0.5$
Raterron <i>et al.</i> (2007)	<011>	$4.0 \times 10^{-26}$	$2.7 \pm 0.3$	$104 \pm 40$	$1.0 \pm 0.5$
<b>Single crystal MgO</b>					
Source	$\sigma_1$ direction <hkl>	$A$ [ $s^{-1} \cdot Pa^{-n}$ ]	$n$	$E^*$ [kJ/mol]	$V^*$ [ $cm^3/mol$ ]
This study	<100>	$1.2 \times 10^{-25} \pm 4.5 \times 10^{-26}$	$3^f$	$77 \pm 31$	$9.9 \pm 3.7$
Mei <i>et al.</i> (2008)	<100>	$7.9 \times 10^{-27}$	$3^f$	$72 \pm 50$	$2.4 \pm 0.9$

**Table 26** compares this study data with the literature data for deformation of single crystals at high pressure and temperature (Mei et al., 2008; Raterron et al., 2007). The piezoelectric method stress errors can be estimated based on some assumptions. The integrating capacitor has a manufacturer reported 1% precision, or  $9.964 \times 10^{-9} \pm 9.964 \times 10^{-11}$  F. From the limited number of estimations done on the high-pressure trend of the piezoelectric coefficients through ab-initio calculations, one example shown in **Figure 104**, the coefficient at 3 GPa of GaPO<sub>4</sub> increases by ~18%. Assuming the same increase for CTGS is reasonable in which case this would be the percent error of the value of  $d_{11}$  of CTGS at 3 GPa, or  $4.0 \times 10^{-12} \pm 7.2 \times 10^{-13}$  C/N. The measurement of the 4 mm diameter piezoelectric crystal is estimated at 2% error (80  $\mu$ m) through measurements of multiple crystals, or an area error of  $1.26 \times 10^{-5} \pm 5.03 \times 10^{-7}$  m<sup>2</sup>. So, propagating the error in Eq. 95 and Eq. 96, a simple error approximation is 18.5% of calculated stress. The largest contributor to the error is  $d_{11}$ . Being able to measure this value at high pressure or at least correct it using ab-initio calculations would do the best at reducing the error.

The error bars reported by other studies are surprisingly large. This type of fitting is highly sensitive and can easily be numerically unstable because of the exponential term and large value ranges.

Additionally, XRD errors are quite large, as noted by Mei et al. 2008 where a thin disk of polycrystalline MgO was placed between the two single crystals and was used to calculate the stress with XRD. As they report, only two MgO peaks were fit from the XRD patterns, (111) and (200). The (111) peaks showed consistently higher, roughly double, stress compared to the (200) peaks and thus those were used for solving the power law creep equation. This highlights the inherent uncertainty present in XRD stress measurements.

## 4. Discussion

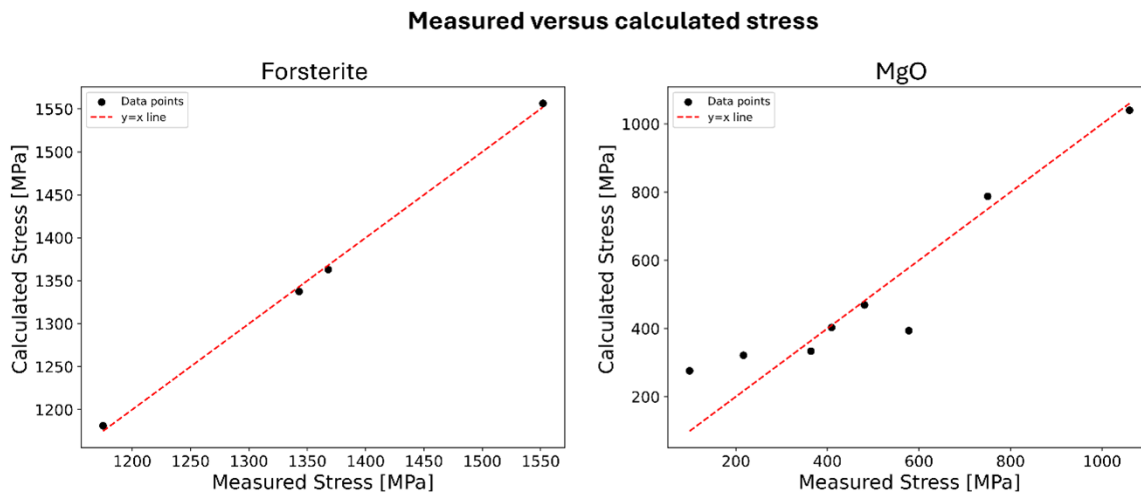


**Figure 102.** The quality of fit with the power law creep equation to the single crystal forsterite and MgO deformation from this study. The experimentally measured stress is on the horizontal axis and the calculated stress using the fitted values is on the vertical axis. The diagonal red dashed line is the 1:1 agreement.

Using the fitted values, the power law creep equation (Eq. 123) can be used to calculate the expected creep stress for given sets of conditions. These calculated stresses, using the deformation experimental conditions from **Table 19**, are displayed in **Figure 102**. The forsterite fits are excellent, with the points falling almost exactly on the 1:1 line. For MgO, the fit is more scattered but is still quite good given the numerical range of possible fits for the power law creep equation. The values for the power law creep equation can be used to compare the creep stress directly with literature data. These are plotted in **Figure 103** by solving the power law equation for the creep stress for a constant strain rate and constant pressure. The large errors in the literature data result in a wide margin of error for creep stress, shown with the shaded color regions. The study creep stress error is also shown.

#### 4. Discussion

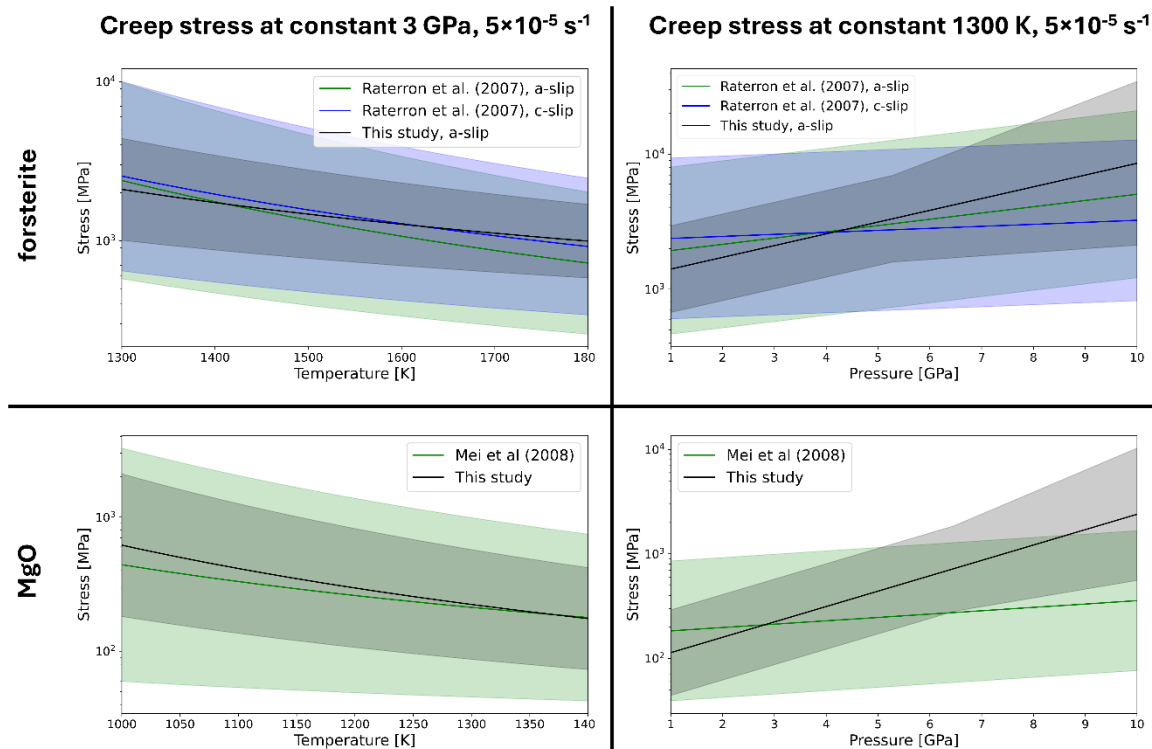


**Figure 103.** The trend of creep stress with temperature and pressure at a constant strain rate of  $5 \times 10^{-5}$ . The top plots are of forsterite, and the bottom of MgO. The left are at constant hydrostatic pressure of 3 GPa and the right at constant temperature of 1300 K. This study data and literature data from Raterron *et al.* (2007) and Mei *et al.* (2008) are shown for comparison. The shaded colored area are the respective error ranges of each set of values.

The creep stress trend for single crystal forsterite demonstrates an overall better fit, particularly with an excellent temperature trend. However, the larger activation volume results in greater material strengthening under pressure. A similar trend is observed in MgO, where an activation volume of  $9.9 \text{ cm}^3/\text{mol}$  leads to increased strengthening at higher pressures. Notably, the data from Mei *et al.* (2008) spans pressures from 1.5 to 10 GPa, whereas this study only reached up to 3 GPa. This discrepancy might explain why the extrapolation to higher pressures indicates a stiffer MgO. Additional high-pressure data would be necessary to determine if MgO strength increases less dramatically with pressure. It is also possible that the sequential nature of the experiments on the same MgO sample contributed to strain strengthening. As pressure increased incrementally during the experiments, the MgO may have become stronger due to prior deformations at lower pressures. However, it's important to note that Mei *et al.* (2008) measured stress from a single MgO peak, (200), which may not provide a comprehensive stress estimation. The (111) peak exhibited about half the measured stress. Therefore, fitting more

#### 4. Discussion

peaks could yield a more accurate stress estimation in the sample. It is plausible that other peaks experienced much higher stress.

Determining the strain rate error using the piezoelectric method is challenging. Without X-ray radiography, only the anvil advancement rate can be used as a first-order approximation. For more accurate measurements, new methods to assess sample strain need to be developed. Using the current method, which assumes the strain rate from the anvil movement as indicated by the position encoder, the error is likely not more than a factor of 4, and usually less in most cases.

However, the stress measurement is likely more precise, as demonstrated by XRD experiments. An optimal approach would combine X-ray radiography for strain measurement with a piezoelectric crystal for stress measurement. Additional errors arise from the uncertainty in the high-pressure trend of the piezoelectric coefficient. Previous research on measuring the piezoelectric coefficient at high pressures is sparse. Only recently have DFT ab-initio calculations been used to predict high-pressure trends (Alathlawi et al., 2024; Almaghbash & Arbouche, 2021; Daoud & Bouarissa, 2019; Demartin & Damjanovic, 1996; Gao et al., 2011). While elastic stiffness coefficients generally increase with pressure, piezoelectric coefficients do not follow a uniform trend. Some coefficients may increase, some decrease, and some may even reverse trends, as shown in the DFT ab-initio calculations for GaPO<sub>4</sub> illustrated in **Figure 104**. GaPO<sub>4</sub> shares the same space group and point group as  $\alpha$ -quartz and CTGS.

## 4. Discussion

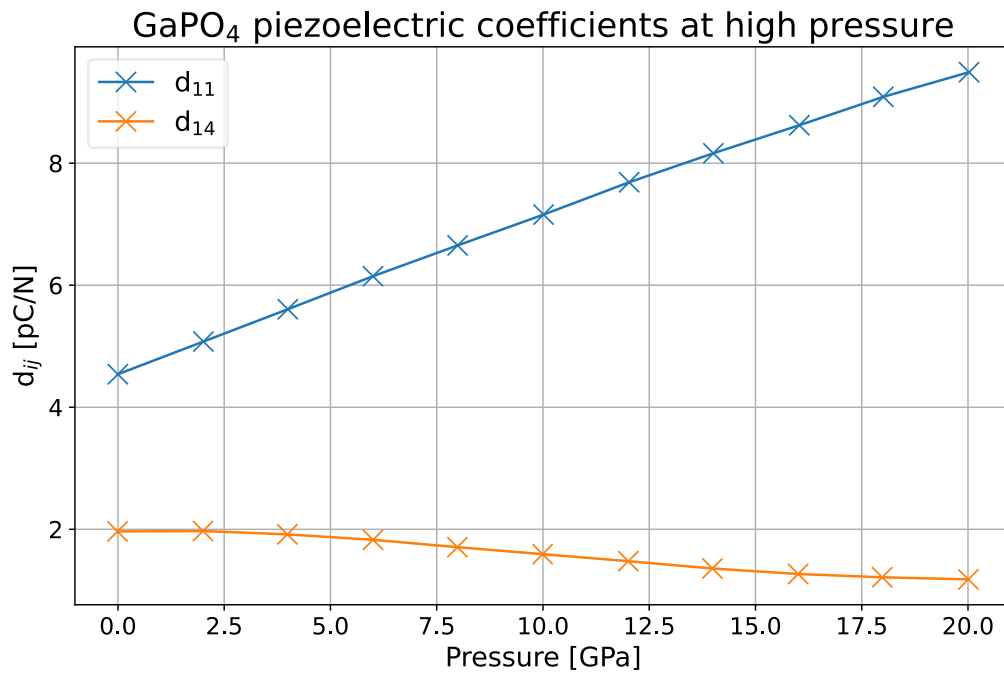


**Figure 104.** *Ab-initio* calculation of the piezoelectric coefficient  $d_{ij}$  of GaPO<sub>4</sub>. GaPO<sub>4</sub> has the same point group as  $\alpha$ -quartz and CTGS. Calculations provided through personal communication from Razvan Caracas.

The piezoelectric method to measure stress of deformation in LVPs relies on a high degree of accuracy in the piezoelectric coefficient as it directly affects the measured stress. Until more work is done to determine the dependence with hydrostatic pressure on the piezoelectric coefficient of CTGS, the errors cannot be further constrained. Future work to improve the method would concentrate on characterizing the high-pressure piezoelectric trends in CTGS as well as new methods to measure the strain of a sample at high pressure without using XRD.

### 4.4. Brillouin spectroscopy on CTGS

#### 4.4.1 Linear modeling of elastic stiffness coefficients

The results from Brillouin spectroscopy on CTGS are displayed in **Figure 105** with elastic stiffness coefficients and the bulk modulus,  $K$ , plotted. The top plot is the data with the linear fits and the bottom are the residuals of the fits.

## 4. Discussion

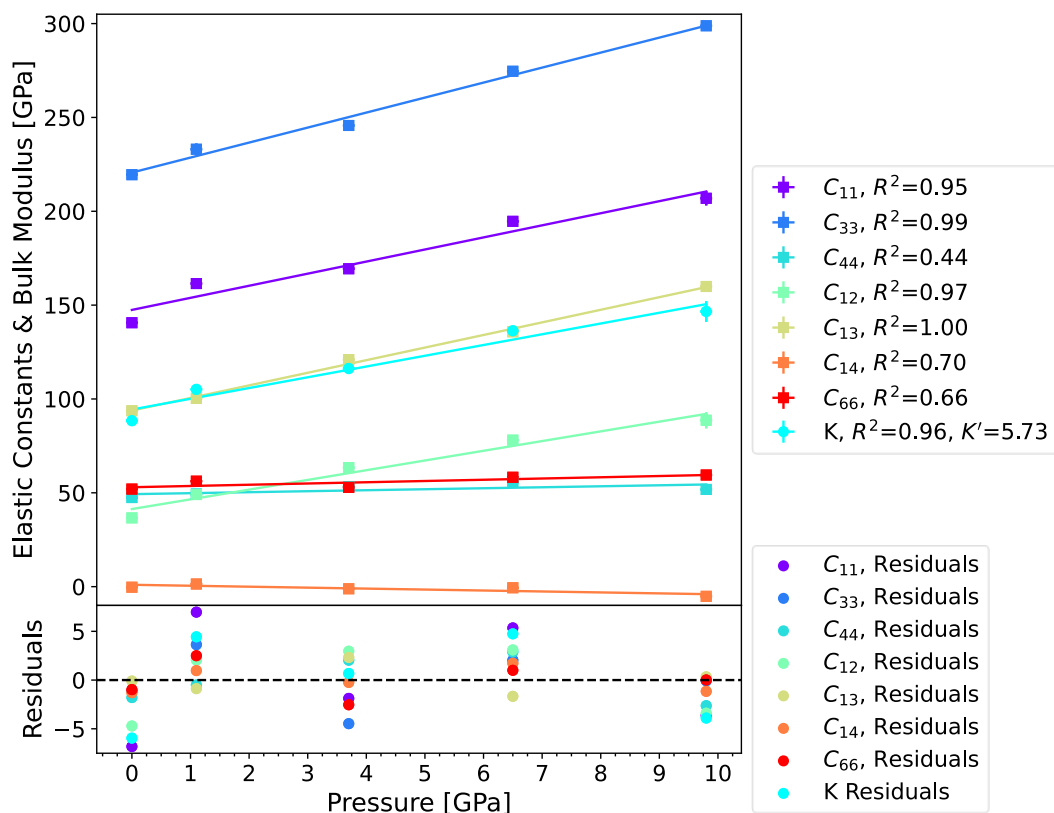


**Figure 105.** Elastic stiffness coefficients and bulk modulus fits to the velocity dispersion curves for each pressure point are plotted in the top graph. The goodness of fit, as an  $R^2$  value, is displayed in the legend. The bottom plot illustrates the residuals of the fits. The bulk modulus,  $K$ , calculated from the elastic coefficients for each pressure point is also shown, with the derivative of the bulk modulus,  $K'$ , also displayed.

As expected, the elastic coefficients increase with pressure. The derivative of the bulk modulus is unexpectedly high at 5.7. Most crystals are expected to be close to  $K' = 4$  (Pandit & Bongiorno, 2023). A  $K_0$  of  $88.4 \pm 1.6$  GPa is reasonable compared to reported literature range in **Table 28** of 75.4 – 110.4 GPa. This value of  $K_0$  is reported as the bulk modulus calculated with Eq. 115 using the elastic coefficients measured at 1 bar. Since XRD was taken at each pressure point, density can also be plotted against the hydrostatic pressure as displayed in **Figure 106**.

## 4. Discussion

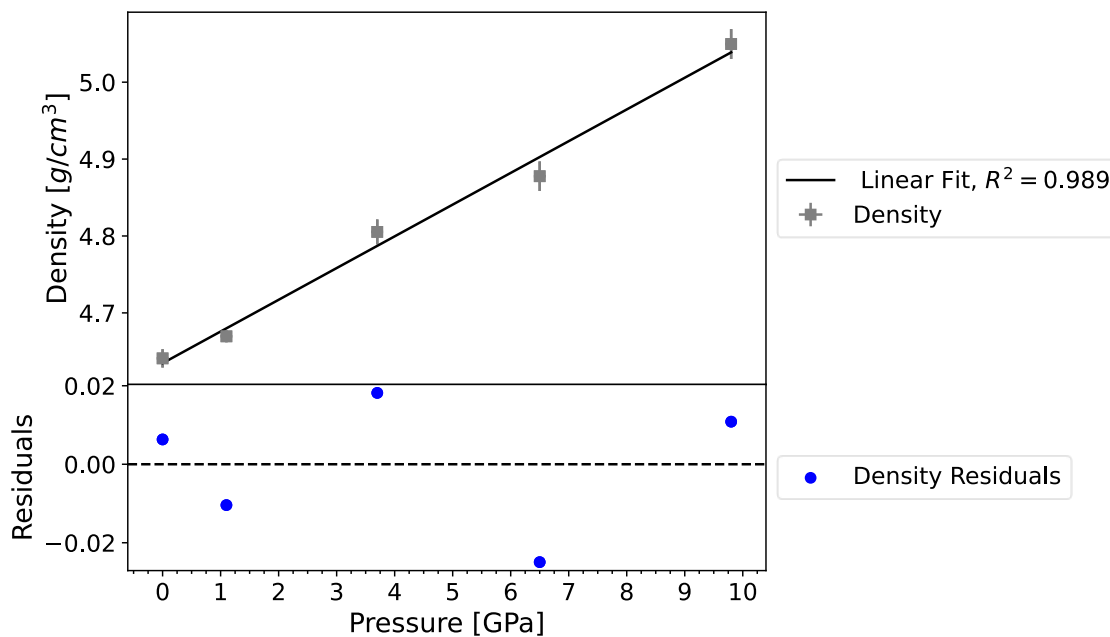


**Figure 106.** Plot of density in  $\text{g/cm}^3$  against pressure along with the linear fit and residuals.

### 4.4.2. Elastic compliance coefficient $S_{14}$ of CTGS

Through the collection of Brillouin data on CTGS, the elastic stiffness coefficients were derived. To evaluate the magnitude of the critically important  $S_{14}$  stiffness coefficients and understand its trend with pressure, it is compared with literature data on the elasticity of  $\alpha$ -quartz. This comparison is essential because the  $S_{14}$  stiffness coefficient controls the Dauphiné twinning process in P321 space group crystals. A smaller value of  $S_{14}$  indicates that more deviatoric stress is required to induce twinning, similar to what is observed in  $\alpha$ -quartz where twinning occurs. The elastic stiffness matrix was inverted, as per Eq. 83, to acquire the elastic compliance matrix. Two datasets on  $\alpha$ -quartz at high pressure, measured with Brillouin spectroscopy to keep consistent with this study's method, are used for comparison (Gregoryanz et al., 2000; J. Wang et al., 2015).

The final values are displayed in **Figure 107**. The two  $\alpha$ -quartz trends are similar and both display that at ambient pressure and up to 6.5 GPa,  $S_{14}$  of  $\alpha$ -quartz is substantially higher than that of CTGS. This study's data shows that  $S_{14}$  of CTGS is an average of  $5.5 \times 10^{-5} \text{ GPa}^{-1}$  for most of the deformation experiment pressure range, 0 – 8 GPa, only rising above that of  $\alpha$ -quartz, an average of  $2.1 \times 10^{-3} \text{ GPa}^{-1}$  across the same pressure range, beginning above 8 GPa. This is likely the reason why, as per Eq. 99, CTGS has not undergone ferroelastic switching in the majority of the high-pressure deformation experiments whereas  $\alpha$ -quartz frequently

#### 4. Discussion

switched. For experiments below 8 GPa, CTGS is the better choice over  $\alpha$ -quartz for these experiments, not only due to the order of magnitude higher electrical resistivity, but also the larger coercive stress required to undergo switching. The term in Eq. 99 that is relevant is the second term, repeated below in Eq. 124.

$$2S_{14}(\sigma_1\sigma_4 - \sigma_2\sigma_4 + 2\sigma_6\sigma_6) \quad \text{Eq. 124}$$

Since a ferroelastic switch flips the direction of the piezoelectric vector as well as  $S_{14}$ , a Dauphiné twin has necessarily an elastic coefficient  $S_{14}$  with opposite sign (Tichý et al, 2010; Shiao et al., 1984). This is what drives the mechanical component of the ferroelastic switch due to deviatoric stress alone. When the stresses reach a threshold sufficiently high enough to reverse the sign of the full  $S_{14}$  term in Eq. 124 the crystal begins to twin (Bertagnolli et al., 1979; Markgraaff & Roering, 1995; Shiao et al., 1984). This is through a Gibbs free energy sign switch driven by the term in Eq. 115. With CTGS having a smaller  $S_{14}$  which acts as a multiplier to the stresses, a much larger stress is required to overcome the metastability of the crystal (Yamni, 2001) and induce twinning. This is why a piezoelectric crystal with a low  $S_{14}$  is ideal for stress determination in these types of deformation experiments.

The Brillouin spectroscopy measurements on CTGS display that at least up to 7 – 8 GPa, it is preferable to  $\alpha$ -quartz. Beyond this point it is unclear which is preferred as the trend of  $S_{14}$  is unclear.  $\alpha$ -quartz may continue the trend downwards and become further negative while CTGS

## 4. Discussion

could continue increasing upwards. The sign of  $S_{14}$  is irrelevant, as shown by Eq. 23, only the absolute value matters.

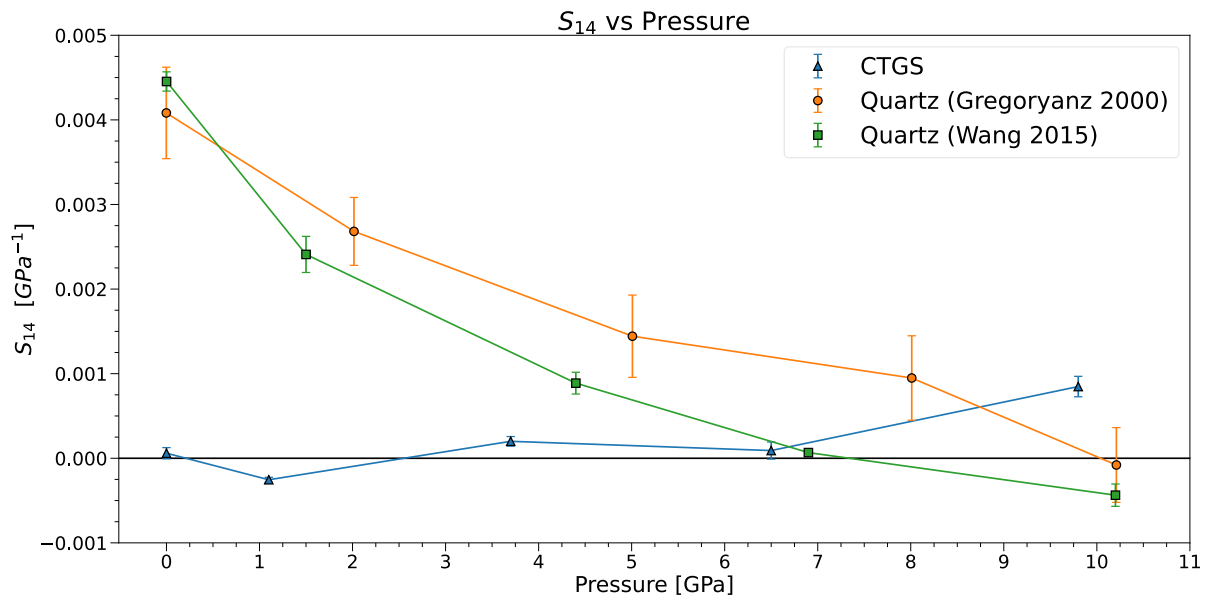


**Figure 107.** The trend of  $S_{14}$  with pressure. The blue points are from this study on CTGS, and the others are from the cited studies on  $\alpha$ -quartz. All data was measured with Brillouin spectroscopy utilizing a DAC for the high-pressure data points.

Another strategy would be to choose a piezoelectric crystal with a high  $S_{14}$  coefficient. In this case, the twinning would occur right at the start of the deformation, with the smallest applied stress, and then be stable up to an arbitrarily high stress. In this case, the goal would be to twin the crystal as soon as possible to eliminate the twinning error at increasing deviatoric stresses. However, care would have to be taken as the twinning process can be confined only to small domains within the whole crystal body (Bertagnolli et al., 1979; Markgraaff & Roering, 1995; Shiau et al., 1984; L. A. Thomas et al., 1951). Unless the whole crystal twins rapidly, twinned domains can remain or grow slowly, causing the voltage generated by the deviatoric stress to be lowered. Consider a possible partially twinned state of a crystal in **Figure 108**.

#### 4. Discussion

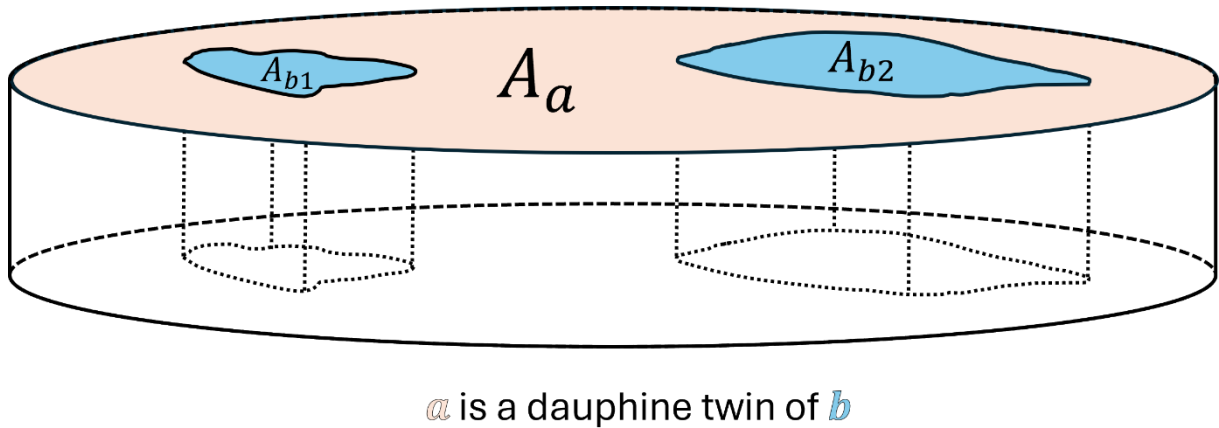


**Figure 108.** Schematic diagram of a piezoelectric crystal that has subdomains within it that have undergone ferrobielastic switching. *a* is the original untwinned crystal and *b* are the twinned domains.  $A_a$  is the area of twin *a* and  $A_{b1} + A_{b2}$  is the total area of twin *b*.

In the twinned area of *b*, voltage of the opposite sign is generated. If the total physical area of the crystal is  $A_0$ , and the area of the initial twin state *a* is  $A_a$ , the area of twin *b* is  $A_b = (A_{b1} + A_{b2}) = A_0 - A_a$ , then the true stress that is calculated from the integrated charge during the deformation experiment is described by Eq. 125.

$$\sigma_{11} = \frac{\Delta V \left( \frac{A_a}{A_0} - \frac{A_b}{A_0} \right) C_F}{A_0 \cdot d_{11}} \quad \text{Eq. 125}$$

The other terms are described previously by Eq. 95 and Eq. 96. Since  $A_a$  and  $A_b$  are unknown during a deformation experiment, any increase in  $A_b$  is an error in the measured stress, working to reduce the actual stress measured. As can be seen, if  $A_b = 0$ , there is no error, and as  $A_b$  increases the measured stress reduces until  $A_a = A_b$  at which point the stress measured is zero as long as the relation holds. After fully twinning,  $A_a = 0$  and now the generated voltage is reversed and thus the stress accumulation is reversed. The speed of the increase in  $A_b$  is dependent on temperature and how much the deviatoric stress ‘overshoots’ the critical stress of ferrobielastic switching  $\sigma_c$  (Shiau et al., 1984; Westbrook, 1958). In deformation experiments at high-pressure with  $\alpha$ -quartz as the piezoelectric crystal, ferrobielastic twinning was always, even in room temperature experiments, gradual and over a period of at least 10 minutes forming a smooth curve, as seen in **Figure 40**. This is unlike previous studies on ferrobielastic switching at room temperature in which the crystal twins on a very short time scale of a few seconds to even under one second, forming a sharp sawtooth pattern (Bertagnolli et al., 1979; Mansfel’d et al., 1997; Shiau et al., 1984; Yamni, 2001). There is a possibility that hydrostatic pressure

## 4. Discussion

has a yet unknown effect acting to slow down the domain growth of the Dauphiné twin. Additionally, larger crystals tend to twin through slower growing domains as opposed to smaller crystals in which the twinning process can be rapidly completed.

### 4.4.3. Third order finite strain modeling of elastic stiffness coefficients

When considering the trend in  $S_{14}$  with pressure, the linear fitting of the  $C_{ij}$  coefficients in **Figure 105** is adequate for the lower pressure regions. However, to extrapolate to higher pressures a more precise and accurate fit is obtained through a third-order finite-strain equation using (Birch, 1978). These equations, similar to the third-order Birch-Murnaghan EOS, more precisely capture the trend with pressure.

$$C_{ijkl}(f) = (1 + 2f)^{7/2}(C_{ijkl}^0 + b_1 f) - P\Delta_{ijkl} \quad \text{Eq. 126}$$

$$b_1 = 3K_0(C'_{ijkl} + \Delta_{ijkl}) - 7C_{ijkl}^0 \quad \text{Eq. 127}$$

$$\Delta_{ijkl} = -\delta_{ij}\delta_{kl} - \delta_{ik}\delta_{jl} - \delta_{il}\delta_{jk} \quad \text{Eq. 128}$$

$$f = \frac{1}{2}[(V_0/V)^{2/3} - 1] \quad \text{Eq. 129}$$

The above equations, modified from (Wang et al., 2015), were fit for  $C'_{ijkl}$  and  $C_{ijkl}^0$  to each coefficient.  $P$  is pressure in GPa,  $K_0$  is the bulk modulus at ambient pressure,  $V_0$  is the unit cell volume at ambient pressure,  $V$  is the high-pressure unit cell volume, and  $\delta_{ij}$  is the Kronecker delta. The notation used for these calculations is the tensor, 4-subscript notation. The conversion between the matrix 2-subscript and the tensor notation was previously described in Table 1.  $V$  is solved for each pressure numerically utilizing the third-order Birch-Murnaghan EOS with the previously calculated bulk modulus and derivative of the bulk modulus. Through numerical solutions of Eq. 126 – Eq. 129, a more theoretically precise value of  $C_{ij}^0$  and  $C'_{ij}$  with pressure can be found. The data points along with the curves fit to the points are displayed in Figure 109. The longitudinal coefficients have adequate fits along with the  $C_{13}$  and  $C_{12}$  off-diagonal coefficients. However, the independent shear coefficient  $C_{44}$  and dependent  $C_{66}$  do not fit well in addition to the off diagonal  $C_{14}$ . This is likely due to errors in peak positions from the Brillouin spectra resulting in errors in the calculated dispersion curve for CTGS. The fitting has been extrapolated to 20 GPa. Further work would extend the pressure range to better constrain the finite third-order curves. At these lower pressures, the change in the elastic coefficients is close to linear. Higher pressure measurements would better constrain the curvature. Issues can arise above 11.7 GPa as He solidifies above this hydrostatic pressure (Vos et al., 1990) but

#### 4. Discussion

generally He can remain soft enough to ensure near-hydrostatic stress within the DAC. He strength remains  $<0.1$  GPa up to 20 GPa, reaching 1 GPa at 50 GPa of pressure (Singh, 2012).

**Table 27.** Ambient pressure  $C_{ij}$  and derivative with pressure fits of CTGS using third order finite strain equations.

	$C_{11}$	$C_{33}$	$C_{44}$	$C_{12}$	$C_{13}$	$C_{14}$	$C_{66}$
$C_{ij}^0$ [GPa]	149.0	222.2	49.2	43.2	95.6	0.96	52.8
$C'_{ij}$	6.46	8.19	0.64	4.92	6.61	-0.51	0.80

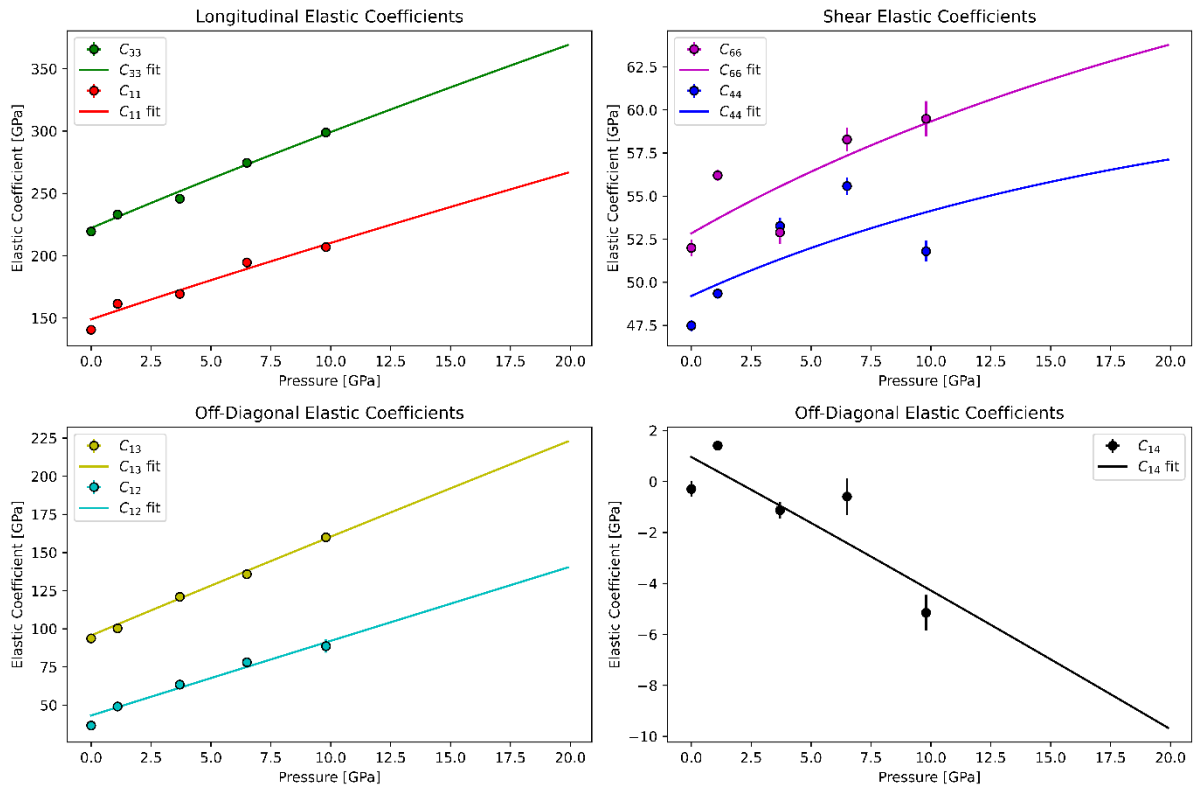


**Figure 109.** Elastic stiffness coefficients with the hydrostatic pressure trend. The data is fit with third-order finite strain equation. The fit has been extrapolated to 20 GPa.

By taking the 1 bar of hydrostatic pressure elastic coefficients from the third-order finite strain fits, ambient condition  $C_{ij}$  can be compared, including the calculated bulk modulus,  $K_0$ , with literature data that utilized different methods to derive the elastic constants. These are listed and compared in **Table 28**. As can be seen, the elastic constants as compared with other studies are widely distributed. In particular,  $C_{12}^0$  varies more widely between the different studies.

## 4. Discussion

**Table 28.** Third-order finite strain equations fits to the high-pressure CTGS data and used to derive the 1 bar elastic stiffness coefficients and the calculated bulk modulus using Eq. 115 labeled (FS). The direct 1 bar measurements are also provided, labeled (1 bar). Data from (Biryukov et al., 2014; Ma et al., 2017; Shi et al., 2007; Sotnikov et al., 2013; Suhak et al., 2018; Zu et al., 2016). The average and population standard deviation of all literature data, including this study data, is listed on the last two rows.

Source	Method	$C_{11}^0$ [GPa]	$C_{33}^0$ [GPa]	$C_{44}^0$ [GPa]	$C_{12}^0$ [GPa]	$C_{13}^0$ [GPa]	$C_{14}^0$ [GPa]	$C_{66}^0$ [GPa]	$K_0$ [GPa]
<i>This study (FS)</i>	<i>Brillouin spec.</i>	149.0	222.2	49.2	43.2	95.6	0.96	52.8	96.08
<i>This study (1 bar)</i>	<i>Brillouin spec.</i>	140.6	219.5	47.49	36.6	93.7	-0.30	52.0	88.4
Ma et al, 2017	Pulse-echo	157.4	225.3	41.8	74.4	80.6	0.77	41.5	109.1
Ma et al, 2017	Pulse-echo	156.3	227.5	41.5	75.2	85.5	0.51	40.6	110.44
Ma et al, 2017	Impedance	131.2	195.3	40.9	43.4	56.7	0.42	43.9	87.11
Shi et al., 2007	Resonant	123.1	178.1	40.9	32.9	44.7	0.44	45.1	71.35
Sotnikov et al., 2013	Pulse-echo	157.3	210.6	41.8	75.75	64.15	0.54	40.8	102.73
Suhak et al., 2018	Resonant	148.8	219.3	47.4	57.9	80.6	0.093	44.9	100.14
Suhak et al., 2018	Pulse-echo	155.6	211.6	42.0	73.6	70.1	0.84	41.1	103.95
Biryukov et al., 2014	SAW	154.8	211.3	42.0	73.0	70.5	0.63	40.9	103.67
Zu et al., 2016	Impedance	142.6	203.3	48.53	51.91	62.52	-0.41	45.35	90.38
	Mean	147.62	210.45	43.61	60.12	71.09	0.47	43.70	96.95
	Standard deviation	11.32	14.34	3.18	15.50	14.20	0.38	3.55	11.81

### 4.4.4. Born stability criteria of CTGS

Previous work has shown that when a single crystal of  $\alpha$ -quartz is compressed at room temperature, a pressure is reached where it undergoes amorphization (Badro et al., 1998; Binggeli et al., 1994; Wentzcovitch et al., 1998). This is a limit on how high pressure the piezoelectric crystal could be used in the assembly to measure stress. Beyond this point, the amorphization would completely eliminate any possible measurement of stress. Theoretical studies have suggested that this could be triggered by elastic instability when the Born stability criteria are violated (Born, 1940; Born & Huang, 2002; Coulson, 1958). These provide the necessary conditions for a crystal to be mechanically stable. The Born stability criteria conditions for trigonal crystals, applicable equally to  $\alpha$ -quartz and CTGS, which are necessary and sufficient, are described below (Mouhat & Coudert, 2014). If the elastic stiffness

#### 4. Discussion

coefficients at a given pressure violate any of these conditions, the phase is predicted to become mechanically unstable and is likely to either amorphize or transition to a new phase.

$$\left\{ \begin{array}{l} C_{11} > |C_{12}| \\ C_{44} > 0 \\ C_{13}^2 < \frac{1}{2} C_{33} (C_{11} + C_{12}) \\ C_{14}^2 < \frac{1}{2} C_{44} (C_{11} - C_{12}) \end{array} \right. \quad \text{Eq. 130}$$

With the third-order finite strain equations numerically solved, the bulk moduli and derivative of bulk moduli with pressure can be used to predict at what hydrostatic pressure a Born stability criterion is first violated. By taking the difference across the inequalities, an equation can be derived for each criterion. Numerically solving for the elastic coefficients to arbitrarily high hydrostatic pressures and using the conditions, a criterion is violated when the resultant equation  $f_i \leq 0$ . The plots in **Figure 110** are the result of this process using the CTGS elastic coefficients measured with the Brillouin spectroscopy method. The plotted curves are the result of repeatedly numerically solving Eq. 126 – Eq. 129, in steps of 0.001 GPa and using the  $C_{ij}$  at each pressure to check for any violation of the criteria in Eq. 130. In this case, the  $K_0$  was fixed to 96.08 GPa and corrected to higher pressures using a  $K'_0$  of 4.77, which was previously calculated using the finite 3<sup>rd</sup> order strain equations. The volume at each pressure was derived using the third-order Birch-Murnaghan equation (Eq. 107).

## 4. Discussion

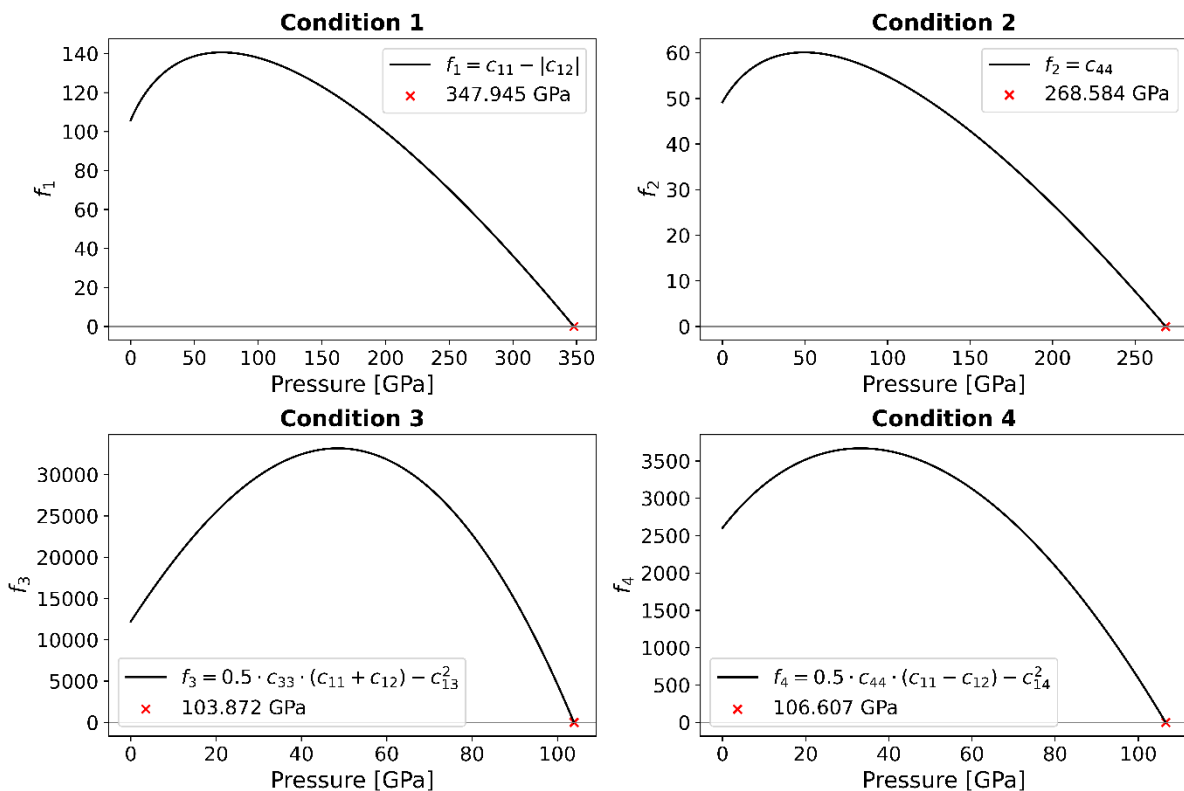


**Figure 110.** The Born criterion conditions of CTGS plotted with the functions listed in the legends. The point at which each criterion reaches 0, or in other words is violated, is marked and the hydrostatic pressure provided for each criterion.

As is displayed in the figures, criterion or condition 3 is violated at the lowest hydrostatic pressure of 103.9 GPa,  $f_3 = 0$ . Since all four criteria are necessary, only one violation is required to render the crystal mechanically unstable. Thus, according to the Brillouin spectroscopy data acquired, CTGS becomes mechanically unstable at 103.9 GPa through the violation of condition 3. It is important to keep in mind that even minor errors in the third-order finite strain fitting would shift this pressure dramatically because of the high sensitivity to the derivative of the elastic coefficient. Constraining this pressure would require more Brillouin spectroscopy measurements and at higher pressures as well.

The same process has been accomplished for  $\alpha$ -quartz in literature. The pressure at which  $\alpha$ -quartz violates a Born criterion has been reported at 26 GPa (Wang et al., 2015), 30 GPa (Choudhury & Chaplot, 2006; Kimizuka et al., 2007), and even up to 49 GPa (Gregoryanz et al., 2000). Experimentally,  $\alpha$ -quartz remains mechanically stable at room temperature up to approximately 18 GPa. While discrepancies exist as to when amorphization begins, in general the range reported experimentally is 18 – 35 GPa (Dong et al., 2015; Haines et al., 2001).

## 5. Conclusion

Generally, it seems to not be a sharp transition and instead there is a gradual increase of amorphization producing heterogeneous samples of coexisting crystalline and amorphous phases (Calderon et al., 2007). It's clear that the amorphization of  $\alpha$ -quartz is well predicted by the Born criteria. There is no reason to believe CTGS, belonging to the same space group as  $\alpha$ -quartz, would undergo amorphization in a different way except at significantly higher pressure as suggested by the Brillouin spectroscopy results. Based on the Born criteria, CTGS should be stable up to very high pressure as long as the temperature remains low. Of course, this is hypothetical and would require experimental verification.

## 5. Conclusion

The development and implementation of the piezoelectric method for measuring stress at high pressures represents a significant advancement in assessing material strength under extreme conditions. This novel technique has proven not only feasible but also highly effective, complementing the conventional X-ray diffraction (XRD) methods traditionally used for stress measurements in similar environments.

The piezoelectric method offers several advantages over XRD, particularly its ability to provide continuous, real-time measurements of stress changes within a sample during deformation experiments. This capability is crucial for understanding the dynamic processes occurring at high pressures, especially when strain rates are high or in the brittle zone of the Earth's upper mantle and crust. Unlike XRD, which requires an exposure time that averages stress measurements over the collection period, the piezoelectric method captures near-instantaneous stress changes.

One significant limitation of XRD is the variability in stress measurements depending on the crystallographic plane, or (hkl) peak, being analyzed. In this study, stress values obtained from different (hkl) peaks in San Carlos olivine showed considerable spread, ranging from -2 GPa to 4 GPa at the worst. This variability introduces potential bias and complicates data interpretation, as different planes respond differently to stress. The piezoelectric method showed excellent fit partly because a large number of peaks (up to 23) of San Carlos olivine were analyzed, whereas most studies typically fit only up to 6 or 7 peaks (Burnley, 2015; Burnley & Kaboli, 2019; Dixon & Durham, 2018; Hansen et al., 2019).

The ability of the piezoelectric method to measure stress off the beamline also offers significant practical advantages. It reduces dependence on synchrotron facilities, which are not always accessible for extended periods. This flexibility enables a larger number of experiments to be

## 5. Conclusion

conducted. Since the strength of minerals depends on multiple parameters, the variable space is complex, and many deformation experiments are inherently required, including those involving mixed rheology as present in the Earth.

Comparative studies between the piezoelectric method and XRD have demonstrated strong correlations between the two techniques, validating the reliability of the piezoelectric measurements. Experiments conducted on polycrystalline samples of San Carlos olivine, Mg-Al spinel, and MgO at various pressures and temperatures have shown that stress values obtained using the piezoelectric method are consistent with those derived from XRD. The piezoelectric method has also proven to be more precise, capable of measuring small stress changes down to an estimated 10 MPa with an uncertainty of 18.5%. The XRD technique is generally limited to 100 MPa with an uncertainty of 100 MPa.

The results of the deformation experiments conducted with the piezoelectric method have provided new insights into the mechanical behavior of minerals under high-pressure conditions. For instance, the stress-strain relationships obtained from these experiments have allowed for a more precise determination of the elastic and plastic deformation regimes in minerals like San Carlos olivine and Mg-Al spinel. These findings have implications for understanding the rheological properties of the Earth's mantle, where these minerals are abundant.

Moreover, comparative deformation experiments on single crystals like MgO and forsterite at high pressures further highlighted the method's effectiveness. These experiments, which evaluated specific slip planes, confirmed that the piezoelectric method provides stable and precise stress measurements during both compressive and tensile deformations. The weakening in strength due to high pressures has been clearly recorded using the piezoelectric method, and although the data is relatively sparse in this work, the power creep equation fits are largely consistent with those from literature and with smaller uncertainty ranges as well.

Despite the promising results, there are areas where further refinement and research are needed. For example, understanding the long-term stability and durability of piezoelectric crystals under prolonged high-pressure conditions is essential for their practical application. Additionally, integrating the piezoelectric method with other analytical techniques could provide a more comprehensive understanding of stress and deformation mechanisms in various materials. A key advancement would be a method to measure strain in situ. Currently, a beamline at the synchrotron is still required for this. However, it has been shown that the strain on the sample

## 5. Conclusion

is within a factor of 2 to 3 of that measured by the position encoder on the anvils. As a first-order approximation, this can be used to get a reasonable estimate of the strain and strain rate.

One notable issue encountered was voltage drift in the piezoelectric measurements, particularly under high deviatoric stresses. This drift can lead to inaccuracies in the stress data, especially in long-duration experiments. Addressing this problem will require improvements in the design and calibration of the piezoelectric sensors to ensure stable and reliable measurements over extended periods. Solutions could include measuring the electrical resistance across the crystal during deformations, optimizing the material around the piezoelectric crystal to reduce conduction, and thermally insulating the piezoelectric crystal better to reduce temperature-induced drift. The Arrhenius equation describing the electrical conductivity of dielectric crystals indicates that temperature changes significantly affect voltage drift, becoming more severe at higher temperatures.

Additionally, the piezoelectric method's dependence on initial calibration and the assumption that the stress state starts at zero can introduce errors if the sample is not properly annealed or if residual stresses are present. This can be mitigated by pre-heating the sample at high temperatures for a sufficient duration, although this may lead to grain growth, making the actual grain size uncertain. Therefore, the temperature and annealing time must be carefully chosen.

In addition to comparing with XRD, the study also explored using Brillouin spectroscopy to investigate the elastic properties of  $\text{Ca}_3\text{TaGa}_3\text{Si}_2\text{O}_{14}$  (CTGS). The Brillouin spectroscopy results were significant in determining the elastic stiffness coefficients and the mechanical stability of CTGS under high pressures. This aspect of the study is crucial to understanding how prone CTGS is to ferrobielastic switching compared to  $\alpha$ -quartz. The results of the Brillouin spectroscopy measurements showed that CTGS has an  $S_{14}$  value close to zero, a factor of 30-40 times smaller than  $\alpha$ -quartz. This confirms that CTGS is a better choice for the piezoelectric assembly because ferrobielastic switching is driven by  $S_{14}$ . Experiments verified this with only a single obvious ferrobielastic switch occurring in CTGS during a deformation experiment at the synchrotron (San Carlos olivine, run C1) compared to the frequent switches observed in  $\alpha$ -quartz.

As far as is currently known, this is the only method developed to measure in situ stress without XRD in a large volume press (LVP). Other in situ methods in the Paterson apparatus that use a fluid medium or Grigg's apparatus with a solid medium are highly limited to low hydrostatic pressures below 500 MPa at high temperature, or up to 2 GPa at low temperatures.

## 5. Conclusion

In conclusion, the piezoelectric method for measuring stress at high pressures represents a transformative approach in studying material behavior under extreme conditions. Its advantages over traditional XRD methods, including continuous real-time monitoring and off-beamline capabilities, position it as a valuable tool for both scientific research and potential industrial applications. The integration of Brillouin spectroscopy further enhances the capability of this novel method, providing comprehensive insights into the mechanical properties of piezoelectric materials like CTGS under high-pressure conditions.

## Bibliography

- Adams, F. D., Nicolson, J. T., & Callendar, H. L. (1901). XI. An experimental investigation into the flow of Marble. *Philosophical Transactions of the Royal Society of London. Series A, Containing Papers of a Mathematical or Physical Character*, 195(262–273), 363–401. <https://doi.org/10.1098/rsta.1900.0032>
- Ai, L., Sun, Z., Jiang, L., Pan, J., Zheng, Y., & Pan, S. (2024). Piezoelectric properties of  $(\text{Sr}_{0.2}\text{Ca}_{0.8})_3\text{TaGa}_3\text{Si}_2\text{O}_{14}$  and  $\text{Ca}_3\text{TaGa}_3\text{Si}_2\text{O}_{14}$  single crystals grown via vertical Bridgman method. *CrystEngComm*, 26 (11), 1550–1555. <https://doi.org/10.1039/D3CE01126G>
- Akimoto, S., & Fujisawa, H. (1968). Olivine-spinel solid solution equilibria in the system  $\text{Mg}_2\text{SiO}_4\text{-Fe}_2\text{SiO}_4$ . *Journal of Geophysical Research*, 73(4), 1467–1479. <https://doi.org/10.1029/JB073i004p01467>
- Alathlawi, H. J., Tariq, S., Al-Dossari, M., Mubarak, A. A., Saleem, M., Saad H-E, M. M., Ali, M., & Kanwal, B. (2024). Pressure-Induced Effects on  $\text{BaPbO}_3$ : A Prospectively Valuable Material for Piezoelectric Applications via DFT. *Crystal Research and Technology*, 60, 2300293. <https://doi.org/10.1002/crat.202300293>
- Almaghbash, Z. A. A. R., & Arbouche, O. (2021). The Influence of Pressure on Structural, Elastic, Piezoelectric and Dielectric Properties of  $\text{R}_3\text{c-BiAlO}_3$  Based on Ab Initio Calculations. *ChemistrySelect*, 6(22), 5559–5566. <https://doi.org/10.1002/slct.202100939>
- IEEE Standards Board (1984). IEEE Standard on Piezoelectricity (ANSI/IEEE Std 176-1987). *IEEE*, New York, 49 pp. <https://doi.org/10.1109/T-SU.1984.31464>
- Amodeo, J., Merkel, S., Tromas, C., Carrez, P., Korte-Kerzel, S., Cordier, P., & Chevalier, J. (2018). Dislocations and Plastic Deformation in  $\text{MgO}$  Crystals: A Review. *Crystals*, 8(6), 240, 18 pp. <https://doi.org/10.3390/cryst8060240>

## Bibliography

- Badro, J., Gillet, P., & Barrat, J.-L. (1998). Melting and pressure-induced amorphization of quartz. *Europhysics Letters*, *42*(6), 643-648. <https://doi.org/10.1209/epl/i1998-00299-3>
- Bansal, N. P., & Zhu, D. (2005). Thermal conductivity of zirconia–alumina composites. *Ceramics International*, *31*(7), 911–916. <https://doi.org/10.1016/j.ceramint.2004.09.018>
- Bassett, W. A. (2006). Deviatoric stress: A nuisance or a gold mine? *Journal of Physics: Condensed Matter*, *18*(25), S921-S938. <https://doi.org/10.1088/0953-8984/18/25/S01>
- Beaurain, M., Armand, P., & Papet, P. (2006). Synthesis and characterization of  $\alpha$ -GaPO<sub>4</sub> single crystals grown by the flux method. *Journal of Crystal Growth*, *294*(2), 396–400. <https://doi.org/10.1016/j.jcrysgro.2006.05.074>
- Bertagnolli, E., Kittinger, E., & Tichý, J. (1979). Ferrobielastic hysteresis in  $\alpha$ -quartz. *Journal of Applied Physics*, *50*(10), 6267–6271. <https://doi.org/10.1063/1.325765>
- Besson, J. M., Hamel, G., Grima, T., Nelmes, R. J., Loveday, J. S., Hull, S., & Häusermann, D. (1992). A large volume pressure cell for high temperatures. *High Pressure Research*, *8*(5–6), 625–630. <https://doi.org/10.1080/08957959208206312>
- Binggeli, N., Keskar, N. R., & Chelikowsky, J. R. (1994). Pressure-induced amorphization, elastic instability, and soft modes in  $\alpha$ -quartz. *Physical Review B*, *49*(5), 3075–3081. <https://doi.org/10.1103/PhysRevB.49.3075>
- Birch, F. (1978). Finite strain isotherm and velocities for single-crystal and polycrystalline NaCl at high pressures and 300 K. *Journal of Geophysical Research: Solid Earth*, *83*(B3), 1257–1268. <https://doi.org/10.1029/JB083iB03p01257>
- Biryukov, S. V., Schmidt, H., Sotnikov, A., Weihnacht, M., Sakharov, S., & Buzanov, O. (2014). CTGS material parameters obtained by versatile SAW measurements. *2014 IEEE International Ultrasonics Symposium (IUS)*, Chicago, IL, USA, pp. 882–885. IEEE. <https://doi.org/10.1109/ULTSYM.2014.0217>

## Bibliography

- Blachowicz, T., Bukowski, R., & Kleszczewski, Z. (1996). Fabry–Pérot interferometer in Brillouin scattering experiments. *Review of Scientific Instruments*, 67(12), 4057–4060. <https://doi.org/10.1063/1.1147550>
- Boioli, F., Tommasi, A., Cordier, P., Demouchy, S., & Mussi, A. (2015). Low steady-state stresses in the cold lithospheric mantle inferred from dislocation dynamics models of dislocation creep in olivine. *Earth and Planetary Science Letters*, 432, 232–242. <https://doi.org/10.1016/j.epsl.2015.10.012>
- Born, M. (1940). On the stability of crystal lattices. I. *Mathematical Proceedings of the Cambridge Philosophical Society*, 36(2), 160–172. <https://doi.org/10.1017/S0305004100017138>
- Born, M., & Huang, K. (2002). *Dynamical theory of crystal lattices*. Oxford: Clarendon Press, 23(7): 428 pp. <https://doi.org/10.1119/1.1934059>
- Bridgman, P. W. (1931). *The Physics of High Pressure* (1st ed.). Cambridge, MA: Harvard University Press, 243 pp. <https://doi.org/10.1038/131259a0>
- Bridgman, P. W. (1946). Recent Work in the Field of High Pressures. *Reviews of Modern Physics*, 18(1), 46 pp. <https://doi.org/10.1103/RevModPhys.18.1>
- Buchen, J. (2018). *The Elastic Properties of Wadsleyite and Stishovite at High Pressures: Tracing Deep Earth Material Cycles*, Doctoral thesis, Universität Bayreuth, Fakultät für Biologie, Chemie und Geowissenschaften. Bayreuth, Germany, 199 pp. [https://doi.org/10.15495/EPub\\_UBT\\_00004410](https://doi.org/10.15495/EPub_UBT_00004410)
- Burnley, P. C. (2015). Elastic plastic self-consistent (EPSC) modeling of plastic deformation in fayalite olivine. *American Mineralogist*, 100(7), 1424–1433. <https://doi.org/10.2138/am-2015-5234ccbyncnd>
- Burnley, P. C., & Kaboli, S. (2019). Elastic plastic self-consistent (EPSC) modeling of San Carlos olivine deformed in a D-DIA apparatus. *American Mineralogist*, 104(2), 276–281. <https://doi.org/10.2138/am-2019-6666>

## Bibliography

- Powell, R. C. (2010). *Symmetry, Group Theory, and the Physical Properties of Crystals*. Springer, New York, 230 pp.
- Calderon, E., Gauthier, M., Decremps, F., Hamel, G., Syfosse, G., & Polian, A. (2007). Complete determination of the elastic moduli of  $\alpha$ -quartz under hydrostatic pressure up to 1 GPa: An ultrasonic study. *Journal of Physics: Condensed Matter*, 19(43), Art. 436228, 12 pp. <https://doi.org/10.1088/0953-8984/19/43/436228>
- Carter, N. L., Christie, J. M., & Griggs, D. T. (1964). Experimental Deformation and Recrystallization of Quartz. *The Journal of Geology*, 72(6), 687–733. <https://doi.org/10.1086/627029>
- Choudhury, N., & Chaplot, S. L. (2006). Ab initio studies of phonon softening and high-pressure phase transitions of  $\alpha$ -quartz SiO<sub>2</sub>. *Physical Review B*, 73(9), Art. 094304. American Physical Society. <https://doi.org/10.1103/PhysRevB.73.094304>
- Cook, R. K., & Weissler, P. G. (1950). Piezoelectric Constants of Alpha-and Beta-Quartz at Various Temperatures. In *Physical Review* (Vol. 80, Issue 4). 712–716 pp. <https://doi.org/10.1103/PhysRev.80.712>
- Cornelio, C., & Violay, M. (2020). Effect of Fluid Viscosity on Earthquake Nucleation. *Geophysical Research Letters*, 47(12), e2020GL087854, 10 pp. <https://doi.org/10.1029/2020GL087854>
- Curie, J., & Curie, P. (1880). Développement par compression de l'électricité polaire dans les cristaux hémihédres à faces inclinées. *Bulletin de la Société minéralogique de France*, 3(4), 90–93. <https://doi.org/10.3406/bulmi.1880.1564>
- Damjanovic, D., & Demartin, M. (1996). The Rayleigh law in piezoelectric ceramics. *Journal of Physics D: Applied Physics*, 29(7), 2057–2060. <https://doi.org/10.1088/0022-3727/29/7/046>

## Bibliography

- Daoud, S., & Bouarissa, N. (2019). Elastic, piezoelectric and thermal properties of zinc-blende AlN under pressure. *Theoretical Chemistry Accounts*, 138(4), Art. 49, 8 pp.  
<https://doi.org/10.1007/s00214-019-2439-9>
- Darot, M., & Gueguen, Y. (1981). High-temperature creep of forsterite single crystals. *Journal of Geophysical Research: Solid Earth*, 86(B7), 6219–6234.  
<https://doi.org/10.1029/JB086iB07p06219>
- Demartin, M., & Damjanovic, D. (1996). Dependence of the direct piezoelectric effect in coarse and fine grain barium titanate ceramics on dynamic and static pressure. *Applied Physics Letters*, 68(21), 3046–3048. <https://doi.org/10.1063/1.115572>
- Demouchy, S., Mussi, A., Barou, F., Tommasi, A., & Cordier, P. (2014). Viscoplasticity of polycrystalline olivine experimentally deformed at high pressure and 900 °C. *Tectonophysics*, 623, 123–135. <https://doi.org/10.1016/j.tecto.2014.03.022>
- Demouchy, S., Schneider, S. E., Mackwell, S. J., Zimmerman, M. E., & Kohlstedt, D. L. (2009). Experimental deformation of olivine single crystals at lithospheric temperatures. *Geophysical Research Letters*, 36(4), L04304.  
<https://doi.org/10.1029/2008GL036611>
- Demouchy, S., Tommasi, A., Boffa Ballaran, T., & Cordier, P. (2013). Low strength of Earth's uppermost mantle inferred from tri-axial deformation experiments on dry olivine crystals. *Physics of the Earth and Planetary Interiors*, 220, 37–49.  
<https://doi.org/10.1016/j.pepi.2013.04.008>
- Dil, J. G., & Brody, E. M. (1976). Brillouin scattering from isotropic metals. *Physical Review B*, 14(12), 5218–5227. <https://doi.org/10.1103/PhysRevB.14.5218>
- Dil, J. G., Hijningen, N. C. J. A. van, Dorst, F. van, & Aarts, R. M. (1981). Tandem multipass Fabry-Pérot interferometer for Brillouin scattering. *Applied Optics*, 20(8), 1374–1381.  
<https://doi.org/10.1364/AO.20.001374>

## Bibliography

- Dixon, N. A., & Durham, W. B. (2018). Measurement of Activation Volume for Creep of Dry Olivine at Upper-Mantle Conditions. *Journal of Geophysical Research: Solid Earth*, *123*(10), 8459–8473. <https://doi.org/10.1029/2018JB015853>
- Dong, J., Zhu, H., & Chen, D. (2015). Universal elastic-hardening-driven mechanical instability in  $\alpha$ -quartz and quartz homeotypes under pressure. *Scientific Reports*, *5*(1), 10810. <https://doi.org/10.1038/srep10810>
- Druiventak, A., Trepmann, C. A., Renner, J., & Hanke, K. (2011). Low-temperature plasticity of olivine during high stress deformation of peridotite at lithospheric conditions—An experimental study. *Earth and Planetary Science Letters*, *311*(3), 199–211. <https://doi.org/10.1016/j.epsl.2011.09.022>
- Dubrovinskaia, N., Dubrovinsky, L., Solopova, N. A., Abakumov, A., Turner, S., Hanfland, M., Bykova, E., Bykov, M., Prescher, C., & Prakapenka, V. B. (2016). Terapascal static pressure generation with ultrahigh yield strength nanodiamond. *Science Advances*, *2*(7), e1600341. <https://doi.org/10.1126/sciadv.1600341>
- Dubrovinsky, L., Dubrovinskaia, N., Prakapenka, V. B., & Abakumov, A. M. (2012). Implementation of micro-ball nanodiamond anvils for high-pressure studies above 6 Mbar. *Nature Communications*, *3*(1), 1163. <https://doi.org/10.1038/ncomms2160>
- Dudka, A. P. (2016). Accurate structural study of langasite-family  $\text{Ca}_3\text{TaGa}_3\text{Si}_2\text{O}_{14}$  crystal. *Crystallography Reports*, *61*(2), 187–192. <https://doi.org/10.1134/S1063774516020073>
- Duffy, T. S., Shen, G., Heinz, D. L., Shu, J., Ma, Y., Mao, H.-K., Hemley, R. J., & Singh, A. K. (1999). Lattice strains in gold and rhenium under nonhydrostatic compression to 37 GPa. *Physical Review B*, *60*(22), 15063–15073. <https://doi.org/10.1103/PhysRevB.60.15063>
- Duffy, T. S., Shen, G., Shu, J., Mao, H.-K., Hemley, R. J., & Singh, A. K. (1999). Elasticity, shear strength, and equation of state of molybdenum and gold from x-ray diffraction

## Bibliography

- under nonhydrostatic compression to 24 GPa. *Journal of Applied Physics*, 86(12), 6729–6736. <https://doi.org/10.1063/1.371723>
- Durham, W. B., Mei, S., Kohlstedt, D. L., Wang, L., & Dixon, N. A. (2009). New measurements of activation volume in olivine under anhydrous conditions. *Physics of the Earth and Planetary Interiors*, 172(1), 67–73. <https://doi.org/10.1016/j.pepi.2008.07.045>
- Eccles, D., Sammonds, P. R., & Clint, O. C. (2005). Laboratory studies of electrical potential during rock failure. *International Journal of Rock Mechanics and Mining Sciences*, 42(7), 933–949. <https://doi.org/10.1016/j.ijrmms.2005.05.018>
- Evans, B., & Goetze, C. (1979). The temperature variation of hardness of olivine and its implication for polycrystalline yield stress. *Journal of Geophysical Research: Solid Earth*, 84(B10), 5505–5524. <https://doi.org/10.1029/JB084iB10p05505>
- Evans, B. & Wong, T.-F. (eds) 1992. Fault Mechanics and Transport Properties of Rocks. *International Geophysics Series 51*. Academic Press, London & San Diego, xxiv + 524 pp., ch. 9, pp. 213–252. [https://doi.org/10.1016/S0074-6142\(08\)62824-7](https://doi.org/10.1016/S0074-6142(08)62824-7)
- Fang, L., He, D., Chen, C., Ding, L., & Luo, X. (2007). Effect of precompression on pressure-transmitting efficiency of pyrophyllite gaskets. *High Pressure Research*, 27(3), 367–374. <https://doi.org/10.1080/08957950701553796>
- Farla, R., Bhat, S., Sonntag, S., Chanyshv, A., Ma, S., Ishii, T., Liu, Z., Néri, A., Nishiyama, N., Faria, G. A., Wroblewski, T., Schulte-Schrepping, H., Drube, W., Seeck, O., & Katsura, T. (2022). Extreme conditions research using the large-volume press at the P61B endstation, PETRA III. *Journal of Synchrotron Radiation*, 29(2), 409–423. <https://doi.org/10.1107/S1600577522001047>
- French, M., Mattsson, T. R., Nettelmann, N., & Redmer, R. (2009). Equation of state and phase diagram of water at ultrahigh pressures as in planetary interiors. *Physical Review B*, 79(5), Art. 054107 (6 pp.) <https://doi.org/10.1103/PhysRevB.79.054107>

## Bibliography

- Freund, F., Freund, M. M., & Batllo, F. (1993). Critical review of electrical conductivity measurements and charge distribution analysis of magnesium oxide. *Journal of Geophysical Research: Solid Earth*, *98*(B12), 22209–22229.  
<https://doi.org/10.1029/93JB01327>
- Freund, F., Masuda, M. M., & Freund, M. M. (1991). Highly mobile oxygen hole-type charge carriers in fused silica. *Journal of Materials Research*, *6*(8), 1619–1622.  
<https://doi.org/10.1557/JMR.1991.1619>
- Fritze, H., Schneider, O., Seh, H., Tuller, H. L., & Borchardt, G. (2003). High temperature bulk acoustic wave properties of langasite. *Physical Chemistry Chemical Physics*, *5*(23), 5207–5214. <https://doi.org/10.1039/b307503f>
- Frost, H. J., & Ashby, M. F. (1982). Deformation-mechanism maps: The plasticity and creep of metals and ceramics. *Oxford: Pergamon Press*, 166 pp.  
<https://cir.nii.ac.jp/crid/1130282270220220800>
- Gao, J., Xu, Z., Li, F., Zhang, C., Liu, Y., Liu, G., & He, H. (2011). The hydrostatic pressure dependence of the piezoelectric properties for the barium titanate and lead titanate crystals: Thermodynamic analysis. *Journal of Applied Physics*, *109*(11), Art. 114111 (9 pp.) <https://doi.org/10.1063/1.3596816>
- Girard, J., Chen, J., & Raterron, P. (2012). Deformation of periclase single crystals at high pressure and temperature: Quantification of the effect of pressure on slip-system activities. *Journal of Applied Physics*, *111*(11), Art. 112607 (7 pp.).  
<https://doi.org/10.1063/1.4726200>
- Gleason, G. C., & Tullis, J. (1995). A flow law for dislocation creep of quartz aggregates determined with the molten salt cell. *Tectonophysics*, *247*(1), 1–23.  
[https://doi.org/10.1016/0040-1951\(95\)00011-B](https://doi.org/10.1016/0040-1951(95)00011-B)
- Gouriet, K., Cordier, P., Garel, F., Thoraval, C., Demouchy, S., Tommasi, A., & Carrez, P. (2019). Dislocation dynamics modelling of the power-law breakdown in olivine single

## Bibliography

- crystals: Toward a unified creep law for the upper mantle. *Earth and Planetary Science Letters*, 506, 282–291. <https://doi.org/10.1016/j.epsl.2018.10.049>
- Gregori, G., Merkle, R., & Maier, J. (2017). Ion conduction and redistribution at grain boundaries in oxide systems. *Progress in Materials Science*, 89, 252–305. <https://doi.org/10.1016/j.pmatsci.2017.04.009>
- Gregoryanz, E., Hemley, R. J., Mao, H., & Gillet, P. (2000). High-Pressure Elasticity of  $\alpha$ -Quartz: Instability and Ferroelastic Transition. *Physical Review Letters*, 84(14), 3117–3120. <https://doi.org/10.1103/PhysRevLett.84.3117>
- Griggs, D. T. (1936). Deformation of Rocks under High Confining Pressures: I. Experiments at Room Temperature. *The Journal of Geology*, 44(5), 541–577. <https://doi.org/10.1086/624455>
- Guignard, J., & Crichton, W. A. (2015). The large volume press facility at ID06 beamline of the European synchrotron radiation facility as a High Pressure-High Temperature deformation apparatus. *Review of Scientific Instruments*, 86(8), Art. 085112 (8 pp.). <https://doi.org/10.1063/1.4928151>
- Guo, S. (2010). An eigen expression for piezoelectrically stiffened elastic and dielectric constants based on the static theory. *Acta Mechanica*, 210(3–4), 345–350. <https://doi.org/10.1007/s00707-009-0223-y>
- Guzzo, P. L., & Boy, J. J. (2000). Roles of crystallographic orientation and crystal origin in ferroelastic twinning of quartz under uniaxial stress. *EPJ Applied Physics*, 12(1), 17–30. <https://doi.org/10.1051/epjap:2000167>
- Haines, J., Léger, J. M., Gorelli, F., & Hanfland, M. (2001). Crystalline Post-Quartz Phase in Silica at High Pressure. *Physical Review Letters*, 87(15), Art. 155503 (4 pp), <https://doi.org/10.1103/PhysRevLett.87.155503>

## Bibliography

- Hall, H. T. (1958). Some High-Pressure, High-Temperature Apparatus Design Considerations: Equipment for Use at 100000 Atmospheres and 3000 °C. *Review of Scientific Instruments*, 29(4), 267–275. <https://doi.org/10.1063/1.1716172>
- Hall, H. T. (1967). High pressure apparatus: Ram-in-tie-bar multianvil presses. *The Review of Physical Chemistry of Japan*, 37(2), 63–71. <http://hdl.handle.net/2433/46900>
- Hanayama, Y., & Kimura, M. (1995). Condensed State of Noble Gases and Its Sound Velocity under High Pressure. *Netsu Bussei*, 9(3), 189–194. <https://doi.org/10.2963/jjtp.9.189>
- Hansen, L. N., Kumamoto, K. M., Thom, C. A., Wallis, D., Durham, W. B., Goldsby, D. L., Breithaupt, T., Meyers, C. D., & Kohlstedt, D. L. (2019). Low-Temperature Plasticity in Olivine: Grain Size, Strain Hardening, and the Strength of the Lithosphere. *Journal of Geophysical Research: Solid Earth*, 124(6), 5427–5449. <https://doi.org/10.1029/2018JB016736>
- Hawke, R. S., Syassen, K., & Holzapfel, W. B. (1974). An apparatus for high pressure Raman spectroscopy. *Review of Scientific Instruments*, 45(12), 1598–1601. <https://doi.org/10.1063/1.1686569>
- Hearmon, R. F. S. (1956). The elastic constants of anisotropic materials—II. *Advances in Physics*, 5(19), 323–382. <https://doi.org/10.1080/00018732.1956.tADP0323>
- Heismann, B. J., Leppert, J., & Stierstorfer, K. (2003). Density and atomic number measurements with spectral x-ray attenuation method. *Journal of Applied Physics*, 94(3), 2073–2079. <https://doi.org/10.1063/1.1586963>
- Herzbach, D., & Müser, M. H. (2006). Piezoelectric coefficients by molecular dynamics simulations in the constant stress ensemble: A case study of quartz. *Computer Physics Communications*, 174(1), 17–23. <https://doi.org/10.1016/j.cpc.2005.07.012>

## Bibliography

- Heyliger, P., Ledbetter, H., & Kim, S. (2003). Elastic constants of natural quartz. *The Journal of the Acoustical Society of America*, *114*(2), 644–650.  
<https://doi.org/10.1121/1.1593063>
- Hicks, T. L., & Secco, R. A. (1997). Dehydration and decomposition of pyrophyllite at high pressures: Electrical conductivity and X-ray diffraction studies to 5 GPa. *Canadian Journal of Earth Sciences*, *34*(6), 875–882. <https://doi.org/10.1139/e17-071>
- Hilaireret, N., Wang, Y., Sanehira, T., Merkel, S., & Mei, S. (2012). Deformation of olivine under mantle conditions: An in situ high-pressure, high-temperature study using monochromatic synchrotron radiation. *Journal of Geophysical Research: Solid Earth*, *117*(B1), B01203. <https://doi.org/10.1029/2011JB008498>
- Hirth, G., & Kohlstedt, D. (2003). Rheology of the upper mantle and the mantle wedge: A view from the experimentalists. In J. Eiler (ed.) *Inside the Subduction Factory*. Geophysical Monograph 138. American Geophysical Union, Washington DC, pp. 83–105. <https://doi.org/10.1029/138GM06>
- Hulse, C. O., & Graf, R. B. (1965). Effect of Temperature on the Mechanical Properties of Solid Pressure-Transmitting Media. II. Pyrophyllite. *Journal of Applied Physics*, *36*(5), 1593–1596. <https://doi.org/10.1063/1.1703092>
- Ike, Y., Tsukada, S., & Kojima, S. (2007). High-resolution Brillouin spectroscopy with angular dispersion-type Fabry-Pérot interferometer and its application to a quartz crystal. *Review of Scientific Instruments*, *78*(7), Art. 076104 (4 pp.).  
<https://doi.org/10.1063/1.2753593>
- Ishii, T., Shi, L., Huang, R., Tsujino, N., Druzhbin, D., Myhill, R., Li, Y., Wang, L., Yamamoto, T., Miyajima, N., Kawazoe, T., Nishiyama, N., Higo, Y., Tange, Y., & Katsura, T. (2016). Generation of pressures over 40 GPa using Kawai-type multi-anvil press with tungsten carbide anvils. *Review of Scientific Instruments*, *87*(2), Art. 024501 (8 pp). <https://doi.org/10.1063/1.4941716>

## Bibliography

- Jacques, Mm., & Curie, P. (1881). On the liberation of electricity in tourmaline by pressure. *The London, Edinburgh, and Dublin Philosophical Magazine and Journal of Science*, 11(67), 224–225. <https://doi.org/10.1080/14786448108627004>
- Jain, C., Korenaga, J., & Karato, S. I. (2018). On the Grain Size Sensitivity of Olivine Rheology. *Journal of Geophysical Research: Solid Earth*, 123(1), 674–688. <https://doi.org/10.1002/2017JB014847>
- Jayaraman, A. (1983). Diamond anvil cell and high-pressure physical investigations. *Reviews of Modern Physics*, 55(1), 65–108. <https://doi.org/10.1103/RevModPhys.55.65>
- Jonnard, P., & Bonnelle, C. (2011). Cauchois and Sénémaud Tables of wavelengths of X-ray emission lines and absorption edges. *X-Ray Spectrometry*, 40(1), 12–16. <https://doi.org/10.1002/xrs.1293>
- Kaboli, S., Burnley, P. C., Xia, G., & Green II, H. W. (2017). Pressure Dependence of Creep in Forsterite Olivine: Comparison of Measurements From the D-DIA and Griggs Apparatus. *Geophysical Research Letters*, 44(21), 10939–10947. <https://doi.org/10.1002/2017GL075177>
- Kang, S.-J. L. (1994). Chemically induced interface migration in oxides. *Proc. 96th Annual Meeting of the American Ceramic Society*, Indianapolis, IN, USA, pp. 35–51. Westerville, OH: American Ceramic Society.
- Karato, S. (2010). Rheology of the Earth's mantle: A historical review. *Gondwana Research*, 18(1), 17–45. <https://doi.org/10.1016/j.gr.2010.03.004>
- Karato, S., & Rubie, D. C. (1997). Toward an experimental study of deep mantle rheology: A new multianvil sample assembly for deformation studies under high pressures and temperatures. *Journal of Geophysical Research: Solid Earth*, 102(B9), 20111–20122. <https://doi.org/10.1029/97JB01732>

## Bibliography

- Karato, S.-I., & Jung, H. (2003). Effects of pressure on high-temperature dislocation creep in olivine. *Philosophical Magazine*, 83(3), 401–414.  
<https://doi.org/10.1080/0141861021000025829>
- Katayama, I., & Karato, S. (2008). Low-temperature, high-stress deformation of olivine under water-saturated conditions. *Physics of the Earth and Planetary Interiors*, 168(3), 125–133. <https://doi.org/10.1016/j.pepi.2008.05.019>
- Kawai, N. (1966). A Static High Pressure Apparatus with Tapering Multi-Pistons Forming a Sphere. I. *Proceedings of the Japan Academy, Series B Physical and Biological Sciences*, 42(4), 385–388. <https://doi.org/10.2183/pjab1945.42.385>
- Kawai, N., Endo, S., & Itho, K. (1970). Split sphere high pressure vessel and phase equilibrium relation in the system  $Mg_2SiO_4$ - $Fe_2SiO_4$ . *Physics of the Earth and Planetary Interiors*, 3(3), 182–185. [https://doi.org/10.1016/0031-9201\(70\)90052-X](https://doi.org/10.1016/0031-9201(70)90052-X)
- Kawai, N., & Endo, S. (1970). The Generation of Ultrahigh Hydrostatic Pressures by a Split Sphere Apparatus. *Review of Scientific Instruments*, 41(8), 1178–1181.  
<https://doi.org/10.1063/1.1684753>
- Kawai, N., Togaya, M., & Onodera, A. (1973). A New Device for Pressure Vessels. *Proceedings of the Japan Academy, Series B*, 49(8), 623–626.  
<https://doi.org/10.2183/pjab1945.49.623>
- Kawazoe, T., Karato, S., Otsuka, K., Jing, Z., & Mookherjee, M. (2009). Shear deformation of dry polycrystalline olivine under deep upper mantle conditions using a rotational Drickamer apparatus (RDA). *Physics of the Earth and Planetary Interiors*, 174(1), 128–137. <https://doi.org/10.1016/j.pepi.2008.06.027>
- Kawazoe, T., Nishiyama, N., Nishihara, Y., & Irifune, T. (2010). Pressure generation to 25 GPa using a cubic anvil apparatus with a multi-anvil 6-6 assembly. *High Pressure Research*, 30(1), 167–174. <https://doi.org/10.1080/08957950903503912>

## Bibliography

- Kerber, M., Spieckermann, F., Schuster, R., Joni, B., Schell, N., & Schafner, E. (2019). In-situ synchrotron profile analysis after high-pressure torsion deformation. *Crystals*, 9(5), Art. 232 (12 pp.). <https://doi.org/10.3390/cryst9050232>
- Keshav, S., Corgne, A., Gudfinnsson, G. H., Bizimis, M., McDonough, W. F., & Fei, Y. (2005). Kimberlite petrogenesis: Insights from clinopyroxene-melt partitioning experiments at 6 GPa in the CaO-MgO-Al<sub>2</sub>O<sub>3</sub>-SiO<sub>2</sub>-CO<sub>2</sub> system. *Geochimica et Cosmochimica Acta*, 69(11), 2829–2845. <https://doi.org/10.1016/j.gca.2005.01.012>
- Kholkin, A., Pertsev, N., & Goltsev, A. (2008). Piezoelectricity and Crystal Symmetry. In A. Safari & E. K. Akdogan (eds.), *Piezoelectric and Acoustic Materials for Transducer Applications*. Springer, New York, pp. 17–38. [https://doi.org/10.1007/978-0-387-76540-2\\_2](https://doi.org/10.1007/978-0-387-76540-2_2)
- Kimizuka, H., Ogata, S., Li, J., & Shibutani, Y. (2007). Complete set of elastic constants of  $\alpha$ -quartz at high pressure: A first-principles study. *Physical Review B*, 75(5), Art. 054109 (7 pp.). <https://doi.org/10.1103/PhysRevB.75.054109>
- Kitaura, M., Ang, A. K. R., Yamamoto, Y., Happo, N., Kimura, K., Hayashi, K., Watanabe, S., Yokota, Y., Ohashi, Y., Kamada, K., Yoshikawa, A., Yamane, H., & Ohnishi, A. (2022). Atomic positions and displacements in piezoelectric materials Ca<sub>3</sub>TaGa<sub>3</sub>Si<sub>2</sub>O<sub>14</sub> and Ca<sub>3</sub>TaGa<sub>1.5</sub>Al<sub>1.5</sub>Si<sub>2</sub>O<sub>14</sub> investigated by Ta-L $\alpha$  X-ray fluorescence holography. *Frontiers in Materials*, 9, Art. 977371 (16 pp.). <https://doi.org/10.3389/fmats.2022.977371>
- Klemens, P. G. (1996). Thermal Conductivity of Zirconia. In T. Tong & A. Tien (eds.), *Thermal Conductivity 23*. CRC Press, Boca Raton, FL, pp. 13–22.
- Klotz, S., Chervin, J.-C., Munsch, P., & Marchand, G. L. (2009). Hydrostatic limits of 11 pressure transmitting media. *Journal of Physics D: Applied Physics*, 42(7), Art. 075413 (12 pp.). <https://doi.org/10.1088/0022-3727/42/7/075413>

## Bibliography

- Knowles, K. M., & Howie, P. R. (2015). The Directional Dependence of Elastic Stiffness and Compliance Shear Coefficients and Shear Moduli in Cubic Materials. *Journal of Elasticity*, 120(1), 87–108. <https://doi.org/10.1007/s10659-014-9506-1>
- Kohlstedt, D. L., Evans, B., & Mackwell, S. J. (1995). Strength of the lithosphere: Constraints imposed by laboratory experiments. *Journal of Geophysical Research: Solid Earth*, 100(B9), 17587–17602. <https://doi.org/10.1029/95JB01460>
- Kojima, S. (2022). 100th Anniversary of Brillouin Scattering: Impact on Materials Science. *Materials*, 15, Art. 3518 (20 pp.). <https://doi.org/10.3390/ma15103518>
- Kong, L. F., Yu, F. P., Qin, L. F., Cheng, X. F., & Zhao, X. (2018). Performance improvement of CTGS and YCOB crystals for high temperature piezoelectric accelerometer applications. *Proceedings of the 2017 Symposium on Piezoelectricity, Acoustic Waves, and Device Applications, SPAWDA 2017, 2018-April*, 117–120. <https://doi.org/10.1109/SPAWDA.2017.8340301>
- Konstantinova, A. F., Golovina, T. G., Dudka, A. P., & Sizova, N. L. (2022). Some Optical and Mechanical Properties of Right- and Left-Handed Langasite Family Crystals and Their Structural Basis. *Crystallography Reports*, 67(3), 398–406. <https://doi.org/10.1134/S1063774522030105>
- Korobeynikov, S. M., Melekhov, A. V., Soloveitchik, Y. G., Royak, M. E., Agoris, D. P., & Pyrgioti, E. (2005). Surface conductivity at the interface between ceramics and transformer oil. *Journal of Physics D: Applied Physics*, 38(6), 915–923. <https://doi.org/10.1088/0022-3727/38/6/021>
- Kosinski, J. A., Pastore, R. A., Bigler, E., da Cunha, M. P., Malocha, D. C., & Detaint, J. (2001). A review of langasite material constants from BAW and SAW data: Toward an improved data set. *Proceedings of the 2001 IEEE International Frequency Control Symposium and PDA Exhibition (Cat. No.01CH37218)*, IEEE International Frequency

## Bibliography

- Control Symposium, Seattle, WA, USA, pp. 278–286. IEEE.  
<https://doi.org/10.1109/FREQ.2001.956203>
- Kronenberg, A. K., & Tullis, J. (1984). Flow strengths of quartz aggregates: Grain size and pressure effects due to hydrolytic weakening. *Journal of Geophysical Research: Solid Earth*, 89(B6), 4281–4297. <https://doi.org/10.1029/JB089iB06p04281>
- Lazzari, S., Martini, M., Paleari, A., Spinolo, G., & Vedda, A. (1988). DC and AC ionic conductivity in quartz: A new high temperature mechanism and a general assessment. *Nuclear Instruments and Methods in Physics Research Section B: Beam Interactions with Materials and Atoms*, 32(1–4), 299–302. [https://doi.org/10.1016/0168-583X\(88\)90227-3](https://doi.org/10.1016/0168-583X(88)90227-3)
- L. Lei, B. Yan, & X. Ji-An. (2013). Ruby fluorescence pressure scale: Revisited. *Chinese Physics B*, 22(5), Art. 056201 (6 pp.). <https://doi.org/10.1088/1674-1056/22/5/056201>
- Lan, J., Lu, G., Wang, Z., Zhu, G., Yuan, D., & Xia, H. (2005). Raman scattering spectra of  $\text{Ca}_3\text{NbGa}_3\text{Si}_2\text{O}_{14}$  (CNGS) crystals. *Physica Status Solidi B*, 242(10), 1996–2004. <https://doi.org/10.1002/pssb.200440072>
- Laughner, J. W., Newnham, R. E., & Cross, L. E. (1979). Ferroelastoelectricity in quartz. *Physica Status Solidi (a)*, 56(2), K83–K86. <https://doi.org/10.1002/pssa.2210560248>
- Leinenweber, K. D., Tyburczy, J. A., Sharp, T. G., Soignard, E., Diedrich, T., Petuskey, W. B., Wang, Y., & Mosenfelder, J. L. (2012). Cell assemblies for reproducible multi-anvil experiments (the COMPRES assemblies). *American Mineralogist*, 97(2–3), 353–368. <https://doi.org/10.2138/am.2012.3844>
- Li, J. F., Song, M. S., Shao, T. B., Zheng, X. D., & Jiang, Z. X. (2023). Mechanical data corrections for triaxial compression testing at high pressures and high temperatures with a Paterson gas-medium mechanical testing apparatus. *Review of Scientific Instruments*, 94(8), Art. 083907 (10 pp.). <https://doi.org/10.1063/5.0124440>

## Bibliography

- Li, L., Weidner, D., Raterron, P., Chen, J., & Vaughan, M. (2004). Stress measurements of deforming olivine at high pressure. *Physics of the Earth and Planetary Interiors*, 143–144, 357–367. <https://doi.org/10.1016/j.pepi.2003.09.022>
- Li, R., Ma, H. A., Han, Q. G., Liang, Z. Z., Yin, B. H., Liu, W. Q., & Jia, X. (2007). Simulation of pressure distribution in a pyrophyllite high-pressure cell by finite-element analysis. *High Pressure Research*, 27(2), 249–257. <https://doi.org/10.1080/08957950701385819>
- Liang, Z., Chen, Z., & Rahman, S. S. (2020). Experimental investigation of the primary and secondary creep behaviour of shale gas reservoir rocks from deep sections of the Cooper Basin. *Journal of Natural Gas Science and Engineering*, 73, Art. 103044 (12 pp.). <https://doi.org/10.1016/j.jngse.2019.103044>
- Liebermann, R. C. (2011). Multi-anvil, high pressure apparatus: A half-century of development and progress. *High Pressure Research*, 31(4), 493–532. <https://doi.org/10.1080/08957959.2011.618698>
- Liermann, H.-P., Konôpková, Z., Morgenroth, W., Glazyrin, K., Bednarčík, J., McBride, E. E., Petitgirard, S., Delitz, J. T., Wendt, M., Bican, Y., Ehnes, A., Schwark, I., Rothkirch, A., Tischer, M., Heuer, J., Schulte-Schrepping, H., Kracht, T., & Franz, H. (2015). The Extreme Conditions Beamline P02.2 and the Extreme Conditions Science Infrastructure at PETRA III. *Journal of Synchrotron Radiation*, 22(4), 908–924. <https://doi.org/10.1107/S1600577515005937>
- Lin, L., Ji, C., & Ma, Y. (2022). Macro strain-stress determination in a high pressure rotational anvil apparatus. *Journal of Applied Physics*, 131(1), Art. 015904 (8 pp.). <https://doi.org/10.1063/5.0075090>
- Lindsay, S. M., Anderson, M. W., & Sandercock, J. R. (1981). Construction and alignment of a high performance multipass vernier tandem Fabry–Pérot interferometer. *Review of Scientific Instruments*, 52(10), 1478–1486. <https://doi.org/10.1063/1.1136479>

## Bibliography

- Lippmann, G. (1881). Principe de la conservation de l'électricité, ou second principe de la théorie des phénomènes électriques. *Journal de Physique Théorique et Appliquée*, *10*(1), 381–394. <https://doi.org/10.1051/jphystap:0188100100038100>
- Long, H., Weidner, D. J., Li, L., Chen, J., & Wang, L. (2011). Deformation of olivine at subduction zone conditions determined from *in situ* measurements with synchrotron radiation. *Physics of the Earth and Planetary Interiors*, *186*(1), 23–35. <https://doi.org/10.1016/j.pepi.2011.02.006>
- Lu, G. W., Li, C. X., Wang, W. C., Wang, Z. H., Wang, Z. M., Yuan, D. R., & Xia, H. R. (2004). Raman scattering spectra of  $\text{La}_3\text{Ga}_5\text{SiO}_{14}$  (LGS) crystals. *Physica Status Solidi (b)*, *241*(2), 439–446. <https://doi.org/10.1002/pssb.200301922>
- Luan, F. C., & Paterson, M. S. (1992). Preparation and deformation of synthetic aggregates of quartz. *Journal of Geophysical Research: Solid Earth*, *97*(B1), 301–320. <https://doi.org/10.1029/91JB01748>
- Ma, T., Hou, S., Yu, F., Xie, C., Zhang, S., Wang, J., Du, J., Zhan, J., Cheng, X., Wang, S., & Zhao, X. (2017). Electro-elastic characterization of  $\text{Ca}_3\text{TaGa}_3\text{Si}_2\text{O}_{14}$  crystals for lateral-field-excitation acoustic wave sensing applications. *Journal of Alloys and Compounds*, *728*, 518–524. <https://doi.org/10.1016/j.jallcom.2017.08.284>
- Malki, M., Hoo, C. M., Mecartney, M. L., & Schneider, H. (2014). Electrical Conductivity of Mullite Ceramics. *Journal of the American Ceramic Society*, *97*(6), 1923–1930. <https://doi.org/10.1111/jace.12867>
- Mansfeld, G. D., Besson, R., & Guzzo, P. (1997). Study of ferroelastic twinning in quartz under conditions of uniaxial pressure by the compound acoustic resonator method. *Physics of the Solid State*, *39*(2), 254–258. <https://doi.org/10.1134/1.1129794>
- Manthilake, M. A. G. M., Walte, N., & Frost, D. J. (2012). A new multi-anvil press employing six independently acting 8 MN hydraulic rams. *High Pressure Research*:

## Bibliography

- An International Journal*, 32:2, 195-207,  
<https://doi.org/10.1080/08957959.2012.680450>
- Mao, Z., Fan, D., Lin, J.-F., Yang, J., Tkachev, S. N., Zhuravlev, K., & Prakapenka, V. B. (2015). Elasticity of single-crystal olivine at high pressures and temperatures. *Earth and Planetary Science Letters*, 426, 204–215.  
<https://doi.org/10.1016/j.epsl.2015.06.045>
- Markgraaff, J., & Roering, C. (1995). The energy difference between Dauphine twin states in alpha quartz with reference to deep-level South African gold mines. *South African Journal of Geology*, 98(4), 393–398.
- May, D. L., Gordon, A. P., & Segletes, D. S. (2013). The Application of the Norton-Bailey Law for Creep Prediction Through Power Law Regression. *Proceedings of ASME Turbo Expo 2013: Turbine Technical Conference and Exposition*. GT20131 San Antonio, Texas, USA. <https://doi.org/10.1115/GT2013-96008>
- McMillan, P. F. (2005). Pressing on: The legacy of Percy W. Bridgman. *Nature Materials*, 4(10), 715–717. <https://doi.org/10.1038/nmat1488>
- Mei, S., Kohlstedt, D. L., Durham, W. B., & Wang, L. (2008). Experimental investigation of the creep behavior of MgO at high pressures. *Physics of the Earth and Planetary Interiors*, 170(3–4), 170–175. <https://doi.org/10.1016/j.pepi.2008.06.030>
- Mei, S., Suzuki, A. M., Kohlstedt, D. L., & Xu, L. (2010). Experimental investigation of the creep behavior of garnet at high temperatures and pressures. *Journal of Earth Science*, 21(5), 532–540. <https://doi.org/10.1007/s12583-010-0127-8>
- Merkel, S. (2006). X-ray diffraction evaluation of stress in high pressure deformation experiments. *Journal of Physics: Condensed Matter*, 18(25), S949–S962.  
<https://doi.org/10.1088/0953-8984/18/25/S03>
- Merkel, S., Wenk, H. R., Shu, J., Shen, G., Gillet, P., Mao, H., & Hemley, R. J. (2002). Deformation of polycrystalline MgO at pressures of the lower mantle. *Journal of*

## Bibliography

- Geophysical Research: Solid Earth*, 107(B11), Art. 2271.  
<https://doi.org/10.1029/2001JB000920>
- Meyer, G. G., Acosta, M., Leclere, H., Morier, L., Teuscher, M., Garrison, G., Schubnel, A., & Violay, M. (2023). A new high-pressure high-temperature deformation apparatus to study the brittle to ductile transition in rocks. *Review of Scientific Instruments*, 94(4), Art. 043903 (10 pp.). <https://doi.org/10.1063/5.0135947>
- Mock, R., Hillebrands, B., & Sandercock, R. (1987). Construction and performance of a Brillouin scattering set-up using a triple-pass tandem Fabry-Pérot interferometer. *Journal of Physics E: Scientific Instruments*, 20(6), 656–660.  
<https://doi.org/10.1088/0022-3735/20/6/017>
- Momma, K., & Izumi, F. (2011). VESTA 3 for three-dimensional visualization of crystal, volumetric and morphology data. *Journal of Applied Crystallography*, 44(6), 1272–1276. <https://doi.org/10.1107/S0021889811038970>
- Mouhat, F., & Coudert, F.-X. (2014). Necessary and sufficient elastic stability conditions in various crystal systems. *Physical Review B*, 90(22), Art. 224104 (6 pp.).  
<https://doi.org/10.1103/PhysRevB.90.224104>
- Nesse, W. D. (2018). Introduction to Mineralogy (Second Edition). *Oxford: Oxford University Press*, 496 pp.
- Noël, C., Passelègue, F. X., Giorgetti, C., & Violay, M. (2019). Fault Reactivation During Fluid Pressure Oscillations: Transition From Stable to Unstable Slip. *Journal of Geophysical Research: Solid Earth*, 124(11), 10940–10953.  
<https://doi.org/10.1029/2019JB018517>
- Nuernberg, R. B. (2020). Numerical comparison of usual Arrhenius-type equations for modeling ionic transport in solids. *Ionics*, 26(5), 2405–2412.  
<https://doi.org/10.1007/s11581-019-03243-7>

## Bibliography

- Nye, J. F. (1957). *Physical Properties of Crystals: Their representation by tensors and matrices*. Oxford: Clarendon Press, 322 pp. <https://doi.org/10.2307/3610487>
- O'Bannon, E. F., III, Jenei, Z., Cynn, H., Lipp, M. J., & Jeffries, J. R. (2018). Contributed Review: Culet diameter and the achievable pressure of a diamond anvil cell: Implications for the upper pressure limit of a diamond anvil cell. *Review of Scientific Instruments*, 89(11), 111501 (7 pp.). <https://doi.org/10.1063/1.5049720>
- Osugi, J., Shimizu, K., Inoue, K., & Yasunami, K. (1964). A compact cubic anvil high pressure apparatus. *The Review of Physical Chemistry of Japan*, 34(1), 1–6.
- Pabst, W., & Gregorová, E. (2013). Elastic properties of silica polymorphs – A review. In *Original papers Ceramics – Silikáty*, 57(3), 167–184.
- Palmour, H., Choi, D. M., Barnes, L. D., McBrayer, R. D., & Kriegel, W. W. (1963). Deformation in Hot-Pressed Polycrystalline Spinel. In H. H. Stadelmaier & W. W. Austin (Eds.), *Materials Science Research*, Springer US, New York, pp. 158–197. [https://doi.org/10.1007/978-1-4899-5537-1\\_10](https://doi.org/10.1007/978-1-4899-5537-1_10)
- Pandit, A., & Bongiorno, A. (2023). First-principles calculation of the pressure derivative of the bulk modulus from second- and third-order elastic constants. *Physical Review Materials*, 7(7), Art. 073801 (8 pp.). <https://doi.org/10.1103/PhysRevMaterials.7.073801>
- Passelègue, F. X., Almakari, M., Dublanchet, P., Barras, F., Fortin, J., & Violay, M. (2020). Initial effective stress controls the nature of earthquakes. *Nature Communications*, 11(1), Art. 5132 (12 pp.). <https://doi.org/10.1038/s41467-020-18937-0>
- Paterson, M. S. (1970). A high-pressure, high-temperature apparatus for rock deformation. *International Journal of Rock Mechanics and Mining Sciences & Geomechanics Abstracts*, 7(5), 517–526. [https://doi.org/10.1016/0148-9062\(70\)90004-5](https://doi.org/10.1016/0148-9062(70)90004-5)

## Bibliography

- Paterson, M. S. (1990). Rock Deformation Experimentation. In *The Brittle-Ductile Transition in Rocks. Geophysical Monograph 56*. American Geophysical Union, Washington DC, pp. 187–194. <https://doi.org/10.1029/GM056p0187>
- Patterson, J. D., & Bailey, B. C. (2018). *Solid-State Physics: Introduction to the Theory (Third Edition)*. Cham, Switzerland: Springer, 954 pp. <https://doi.org/10.1007/978-3-319-75322-5>
- Phakey, P., Dollinger, G., & Christie, J. (1972). Transmission electron microscopy of experimentally deformed olivine crystals. In *Flow and fracture of rocks* (Vol. 16, pp. 117–138). American Geophysical Union. <https://doi.org/10.1029/GM016p0117>
- Pisarevsky, Yu. V., Mill, B. V., Moiseeva, N. A., & Yakimov, A. V. (2004). Ordered  $\text{Ca}_3\text{TaGa}_3\text{Si}_2\text{O}_{14}$  crystals: Growth, electromechanical and optical properties. *2004 18th European Frequency and Time Forum (EFTF 2004)*, IET, Guildford, UK, 216–219 pp. <https://ieeexplore.ieee.org/abstract/document/5074944>
- Poirier, J.-P. (1985). *Creep of Crystals: High-Temperature Deformation Processes in Metals, Ceramics and Minerals (Illustrated edition)*. Cambridge, United Kingdom: Cambridge University Press, 234 pp. <https://doi.org/10.1017/cbo9780511564451>
- Polian, A. (2003). Brillouin scattering at high pressure: An overview. *Journal of Raman Spectroscopy*, *34*(7–8), 633–637. <https://doi.org/10.1002/jrs.1031>
- Poplavko, Ū. M. (2019). *Electronic materials: Principles and applied science (First Edition)*. Amsterdam NL: Elsevier, 126 pp.
- Price, G. D. (2010). In: *Schubert, G. (ed.), Treatise on Geophysics, Vol. 2 – Mineral Physics*. Amsterdam, Netherlands: Elsevier, 567–570 pp.
- Pugh, H. Ll. D. (1979). Mechanical Behavior of Solids at High Pressure. In K. D. Timmerhaus & M. S. Barber (eds.), *High-Pressure Science and Technology*, Springer US, New York, pp. 1515–1543. [https://doi.org/10.1007/978-1-4684-7470-1\\_191](https://doi.org/10.1007/978-1-4684-7470-1_191)

## Bibliography

- Raterron, P., Chen, J., Li, L., Weidner, D., & Cordier, P. (2007). Pressure-induced slip-system transition in forsterite: Single-crystal rheological properties at mantle pressure and temperature. *American Mineralogist*, *92*(8–9), 1436–1445.  
<https://doi.org/10.2138/am.2007.2474>
- Raterron, P., Wu, Y., Weidner, D. J., & Chen, J. (2004). Low-temperature olivine rheology at high pressure. *Physics of the Earth and Planetary Interiors*, *145*(1), 149–159.  
<https://doi.org/10.1016/j.pepi.2004.03.007>
- Renner, J., Stöckhert, B., Zerbian, A., Röller, K., & Rummel, F. (2001). An experimental study into the rheology of synthetic polycrystalline coesite aggregates. *Journal of Geophysical Research: Solid Earth*, *106*(B9), 19411–19429.  
<https://doi.org/10.1029/2001JB000431>
- Reuss, A. (1929). Berechnung der Fließgrenze von Mischkristallen auf Grund der Plastizitätsbedingung für Einkristalle. *ZAMM - Journal of Applied Mathematics and Mechanics / Zeitschrift Für Angewandte Mathematik Und Mechanik*, *9*(1), 49–58.  
<https://doi.org/10.1002/zamm.19290090104>
- Rufner, J. F., Castro, R. H. R., Holland, T. B., & van Benthem, K. (2014). Mechanical properties of individual MgAl<sub>2</sub>O<sub>4</sub> agglomerates and their effects on densification. *Acta Materialia*, *69*, 187–195. <https://doi.org/10.1016/j.actamat.2014.01.051>
- Salzmann, C. G. (2019). Advances in the experimental exploration of water's phase diagram. *The Journal of Chemical Physics*, *150*(6), Art. 060901 (25 pp.)  
<https://doi.org/10.1063/1.5085163>
- Sano-Furukawa, A., Hattori, T., Arima, H., Yamada, A., Tabata, S., Kondo, M., Nakamura, A., Kagi, H., & Yagi, T. (2014). Six-axis multi-anvil press for high-pressure, high-temperature neutron diffraction experiments. *Review of Scientific Instruments*, *85*(11), Art. 115903 (10 pp.). <https://doi.org/10.1063/1.4901095>

## Bibliography

- Scarponi, F., Mattana, S., Corezzi, S., Caponi, S., Comez, L., Sassi, P., Morresi, A., Paolantoni, M., Urbanelli, L., Emiliani, C., Roscini, L., Corte, L., Cardinali, G., Palombo, F., Sandercock, J. R., & Fioretto, D. (2017). High-Performance Versatile Setup for Simultaneous Brillouin-Raman Microspectroscopy. *Physical Review X*, 7(3), Art. 031015 (17 pp.). 031015. <https://doi.org/10.1103/PhysRevX.7.031015>
- Schlichting, K. W., Padture, N. P., & Klemens, P. G. (2001). Thermal conductivity of dense and porous yttria-stabilized zirconia. *Journal of Materials Science*, 36(12), 3003–3010. <https://doi.org/10.1023/A:1017970924312>
- Sciamanna, V., Nait-Ali, B., & Gonon, M. (2015). Mechanical properties and thermal conductivity of porous alumina ceramics obtained from particle stabilized foams. *Ceramics International*, 41(2, Part A), 2599–2606. <https://doi.org/10.1016/j.ceramint.2014.10.011>
- Shim, Dan S.-H. (2022). X-ray diffraction data analysis for high pressure and high temperature experiments (Version 7.7.34), Zenodo, Geneva [Computer software]. <https://doi.org/10.5281/ZENODO.6640493>
- Shannon, R. D. (1993). Dielectric polarizabilities of ions in oxides and fluorides. *Journal of Applied Physics*, 73(1), 348–366. <https://doi.org/10.1063/1.353856>
- Sherrit, S., Van Nice, D. B., Graham, J. T., Mukherjee, B. K., & Wiederick, H. D. (1992). Domain wall motion in piezoelectric materials under high stress. *ISAF 1992 - Proceedings of the 8th IEEE International Symposium on Applications of Ferroelectrics*, IEEE, Greenville, SC, USA, 167–170. <https://doi.org/10.1109/ISAF.1992.300653>
- Shi, X., Yuan, D., Yin, X., Wei, A., Guo, S., & Yu, F. (2007). Crystal growth and dielectric, piezoelectric and elastic properties of Ca<sub>3</sub>TaGa<sub>3</sub>Si<sub>2</sub>O<sub>14</sub> single crystal. *Solid State Communications*, 142(3), 173–176. <https://doi.org/10.1016/j.ssc.2007.01.047>

## Bibliography

- Shiau, S. M., Anderson, T. L., Newnham, R. E., & Cross, L. E. (1984). Temperature dependence of ferroelastic switching in quartz. In *Materials Research Bulletin*, 19, 831–836. [https://doi.org/10.1016/0025-5408\(84\)90044-8](https://doi.org/10.1016/0025-5408(84)90044-8)
- Shimada, M. (1981). The method of compression test under high pressures in a cubic press and the strength of granite. *Tectonophysics*, 72(3), 343–357. [https://doi.org/10.1016/0040-1951\(81\)90245-6](https://doi.org/10.1016/0040-1951(81)90245-6)
- Singh, A. K. (2012). Strength of solid helium under high pressure. *Journal of Physics: Conference Series*, 377(1), Art. 012007 (6 pp.). <https://doi.org/10.1088/1742-6596/377/1/012007>
- Singh, A. K., Balasingh, C., Mao, H., Hemley, R. J., & Shu, J. (1998). Analysis of lattice strains measured under nonhydrostatic pressure. *Journal of Applied Physics*, 83(12), 7567–7575. <https://doi.org/10.1063/1.367872>
- Sin'ko, G. V. (2008). Ab initio calculations of the second-order elastic constants of crystals under arbitrary isotropic pressure. *Physical Review B*, 77(10), Art. 104118 (8 pp.). <https://doi.org/10.1103/PhysRevB.77.104118>
- Sinogeikin, S., Bass, J., Prakapenka, V., Lakshtanov, D., Shen, G., Sanchez-Valle, C., & Rivers, M. (2006). Brillouin spectrometer interfaced with synchrotron radiation for simultaneous x-ray density and acoustic velocity measurements. *Review of Scientific Instruments*, 77(10), Art. 103905 (7 pp.). <https://doi.org/10.1063/1.2360884>
- Skemer, P. A., Kranjc, K., Rouse, Z., & Flores, K. (2015). Low Temperature Plasticity of Olivine Determined by Nano-indentation. *abstract MR23C-01. AGU Fall Meeting Abstracts*. San Francisco, California, USA.
- Sokol, M., Kalabukhov, S., Shneck, R., Zaretsky, E., & Frage, N. (2017). Effect of grain size on the static and dynamic mechanical properties of magnesium aluminate spinel (MgAl<sub>2</sub>O<sub>4</sub>). *Journal of the European Ceramic Society*, 37(10), 3417–3424. <https://doi.org/10.1016/j.jeurceramsoc.2017.04.025>

## Bibliography

- Sotnikov, A., Schmidt, H., Weihnacht, M., Buzanov, O., & Sakharov, S. (2013). Material parameters of  $\text{Ca}_3\text{TaGa}_3\text{Si}_2\text{O}_{14}$  single crystal revisited. *2013 IEEE International Ultrasonics Symposium (IUS)*, Prague, Czech Rep. 1688–1691.  
<https://doi.org/10.1109/ULTSYM.2013.0430>
- Speziale, S., Marquardt, H., & Duffy, T. S. (2014). Brillouin Scattering and its Application in Geosciences. *Reviews in Mineralogy and Geochemistry*, *78*(1), 543–603.  
<https://doi.org/10.2138/rmg.2014.78.14>
- Suhak, Y., Schulz, M., Johnson, W. L., Sotnikov, A., Schmidt, H., & Fritze, H. (2018). Electromechanical properties and charge transport of  $\text{Ca}_3\text{TaGa}_3\text{Si}_2\text{O}_{14}$  (CTGS) single crystals at elevated temperatures. *Solid State Ionics*, *317*, 221–228.  
<https://doi.org/10.1016/j.ssi.2018.01.032>
- Sun, S., Zhang, X., Cui, J., & Liang, S. (2020). Identification of the Miller indices of a crystallographic plane: A tutorial and a comprehensive review on fundamental theory, universal methods based on different case studies and matters needing attention. *Nanoscale*, *12*(32), 16657–16677. <https://doi.org/10.1039/D0NR03637D>
- Swab, J. J., & Pittari III, J. J. (2023). Compression strength of tungsten carbide–cobalt hard metals. *International Journal of Applied Ceramic Technology*, *20*(1), 509–518.  
<https://doi.org/10.1111/ijac.14208>
- Tange, Y., Nishihara, Y., & Tsuchiya, T. (2009). Unified analyses for P-V-T equation of state of MgO: A solution for pressure-scale problems in high P-T experiments. *Journal of Geophysical Research: Solid Earth*, *114*(B3), Art. B03208.  
<https://doi.org/10.1029/2008JB005813>
- Tekkaya, A. E., & Lange, K. (2000). An Improved Relationship between Vickers Hardness and Yield Stress for Cold Formed Materials and its Experimental Verification. *CIRP Annals – Manufacturing Technology*, *49*(1), 205–208. [https://doi.org/10.1016/S0007-8506\(07\)62929-1](https://doi.org/10.1016/S0007-8506(07)62929-1)

## Bibliography

- Ter Heege, J. H., & Renner, J. (2007). In situ impedance spectroscopy on pyrophyllite and CaCO<sub>3</sub> at high pressure and temperature: Phase transformations and kinetics of atomistic transport. *Physics and Chemistry of Minerals*, 34(7), 445–465.  
<https://doi.org/10.1007/s00269-007-0162-x>
- Tichý, J., Erhart, J., Kittinger, E., & Přívratská, J. (2010). *Fundamentals of Piezoelectric Sensorics: Mechanical, Dielectric, and Thermodynamical Properties of Piezoelectric Materials*. Springer-Verlag, Berlin & Heidelberg, 207 pp.  
<https://doi.org/10.1007/978-3-540-68427-5>
- Thieme, M., Demouchy, S., Mainprice, D., Barou, F., & Cordier, P. (2018). Stress evolution and associated microstructure during transient creep of olivine at 1000–1200 °C. *Physics of the Earth and Planetary Interiors*, 278, 34–46.  
<https://doi.org/10.1016/j.pepi.2018.03.002>
- Thomas, E. (2006). Crystal growth and the search for highly correlated ternary intermetallic antimonides and stannides. *PhD thesis*, Louisiana State University, Baton Rouge, 172 pp. [https://doi.org/10.31390/gradschool\\_dissertations.1788](https://doi.org/10.31390/gradschool_dissertations.1788)
- Thomas, L. A., Wooster, W. A., & Ryde J. W. (1951). Piezoescence—The growth of Dauphiné twinning in quartz under stress. *Proceedings of the Royal Society of London. Series A. Mathematical and Physical Sciences*, 208(1092), 43–62.  
<https://doi.org/10.1098/rspa.1951.0143>
- Thompson, R. M., Downs, R. T., & Dera, P. (2011). The compression pathway of quartz. *American Mineralogist*, 96(10), 1495–1502. <https://doi.org/10.2138/am.2011.3843>
- Tielke, J. A., Zimmerman, M. E., & Kohlstedt, D. L. (2016). Direct shear of olivine single crystals. *Earth and Planetary Science Letters*, 455, 140–148.  
<https://doi.org/10.1016/j.epsl.2016.09.002>

## Bibliography

- Ting, C.-J., & Lu, H.-Y. (1999). Defect Reactions and the Controlling Mechanism in the Sintering of Magnesium Aluminate Spinel. *Journal of the American Ceramic Society*, 82(4), 841–848. <https://doi.org/10.1111/j.1151-2916.1999.tb01844.x>
- Ugarak, F., Iglesias Martínez, J. A., Mosset, A., & Laude, V. (2023). Estimation of the elastic and piezoelectric tensors of sapphire and lithium niobate from Brillouin light backscattering measurements of a single crystal sample. *Journal of Applied Physics*, 134(18), Art. 185103 (9 pp). <https://doi.org/10.1063/5.0169889>
- Vartanyants, I. A., & Zegenhagen, J. (1999). Photoelectric scattering from an X-ray interference field. *Solid State Communications*, 113(6), 299–320. [https://doi.org/10.1016/S0038-1098\(99\)00399-3](https://doi.org/10.1016/S0038-1098(99)00399-3)
- Violay, M., Gibert, B., Mainprice, D., & Burg, J.-P. (2015). Brittle versus ductile deformation as the main control of the deep fluid circulation in oceanic crust. *Geophysical Research Letters*, 42(8), 2767–2773. <https://doi.org/10.1002/2015GL063437>
- Violay, M., Heap, M. J., Acosta, M., & Madonna, C. (2017). Porosity evolution at the brittle-ductile transition in the continental crust: Implications for deep hydro-geothermal circulation. *Scientific Reports*, 7(1), Art. 7705 (11 pp). <https://doi.org/10.1038/s41598-017-08108-5>
- Vos, W. L., van Hinsberg, M. G. E., & Schouten, J. A. (1990). High-pressure triple point in helium: The melting line of helium up to 240 kbar. *Physical Review B*, 42(10), 6106–6109. <https://doi.org/10.1103/PhysRevB.42.6106>
- Walker, A. N., Rutter, E. H., & Brodie, K. H. (1990). Experimental study of grain-size sensitive flow of synthetic, hot-pressed calcite rocks. *Geological Society, London, Special Publications*, 54(1), 259–284. <https://doi.org/10.1144/GSL.SP.1990.054.01.24>
- Wallis, D., Hansen, L. N., Kumamoto, K. M., Thom, C. A., Plümper, O., Ohl, M., Durham, W. B., Goldsby, D. L., Armstrong, D. E. J., Meyers, C. D., Goddard, R. M., Warren, J. M., Breithaupt, T., Drury, M. R., & Wilkinson, A. J. (2020). Dislocation interactions

## Bibliography

- during low-temperature plasticity of olivine and their impact on the evolution of lithospheric strength. *Earth and Planetary Science Letters*, 543, Art. 116349 (12 pp).  
<https://doi.org/10.1016/j.epsl.2020.116349>
- Wang, Durham, W. B., Getting, I. C., & Weidner, D. J. (2003). The deformation-DIA: A new apparatus for high temperature triaxial deformation to pressures up to 15 GPa. *Review of Scientific Instruments*, 74(6), 3002–3011. <https://doi.org/10.1063/1.1570948>
- Wang, H., He, D., Yan, X., Xu, C., Guan, J., Tan, N., & Wang, W. (2011). Quantitative measurements of pressure gradients for the pyrophyllite and magnesium oxide pressure-transmitting mediums to 8 GPa in a large-volume cubic cell. *High Pressure Research*, 31(4), 581–591. <https://doi.org/10.1080/08957959.2011.614238>
- Wang, J., Mao, Z., Jiang, F., & Duffy, T. S. (2015). Elasticity of single-crystal quartz to 10 GPa. *Physics and Chemistry of Minerals*, 42(3), 203–212.  
<https://doi.org/10.1007/s00269-014-0711-z>
- Wang, W., Liu, B., & Kodur, V. (2013). Effect of Temperature on Strength and Elastic Modulus of High-Strength Steel. *Journal of Materials in Civil Engineering*, 25(2), 174–182. [https://doi.org/10.1061/\(ASCE\)MT.1943-5533.0000600](https://doi.org/10.1061/(ASCE)MT.1943-5533.0000600)
- Weidner, D., Wang, Y., Chen, G., Ando, J., & Vaughan, M. (1998). In M. H. Manghnani & T. Yagi (eds.), *Properties of Earth and Planetary Materials at High Pressure and Temperature*. Geophysical Monograph 101. American Geophysical Union, Washington DC, pp. 473–482. <https://doi.org/10.1029/GM101>
- Wentorf, R. H. (Robert H. ). (1962). *Modern very high pressure techniques*. London, United Kingdom: Butterworths. 256 pp. <https://cir.nii.ac.jp/crid/1130000794613216768>
- Wentzcovitch, R. M., da Silva, C., Chelikowsky, J. R., & Binggeli, N. (1998). A New Phase and Pressure Induced Amorphization in Silica. *Physical Review Letters*, 80(10), 2149–2152. <https://doi.org/10.1103/PhysRevLett.80.2149>

## Bibliography

- Westbrook, J. H. (1958). Temperature Dependence of Strength and Brittleness of Some Quartz Structures. *Journal of the American Ceramic Society*, 41(11), 433–440.  
<https://doi.org/10.1111/j.1151-2916.1958.tb12891.x>
- Wilshire, B. (1995). Creep mechanisms in single and polycrystalline MgO. *British Ceramic Transactions*, 94(2), 57–63. Maney, London.
- Wojdyr, M. (2010). Fityk: A general-purpose peak fitting program. *Journal of Applied Crystallography*, 43(5), 1126–1128. <https://doi.org/10.1107/S0021889810030499>
- Voigt, W. (1928). *Lehrbuch der Kristallphysik (Textbook of crystal physics)*. Leipzig & Berlin, Germany: BG Teubner, 62 pp.
- Wolff, C., Smith, M. J. A., Stiller, B., & Poulton, C. G. (2021). Brillouin scattering—theory and experiment: Tutorial. *Journal of the Optical Society of America B*, 38(4), 1243–1289. <https://doi.org/10.1364/JOSAB.416747>
- Xiuwei, F. (2016). Influence of Oxygen Partial Pressure and Al Content on the Resistivity and Piezoelectric Properties of  $\text{Ca}_3\text{TaGa}_{3-x}\text{Al}_x\text{Si}_2\text{O}_{14}$  Single Crystals. (*Doctoral dissertation, Waseda University*).
- Yamaoka, H., Zekko, Y., Jarrige, I., Lin, J.-F., Hiraoka, N., Ishii, H., Tsuei, K.-D., & Mizuki, J. (2012). Ruby pressure scale in a low-temperature diamond anvil cell. *Journal of Applied Physics*, 112(12), Art. 124503 (7 pp.). <https://doi.org/10.1063/1.4769305>
- Yamazaki, D. (2020). Pressure generation in the Kawai-type multianvil apparatus and rheology of the earth's interior. *Japanese Magazine of Mineralogical and Petrological Sciences*, 49(1), 15–27. <https://doi.org/10.2465/GKK.191226>
- Yamazaki, D., & Karato, S. (2001). High-pressure rotational deformation apparatus to 15 GPa. *Review of Scientific Instruments*, 72(11), 4207–4211.  
<https://doi.org/10.1063/1.1412858>

## Bibliography

- Yamni, K. (2001). Temperature effect on the ferrobielastic behaviour of quartz crystals. *Annales de Chimie Science des Matériaux*, 26(1), 19–22.  
[https://doi.org/10.1016/S0151-9107\(01\)90005-4](https://doi.org/10.1016/S0151-9107(01)90005-4)
- Yang, J. (2004). *An Introduction to the Theory of Piezoelectricity (Second Edition)*. New York, United States: Springer. 327 pp.
- Yoneda, A. (1990). Pressure Derivatives of Elastic Constants of Single Crystal MgO and MgAl<sub>2</sub>O<sub>4</sub>. *Journal of Physics of the Earth*, 38(1), 19–55.  
<https://doi.org/10.4294/jpe1952.38.19>
- Yusuke, S. (2010). Development of a software suite on X-ray diffraction experiments. *The Review of High Pressure Science and Technology*, 20, 269–276.
- Zha, C.-S., Mao, H., & Hemley, R. J. (2004). Elasticity of dense helium. *Physical Review B*, 70(17), Art. 174107 (8 pp.). <https://doi.org/10.1103/PhysRevB.70.174107>
- Zhang, J., Liu, F., Wu, J., Liu, Y., Hu, Q., Liu, J., Liang, A., Wang, Q., & He, D. (2018). Experimental study on the pressure-generation efficiency and pressure-seal mechanism for large volume cubic press. *Review of Scientific Instruments*, 89(7), 075106. <https://doi.org/10.1063/1.5030092>
- Zhang, S., & Yu, F. (2011). Piezoelectric materials for high temperature sensors. *Journal of the American Ceramic Society*, 89(7), Art. 075106 (8 pp.).  
<https://doi.org/10.1111/j.1551-2916.2011.04792.x>
- Zhang, S., Zheng, Y., Kong, H., Xin, J., Frantz, E., & Shrout, T. R. (2009). Characterization of high temperature piezoelectric crystals with an ordered langasite structure. *Journal of Applied Physics*, 105(11), Art. 114110 (8 pp.). <https://doi.org/10.1063/1.3142429>
- Zu, H., Lin, Q., Wu, H., Zheng, Y., & Wang, Q.-M. (2016). Characterization of the Dielectric, Piezoelectric, and Elastic Coefficients of Ca<sub>3</sub>TaGa<sub>3</sub>Si<sub>2</sub>O<sub>14</sub> Single Crystals up to 800 °C. *IEEE Transactions on Ultrasonics, Ferroelectrics, and Frequency Control*, 63(5), 764–777. <https://doi.org/10.1109/TUFFC.2016.2544662>

## Bibliography

## **(Eidesstattliche) Versicherungen und Erklärungen**

(§ 9 Satz 2 Nr. 3 PromO BayNAT)

*Hiermit versichere ich eidesstattlich, dass ich die Arbeit selbstständig verfasst und keine anderen als die von mir angegebenen Quellen und Hilfsmittel benutzt habe (vgl. Art. 97 Abs. 1 Satz 8 BayHIG).*

(§ 9 Satz 2 Nr. 3 PromO BayNAT)

*Hiermit erkläre ich, dass ich die Dissertation nicht bereits zur Erlangung eines akademischen Grades eingereicht habe und dass ich nicht bereits diese oder eine gleichartige Doktorprüfung endgültig nicht bestanden habe.*

(§ 9 Satz 2 Nr. 4 PromO BayNAT)

*Hiermit erkläre ich, dass ich Hilfe von gewerblichen Promotionsberatern bzw. -vermittlern oder ähnlichen Dienstleistern weder bisher in Anspruch genommen habe noch künftig in Anspruch nehmen werde.*

(§ 9 Satz 2 Nr. 7 PromO BayNAT)

*Hiermit erkläre ich mein Einverständnis, dass die elektronische Fassung meiner Dissertation unter Wahrung meiner Urheberrechte und des Datenschutzes einer gesonderten Überprüfung unterzogen werden kann.*

(§ 9 Satz 2 Nr. 8 PromO BayNAT)

*Hiermit erkläre ich mein Einverständnis, dass bei Verdacht wissenschaftlichen Fehlverhaltens Ermittlungen durch universitätsinterne Organe der wissenschaftlichen Selbstkontrolle stattfinden können.*

.....  
Ort, Datum, Unterschrift